

2  
1

3 THÈSE DE DOCTORAT DE L'UNIVERSITÉ PARIS-SACLAY PRÉPARÉE À  
4 L'UNIVERSITÉ PARIS-SUD

5 ÉCOLE DOCTORALE N°576

# 6 Particules Hadrons Énergie et Noyau : Instrumentation, Image, Cosmos et Simulation (PHENIICS)

## 7 Spécialité de doctorat : Physique des particules expérimentale

Par 8

9 M. Mykola Khandoga

10 CALIBRATION OF ELECTRON SHOWER SHAPES, HADRONIC RECOIL RECONSTRUCTION  
11 USING DEEP LEARNING ALGORITHMS AND THE MEASUREMENT OF  $W$  BOSON  
12 TRANSVERSE MOMENTUM DISTRIBUTION WITH THE ATLAS DETECTOR.

*1Thèse présentée et soutenue à ??, le ?? septembre 2020*

#### 14 Composition de jury:

<sup>15</sup>Alessandro Viccini, *Professeur, Université de Lefutur, Rapporteur*

<sup>16</sup>Andrew Pilkington, *Professeur, Université de Serenity, Rapporteur*

<sup>17</sup>David Rousseau, Directeur de recherche, Université de l'Alliance, Examinateur

<sup>18</sup>Aram Apyan, *Staff researcher, TU Arcturan, Examinatrice*

<sup>19</sup>Fabrice Balli, Ingénieur-chercheur, CEA Saclay CoDirecteur de thèse

<sup>20</sup>Maarten Boonekamp, Ingénieur-chercheur, CEA Saclay, Directeur de thèse



**Titre:** Un titre long et beau qui prend probablement plus d'une ligne

**Mots clés:** *physique de particules, electrofaible precision, boson W, dark arts, space travel*

**Résumé:** Lorem ipsum dolor sit amet, consectetur adipiscing elit. Ut purus elit, vestibulum ut, placerat ac, adipiscing vitae, felis. Curabitur dictum gravida mauris. Nam arcu libero, nonummy eget, consectetur id, vulputate a, magna. Donec vehicula augue eu neque. Pellentesque habitant morbi tristique senectus et netus et malesuada fames ac turpis egestas. Mauris ut leo. Cras viverra metus rhoncus sem. Nulla et lectus vestibulum urna fringilla ultrices. Phasellus eu tellus sit amet tortor gravida placerat. Integer sapien est, iaculis in, pretium quis, viverra ac, nunc. Praesent eget sem vel leo ultrices bibendum. Aenean faucibus. Morbi dolor nulla, malesuada eu, pulvinar at, mollis ac, nulla. Curabitur auctor semper nulla. Donec varius orci eget risus. Duis nibh mi, congue eu, accumsan eleifend, sagittis quis, diam. Duis eget orci sit amet orci dignissim rutrum.

Nam dui ligula, fringilla a, euismod sodales, sollicitudin vel, wisi. Morbi auctor lorem non justo. Nam lacus libero, pretium at, lobortis vitae, ultricies et, tellus. Donec aliquet, tortor sed accumsan bibendum, erat ligula aliquet magna, vitae ornare odio metus a mi. Morbi ac orci et nisl hendrerit mollis. Suspendisse ut massa. Cras nec ante. Pellentesque a nulla. Cum sociis natoque penatibus et magnis dis parturient montes, nascetur ridiculus mus. Aliquam tincidunt urna. Nulla ullamcorper vestibulum turpis. Pellentesque cursus luctus mauris.

Nulla malesuada porttitor diam. Donec felis erat, congue non, volutpat at, tincidunt tristique, libero. Vivamus viverra fermentum felis. Donec nonummy pellentesque ante. Phasellus adipiscing semper elit. Proin fermentum massa ac quam. Sed diam turpis, molestie vitae, placerat a, molestie nec, leo. Maecenas lacinia. Nam ipsum ligula, eleifend at, accumsan nec, suscipit a, ipsum. Morbi blandit ligula feugiat magna. Nunc eleifend consequat lorem. Sed lacinia nulla vitae enim. Pellentesque tincidunt purus vel magna. Integer non enim. Praesent euismod nunc eu purus. Donec bibendum quam in tellus. Nullam cursus pulvinar lectus. Donec et mi. Nam vulputate metus eu enim. Vestibulum pellentesque felis eu massa.





**Title:** A long and beautiful title that probably takes more than one line

**Key words:** particle physics, electroweak precision, W boson, dark arts, space travel

**Abstract:** Lorem ipsum dolor sit amet, consectetur adipiscing elit. Ut purus elit, vestibulum ut, placerat ac, adipiscing vitae, felis. Curabitur dictum gravida mauris. Nam arcu libero, nonummy eget, consectetur id, vulputate a, magna. Donec vehicula augue eu neque. Pellentesque habitant morbi tristique senectus et netus et malesuada fames ac turpis egestas. Mauris ut leo. Cras viverra metus rhoncus sem. Nulla et lectus vestibulum urna fringilla ultrices. Phasellus eu tellus sit amet tortor gravida placerat. Integer sapien est, iaculis in, pretium quis, viverra ac, nunc. Praesent eget sem vel leo ultrices bibendum. Aenean faucibus. Morbi dolor nulla, malesuada eu, pulvinar at, mollis ac, nulla. Curabitur auctor semper nulla. Donec varius orci eget risus. Duis nibh mi, congue eu, accumsan eleifend, sagittis quis, diam. Duis eget orci sit amet orci dignissim rutrum.

Nam dui ligula, fringilla a, euismod sodales, sollicitudin vel, wisi. Morbi auctor lorem non justo. Nam lacus libero, pretium at, lobortis vitae, ultricies et, tellus. Donec aliquet, tortor sed accumsan bibendum, erat ligula aliquet magna, vitae ornare odio metus a mi. Morbi ac orci et nisl hendrerit mollis. Suspendisse ut massa. Cras nec ante. Pellentesque a nulla. Cum sociis natoque penatibus et magnis dis parturient montes, nascetur ridiculus mus. Aliquam tincidunt urna. Nulla ullamcorper vestibulum turpis. Pellentesque cursus luctus mauris.

Nulla malesuada porttitor diam. Donec felis erat, congue non, volutpat at, tincidunt tristique, libero. Vivamus viverra fermentum felis. Donec nonummy pellentesque ante: Phasellus adipiscing semper elit. Proin fermentum massa ac quam. Sed diam turpis, molestie vitae, placerat a, molestie nec, leo. Maecenas lacinia. Nam ipsum ligula, eleifend at, accumsan nec, suscipit a, ipsum. Morbi blandit ligula feugiat magna. Nunc eleifend consequat lorem. Sed lacinia nulla vitae enim. Pellentesque tincidunt purus et magna. Integer non enim.. Praesent euismod nunc eu purus.. Donec bibendum quam in tellus. Nullam cursus pulvinar lectus. Donec et mi. Nam vulputate metus eu enim. Vestibulum pellentesque felis eu massa.

30      Bibliography

5

## Contents

31	<b>1 The Standard Model</b>	7
32	1.1 General composition and key parameters . . . . .	7
33	1.2 Classical fields and gauge invariance principle . . . . .	10
34	1.3 Quantum electrodynamics . . . . .	12
35	1.4 Electroweak theory and the Higgs mechanism . . . . .	13
36	1.4.1 Electroweak gauge fields . . . . .	14
37	1.4.2 Fermion sector . . . . .	14
38	1.4.3 Higgs field breaking the symmetry . . . . .	15
39	1.4.4 Physical interpretation of gauge fields and parameters . . . . .	16
40	1.5 Chromodynamics . . . . .	17
41	Bibliography . . . . .	19
42	<b>2 The W boson</b>	23
43	2.1 The motivation for the W mass measurement . . . . .	23
44	2.2 Massive boson production at hadron colliders . . . . .	24
45	2.2.1 Deep Inelastic scattering . . . . .	25
46	2.2.2 The Drell-Yan process . . . . .	27
47	2.3 Transverse momentum of massive vector bosons . . . . .	29
48	Bibliography . . . . .	32
49	<b>3 The Large Hadron Collider</b>	35
50	3.1 Introduction . . . . .	35
51	3.2 The LHC running sequence . . . . .	35
52	3.3 Special low pile-up run during LHC Run 2 . . . . .	39
53	Bibliography . . . . .	40



54	<b>4 The ATLAS detector</b>	43
55	4.1 General description and layout . . . . .	43
56	4.2 Coordinate system . . . . .	43
57	4.3 Magnet system and magnetic field . . . . .	44
58	4.4 Inner detector . . . . .	44
59	4.5 Calorimeter system . . . . .	46
60	4.5.1 Electromagnetic calorimeter . . . . .	48
61	4.5.2 Hadronic calorimeter . . . . .	50
62	4.6 Muon detectors . . . . .	51
63	4.7 Forward detectors . . . . .	53
64	4.8 Trigger system . . . . .	55
65	Bibliography . . . . .	57
66	<b>5 Electromagnetic shower shapes correction in the electromagnetic calorimeter</b>	59
67	5.1 Introduction . . . . .	59
68	5.2 Shower shapes measurement and correction . . . . .	62
69	5.2.1 Event selection . . . . .	62
70	5.2.2 Data/MC discrepancies . . . . .	62
71	5.2.3 The correction procedure . . . . .	64
72	5.3 Results . . . . .	65
73	5.4 Appendix: control plots . . . . .	66
74	Bibliography . . . . .	68
75	<b>6 Event reconstruction</b>	77
76	6.1 Charged particles track reconstruction . . . . .	77
77	6.2 Determining the primary vertex of the event . . . . .	78
78	6.3 Muon reconstruction and identification . . . . .	80
79	6.3.1 Muon reconstruction . . . . .	80
80	6.3.2 Muon identification . . . . .	82
81	6.3.3 Muon isolation . . . . .	83
82	6.4 Electron reconstruction and identification . . . . .	83
83	6.4.1 Electron reconstruction . . . . .	83
84	6.4.2 Electron identification . . . . .	87
85	6.4.3 Electron isolation . . . . .	88
86	6.5 Particle flow objects . . . . .	90
87	Bibliography . . . . .	92
88	<b>7 Calibrations and corrections</b>	95
89	7.1 Electron corrections . . . . .	95
90	7.1.1 Energy scale and resolution correction . . . . .	95

---

91	7.1.2	Electron selection efficiency . . . . .	100
92	7.1.3	SF uncertainties propagation . . . . .	104
93	7.2	Muon corrections . . . . .	112
94	7.2.1	Muon momentum calibration . . . . .	112
95	7.2.2	Correction for charge-dependent momentum bias . . . . .	113
96	7.2.3	Muon efficiency measurements . . . . .	120
97	7.3	Hadronic recoil calibration . . . . .	125
98	7.3.1	SET- $u_T$ reweighting . . . . .	126
99	7.3.2	$u_X$ and $u_Y$ correction . . . . .	129
100	7.3.3	Resolution and response corrections . . . . .	130
101	7.3.4	Hadronic recoil calibration uncertainties . . . . .	132
102	7.4	Angular coefficients correction . . . . .	133
103	Bibliography . . . . .		134
104	<b>8</b>	<b>MC samples and selection</b>	<b>137</b>
105	8.1	Data and MC samples . . . . .	137
106	8.1.1	Data samples . . . . .	137
107	8.1.2	MC samples and cross-sections . . . . .	139
108	8.2	Multijet background . . . . .	144
109	8.3	Z vertex reweighting . . . . .	150
110	8.4	W analysis event selection and control plots . . . . .	150
111	8.4.1	Event selection . . . . .	151
112	8.4.2	$\sqrt{s} = 13$ TeV dataset control plots . . . . .	151
113	8.4.3	$\sqrt{s} = 5$ TeV dataset control plots . . . . .	161
114	Bibliography . . . . .		168
115	<b>9</b>	<b>W boson pT spectrum</b>	<b>171</b>
116	9.1	Unfolding . . . . .	171
117	9.2	Propagation of uncertainties . . . . .	172
118	9.2.1	Statistical uncertainty propagation using Bootstrap method . . . . .	172
119	9.2.2	Systematic uncertainty propagation . . . . .	173
120	9.2.3	Unfolded uncertainty breakdown . . . . .	173
121	9.3	Unfolding bias . . . . .	178
122	9.4	Results . . . . .	180
123	Bibliography . . . . .		181
124	<b>10</b>	<b>Hadronic recoil regression with deep neural networks</b>	<b>183</b>
125	10.1	Deep neural networks . . . . .	183
126	10.1.1	Gradient descent optimization . . . . .	183
127	10.1.2	DNN structure and training . . . . .	185

---

128	10.1.3 Batch normalization . . . . .	187
129	10.2 HR regression . . . . .	188
130	10.2.1 Input features and model . . . . .	188
131	10.2.2 Kinematic distributions . . . . .	190
132	10.3 Conclusions . . . . .	192
133	Bibliography . . . . .	194
134	<b>11 Appendix A</b>	<b>197</b>
135	11.1 Experimental uncertainties of main observables . . . . .	197
136	<b>12 Appendix B</b>	<b>205</b>

## List of Figures

138	11 The list of particles that enters the Standard Model (SM)[ <a href="#">sm_wiki</a> ]. . . . .	9
139	12 The running of the inverted SM coupling constants [ <a href="#">coupl_wiki</a> ]. . . . .	10
140	13 Examples of QED diagrams: Compton scattering, electron self-energy, photon self-energy.	13
141	14 Electroweak sector and the Weinberg rotation [ <a href="#">coupl_wiki</a> ]. . . . .	18
142	15 The formation of a hadron jet [ <a href="#">conf_wiki</a> ]. . . . .	19
143	21 Next-to-leading order diagrams for W boson propagator containing contributions from heavy quarks and the Higgs boson. . . . .	23
144	22 W mass measurements and predictions [20]. . . . .	24
145	23 Examples of hard QCD scatterings. . . . .	25
146	24 The evolution of a PDF4LHC15 NNLO Hessian set from $Q^2 = 10^2$ GeV to $Q^2 = 10^4$ GeV using the DokshitzerGribovLipatovAltarelliParisi (DGLAP). Notice the increase in the sea quark density. The PDFs include one standard deviation uncertainty band [ <a href="#">proton_struct</a> ].	27
147	25 Rapidity distribution for the vector bosons using MSTW2008 and CTEQ6.6 PDF sets for the centre-of-mass energies of 7 and 14 TeV [ <a href="#">Halzen:2013bqa</a> ]. . . . .	28
148	26 Parton contributions to the cross-sections of $W^+$ and $W^-$ bosons for LHC and Tevatron cases [ <a href="#">Martin:392675</a> ]. . . . .	29
149	27 W and Z boson cross sections LHC at 7 TeV. ATLAS and CMS results, compared to NNLO predictions for various PDF sets [ <a href="#">Mangano:2015ejw</a> ]. . . . .	30

156	28	Kinematic distributions for $W^\pm$ with corrections. . . . .	31
157	31	A hydrogen tank supplies LHC with protons [ <b>hydro</b> ]. . . . .	36
158	32	Schematic depiction of the LHC ring. . . . .	37
159	33	Bunching at RF cavities . . . . .	37
160	34	Bunch crossing at the LHC. . . . .	38
161	35	Number of Interactions per bunch crossing in A Toroidal LHC ApparatuS (ATLAS) Run 2 [ <b>run2lumi</b> ]. The little bump around $\mu \approx 2$ corresponds to special low pile-up runs. . . . .	40
163	41	ATLAS detector general layout . . . . .	44
164	42	Geometry of ATLAS magnet windings . . . . .	45
165	44	ATLAS calorimeter general layout . . . . .	48
166	45	ATLAS EM calorimeter layers . . . . .	49
167	46	Accordion absorbers of the electromagnetic calorimeter (EMC) . . . . .	50
168	47	ATLAS muon system . . . . .	51
169	48	Cut views of the muon systems . . . . .	53
170	49	ATLAS forward detectors . . . . .	55
171	410	The scheme of ATLAS trigger systems . . . . .	57
172	51	The schematic portrayal of EM shower development . . . . .	59
173	52	Visualisations of the 7x11 calorimeter cluster . . . . .	60
174	53	Shower shapes in the second layer of the electromagnetic calorimeter . . . . .	60
175	54	Distribution of $R_\eta$ in simulation (GEANT4) for electrons and jets [ <b>sshapes_simulation</b> ]. . . . .	61
176	55	Data/MC Comparison for Calorimeter Shower Shapes of High Et Electrons [ <b>geant_corr</b> ]. . . . .	62
177	56	$R_\eta$ in the barrel and in the end-cap, Data vs MC . . . . .	63
178	57	$R_\phi$ in the barrel and in the end-cap, Data vs MC . . . . .	63
179	58	$W_\eta^2$ in the barrel and in the end-cap, Data vs MC . . . . .	64
180	59	$R_\phi$ in the barrel and in the end-cap, Data vs MC . . . . .	65
181	510	Schematic energy profile in $\phi$ dimension. Bremsstrahlung tails subtraction based on $e^+$ and $e^-$ energy profiles. . . . .	65
183	511	$R_\eta$ in the barrel and in the end-cap . . . . .	66
184	512	$R_\phi$ in the barrel and in the end-cap, Data, MC, reweighted MC . . . . .	67
185	513	$W_\eta^2$ in the barrel and in the end-cap, Data, MC, reweighted MC . . . . .	67
186	514	Distributions integrated over pT (a) $R_\phi$ ; (b) $R_\eta$ ; (c) $W_{\eta 2}$ . . . . .	68
187	515	Electron identification efficiency as a function of the electron pseudo-rapidity . . . . .	68
188	516	Reta 2 . . . . .	69
189	517	Rphi in all eta slices . . . . .	70
190	518	Reta 2 . . . . .	71
191	519	Reta 2 . . . . .	72
192	520	Reta 2 . . . . .	73

---

193	521	Reta 2 . . . . .	74
194	522	Reta 2 . . . . .	75
195	61	Impact parameters . . . . .	77
196	62	Ambiguity solving process [ATLAS:track2]. . . . .	79
197	63	Vertices . . . . .	80
198	64	sagitta . . . . .	81
199	65	Muon reconstruction . . . . .	82
200	66	Electron path . . . . .	84
201	67	topocluster . . . . .	85
202	68	Supercluster . . . . .	86
203	69	Isolation plot . . . . .	88
204	610	pflow . . . . .	90
205	71	Schematic overview of energy response calibration procedure for electrons and photons. . . . .	95
206	72	Energy scale factors $\alpha$ for low pile-up runs of 2017 (left), 2018 (right) and 2017 at 5TeV (bottom) using 68, 48 and 24 $\eta$ bins. It can be seen, that the extraction is unstable in case of 68 bins, resulting in $\alpha$ factors with very large uncertainties [int_note_electrons]. . . . .	97
209	73	Additional constant term $c'_i$ for low pile-up runs of 2017 (13 TeV), 2018 (13 TeV) and 2017 at 5 TeV using 24 bins. The lower panel shows the difference of $c'_i$ to the 2017 5 TeV run [int_note_electrons]. . . . .	98
212	74	The invariant mass distribution around the Z-mass for low pile-up Data for 2017 (13 TeV) [int_note_electrons] . . . . .	98
214	75	The invariant mass distribution around the Z-mass for low-pileup data for the $\sqrt{s} = 5$ TeV data taken in 2017 (a) and the $\sqrt{s} = 13$ TeV 2018 data (b) [int_note_electrons]. . . . .	99
216	76	Electron reconstruction efficiencies compared for low-pileup and high-pileup MC16 in $\eta$ range [0.60-0.80] (left) and [2.01-2.37] (right). The statistical uncertainties are shown [int_note_electrons]. . . . .	101
218	77	Comparison of the uncertainties due to electron reconstruction, contrasting the high- $\mu$ -extrapolated and in-situ-measured SF uncertainties in a $W^+ \rightarrow e^+ \nu$ selection at 13 TeV as function of typical kinematic variables [int_note_electrons]. . . . .	102
221	78	$E_T^{\text{cone}0.3}/25\text{GeV}$ isolation distribution of probe electrons in the ZIso-method using 13 TeV $339\text{ pb}^{-1}$ low-pileup data. Left the denominator and right the numerator distributions are shown, with the data as crosses, the signal $Z \rightarrow ee$ expectation as open line and the background estimate as cyan area (template normalised at high values) [int_note_electrons]. . . . .	103
225	79	Comparison of electron reconstruction SFs with 5 TeV and 13 TeV data as well as the 5+13 TeV combination in nine $\eta$ ranges as written in the plot legend, from most central $\eta = 0 - 0.1$ (top left) to most forward $\eta = 2.37 - 2.47$ (bottom right). The bottom panel shows the ratio of 5 TeV and 13 TeV SFs. The total uncertainties are shown [int_note_electrons]. . . . .	105

229	710	Electron isolation efficiencies (top panels) and scale factors (lower panels) for the $ptvarcone20/p_T^e < 0.1$ working point using 13 TeV $339 \text{ pb}^{-1}$ low-pileup data as function of $\eta$ in bins of $p_T$ [ <a href="#">int_note_electrons</a> ]. . . . .	106
232	711	Electron trigger efficiencies (top panels) and scale factors (lower panels) for HLT_e15_1hloose_nod0_L1EM using 13 TeV $339 \text{ pb}^{-1}$ low-pileup data as function of $\eta$ in bins of $p_T$ [ <a href="#">int_note_electrons</a> ]. . . . .	107
234	712	Total relative uncertainties of electron scale factors at 13 TeV measured with tag-and-probe method [ <a href="#">int_note_electrons</a> ]. . . . .	109
236	713	Contributions to the electron uncertainties related to efficiency SF (reconstruction, identification, isolation and trigger) in a $W^+ \rightarrow e^+ \nu$ selection at 13 TeV as function of typical kinematic variables [ <a href="#">int_note_electrons</a> ]. . . . .	110
239	714	Contributions to the electron uncertainties related to efficiency SF (reconstruction, identification, isolation and trigger) in a $W^+ \rightarrow e^+ \nu$ selection at 5 TeV as function of typical kinematic variables [ <a href="#">int_note_electrons</a> ]. . . . .	111
242	715	Example fits to $J/\psi \rightarrow \mu\mu$ (left) and $Z \rightarrow \mu\mu$ (right) mass peaks for pairs with leading muon pseudorapidity in the range $-0.62 < \eta < -0.52$ in low-pile-up 2017 13 TeV data [ <a href="#">int_note_muons</a> ]. . . . .	113
245	716	Mean (left) and width (right) of the $J/\psi \rightarrow \mu\mu$ mass peak as a function of the leading muon $\eta$ in 5.02 TeV data and MC. The mean and width are extracted from Crystal Ball components of the fits. In case of the simulation, both the uncorrected (dashed histogram) and corrected parameters (solid histogram) are shown. The fit results are presented for mass peaks constructed using kinematics of the muon ID tracks (top), ME tracks (middle) or CB tracks (bottom). The bottom panels in each plot show the data/MC ratio for uncorrected (dashed histogram) and corrected simulation (points) [ <a href="#">int_note_muons</a> ]. . . . .	115
252	717	Mean (left) and width (right) of the $J/\psi \rightarrow \mu\mu$ mass peak as a function of the leading muon $\eta$ in 2017 13 TeV data and MC at low pile-up. The mean and width are extracted from Crystal Ball components of the fits. In case of the simulation, both the uncorrected (dashed histogram) and corrected parameters (solid histogram) are shown. The fit results are presented for mass peaks constructed using kinematics of the muon ID tracks (top), ME tracks (middle) or CB tracks (bottom). The bottom panels in each plot show the data/MC ratio for uncorrected (dashed histogram) and corrected simulation (points) [ <a href="#">int_note_muons</a> ]. . . . .	116
259	718	Mean (left) and width (right) of the $Z \rightarrow \mu\mu$ mass peak as a function of the leading muon $\eta$ in 5.02 TeV data and MC. The mean and width are extracted from Crystal Ball components of the fits. In case of the simulation, both the uncorrected (dashed histogram) and corrected parameters (solid histogram) are shown. The fit results are presented for mass peaks constructed using kinematics of the muon ID tracks (top), ME tracks (middle) or CB tracks (bottom). The bottom panels in each plot show the data/MC ratio for uncorrected (dashed histogram) and corrected simulation (points) [ <a href="#">int_note_muons</a> ]. . . . .	117

266	719 Mean (left) and width (right) of the $Z \rightarrow \mu\mu$ mass peak as a function of the leading muon 267 $\eta$ in 2017 13 TeV data and MC at low pile-up. The mean and width are extracted from 268   Crystal Ball components of the fits. In case of the simulation, both the uncorrected (dashed 269   histogram) and corrected parameters (solid histogram) are shown. The fit results are 270   presented for mass peaks constructed using kinematics of the muon ID tracks (top), ME 271   tracks (middle) or CB tracks (bottom). The bottom panels in each plot show the data/MC 272   ratio for uncorrected (dashed histogram) and corrected simulation (points) [int_note_muons]. . . . .	118
273	720 Sagitta bias corrections derived for 2017 low-pile-up data (left) and simulation (right) at 274 $\sqrt{s} = 13$ TeV. The corrections are evaluated with two $Z$ -mass methods (“ $M_{\mu\mu\_MCP}$ ” and 275   “ $M_{\mu\mu\_Align}$ ”), the $E/p$ method applied to $W \rightarrow e\nu$ (“ $W_{\text{env}}\text{E}/p$ ”) and $Z \rightarrow ee$ (“ $Z_{\text{ee}}\text{E}/p$ ”) 276   events, and the $p_T(\mu)$ method, all of which are discussed in the text [int_note_muons]. . . . .	119
277	721 Sagitta bias correction based on 2017 low-pile-up data at $\sqrt{s} = 13$ TeV. The statistical 278   uncertainty (combined from uncertainties of the $\eta$ -dependent correction and the global 279   offset correction) is represented by error bars [int_note_muons]. . . . .	119
280	722 Comparison of reconstruction efficiencies for Medium muons using the low- $\mu$ runs of 2017 281   and 2018 at a centre-of-mass energy of $\sqrt{s} = 13$ TeV and $\sqrt{s} = 5$ TeV. Efficiencies are shown as 282   a function of muon $\eta, p_T$ . Red (orange) points correspond to low- $\mu$ data (MC), while the black 283   (blue) points are high- $\mu$ data (MC). The bottom panels show the data/MC ratio for the low- $\mu$ 284   (red) and high- $\mu$ (blue) sets with statistical and total uncertainties [int_note_muons]. . . . .	121
285	723 Comparison of TTVA efficiencies for Medium muons using the low- $\mu$ runs of 2017+18 at 286 $\sqrt{s} = 13$ TeV (top row) and low- $\mu$ runs of 2017 at $\sqrt{s} = 5$ TeV (lower row). The low- $\mu$ results 287   compared to a high- $\mu$ data set as specified in the plot legend. Efficiencies are shown as 288   function of muon $\eta$ (left) and $p_T$ (middle) and the mean number of interactions $\langle \mu \rangle$ (right). 289   Red (orange) points correspond to low- $\mu$ data (MC), while the black (blue) points are high- $\mu$ 290   data (MC). The bottom panels show the data/MC ratio for the low- $\mu$ (orange) and high- $\mu$ 291   (blue) sets with statistical and total uncertainties [int_note_muons]. . . . .	122
292	724 1D trigger efficiency and systematic uncertainty in data and MC, 5 and 13 TeV from 2017 293   and 2018 for probes from the eta barrel region and inclusive $\phi, p_T$ distributions. Trigger 294   sectors in the barrel and endcap regions are different, only the barrel trigger is shown here. 295   The bin edges correspond to physical edges of the trigger sectors [int_note_muons]. . . . .	123
296	725 Efficiencies for Ptvarcone20 isolation selections measured in 2017 and 2018 data and MC 297   13 TeV and 5 TeV as a function of muon $\eta$ (left) and $p_T$ (right). The bottom panels show 298   the data/MC scale factors with statistical uncertainties represented by blue boxes, while 299   a sum in quadrature of statistical and systematic uncertainties is represented by orange 300   boxes [int_note_muons]. . . . .	124
301	726 Hadronic recoil . . . . .	126
302	727 Comparison of the $\Sigma E_T - p_T^{\ell\ell}$ description in data of the two MC samples PowHEG and SHERPA 303   at 13 TeV, showing $\Sigma E_T - p_T^{\ell\ell}$ inclusively (left). Figure on the right shows the comparison of 304   SHERPA to the data after a dedicated pileup reweighting [int_note_hr]. . . . .	127

305	728	Ratio of data to predictions in $W \rightarrow \mu\nu$ events at 13 TeV for the $\Sigma\bar{E}_T$ distribution, before and after each $\Sigma\bar{E}_T$ modeling reweighting step. The color band is the data statistical uncertainty. The prediction uncertainty only includes the statistical uncertainty. 'Powheg' uses the baseline MC for the signal. 'Powheg+Z2D' has the 2D ( $\Sigma\bar{E}_T$ , $p_T^{true,V}$ ), Z-based reweighting applied. 'Powheg+Z2D+SETUT' adds the $\Sigma\bar{E}_T$ reweighting in bins of $u_T$ . 'Powheg+Z2D+SETUT+1DPT' adds the 1D reweighting to recover the initial $p_T^{true,V}$ spectrum [ <a href="#">int_note_hr</a> ].	128
311	729	Ratio of data to predictions in $W \rightarrow \mu\nu$ events at 5 TeV for the $\Sigma\bar{E}_T$ distribution, before and after each $\Sigma\bar{E}_T$ modeling reweighting step. The color band is the data statistical uncertainty. The prediction uncertainty only includes the statistical uncertainty. 'Powheg' uses the baseline MC for the signal. 'Powheg+Z2D' has the 2D ( $\Sigma\bar{E}_T$ , $p_T^{true,V}$ ), Z-based reweighting applied. 'Powheg+Z2D+SETUT' adds the $\Sigma\bar{E}_T$ reweighting in bins of $u_T$ . 'Powheg+Z2D+SETUT+1DPT' adds the 1D reweighting to recover the initial $p_T^{true,V}$ spectrum [ <a href="#">int_note_hr</a> ].	129
317	730	$\phi(u_T)$ at 5 and 13 TeV, for the data and the simulation before and after $u_X$ and $u_Y$ correction, in $Z$ events. The band in the ratio panel is the data statistical uncertainty [ <a href="#">int_note_hr</a> ].	131
319	81	Distributions for the 5 TeV low- $\mu$ dataset in a $Z/\gamma^* \rightarrow \mu\mu$ (top row) and a $Z/\gamma^* \rightarrow ee$ (bottom row) selection. The data (points) is compared to $Z/\gamma^* \rightarrow \mu\mu$ or $Z/\gamma^* \rightarrow ee$ signal MC, respectively. The left and middle plots show the actual $\mu$ in a coarsely-binned and a finely-binned version. The right plot shows the number of reconstructed primary vertices $N_{PV}$ [ <a href="#">int_note_samples</a> ].	138
324	82	Distributions for the 13 TeV low- $\mu$ datasets taken in 2017 and 2018 in a $Z/\gamma^* \rightarrow \mu\mu$ (top row) and a $Z/\gamma^* \rightarrow ee$ (bottom row) selection. The data (points) is compared to $Z/\gamma^* \rightarrow \mu\mu$ or $Z/\gamma^* \rightarrow ee$ signal MC, respectively. All distributions are (roughly) normalised to the same number of selected events in the 2017 dataset. The left and middle plots show the actual $\mu$ in a coarsely-binned and a finely-binned version. The right plot shows the number of reconstructed primary vertices $N_{PV}$ [ <a href="#">int_note_samples</a> ].	138
330	83	$\langle u_{  }^\ell \rangle$ as a function of $ptcone20$ , before and after correction using data samples at $\sqrt{s} = 13$ TeV.	146
332	84	Isolation scan in the $W^+ \rightarrow e^+\nu$ channel without (left) and with (right) recoil correction [ <a href="#">mjets_int_note_6</a> ].	146
334	85	Isolation scan in the $W^+ \rightarrow \mu^+\nu$ channel without (left) and with (right) recoil correction [ <a href="#">mjets_int_note_6</a> ].	147
336	86	Extrapolation of the multijet distributions for the lepton transverse momentum in the $W^+ \rightarrow e^+\nu$ (left) and $W^+ \rightarrow \mu^+\nu$ (right) channels at $\sqrt{s} = 13$ TeV [ <a href="#">mjets_int_note_6</a> ].	147
338	87	Extrapolation of the multijet distributions for the missing transverse energy (top) and transverse mass (bottom), in the $W^+ \rightarrow e^+\nu$ (left) and $W^+ \rightarrow \mu^+\nu$ (right) channels at $\sqrt{s} = 13$ TeV [ <a href="#">mjets_int_note_6</a> ].	148

---

341	88	Distributions for the 5 TeV (left) and 13 TeV (right) low- $\mu$ dataset(s) in a $Z/\gamma^* \rightarrow \mu\mu$ (top row) and a $Z/\gamma^* \rightarrow ee$ (bottom row) selection. The data (points) is compared to $Z/\gamma^* \rightarrow \mu\mu$ or $Z/\gamma^* \rightarrow ee$ signal MC, respectively. The distributions of the z-position of the primary vertex selected as the hard interaction are compared for the dataset(s) and the MC simulation before (“no $z_{\text{vtx}} \text{ rwgt}$ ”, blue, only 13 TeV) and after reweighting (black). For the 13 TeV data the 2017 and 2018 data are shown separately and all distributions are (roughly) normalised to the same number of selected events in the 2017 dataset [int_note_samples]. . . . .	150
348	89	$\Sigma E_T^-$ distribution in the muon and electron channel for the $\sqrt{s} = 13$ TeV dataset. . . . .	154
349	810	$\Sigma E_T$ distribution in the muon and electron channel for the $\sqrt{s} = 13$ TeV dataset. . . . .	155
350	811	$\vec{E}_T^{\text{miss}}$ distribution in the muon and electron channel for the $\sqrt{s} = 13$ TeV dataset. . . . .	156
351	812	Transverse mass distribution of the W boson in the muon and electron channel for the $\sqrt{s} = 13$ TeV dataset. . . . .	157
353	813	Lepton pseudorapidity distribution in the muon and electron channel for the $\sqrt{s} = 13$ TeV dataset. . . . .	158
355	814	Lepton transverse momentum distribution in the muon and electron channel for the $\sqrt{s} = 13$ TeV dataset. . . . .	159
357	815	W transverse momentum distribution in the muon and electron channel for the $\sqrt{s} = 13$ TeV dataset. . . . .	160
359	816	$\Sigma E_T^-$ distribution in the muon and electron channel for the $\sqrt{s} = 5$ TeV dataset. . . . .	161
360	817	$\Sigma E_T$ distribution in the muon and electron channel for the $\sqrt{s} = 5$ TeV dataset. . . . .	162
361	818	$\vec{E}_T^{\text{miss}}$ distribution in the muon and electron channel for the $\sqrt{s} = 5$ TeV dataset. . . . .	163
362	819	Transverse mass distribution of the W boson in the muon and electron channel for the $\sqrt{s} = 5$ TeV dataset. . . . .	164
364	820	Lepton pseudorapidity distribution in the muon and electron channel for the $\sqrt{s} = 5$ TeV dataset. . . . .	165
366	821	Lepton transverse momentum distribution in the muon and electron channel for the $\sqrt{s} = 5$ TeV dataset. . . . .	166
368	822	W transverse momentum distribution in the muon and electron channel for the $\sqrt{s} = 5$ TeV dataset. . . . .	167
370	91	Unfolding . . . . .	172
371	92	Breakdown of systematic uncertainties for 5 (a,b) and 13 (c,d) TeV in the electron channel at the reconstructed level. . . . .	174
373	93	Breakdown of systematic uncertainties for 5 (a,b) and 13 TeV (c,d) in the electron channel at the unfolded level. . . . .	175
375	94	Breakdown of systematic uncertainties for 5 (a,b) and 13 (c,d) TeV in the muon channel at the reconstructed level. . . . .	176
377	95	Breakdown of systematic uncertainties for 5 (a,b) and 13 TeV (c,d) in the muon channel at the unfolded level. . . . .	177

379	96	Unfolding bias on $p_T^W$ in the electron channel after 3 iterations, for $W^-$ (left) and $W^+$ (right), at 5 TeV (top) and 13 TeV (bottom) [ <b>int_note_1</b> ]. . . . .	179
380			
381	97	Unfolded measurement results in the $W^-$ (left) and $W^+$ (right) electron channels, at 5 TeV (top) and 13 TeV (bottom). . . . .	180
382			
383	98	Unfolded measurement results in the $W^-$ (left) and $W^+$ (right) muon channels, at 5 TeV (top) and 13 TeV (bottom). . . . .	181
384			
385	101	A: The nodes perform a linear transformation of the inputs, then apply a non-linear activation function. B: The architecture of a deep neural network: neurons are arranged into layers [ <b>dnn1</b> ]. . . . .	186
386			
388	102	A model of the Deep Neural Network (DNN) used in the analysis. . . . .	189
389	103	Learning curve of the model. . . . .	190
390	104	The difference between the Cartesian components of the HR vector for the standard $u_T$ and $u_T^{MVA}$ . . . . .	191
391	105	The difference between the polar components of the HR vector for the standard $u_T$ and $u_T^{MVA}$ . . . . .	191
393	106	Comparison of $u_T$ and $u_T^{MVA}$ spectra and response. . . . .	191
394	107	Bias and $u_\perp$ for the standard $u_T$ and $u_T^{MVA}$ . . . . .	192
395	108	Bias and $u_\perp$ as a function of $p_T^{truth}$ . . . . .	192
396	109	Normalized $\frac{u_\perp}{\langle u_T \rangle}$ as a function of $p_T^{truth}$ . . . . .	193
397	1010	. . . . .	193
398	111	$\Sigma E_T$ systematic error breakdown in the muon and electron channel for the $\sqrt{s} = 5$ TeV and $\sqrt{s} = 13$ TeV datasets. . . . .	198
399			
400	112	$\Sigma E_T$ systematic error breakdown in the muon and electron channel for the $\sqrt{s} = 5$ TeV and $\sqrt{s} = 13$ TeV datasets. . . . .	199
401			
402	113	$\vec{E}_T^{miss}$ systematic error breakdown in the muon and electron channel for the $\sqrt{s} = 5$ TeV and $\sqrt{s} = 13$ TeV datasets. . . . .	200
403			
404	114	Transverse mass systematic error breakdown of the W boson in the muon and electron channel for the $\sqrt{s} = 5$ TeV and $\sqrt{s} = 13$ TeV datasets. . . . .	201
405			
406	115	Lepton pseudorapidity systematic error breakdown in the muon and electron channel for the $\sqrt{s} = 5$ TeV and $\sqrt{s} = 13$ TeV datasets. . . . .	202
407			
408	116	Lepton transverse systematic error breakdown distribution in the muon and electron channel for the $\sqrt{s} = 5$ TeV and $\sqrt{s} = 13$ TeV datasets. . . . .	203
409			
410	117	W transverse momentum systematic error breakdown in the muon and electron channel for the $\sqrt{s} = 5$ TeV and $\sqrt{s} = 13$ TeV datasets. . . . .	204
411			
412	121	Comparison of kinematic distributions of $u_T$ vs $u_T^{MVA}$ for $W^+ \rightarrow e^+ \nu$ data sample. . . . .	207
413	122	Comparison of kinematic distributions of $u_T$ vs $u_T^{MVA}$ for $W^- \rightarrow e^- \nu$ data sample. . . . .	209
414	123	Comparison of kinematic distributions of $u_T$ vs $u_T^{MVA}$ for $W^+ \rightarrow \mu^+ \nu$ data sample. . . . .	211
415	124	Comparison of kinematic distributions of $u_T$ vs $u_T^{MVA}$ for $W^- \rightarrow \mu^- \nu$ data sample. . . . .	213

416	125	Comparison of kinematic distributions of $u_T$ vs $u_T^{MVA}$ for $Z \rightarrow \mu\mu$ MC sample. . . . .	215
417	126	Comparison of kinematic distributions of $u_T$ vs $u_T^{MVA}$ for $Z \rightarrow ee$ MC sample. . . . .	217
418	127	Comparison of kinematic distributions of $u_T$ vs $u_T^{MVA}$ for $Z \rightarrow \mu\mu$ data sample. . . . .	219
419	128	Comparison of kinematic distributions of $u_T$ vs $u_T^{MVA}$ for $Z \rightarrow ee$ data sample. . . . .	221

420

## List of Tables

421	31	Energy and luminosity of the special low-mu runs. . . . .	39
422	41	ATLAS calorimeter in numbers . . . . .	47
423	42	ATLAS muon spectrometer subsystems coverage and parameters . . . . .	54
424	71	Values of $\eta_{\text{calo}}$ bin frontiers for energy scale factors for low pile-up runs [int_note_electrons].	96
425	81	Monte Carlo samples at $\sqrt{s} = 13\text{TeV}$ . Given is a short description of the process, the ATLAS 426 MC data set number (DSID), the names and version numbers of the MC generator(s), the 427 used value of the higher order cross section times any branching and filter efficiencies 428 ( $\sigma \cdot \text{BR} \cdot \epsilon_{\text{filter}}$ ) with the theoretical uncertainty in percent (“th. unc.”), and finally the number 429 of events analysed after skimming at derivation production ( $N_{\text{evt}}^{\text{skim}}$ ) as well as the number of 430 events originally processed and simulated ( $N_{\text{evt}}^{\text{unskim}}$ ). In the case of $Z \rightarrow \ell\ell$ samples, the given 431 $\epsilon_{\text{filter}} > 1$ is related to the fact, that the cross sections were calculated for $66 < m_{\ell\ell} < 116\text{GeV}$ , 432 but the generated mass range is larger. The last section of $t\bar{t}$ samples refers to variation 433 samples for systematics studies. The MC equivalent luminosity $N_{\text{evt}}^{\text{unskim}} / (\sigma \cdot \text{BR} \cdot \epsilon_{\text{filter}})$ is 434 generally above $3\text{fb}^{-1}$ for signal and significant backgrounds, the exception are Powheg 435 $W \rightarrow \tau\nu$ and $Z \rightarrow \tau\tau$ samples, that have about $0.45\text{fb}^{-1}$ only [int_note_samples]. . . . .	140
436	82	Alternative signal $Z \rightarrow \ell\ell$ Monte Carlo samples at $\sqrt{s} = 13\text{TeV}$ produced with <b>SHERPA</b> . General 437 description of the table see Table 81. The samples are split into a long list of orthogonal 438 slices based on “max(pTV,HT)” and filtered further into “b/c/light-jet” subcomponents. For 439 the purpose of this analysis, the number of events in each slice is such that the samples are 440 about $2\text{fb}^{-1}$ each (after application of a penalty factor for negative weight events) and an 441 “inclusive sample” is restored after merging the slices [int_note_samples]. . . . .	141

---

442	83	Alternative signal $W \rightarrow \ell\nu$ Monte Carlo samples at $\sqrt{s} = 13\text{TeV}$ produced with <b>SHERPA</b> . See Table 82 for a description of the table. The samples are split into a long list of orthogonal slices based on “max(pTV,HT)” and filtered further into “b/c/light-jet” subcomponents. For the purpose of this analysis, the number of events in each slice is such that the samples are about $1\text{fb}^{-1}$ each (after application of a penalty factor for negative weight events) and an “inclusive sample” is restored after merging the slices [ <b>int_note_samples</b> ]. . . . .	142
448	84	Monte Carlo samples at $\sqrt{s} = 5\text{TeV}$ . The table follows the same format as Table 81. The MC equivalent luminosity $N_{\text{evt}}^{\text{unskim}}/(\sigma \cdot \text{BR} \cdot \epsilon_{\text{filter}})$ is generally above $2.5\text{fb}^{-1}$ for signal and significant backgrounds, the exception are Powheg $W \rightarrow \tau\nu$ and $Z \rightarrow \tau\tau$ samples, that have about $0.20\text{fb}^{-1}$ and $0.45\text{fb}^{-1}$ only [ <b>int_note_samples</b> ]. . . . .	143
452	85	Evalution of multijet background yields at 13 TeV and 5 TeV [ <b>mjets_int_note_6</b> ]. . . . .	149
453	86	Analysis cut flow for $W^+ \rightarrow e^+\nu$ 5 TeV signal selection. Lepton $p_T$ is required to be over 18 GeV before the final cut. . . . .	151
455	87	Analysis cut flow for $W^+ \rightarrow e^+\nu$ 13 TeV signal selection. Lepton $p_T$ is required to be over 18 GeV before the final cut. . . . .	152
457	88	Analysis cut flow for $W^+ \rightarrow \mu^+\nu$ 5 TeV signal selection. Lepton $p_T$ is required to be over 18 GeV before the final cut. . . . .	152
459	89	Analysis cut flow for $W^+ \rightarrow \mu^+\nu$ 13 TeV signal selection. Lepton $p_T$ is required to be over 18 GeV before the final cut. . . . .	152
461	810	Analysis cut flow for $W^- \rightarrow e^-\nu$ 5 TeV signal selection. Lepton $p_T$ is required to be over 18 GeV before the final cut. . . . .	153
463	811	Analysis cut flow for $W^- \rightarrow e^-\nu$ 13 TeV signal selection. Lepton $p_T$ is required to be over 18 GeV before the final cut. . . . .	153
465	812	Analysis cut flow for $W^- \rightarrow \mu^-\nu$ 5 TeV signal selection. Lepton $p_T$ is required to be over 18 GeV before the final cut. . . . .	153
467	813	Analysis cut flow for $W^- \rightarrow \mu^-\nu$ 13 TeV signal selection. Lepton $p_T$ is required to be over 18 GeV before the final cut. . . . .	153
469	814	Observed and Expected yield comparison for all signal selections. . . . .	154



## 470 0.1 Introduction

### 471 0.1.1 Historical retrospective

472 The reductionistic idea that the countless varieties of matter types that surround us could be in fact  
473 simplified to a combination of much fewer substances has existed at least since the time of Ancient  
474 Greece. The thought that you can construct everything you see around out of one or few (e.g. fire, earth,  
475 water and air) indivisible elements (*ἀτομοσ* in Greek) is simple, logical and therefore conceptually  
476 attractive. Knowing all about these elements could potentially grant us profound understanding  
477 of nature. But it wasn't before the XIX<sup>th</sup> century that this idea has become something more than a  
478 philosophical concept and obtained solid scientific evidence.

479

480 The composition of the periodic table of elements that has begun in the early XIX<sup>th</sup> century and  
481 concluded in the 1860s [1] was a tremendous step forward, reducing the number of elements to O(100).  
482 A brilliant (yet not completely true) hypothesis that all the chemical elements are composed out of  
483 hydrogen atoms was published by William Prout as early as 1815 [2]. The elements of the periodic  
484 table resembled the ancient Greek concept so much, that they were christened atoms. But the periodic  
485 character of the table and strong correlation of atom position in the table with its chemical properties  
486 was insinuating on a certain inner structure of the atoms, a possibility for them to be composed out of  
487 even smaller objects. The discovery of isotopes in 1913 [3] left little room for other explanation.

488 Further evidence in favour of the atomistic view kept coming in the late XIX<sup>th</sup> and early XX<sup>th</sup> centuries  
489 from theoretical and experimental sides. The molecular kinetic theory has been heavily criticized  
490 throughout the XIX<sup>th</sup> century, but the explanation of the Brownian motion [4] has secured its dominance  
491 from there on lying a foundation for what is to become the statistical physics. Of particular importance  
492 was the discovery of the first subatomic particle in 1897, which was called the electron [5]. It was  
493 shortly followed by the identification of a hydrogen ion, subsequently named a proton [6]<sup>1</sup>. Originating  
494 from the Greek word *πρωτοσ* (primal), the name was inspired by the term *protyle* introduced by  
495 William Prout a century before for the hydrogen atom [2].

496 Further studies of radioactive materials have allowed to compose a seemingly consistent understanding  
497 of what matter is composed of. By the time of neutron discovery in 1932 [8] the list of what was called  
498 elementary particles was reasonably short: an electron, a proton, and a neutron. The list could arguably  
499 be supplemented with a hypothetical very light chargeless particle called neutrino, postulated in 1930  
500 in order to explain the continuous electron spectrum in  $\beta$ -decay [9]. It was still left to figure out how  
501 these elements interact forming the known atoms, molecules and all the matter around. That required  
502 additional efforts on the theoretical side, including resolving the inconsistencies between the two new  
503 branches of physics supposed to describe the microworld and the fields, namely the quantum theory  
504 and the field theory.

---

<sup>1</sup>The anode rays were discovered in 1886, though they included diverse ions with different charge-to-mass ratios and could not be identified as a single particle [7].

505 To move forward physicists have made use of another source of elementary particles - the cosmic  
506 rays. Cosmic rays contained particles of much higher energies comparing to the radioactive materials.  
507 Cosmic ray experiments have led to the discovery of the first known antiparticle - the positron [10],  
508 confirming the theoretical predictions by Dirac [11]. Further discoveries of the muon [12], pion [13],  
509 kaon [14] and  $\Lambda_0$  [15] have shown that the list of elementary particles was still far from being completed.  
510 The experimental detection of neutrino in 1956 [16] has confirmed the theoretical prediction made  
511 over quarter of a century before.  
512 The second half of the XX<sup>th</sup> century has pronounced a new era in particle physics with the extensive use  
513 of particle accelerators. Accelerators have become the main experimental tool in the discovery of new  
514 particles and investigation of their properties. Comparing to the cosmic rays, accelerators could offer a  
515 more stable flow of high energy particles and better control over the experimental conditions. Thanks  
516 to these new tools by the end of 1960s the number of newly discovered particles has exceeded one  
517 hundred and kept growing, apparently taking away the reductionistic dream of having a reasonably  
518 small number of elementary particles.  
519 On the other hand, the properties of the newly discovered particles (sometimes called "the particle  
520 zoo") had provided enough experimental data for theorists to make further assumptions. The particles,  
521 if grouped by their properties, have formed patterns - a situation resembling the old story with the  
522 atoms of the periodic table. This observation has allowed to assume the existence of even smaller  
523 fundamental particles with a fractional charge that would make up all the visible hadrons. These  
524 particles were eventually called quarks [17], [18]. By the late 1960s hypothesizing the existence of only  
525 three quarks was enough to explain all the visible particles and successfully predict new ones [19].  
526 Since then three more quarks were discovered and as of now all the experimental evidence suggests  
527 that the quarks are truly fundamental particles being indivisible in the Ancient Greek sense.  
528 At the same time serious theoretical efforts were taken in order to describe the interactions between  
529 fundamental particles, taking into account the known fundamental forces. In the mid-1970s a theory  
530 called The Standard Model was finalized. It included three out of four known fundamental forces  
531 (excluding the gravity) and predicted a number of particles which were not discovered by that time.  
532 All the key predictions of the theory were successfully confirmed by further experiments, making it a  
533 dominant theory in particle physics. The theory was able to describe all the surrounding matter with  
534 only 12 fundamental fermions (and their antiparticles) and 5 bosons. The SM is described in more  
535 detail in Chapter 1.  
536 Theoretical efforts aimed to further simplify the list of fundamental particles are ongoing, but up to  
537 the time of this thesis writing none of them were confirmed experimentally.

---

### 538 0.1.2 Current challenges

539 The establishment of the Standard Model was a colossal step forward in the understanding of mi-  
540 croworld physics. Nevertheless despite its great success and very good agreement with the vast majority  
541 of the experimental data there is a number inconsistencies and lacunae in the theory which do not

---

542 allow to think of the SM as of the final theory. Here are most notable of these problematic questions:

- 543 1. A number of neutrino experiments have established that the neutrinos have a tiny though non-  
544 zero mass. The minimal Standard Model assumes neutrinos to be massless and does not allow to  
545 provide mass to the neutrinos.
- 546 2. Astrophysical and cosmological evidences confirm the existence of dark matter which does not  
547 correspond to any of the particles of the SM.
- 548 3. Cosmological observations show a substantial disproportion between observed matter and anti-  
549 matter in favour of the former. The SM does not provide an explanation how such an imbalance  
550 could have been formed. This fact is probably connected to the problem of CP-violation, which  
551 also lacks explanation from the SM.
- 552 4. The discovery of the gravitational waves in 2016 have confirmed the existence of the graviton -  
553 the mediator of the gravitational force. The gravitational force is not represented in any way in  
554 the SM.
- 555 5. No explanation is provided to the vastly different magnitude of the fundamental forces, i.e. why  
556 the gravity is  $10^{24}$  times weaker than the weak force.
- 557 6. Three generations of fermions are postulated with no explanation for number of generations.

558 In order to attack these and other problems numerous efforts have been taken to either modify  
559 the SM or to replace it with a more fundamental theory, but so far none of these Beyond Standard  
560 Model (BSM) theories were ever confirmed experimentally. The SM is still a source of most accurate  
561 predictions for any physical process that involves elementary particle interactions. Description of the  
562 BSM theories goes beyond the scope of current thesis.

563 The SM depends on the list of 18 free parameters if the neutrinos are assumed massless (25 parameters  
564 if neutrinos are massive). These parameters can not be calculated intrinsically and must be measured  
565 experimentally. The more precisely we know the values of these parameters - the better is the accuracy  
566 of the SM prediction. Precise knowledge of the SM input parameters can also give hints on where to  
567 look for a more fundamental theory.

568 The LHC experiments have already contributed greatly by discovering the last missing piece of the SM,  
569 the Higgs boson. This has ended the era of SM particle discoveries but at the same time started the era  
570 of LHC precision measurements. The LHC experiments were capable to measure some parameters  
571 of the SM for the first time (like the mass of the Higgs boson), but also could improve the existing  
572 measurements, boosting the predictive power of the SM.

573 The scope of this thesis includes the measurement of the W boson transverse momentum spectrum.  
574 This measurement may serve as a test for the SM predictions for differential cross-sections. It is also  
575 an important part of an ongoing effort at the ATLAS experiment to improve the precision of the W  
576 boson mass measurement, which is also among the SM free parameters. The mass of the W boson

577 was first measured at Large Electron-Positron (LEP) after its discovery in 1983. The precision of the  
578 measurement was further improved by the experiments at Tevatron collider. The only LHC result  
579 performed so far was published by ATLAS collaboration in 2018 [20].

580 Hadron colliders are a challenging environment for the W boson-related measurements, the precision  
581 is highly impacted by a number of factors one of them being pile-up. The current analysis is based on  
582 the data collected during two special LHC runs with low pile-up, taken in 2017 and 2018.

583 **0.1.3 Thesis composition outline**

584 The first chapter contains the description of the Standard Model, its constituents and input parameters.  
585 Chapter 2 is dedicated to the W boson and its properties. The chapter contains description of vector  
586 bosons production at hadron colliders and theoretical approach to the cross-section derivation. ATLAS  
587 detector is described in Chapter 3. Chapter 3 tells about the Large Hadron Collider (LHC) and its  
588 operations. Chapter 5 is dedicated to the description of the shower shapes reweighting. And so on and  
589 so forth...

**590 Bibliography**

- 591 [1] Dmitri Mendeleev. *The principles of chemistry*. Saint Petersburg, 1869.
- 592 [2] William Prout. "On the Relation between the Specific Gravities of Bodies in their Gaseous  
593 State and the Weights of their Atoms." In: *Annals of Philosophy* 6 (1815), pp. 321–330. URL:  
594 <http://web.lemoyne.edu/~giunta/PROUT.HTML>.
- 595 [3] F. Soddy. "The Radio-Elements and the Periodic Law". In: *Nature* 91 (20 Mar. 1913), pp. 57–58.  
596 doi: 10.1038/091057a0. URL: <https://doi.org/10.1038/091057a0>.
- 597 [4] A. Einstein. "Über die von der molekularkinetischen Theorie der Wärme geforderte Bewegung  
598 von in ruhenden Flüssigkeiten suspendierten Teilchen". In: *Annalen der Physik* 322 (5 May  
599 1905), pp. 549–560. doi: 10.1002/andp.19053220806. URL: <https://doi.org/10.1002/andp.19053220806>.
- 600 [5] J.J. Thompson. "Cathode Rays". In: *Philosophical Magazine* 44 (Oct. 1897). doi: 10.1002/andp.19053220806. URL: <https://doi.org/10.1002/andp.19053220806>.
- 601 [6] W. Wien. "Über positive Elektronen und die Existenz hoher Atomgewichte". In: *Annalen der  
602 Physik* 318.4 (1904), pp. 669–677. doi: 10.1002/andp.18943180404. eprint: <https://onlinelibrary.wiley.com/doi/pdf/10.1002/andp.18943180404>. URL: <https://onlinelibrary.wiley.com/doi/abs/10.1002/andp.18943180404>.
- 603 [7] Carl E. Moore, Bruno Jaselskis, and Alfred von Smolinski. "The proton". In: *Journal of Chemical  
604 Education* 62.10 (Oct. 1985), p. 859. ISSN: 0021-9584. doi: 10.1021/ed062p859. URL: <https://doi.org/10.1021/ed062p859>.
- 605 [8] J. Chadwick. "The existence of a neutron". In: *Proceedings of the Royal Society A*. 151 (June 1932),  
606 pp. 479–493. doi: 10.1098/rspa.1932.0112. URL: <https://doi.org/10.1098/rspa.1932.0112>.
- 607 [9] A letter by W. Pauli. URL: <https://www.symmetrymagazine.org/article/march-2007/neutrino-invention>.
- 608 [10] C. D. Anderson. "The Positive Electron". In: *Physical Review* 46 (Mar. 1933), pp. 491–494. doi:  
609 10.1103/PhysRev.43.491. URL: <https://doi.org/10.1103/PhysRev.43.491>.
- 610 [11] P. A. M. Dirac. "The quantum theory of the electron". In: *Proceedings of the Royal Society A*. 117  
611 (Feb. 1928), pp. 610–624. doi: 10.1098/rspa.1928.0023. URL: <https://doi.org/10.1098/rspa.1928.0023>.
- 612 [12] Seth H. Neddermeyer and Carl D. Anderson. "Note on the Nature of Cosmic-Ray Particles".  
613 In: *Phys. Rev.* 51 (10 May 1937), pp. 884–886. doi: 10.1103/PhysRev.51.884. URL: <https://link.aps.org/doi/10.1103/PhysRev.51.884>.

- 623 [13] C. M. G. LATTES et al. "PROCESSES INVOLVING CHARGED MESONS". In: *Nature* 159.4047  
624 (May 1947), pp. 694–697. ISSN: 1476-4687. doi: 10.1038/159694a0. URL: <https://doi.org/10.1038/159694a0>.
- 625
- 626 [14] G. D. ROCHESTER and C. C. BUTLER. "Evidence for the Existence of New Unstable Elemen-  
627 tary Particles". In: *Nature* 160.4077 (Dec. 1947), pp. 855–857. ISSN: 1476-4687. doi: 10.1038/  
628 160855a0. URL: <https://doi.org/10.1038/160855a0>.
- 629 [15] V. D. Hopper and S. Biswas. "Evidence Concerning the Existence of the New Unstable Elementary  
630 Neutral Particle". In: *Phys. Rev.* 80 (6 Dec. 1950), pp. 1099–1100. doi: 10.1103/PhysRev.80.1099.  
631 URL: <https://link.aps.org/doi/10.1103/PhysRev.80.1099>.
- 632 [16] C. L. Cowan et al. "Detection of the Free Neutrino: a Confirmation". In: *Science* 124.3212  
633 (1956), pp. 103–104. ISSN: 0036-8075. doi: 10.1126/science.124.3212.103. eprint: <https://science.sciencemag.org/content/124/3212/103.full.pdf>. URL: <https://science.sciencemag.org/content/124/3212/103>.
- 634
- 635
- 636 [17] Murray Gell-Mann. "A Schematic Model of Baryons and Mesons". In: *Phys. Lett.* 8 (1964), pp. 214–  
637 215. doi: 10.1016/S0031-9163(64)92001-3.
- 638 [18] G Zweig. "An SU<sub>3</sub> model for strong interaction symmetry and its breaking; Version 2". In:  
639 CERN-TH-412 (Feb. 1964). Version 1 is CERN preprint 8182/TH.401, Jan. 17, 1964, 80 p. URL:  
640 <http://cds.cern.ch/record/570209>.
- 641 [19] V. E. Barnes et al. "Observation of a Hyperon with Strangeness Minus Three". In: *Phys. Rev. Lett.*  
642 12 (8 Feb. 1964), pp. 204–206. doi: 10.1103/PhysRevLett.12.204. URL: <https://link.aps.org/doi/10.1103/PhysRevLett.12.204>.
- 643
- 644 [20] M et al. Aaboud. "Measurement of the W-boson mass in pp collisions at root s=7 TeV with the  
645 ATLAS detector". In: *European Physical Journal C: Particles and Fields* 78 (Feb. 2018).

# 1

## The Standard Model

648 The SM of particle physics is a quantum field theory that postulates the existence of three generations  
 649 of quarks and leptons interacting through three fundamental forces: electromagnetic, weak and strong.  
 650 From the mathematical point of view the SM is a gauge quantum field theory that has internal sym-  
 651 metries of the unitary product group  $SU(3) \times SU(2)_L \times U(1)$ . The fourth fundamental force, namely  
 652 the gravity, is not included in the SM. Nevertheless, since the magnitude of the gravity interaction is  
 653 negligible on the microscopic scale, it has little to no effect on the precision of the SM predictions. The  
 654 model has 18 free input parameters<sup>1</sup> - the physical constants that can not be predicted from within  
 655 the theory and must be measured experimentally. Evidently, the SM predictions are based on these  
 656 parameters, so the better we know them - the better we can predict how nature behaves on the micro  
 657 level. The free parameters of the SM are briefly described in section 1.1

658

659 A comprehensive description of the quantum field theory formalism goes beyond the scope of the  
 660 current dissertation and can be found in the corresponding textbooks [1], [2], [3], [4], [5], [6]. In the  
 661 following section a brief overview of key SM features and constituent parts is provided.

662

### 663 1.1 General composition and key parameters

664 In this section I will describe the fields that enter the SM. Their existence and interactions result in  
 665 the three fundamental forces that are taken into account by the theory. The quanta of these fields are  
 666 also called fundamental particles and possess a number of properties like mass, charge (or charges)  
 667 and spin (see figure 11). The fundamental particles are divided into two groups based on their spin:  
 668 particles with integer spin are called fermions and those with half-integer spin are bosons.  
 669 Let's start from the fermion sector. According to the Pauli exclusion principle[7] two fermions can not  
 670 occupy the same quantum numbers. This in turn, has a consequence that the fermions must occupy a  
 671 finite volume in space-time and as a result make up matter. Half of the fundamental fermions have  
 672 colour charge and therefore take part in strong interaction - they are called quarks. The other six

---

<sup>1</sup>There are SM extensions that take into account the non-zero neutrino mass. Then the model gets 7 additional parameters, so their total number reaches 25. Although current thesis only considers the SM where neutrinos are massless.

673 fermions do not have colour charge and are called leptons (from Greek " $\lambda\epsilon\pi\tauο\sigma$ " meaning "little", as  
674 they are lighter than the quarks of the same generation). Different types of quarks and leptons are also  
675 called flavours, so there are 6 flavours of quarks and 6 flavours of leptons.

676 For some reason which is yet unknown the twelve elementary fermions make three generations.  
677 Particles in the second and third generations have exactly the same charge and spin as the particles of  
678 the first generation, but are heavier and also unstable. Normally the particles of higher generations  
679 quickly decay down to their lighter kin of the first generation and can only be observed in cosmic rays  
680 and particle accelerators. That means all the matter that surrounds us consists of the four fundamental  
681 fermions of the first generation<sup>2</sup>(the first column in Fig. 11).

682 The two quarks of the first generation are called up-quark and down-quark (or u-quark and d-quark  
683 for short). All the nuclei of the ordinary matter we see around are built out of these two types of  
684 quarks. Quarks are capable of interacting through all three SM forces: electromagnetic, weak and  
685 strong. Electrons, muons and tau-leptons are sensitive to electromagnetic and weak interaction,  
686 while neutrinos can interact (and therefore be detected) only through the weak force. For this reason  
687 in particle physics the term "leptons" is sometimes used in a narrow sense referring to electrically  
688 charged leptons only. For all quarks and charged leptons the antiparticles were observed as well as the  
689 corresponding annihilation phenomena. It is still not clear if neutrinos and antineutrinos of the same  
690 flavour are distinct particles.

691 From our experience we know that matter interacts with matter. But within the SM fermions do not  
692 interact with each other immediately. The interaction is mediated by boson-type particles. The SM  
693 includes five types of bosons: four vector bosons serving as force carriers for electromagnetic, weak  
694 and strong interactions, and a spinless Higgs boson whose role will be described in more detail in the  
695 corresponding subsection 1.4.1. The Higgs boson, along with the W and Z bosons are massive, while  
696 photons and gluons are massless.

697 The masses of the fundamental particles make 12 out of 18 free parameters of the SM<sup>3</sup>.

698 As it was mentioned, bosons interact with fermions through fundamental interactions. The interaction  
699 depends on the charge of the interacting particles and on the type of the interaction itself. Each type of  
700 interaction has a coupling constant that defines the scale of the interaction. Hence two more parameters  
701 to the SM: the strong and electromagnetic coupling constants (the latter is also called the fine structure  
702 constant). The weak coupling constant is redundant since it can be obtained from other parameters.  
703 And the remaining four parameters are coming from the Cabibbo-Kobayashi-Maskawa (CKM) matrix,  
704 that contains information on the strength of the flavour-changing weak interaction [8].

705 An important feature of the Quantum Field Theory (QFT) is that particles also interact with physical  
706 vacuum. For instance, a charged particle polarizes the physical vacuum, so the vacuum screens the  
707 charge of the particle[10].This interaction with virtual particles depends on the energy scale and so

---

<sup>2</sup>Strictly speaking we already know that this is not completely true for the neutrinos, as they oscillate between the flavours due to their tiny mass. But in the SM neutrinos are assumed to be massless.

<sup>3</sup>The masses of the W and Z bosons can be replaced by other parameters, e.g. weak mixing angle  $\theta_W$  and Higgs potential vacuum expectation value (v. e. v.).

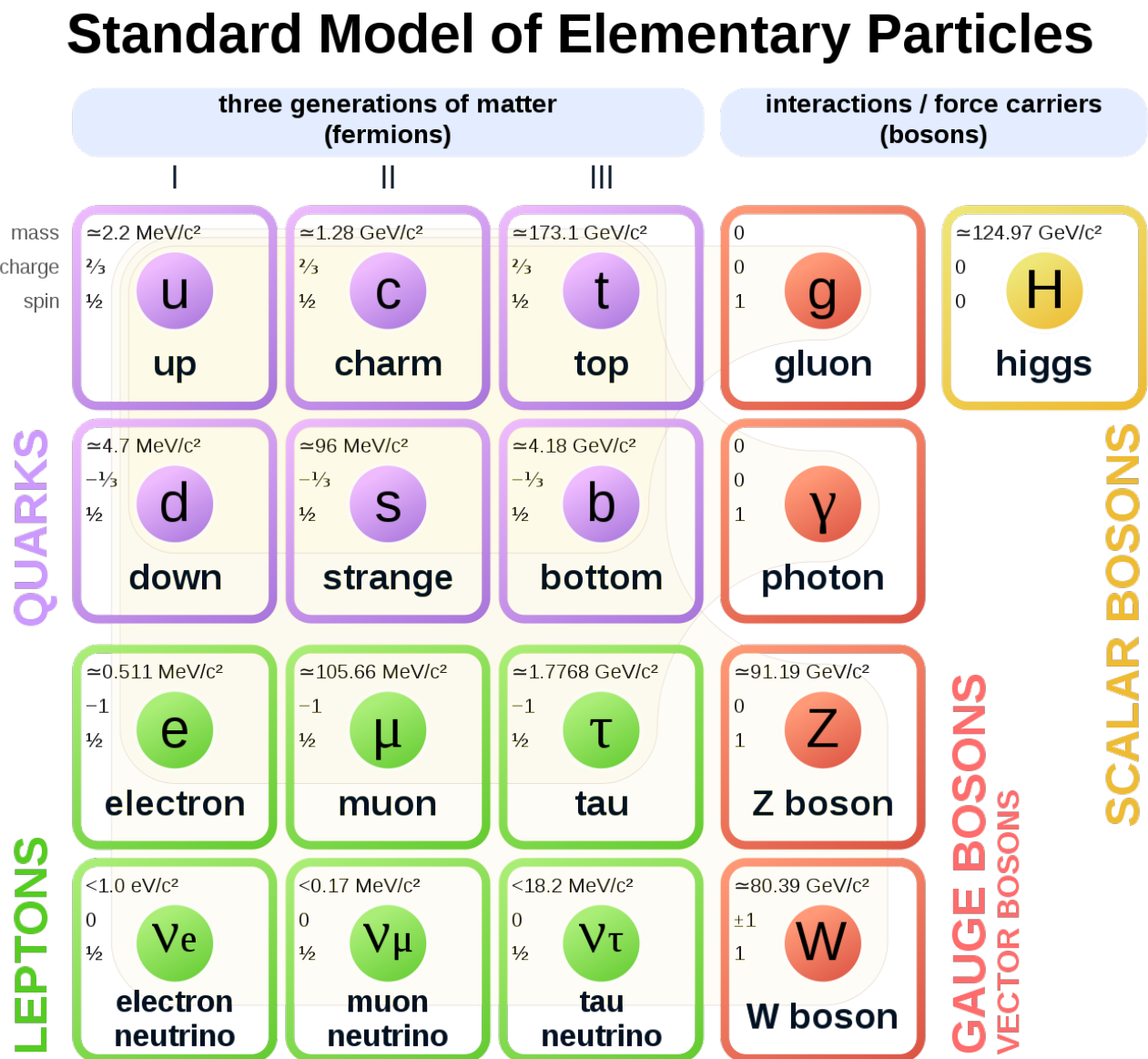


**Figure 11:** The list of particles that enters the SM[9].

708 do the observed quantities like charge, mass etc. The SM is able to predict parameter evolution, so  
 709 if the value of a certain input parameter  $q_0$  is known at the energy  $\Lambda_0$  then it is possible to predict  
 710 its measurable value  $q$  at the energy  $\Lambda$ . This changing of physical parameters is an integral part of  
 711 the QFT and is called *renormalisation* [2], [11]. In the Figure 12 the dependence of the inverted SM  
 712 coupling constants on the energy is shown.

713

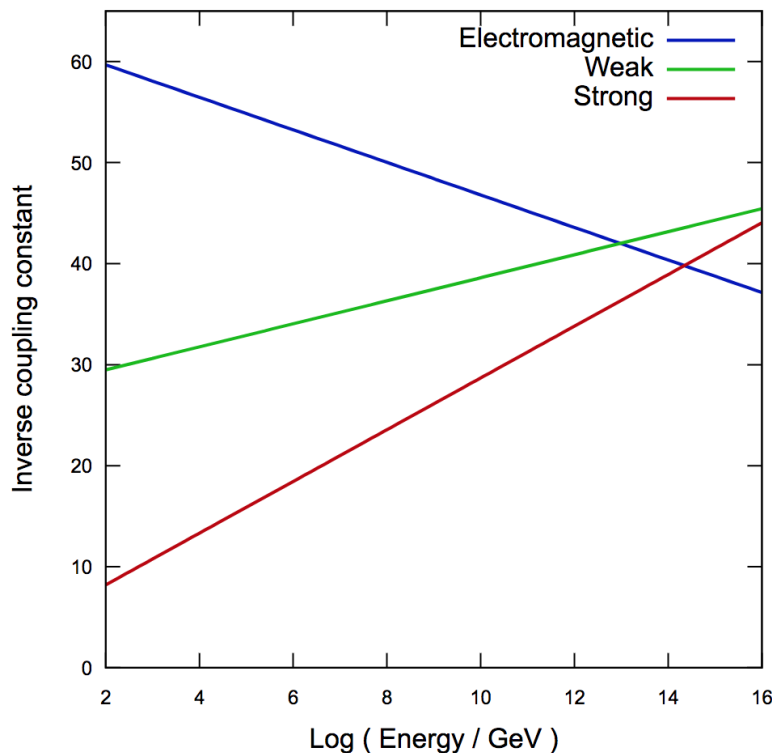


**Figure 12:** The running of the inverted SM coupling constants [12].

714 As we can see from picture 12 the strong coupling constant is decreasing with the energy. This  
 715 phenomenon is called *the asymptotic freedom* [13], [14], [15].

## 716 1.2 Classical fields and gauge invariance principle

717 A consistent mathematical description of fields appears to be a more challenging task compared to  
 718 the description of physical objects that have a definite size and shape even in the classical case. The  
 719 derivation of Maxwell's equations has been a great success and allowed to obtain the first equations of  
 720 motion of relativistic fields. It has also subsequently led to the understanding of special relativity [16],  
 721 [17], [18]. Although for a more general case of fields other than electromagnetic it would be very useful  
 722 to adopt a more systematic approach like that of Lagrangian or Hamiltonian in classical mechanics.  
 723 It has turned out that for the relativistic case the Hamiltonian approach was not quite convenient, as

724 the dedicated role of time over other degrees of freedom was in discord with relativistic space-time  
 725 unification. However it was found possible to describe the fields within the Lagrangian approach. In  
 726 classic mechanics the action of a mechanical system of  $i$  mechanical objects is defined as:

$$S = \int L dt = \int \left( \sum_i T_i - U_i \right) dt,$$

727 where  $T_i$  and  $U_i$  are the kinetic and potential energies of the  $i^{th}$  object. Considering that by definition  
 728 a field exists in every point of space-time, we need to define the Lagrangian density such that  $L =$   
 729  $\int \mathcal{L}(\phi, \partial_k \phi, \dot{\phi}) d^3x$ , where  $\phi$  is a field and  $\partial_k \phi = \nabla \phi$  - the field gradient,  $\partial_k = \frac{\partial}{\partial x^k}$ ,  $k = 1, 2, 3$ . Here and  
 730 further Latin indices run through (1, 2, 3) and are used to denote spatial coordinates, while Greek  
 731 indices denote space-time coordinates and run though (0, 1, 2, 3). So the action would look like:

$$S = \int L dt = \int \mathcal{L}(\phi, \partial_\mu \phi, \dot{\phi}) d^4x, \quad (1.1)$$

732 Now we may use the principle of least action to obtain the equations of motion using the Euler-  
 733 Lagrange formalism. Let's check it with the example of electromagnetic fields. The Lagrangian density  
 734 of electromagnetic fields in a vacuum can be written like:

$$S = -\frac{1}{4} \int F^{\mu\nu} F_{\mu\nu} d^4x. \quad (1.2)$$

735 The electromagnetic tensor can be defined in terms of electric and magnetic field intensities:  $F_{i0} =$   
 736  $-F_{0i} = E_i$ ,  $F_{ij} = \epsilon_{ijk} H_k$ , where  $\epsilon_{ijk}$  is the anti-symmetric Levi-Civita symbol. Alternatively  $F_{\mu\nu}$  can be  
 737 defined in terms of the 4-potential  $A_\mu$ :

$$F_{\mu\nu} = \partial_\mu A_\nu - \partial_\nu A_\mu. \quad (1.3)$$

738 Now we can safely apply the variational principle, and putting  $\delta S = 0$  obtain the Maxwell equations in  
 739 vacuum:

$$\partial_\mu F_{\mu\nu} = 0. \quad (1.4)$$

740 Noticing the symmetries of the system and using the Noether's theorem[19] we can find the invariants  
 741 of electromagnetic field. For example, translational symmetry in time and space ensures conservation  
 742 of energy and momentum. Let's now consider a symmetry of a different kind. The field potential can  
 743 be shifted by a gradient of an arbitrary function  $\alpha = \alpha(x^\mu)$ :

$$\begin{aligned} A_\mu(x) &\rightarrow A'_\mu(x) = A_\mu(x) + \partial_\mu \alpha(x) \\ F_{\mu\nu} &\rightarrow F'_{\mu\nu} = \partial_\mu(A_\nu(x) + \partial_\nu \alpha(x)) - \partial_\nu(A_\mu(x) + \partial_\mu \alpha(x)) = \partial_\mu A_\nu - \partial_\nu A_\mu = F_{\mu\nu}, \end{aligned} \quad (1.5)$$

744 where the commutativity of the derivative operator  $\partial_\mu \partial_\nu \alpha(x) = \partial_\nu \partial_\mu \alpha(x)$  was used. Let us now consider  
 745 the electromagnetic theory in the presence of charges and currents:

$$\mathcal{L} = -\frac{1}{4} F^{\mu\nu} F_{\mu\nu} + j^\mu A_\mu. \quad (1.6)$$

746 Now we have an interaction of a field potential  $A_\mu$  with 4-current  $j^\mu = (-\rho, j^i)$ . It turns out to be a  
 747 general property of the field theories: the only form of interaction allowed is between a gauge field and  
 748 a current. After applying the gradient field transformation and the least action principle we can obtain  
 749 the corresponding conservation law:

$$\partial_\mu j^\mu = 0. \quad (1.7)$$

750 So this gradient symmetry[2] or as it is called more often gauge symmetry leads to the conservation of  
 751 electric current. If a theory is invariant under gauge transformations then it is called a gauge invariant  
 752 theory. As we have just seen electrodynamics is the simplest example of such a theory. Taking gauge  
 753 symmetries into consideration [20] has played a huge role in the development of the SM.

754 Gauge degree of freedom can be constrained in arbitrary way by applying additional conditions on the  
 755 gauge function. This is called fixing the gauge and becomes necessary after quantization. Any physical  
 756 result must be gauge-invariant, i.e. must not depend on the gauge.

### 757 1.3 Quantum electrodynamics

758 Quantum Electrodynamics (QED) is a theory of interaction between light and electrically charged  
 759 particles. Historically it was the first quantum field theory to reach good agreement between quantum  
 760 mechanics and special relativity. QED vacuum has zero expectation value. Nowadays it is considered  
 761 to be one of the most precise physical theories ever: theory predictions and experiment results agree  
 762 up to  $O(10^{-8})$ . It has also served as a model for the composition of the subsequent parts of the SM,  
 763 describing other fundamental interactions.

764 Let us consider the free Dirac field based Lagrangian:

$$\mathcal{L} = \bar{\psi}(x)(i\cancel{D} - m)\psi(x), \quad (1.8)$$

765 where  $\psi$  and  $\bar{\psi}$  are Dirac wave function and its complex conjugate respectively,  $\cancel{D} = \gamma_\mu \partial^\mu$ ,  $\gamma_\mu$  is one of  
 766 the four gamma-matrices and  $m$  is the mass of the Dirac field. Such a theory, though, would not be  
 767 physically consistent. This reflects the fact the quantum nature of spin and spinor fields have to be  
 768 treated as quantum fields. For instance, an attempt to calculate the energy of a Dirac field would lead  
 769 to a contradiction: the energy would not be positively defined, as some spinors would have negative  
 770 energies.

771 This Lagrangian has an internal symmetry to the U(1) transformation:  $\psi \rightarrow e^{-i\alpha(x)}\psi$ ,  $\bar{\psi} \rightarrow e^{i\alpha(x)}\bar{\psi}$ .  
 772 According to Noether's theorem this symmetry implies current conservation:  $j^\mu = \bar{\psi}\gamma^\mu\psi$ . Now let's get  
 773 the combined Lagrangian of electromagnetic and Dirac fields, adding the interaction term:

$$\mathcal{L} = \mathcal{L}_{Dirac^{free}} + \mathcal{L}_{EM^{free}} + \mathcal{L}_{Interaction} = -\frac{1}{4}F^{\mu\nu}F_{\mu\nu} + \bar{\psi}(x)(i\cancel{D} - m)\psi(x) - q\bar{\psi}\gamma^\mu A_\mu\psi, \quad (1.9)$$

774 where  $q$  represents the elementary electric charge. This Lagrangian above is gauge invariant and can be  
 775 rewritten in a more convenient form:

$$\mathcal{L} = -\frac{1}{4}F^{\mu\nu}F_{\mu\nu} + \bar{\psi}(x)(i\cancel{D} - m)\psi(x), \quad (1.10)$$

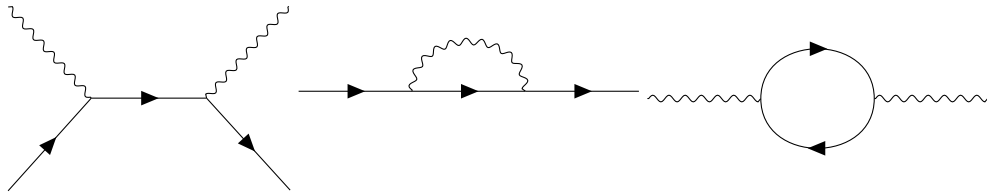


**Figure 13:** Examples of QED diagrams: Compton scattering, electron self-energy, photon self-energy.

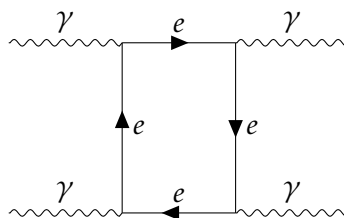
where  $D_\mu = \partial_\mu - iqA_\mu$  is a covariant derivative. If one considers space-time in the presence of a field as curved, then  $A_\mu$  would play a role of connectivity. It must be noted that values like  $m$  and  $q$  meaning electron mass and charge<sup>4</sup> are the SM input parameters mentioned in 1.1.

Further calculations are to be performed by the means of the quantum field theory formalism that treats interaction terms like a perturbation to the free fields, making power series expansion in the coupling constant. In the case of electrodynamics the coupling constant is quite small so good precision is reached soon. Since the photons do not directly interact with other photons, QED allows only one type of vertex - with two electron lines and one photon line.

Although the tree-level processes and diagrams were well understood by 1930th, the loop diagrams were properly explained only by the end of the 1940th making it possible to obtain numerical results of the higher orders of power series expansion and achieve higher precision predictions for QED processes [21], [10], [22], [23], [24], [25], [26], [27]. The examples of QED diagrams are presented in Fig. ??.

It must be noted that although immediate photon-photon interaction is impossible, light-by-light scattering is still possible through loops:

791



792

This process was theoretically described in 1936 [28] and experimentally observed 83 years after in heavy ion collisions at the LHC [29].

## 1.4 Electroweak theory and the Higgs mechanism

All the fermions of the standard model are subject to the weak interaction, so its importance for physical processes can not be underestimated. At low energy the weak interaction manifests itself

<sup>4</sup>Charge of the electron is related to the electromagnetic coupling constant.

mainly through flavour-changing decays like beta-decay and muon decay. The electroweak theory was created in the end of 1950s [11] [5] [30] thanks to numerous experimental results that allowed to shape its properties. The theory assumed that the electromagnetic and weak fundamental forces are actually manifestation of the same field that has a gauge symmetry  $SU(2)_L \times U(1)$  with massive charged and neutral bosons. A few years later the structure of electroweak vacuum was explained along with the mechanism that has allowed the bosons to gain mass [31], [32]. Assuming this the Lagrangian of the electroweak theory must consist of three parts [33]:

- Gauge fields that would mediate the interaction.
- Fermions that interact with gauge fields
- A scalar Higgs field with non-zero vacuum energy that breaks the  $SU(2)$  symmetry and couples to the fermions.

$$\mathcal{L}_{EW} = \mathcal{L}_{Gauge} + \mathcal{L}_{Higgs} + \mathcal{L}_{Fermions} \quad (1.11)$$

#### 1.4.1 Electroweak gauge fields

As it was already pointed out before, knowing the symmetries of a physical system allows one to compose the gauge fields Lagrangian. The part with  $U(1)$  symmetry would look like the electromagnetic field from 1.2 having the hypercharge  $Y$ , a vector potential  $B_\mu$  and a gauge coupling  $g_1$ . The  $SU(2)$  field would have 3 vector components  $W_\mu^{1,2,3}$ , three isospin operators  $I_1, I_2, I_3$  and a gauge coupling  $g_2$ . We can pick the Pauli matrices  $\sigma^i$  as the representation of generators of the  $SU(2)$  group, then the structure constants are  $\epsilon_{abc}$  - Levi-Civita symbol.

$$\begin{aligned} \mathcal{L}_G &= -\frac{1}{4}B_{\mu\nu}B^{\mu\nu} - \frac{1}{4}W_{\mu\nu}^a W^{\mu\nu,a}B_{\mu\nu} = \partial_\mu B_\nu - \partial_\nu B_\mu \\ W_{\mu\nu}^a &= \partial_\mu W_\nu - \partial_\nu W_\mu + g_2 \epsilon_{abc} W_\mu^b W_\nu^c, \end{aligned} \quad (1.12)$$

where the term  $g_2 \epsilon_{abc} W_\mu^b W_\nu^c$  appears due to the non-Abelian nature of the  $SU(2)$  group (the generators don't commute).

#### 1.4.2 Fermion sector

Each fundamental fermion generation expressed as left-handed doublets and right-handed singlets is a fundamental representation of the group  $SU(2) \times U(1)$ :

$$\begin{pmatrix} \nu_e \\ e \end{pmatrix}_L, \begin{pmatrix} \nu_\mu \\ \mu \end{pmatrix}_L, \begin{pmatrix} \nu_\tau \\ \tau \end{pmatrix}_L, (e_R), (\mu_R), (\tau_R), \quad (1.13)$$

$$\begin{pmatrix} u \\ d \end{pmatrix}_L, \begin{pmatrix} c \\ s \end{pmatrix}_L, \begin{pmatrix} b \\ t \end{pmatrix}_L, (u_R), (d_R), (c_R), (s_R), (t_R), (b_R). \quad (1.14)$$

821 Their quantum states are classified using the following quantum numbers: weak isospin  $I_3$ ,  $I$ , weak  
822 hypercharge  $Y$ . Their electric charge can be obtained using the Gell-Mann-Nishijima relation:

$$Q = I_3 + \frac{Y}{2}. \quad (1.15)$$

823 The fermions are divided by their chirality: only the left-handed particles take part in weak  
824 interaction. The left-handed fermion fields of each lepton and quark generation  $j$

$$\psi_j^L = \begin{pmatrix} \psi_{j+}^L \\ \psi_{j-}^L \end{pmatrix} \quad (1.16)$$

825 make SU(2) doublets, with indices  $\sigma = \pm$ , while the right-handed fermions can be written as singlets:

$$\psi_j^R = \psi_{j\sigma}^L. \quad (1.17)$$

826 Like in the electromagnetic case we can define the covariant derivative that would ensure the gauge  
827 invariance of the Lagrangian:

$$D_\mu = \partial_\mu - ig_2 I_a W_\mu^a + ig_1 \frac{Y}{2} B_\mu, \quad (1.18)$$

828 with  $I_a \equiv \frac{\sigma_a}{2}$ , then fermion Lagrangian takes the following form:

$$\mathcal{L}_{Fermions} = \sum_f \bar{\psi}_j^L i \gamma^\mu D_\mu \psi_j^L + \sum_{f,\sigma} \bar{\psi}_{f,\sigma}^R i \gamma^\mu D_\mu \psi_{f,\sigma}^R. \quad (1.19)$$

### 829 1.4.3 Higgs field breaking the symmetry

830 The Higgs field is represented by single complex a scalar doublet field  $\Phi(x)$ , that has 4 independent  
831 components. It spontaneously breaks the  $SU(2) \times U(1)$  gauge symmetry, leaving the  $U(1)_{EM}$  symmetry  
832 intact. The Higgs field doublet has the hypercharge  $Y = 1$ :

$$\Phi(x) = \begin{pmatrix} \phi^+(x) \\ \phi^0(x) \end{pmatrix}. \quad (1.20)$$

833 The Higgs field Lagrangian with non-zero vacuum expectation value is:

$$\mathcal{L}_{Higgs} = (D_\mu \Phi)^+ (D_\mu \Phi) - V(\Phi) + \mathcal{L}_{Yukawa}. \quad (1.21)$$

834 The gauge invariance of the Higgs Lagrangian is ensured in the traditional way by using the covariant  
835 derivative:

$$D_\mu = \partial_\mu - ig_2 I_a W_\mu^a + i \frac{g_1}{2} B_\mu. \quad (1.22)$$

836 The Higgs potential contains the mass term and quartic self-interaction:

$$V(\Phi) = -\mu^2 \Phi^+ \Phi + \frac{\lambda}{4} \partial_\mu (\Phi^+ \Phi)^2, \quad (1.23)$$

837 where  $\lambda$  stands for the quartic Higgs self-coupling constant and  $\mu$  is the mass of the  $\Phi$  field. The  
838 vacuum expectation value  $\langle \Phi \rangle$  does not vanish:

$$\langle \Phi(x) \rangle = \frac{1}{\sqrt(2)} \begin{pmatrix} 0 \\ v \end{pmatrix}, \quad v = \frac{2\mu}{\sqrt(\lambda)}. \quad (1.24)$$

839 Applying the unitarity gauge [34] we can constraint three out of four degrees of freedom of the Higgs  
840 field and rewrite the Higgs doublet in the following way:

$$\Phi(x) = \frac{1}{2} \begin{pmatrix} 0 \\ v + H(x) \end{pmatrix}, \quad (1.25)$$

841 which leaves us with a physical real neutral scalar field  $H(x)$  with

$$M_H = \sqrt(2)\mu. \quad (1.26)$$

842 This real field would couple to itself forming triple and quartic self-coupling vertices, to the gauge  
843 fields through the covariant derivatives and to the charged fermions, giving them mass. The Yukawa  
844 term in Lagrangian the unitary gauge is:

$$\mathcal{L}_{Yukawa} = - \sum_f m_f \bar{\psi}_f \psi_f - \sum_f \frac{m_f}{v} \bar{\psi}_f \psi_f H, \quad (1.27)$$

845 where

$$m_f = g_f \frac{v}{\sqrt(2)} = \sqrt(2) \frac{g_f}{g_2} M_W. \quad (1.28)$$

846 The Higgs coupling constants to the corresponding fermion flavour are denoted as  $g_f$ . This relation  
847 between the Higgs coupling and the mass of the W boson illustrates how much the SM parameters are  
848 intertwined and particularly underlines the importance of the  $M_W$  measurement.

#### 849 1.4.4 Physical interpretation of gauge fields and parameters

850 The Higgs coupling to the gauge fields results in the following terms in the Lagrangian:

$$\frac{1}{2} \frac{g_2}{2} v (W_1^2 + W_2^2) + \frac{v^2}{4} (W_\mu^3, B_\mu) \begin{pmatrix} g_2^2 & g_1 g_2 \\ g_1 g_2 & g_1^2 \end{pmatrix} \begin{pmatrix} W_\mu^3 \\ B_\mu \end{pmatrix}. \quad (1.29)$$

851 In order to get the physical meaning of this expression let us make a transition to the basis of physical  
852 fields:

$$\begin{aligned} W_\mu^\pm &= \frac{1}{\sqrt{2}} (W_\mu^\mp \mp i W_\mu^\mp) \\ \begin{pmatrix} Z_\mu \\ A_\mu \end{pmatrix} &= \begin{pmatrix} \cos \theta_W & \sin \theta_W \\ -\sin \theta_W & \cos \theta_W \end{pmatrix} \begin{pmatrix} W_\mu^3 \\ B_\mu \end{pmatrix}, \end{aligned} \quad (1.30)$$

853 where  $\theta_W$  is called the weak mixing angle or the Weinberg angle. In the new basis expression 1.29 has  
 854 transparent physical sense:

$$M_W^2 W_\mu^+ W^{-\mu} + \frac{1}{2}(A_\mu, Z_\mu) \begin{pmatrix} 0 & 0 \\ 0 & M_Z^2 \end{pmatrix} \begin{pmatrix} A_\mu \\ Z_\mu \end{pmatrix}, \quad (1.31)$$

855 with

$$\begin{aligned} M_W &= \frac{1}{2}g_2 v \\ M_Z &= \frac{1}{2}\sqrt{g_1^2 + g_2^2} v. \end{aligned} \quad (1.32)$$

856 The mixing angle  $\theta_W$  also has a very clear physical meaning:

$$\cos \theta_W = \frac{g_2}{g_1^2 + g_2^2} = \frac{M_W}{M_Z}. \quad (1.33)$$

857 With  $A_\mu$  having a sense of electromagnetic potential its coupling to the electron must have a physical  
 858 meaning of the electric charge  $e = \sqrt{4\pi\alpha}$  we can express  $e$  in terms of gauge couplings:

$$e = \frac{g_1 g_2}{g_1^2 + g_2^2}, \quad g_2 = \frac{e}{\sin \theta_W}, \quad g_1 = \frac{e}{\cos \theta_W}. \quad (1.34)$$

859 Thus the demonstrated Weinberg rotation (see Fig. 14) fully replaces the original parameters  $g_1, g_2, \lambda,$   
 860  $\mu^2, g_f$  by another set of measurable values  $e, M_W, M_Z, M_H, m_f$  which are the input parameters of the  
 861 SM.

## 862 1.5 Chromodynamics

863 Quantum Chromodynamics (QCD) is a non-Abelian gauge theory that describes strong interaction.  
 864 QCD is symmetric under unbroken SU(3) colour symmetry, so the interaction scheme is built in the  
 865 same way as electromagnetic and electroweak theories. To preserve the gauge invariance the gauge  
 866 field of gluons is introduced with 8 components, since SU(N) group has  $\frac{N^2-1}{2}$  independent elements.  
 867 The gluons are massless vector bosons like the photons, although because of the non-Abelian nature of  
 868 the gauge group they couple not only to the fermions but also to the other gluons. The gauge invariant  
 869 QCD Lagrangian with kinetic term containing covariant derivative would look like:

$$\begin{aligned} \mathcal{L}_{QCD} &= -\frac{1}{4}F_{\mu\nu}^a F_a^{\mu\nu} + \bar{\psi}_a(i(\gamma^\mu D_\mu)^{ab} - m\delta^{ab})\psi_b, \\ F_{\mu\nu}^a &= \partial_\mu A_\nu^a - \partial_\nu A_\mu^a + g_s f^{abc} A_\mu^b A_\nu^c, \\ D_\mu &= \partial_\mu + i g_s A_\mu^a t_a. \end{aligned} \quad (1.35)$$

870 with  $\psi$  being the quark field,  $m$  is the mass of the quark,  $a, b = 1, 2, \dots, 8$  are the colour indices,  $g_s$  is the  
 871 strong coupling constant,  $f^{abc}$  are the structure constants of the SU(3) group and  $t_a$  are the generators  
 872 of the SU(3) group.

873 As it was already mentioned in 1.3 quantitative calculations in QFT treat particle interaction as a  
 874 perturbation to the free field theory. The coupling constant is considered to be a small parameter so

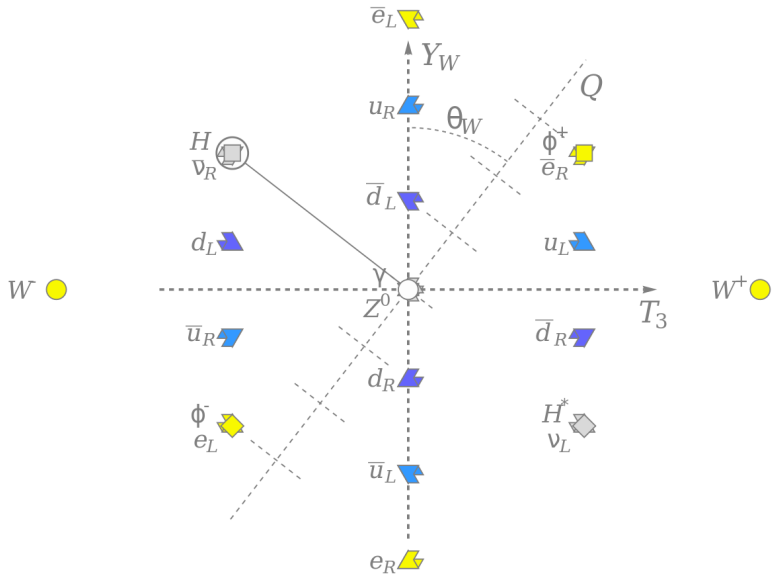


**Figure 14:** Electroweak sector and the Weinberg rotation [12].

every next power of the coupling constant is much smaller than the previous one. Due to asymptotic freedom the constant  $\alpha_s$  becomes small at higher energies and allows perturbative calculations. But at a certain energy scale called  $\Lambda_{QCD} \approx 200$  MeV, QCD becomes non-perturbative. It means we may no longer assume that interaction is a small perturbation of the free fields. This phenomenon is known as the *colour confinement*.

880

Because of colour confinement we can only observe colourless objects like baryons and mesons, but not quarks and gluons. If a high-energetic parton gets torn out of a hadron then it creates an avalanche-like process creating quark-antiquark pairs until it fully hadronizes (see Fig. 15) confining its colour. Such an avalanche is called a hadronic jet.

Currently there is no viable physical theory that would describe QCD vacuum and low-energy behaviour of quarks and gluons. This also means that although nuclear forces are evidently residuals of the QCD interaction of partons within the baryons, there is no continuity between QCD and nuclear physics. Confinement and low-energy QCD remain an unsolved problem of modern physics.

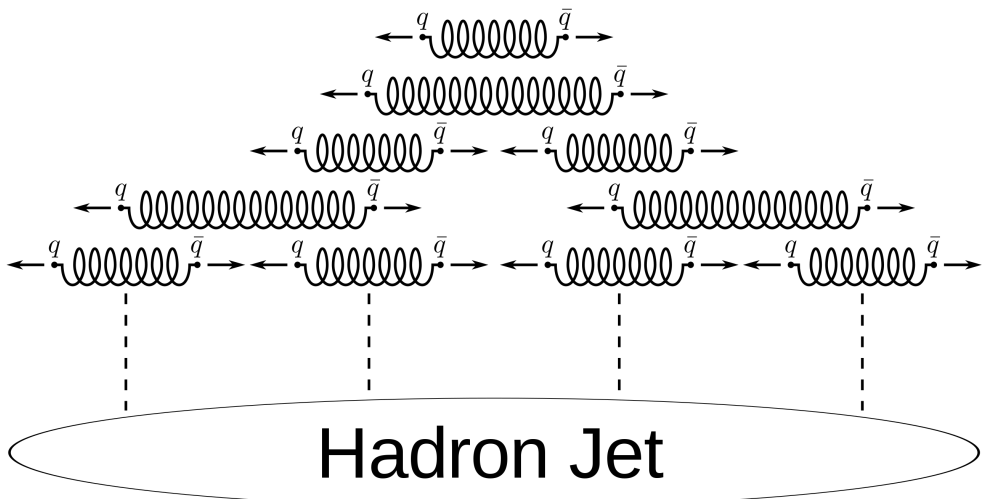


**Figure 15:** The formation of a hadron jet [35].

## 889 Bibliography

- 890 [1] Michael E Peskin and Daniel V Schroeder. *An introduction to quantum field theory*. Includes  
891 exercises. Boulder, CO: Westview, 1995. URL: <https://cds.cern.ch/record/257493>.
- 892 [2] D.V. Shirkov N.N. Bogolyubov. *Quantum fields*. Addison-Wesley, 1982.
- 893 [3] Mark Srednicki. *Quantum Field Theory*. Cambridge: Cambridge Univ. Press, 2007. URL: <https://cds.cern.ch/record/1019751>.
- 894 [4] V.B. Berestetskii. A.I. Akhiezer. *Quantum Electrodynamics*. Interscience Publishers, 1965.
- 895 [5] Steven Weinberg. *The Quantum Theory of Fields, Volume 1: Foundations*. Cambridge University  
896 Press, 2005. ISBN: 0521670535. URL: <http://www.amazon.com/Quantum-Theory-Fields-Foundations/dp/0521670535?SubscriptionId%3D13CT5CVB80YFWJEPWS02%26tag%3Dws%26linkCode%3Dxm2%26camp%3D2025%26creative%3D165953%26creativeASIN%3D0521670535>.
- 900 [6] David J Griffiths. *Introduction to elementary particles; 2nd rev. version*. Physics textbook. New York,  
901 NY: Wiley, 2008. URL: <https://cds.cern.ch/record/111880>.
- 902 [7] W Pauli. “Über den Einfluss der Geschwindigkeitsabhängigkeit der Elektronenmasse auf den  
903 Zeeman-Effekt”. In: *Z. Phys.* 31 (1925), pp. 373–385.
- 904 [8] J. Beringer et al. “Review of Particle Physics”. In: *Phys. Rev. D* 86 (1 July 2012), p. 010001. doi:  
905 [10.1103/PhysRevD.86.010001](https://doi.org/10.1103/PhysRevD.86.010001). URL: <https://link.aps.org/doi/10.1103/PhysRevD.86.010001>.
- 907 [9] *Standard Model particles*. URL: [https://en.wikipedia.org/wiki/Standard\\_Model](https://en.wikipedia.org/wiki/Standard_Model).
- 908 [10] Julian Schwinger. “Quantum Electrodynamics. II. Vacuum Polarization and Self-Energy”. In:  
909 *Phys. Rev.* 75 (4 Feb. 1949), pp. 651–679. doi: [10.1103/PhysRev.75.651](https://doi.org/10.1103/PhysRev.75.651). URL: <https://link.aps.org/doi/10.1103/PhysRev.75.651>.

- 911 [11] Sheldon L. Glashow. "The renormalizability of vector meson interactions". In: *Nucl. Phys.* 10  
912 (1959), pp. 107–117. doi: 10.1016/0029-5582(59)90196-8.
- 913 [12] *Coupling constants*. URL: [https://commons.wikimedia.org/wiki/File:Running\\_coupling\\_constants.svg](https://commons.wikimedia.org/wiki/File:Running_coupling_constants.svg).
- 915 [13] David J. Gross and Frank Wilczek. "Ultraviolet Behavior of Non-Abelian Gauge Theories". In:  
916 *Phys. Rev. Lett.* 30 (26 June 1973), pp. 1343–1346. doi: 10.1103/PhysRevLett.30.1343. URL:  
917 <https://link.aps.org/doi/10.1103/PhysRevLett.30.1343>.
- 918 [14] H. David Politzer. "Reliable Perturbative Results for Strong Interactions?" In: *Phys. Rev. Lett.* 30  
919 (26 June 1973), pp. 1346–1349. doi: 10.1103/PhysRevLett.30.1346. URL: <https://link.aps.org/doi/10.1103/PhysRevLett.30.1346>.
- 921 [15] V. S. Vanyashin and M. V. Terent'ev. "The Vacuum Polarization of a Charged Vector Field". In:  
922 *Soviet Journal of Experimental and Theoretical Physics* 21 (Aug. 1965), p. 375.
- 923 [16] Albert Einstein. "Zur Elektrodynamik bewegter Körper. (German) [On the electrodynamics of  
924 moving bodies]". In: *Annalen der Physik* 322.10 (1905), pp. 891–921. doi: <http://dx.doi.org/10.1002/andp.19053221004>.
- 926 [17] M. H. Poincare. "Sur la dynamique de l'électron". In: *Rendiconti del Circolo Matematico di Palermo*  
927 (1884-1940) 21.1 (Dec. 1906), pp. 129–175. issn: 0009-725X. doi: 10.1007/BF03013466. URL:  
928 <https://doi.org/10.1007/BF03013466>.
- 929 [18] H. A. Lorentz. "Simplified Theory of Electrical and Optical Phenomena in Moving Systems". In:  
930 *Koninklijke Nederlandse Akademie van Wetenschappen Proceedings Series B Physical Sciences* 1 (Jan.  
931 1898), pp. 427–442.
- 932 [19] E. Noether. "Invariante Variationsprobleme". ger. In: *Nachrichten von der Gesellschaft der Wis-  
933 senschaften zu Göttingen, Mathematisch-Physikalische Klasse* 1918 (1918), pp. 235–257. URL: <http://eudml.org/doc/59024>.
- 935 [20] C. N. Yang and R. L. Mills. "Conservation of Isotopic Spin and Isotopic Gauge Invariance".  
936 In: *Phys. Rev.* 96 (1 Oct. 1954), pp. 191–195. doi: 10.1103/PhysRev.96.191. URL: <https://link.aps.org/doi/10.1103/PhysRev.96.191>.
- 938 [21] J. Schwinger. "Quantum Electrodynamics. I. A Covariant Formulation". In: *Physical Review (U.S.)*  
939 *Superseded in part by Phys. Rev. A, Phys. Rev. B: Solid State, Phys. Rev. C, and Phys. Rev. D* 74 (Nov.  
940 1948). doi: 10.1103/PhysRev.74.1439.
- 941 [22] R. P. Feynman. "Mathematical Formulation of the Quantum Theory of Electromagnetic Inter-  
942 action". In: *Phys. Rev.* 80 (3 Nov. 1950), pp. 440–457. doi: 10.1103/PhysRev.80.440. URL:  
943 <https://link.aps.org/doi/10.1103/PhysRev.80.440>.
- 944 [23] R. P. Feynman. "The Theory of Positrons". In: *Phys. Rev.* 76 (6 Sept. 1949), pp. 749–759. doi:  
945 10.1103/PhysRev.76.749. URL: <https://link.aps.org/doi/10.1103/PhysRev.76.749>.

- 946 [24] R. P. Feynman. "Space-Time Approach to Quantum Electrodynamics". In: *Phys. Rev.* 76 (6 Sept.  
947 1949), pp. 769–789. doi: 10.1103/PhysRev.76.769. URL: <https://link.aps.org/doi/10.1103/PhysRev.76.769>.
- 949 [25] S. Tomonaga. "On a Relativistically Invariant Formulation of the Quantum Theory of Wave  
950 Fields\*". In: *Progress of Theoretical Physics* 1.2 (Aug. 1946), pp. 27–42. issn: 0033-068X. doi:  
951 10.1143/PTP.1.27. eprint: <https://academic.oup.com/ptp/article-pdf/1/2/27/24027031/1-2-27.pdf>. URL: <https://doi.org/10.1143/PTP.1.27>.
- 953 [26] F. J. Dyson. "The Radiation Theories of Tomonaga, Schwinger, and Feynman". In: *Phys. Rev.* 75 (3  
954 Feb. 1949), pp. 486–502. doi: 10.1103/PhysRev.75.486. URL: <https://link.aps.org/doi/10.1103/PhysRev.75.486>.
- 956 [27] F. J. Dyson. "The S Matrix in Quantum Electrodynamics". In: *Phys. Rev.* 75 (11 June 1949),  
957 pp. 1736–1755. doi: 10.1103/PhysRev.75.1736. URL: <https://link.aps.org/doi/10.1103/PhysRev.75.1736>.
- 959 [28] A. AKHIESER, L. LANDAU, and I. POMERANCHOOK. "Scattering of Light by Light". In: *Nature*  
960 138.3483 (Aug. 1936), pp. 206–206. issn: 1476-4687. doi: 10.1038/138206a0. URL: <https://doi.org/10.1038/138206a0>.
- 962 [29] G. et al. Aad. "Observation of Light-by-Light Scattering in Ultraperipheral Pb+Pb Collisions with  
963 the ATLAS Detector". In: *Phys. Rev. Lett.* 123 (5 July 2019), p. 052001. doi: 10.1103/PhysRevLett.  
964 123.052001. URL: <https://link.aps.org/doi/10.1103/PhysRevLett.123.052001>.
- 965 [30] Abdus Salam and J. C. Ward. "Weak and electromagnetic interactions". In: *Il Nuovo Cimento*  
966 (1955-1965) 11.4 (Feb. 1959), pp. 568–577. issn: 1827-6121. doi: 10.1007/BF02726525. URL:  
967 <https://doi.org/10.1007/BF02726525>.
- 968 [31] F. Englert and R. Brout. "Broken Symmetry and the Mass of Gauge Vector Mesons". In: *Phys.  
969 Rev. Lett.* 13 (9 Aug. 1964), pp. 321–323. doi: 10.1103/PhysRevLett.13.321. URL: <https://link.aps.org/doi/10.1103/PhysRevLett.13.321>.
- 971 [32] Peter W. Higgs. "Broken Symmetries and the Masses of Gauge Bosons". In: *Phys. Rev. Lett.* 13  
972 (16 Oct. 1964), pp. 508–509. doi: 10.1103/PhysRevLett.13.508. URL: <https://link.aps.org/doi/10.1103/PhysRevLett.13.508>.
- 974 [33] Wolfgang Hollik. "Electroweak Theory". In: *Journal of Physics: Conference Series* 53 (Nov. 2006),  
975 pp. 7–43. doi: 10.1088/1742-6596/53/1/002. URL: <https://doi.org/10.1088%2F1742-6596%2F53%2F1%2F002>.
- 977 [34] Steven Weinberg. "Physical Processes in a Convergent Theory of the Weak and Electromagnetic  
978 Interactions". In: *Phys. Rev. Lett.* 27 (24 Dec. 1971), pp. 1688–1691. doi: 10.1103/PhysRevLett.  
979 27.1688. URL: <https://link.aps.org/doi/10.1103/PhysRevLett.27.1688>.
- 980 [35] *Standard Model particles*. URL: [https://en.wikipedia.org/wiki/Color\\_confinement](https://en.wikipedia.org/wiki/Color_confinement).



981

982

# 2

## The W boson

### 983 2.1 The motivation for the W mass measurement

984 Being one of the cornerstones of the SM, the W boson is tightly connected to the other parameters of  
 985 the theory. In the leading order of the perturbation theory the W mass depends only on the electroweak  
 986 parameters [1]:

$$M_W = \sqrt{\frac{\pi\alpha_{EM}}{\sqrt{2}G_F}} \frac{1}{\sin\theta_W}, \quad (2.1)$$

987 where  $G_F$  stands for the Fermi constant,  $\alpha_{EM} \approx \frac{1}{137}$  is the electromagnetic coupling constant and  $\sin\theta_W$   
 988 is the Weinberg angle (see 1.4.3). The factor  $\sqrt{\frac{\pi\alpha}{\sqrt{2}G_F}} \approx 40$  GeV sets the lower bound for the possible W  
 989 mass. Higher order corrections enter the equation in the following way:

$$M_W = \sqrt{\frac{\pi\alpha}{\sqrt{2}G_F}} \frac{1}{\sin\theta_W} \frac{1}{1 + \Delta r}, \quad (2.2)$$

990 where  $\Delta r$  contains the sum of all possible radiative corrections and depends also on other parameters  
 991 of the SM, first of all on top quark and Higgs boson masses. The correction term is also sensitive to  
 992 possible BSM effects. As it was mentioned in Chapter 1 the mass of the W boson is one of the input  
 993 parameters of the SM, so the predictions of the theory directly depend on how precisely we know the  
 994 value of the boson mass. On the other hand, we can theoretically constrain the value of the W boson  
 995 mass assuming the already known values of the other SM parameters. Figure 22 demonstrates that the  
 996 uncertainty on the theoretical estimate for the W boson mass is about two times lower than that of the  
 997 best available experimental measurement. This motivates the effort for a more precise experimental

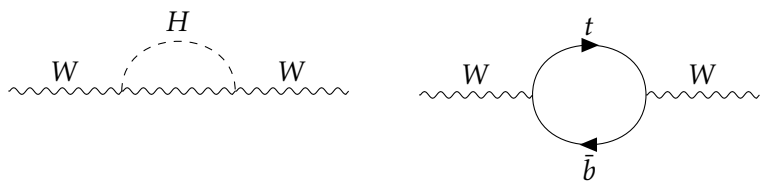
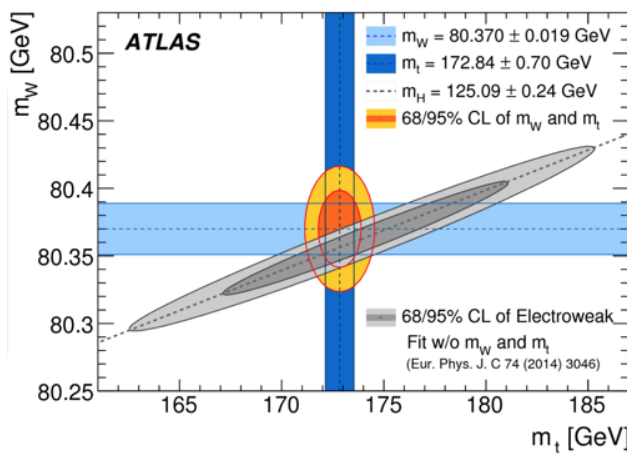
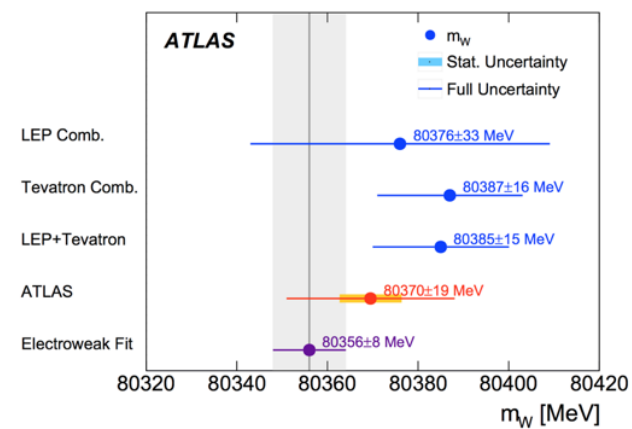


**Figure 21:** Next-to-leading order diagrams for W boson propagator containing contributions from heavy quarks and the Higgs boson.

998 measurement in order to test the consistency of the SM. Should the improved measurement reveal the inconsistency of the Standard Model - it would also allow to reveal viable BSM theories.



(a) W mass constraint from the global electroweak fit.



(b) Available W mass measurements.

Figure 22: W mass measurements and predictions [2].

999

## 1000 2.2 Massive boson production at hadron colliders

1001 Hadron colliders provide a fruitful environment for the production and study of massive electroweak  
 1002 bosons - all of them were discovered at hadron colliders. Hadron colliders allow to achieve much  
 1003 higher centre-of-mass collision energy and luminosity comparing to their lepton counterparts. At the  
 1004 same time precision measurements at hadron colliders demand much deeper theoretical understanding  
 1005 of different aspects of the SM.

1006 The main theoretical complication of proton-proton colliders lies in the fact that contrary to leptons,  
 1007 protons are complex objects. This raises the following problems:

- 1008 • A proton-proton collision is in the general case a many-body problem. The accompanying low-  
 1009 energy QCD processes can not be described from the first principles and introduce additional  
 1010 complications for the precision measurements.
- 1011 • The initial energy of the whole proton is known with good precision, but we don't know how this  
 1012 energy is distributed among the proton constituents. The absence of a consistent theory for the  
 1013 QCD vacuum does not allow to describe the initial states of the proton constituents.
- 1014 • We know that the proton consists of three valence quarks that have non-zero expectation value  
 1015 and interact through gluons. In the course of these interactions all flavours of quarks (called sea  
 1016 quarks) are appearing off-shell. The contribution of these sea quarks to the scattering cross-section  
 1017 must also be taken in account.

1018 In order to attack these problems and obtain accurate predictions for the proton-proton collisions it  
 1019 is necessary to take into account the asymptotic freedom that QCD demonstrates at short distances  
 1020 or high energies. At a certain energy scale of the momentum  $Q$ , transferred during the collision, we  
 1021 can assume that the interacting parts of the proton are asymptotically free and neglect the interaction  
 1022 with the rest of the proton. This is called *the factorization theorem*. The factorization occurs only if  
 1023 the transferred momentum  $Q \gg \Lambda_{QCD}$  is large, and that is why these processes are called "hard". The  
 1024 physical conditions of the hard processes allow to use the perturbative QCD formalism, since at large  
 1025 energy scale the strong coupling constant  $\alpha_s$  becomes small. Processes with lower energy scale of the  
 1026 transferred momentum are called "soft" and do not allow to use the perturbative QCD formalism. As it  
 1027 was mentioned in Section 1, a lot of things in the low-energy non-perturbative sector of the QCD are  
 1028 still unclear.  
 1029 The on-shell production of massive vector bosons occurs during hard processes, however, precise  
 1030 measurements at hadron colliders require understanding of both hard and soft QCD regimes. It is  
 1031 common that the hard scattering of the proton constituents is accompanied by a soft scattering of the  
 1032 remaining proton parts. This forms what is called *underlying event* and also must be taken into account.

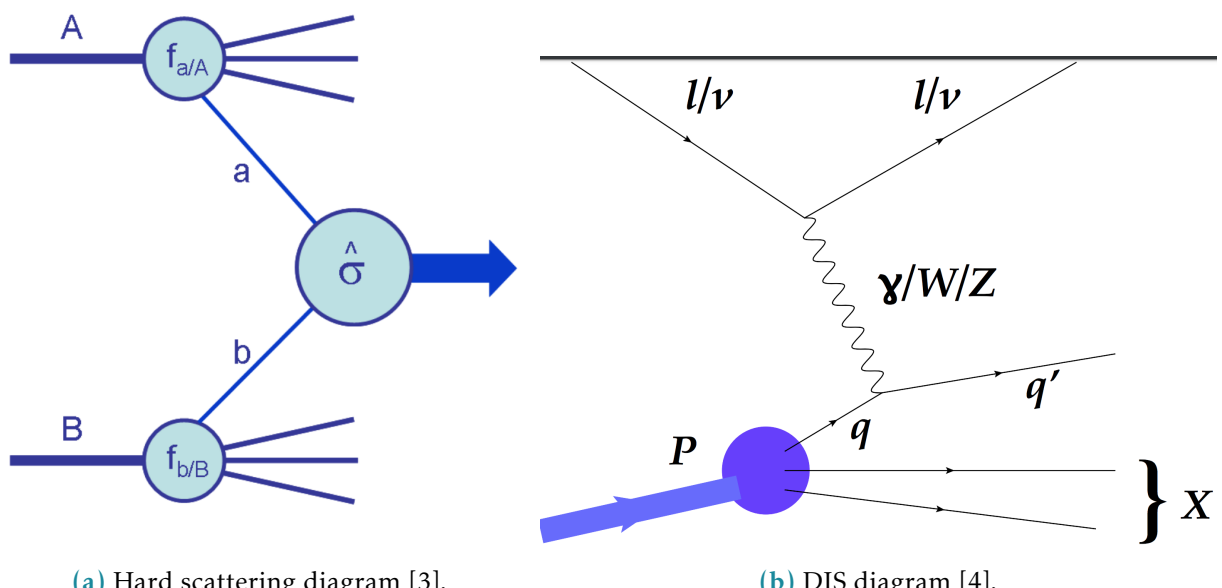


**Figure 23:** Examples of hard QCD scatterings.

1033

### 1034 2.2.1 Deep Inelastic scattering

1035 In order to better illustrate the factorization approach let us first consider the lepton-hadron process  
 1036 called the Deep Inelastic Scattering (DIS). Historically it was the first experimental evidence for the  
 1037 complex structure of the proton and still serves as an indispensable tool for the proton structure study.

1038 Let's try to write a matrix element for a DIS process  $e + A \rightarrow e + X$ , exchanging a virtual photon with  
1039 momentum  $q^\mu$ :

$$|M|_{DIS}^2 = 4\pi M_N \frac{\alpha}{q^4} L_{\mu\nu} W_{hadron}^{\mu\nu}, \quad (2.3)$$

1040 where  $L_{\mu\nu}$  is the transverse lepton tensor,  $q^\mu L_{\mu\nu} = q^\nu L_{\mu\nu} = 0$ . The hadronic tensor  $W_{\mu\nu}$  along with  
1041 its normalization factor  $4\pi M_N$  is unknown, but we can write it down in general form introducing  
1042 longitudinal and transverse parts<sup>1</sup> [5]:

$$W_{\mu\nu} = F_1(x, Q^2) \left( -g_{\mu\nu} + \frac{q_\mu q_\nu}{q^2} \right) + F_2(x, Q^2) \frac{(p_\mu - q_\mu p \cdot q/q^2)(p_\nu - q_\nu p \cdot q/q^2)}{p \cdot q}, \quad (2.4)$$

1043 with  $p_\mu$  being the momentum of the hadron A,  $Q^2$  is the exchange momentum,  $x = \frac{Q^2}{2p \cdot q}$  and the form-  
1044 factor functions  $F_1(x, Q^2), F_2(x, Q^2)$  are unknown.

1045 The cross-section of the DIS process can be measured experimentally, leaving the possibility to study  
1046 the form-factor functions. It turned out that these functions do not depend (at least in the first  
1047 approximation) on  $Q^2$  [6]. Further experiments have revealed that the form-factors depend only on the  
1048 ratio  $x$ , as it was predicted before [7]. This type of behaviour was called the Bjorken scaling.

1049 These results have led to the idea of partons - point-like constituents of the proton [8]. The factorization  
1050 theorem states that it is possible to express the hadronic tensor  $W_{\mu\nu}$  as a sum of all available partons:

$$W_{\mu\nu}(q_\mu, p_\nu) = \sum_a \int_x^1 \frac{d\xi}{\xi} f_{a/A}(\xi, \mu) H_{\mu\nu}^a(q_\mu, p_\nu, \mu, \alpha_s(\mu)) + NLO. \quad (2.5)$$

1051 The functions  $H_{\mu\nu}^a(q_\mu, p_\nu, \mu, \alpha_s(\mu))$  are called the hard scattering structure functions and only depend  
1052 on parton type  $a$ , but not on hadron type  $A$ . These functions describe the high-energy behaviour and  
1053 can be calculated in the framework of perturbative QCD. At the same time  $f_{a/A}(\xi, \mu)$  is called Parton  
1054 Density Function (PDF) and has a physical meaning of finding a parton of type  $a$  (gluon, u-quark,  
1055 d-quark etc) in a hadron of type  $A$  (proton, neutron, meson) carrying the fraction of  $\xi$  of the hadron's  
1056 momentum. These PDFs contain information on the momentum distribution of quarks and gluons  
1057 within the hadron. This corresponds to the non-perturbative sector of the QCD which is beyond the  
1058 reach of theoretical methods available so far. Note that they do not directly depend on the momentum  
1059  $Q^2$ , but only on the energy scale  $\mu$ .

1060 The DGLAP equations show that once the PDFs are known at a certain energy scale  $\mu$  they can be  
1061 perturbatively extrapolated to a different energy scale [9], [10], [11], [12]. This means that the PDFs  
1062 are universal - they can be measured experimentally at certain conditions in the course of the DIS  
1063 (or any other) process and then used for numerical calculations of any other process (e.g. Drell-Yan  
1064 (DY) process) at different conditions. Such a measurement allows a workaround - we may not be able  
1065 to solve the many-body problem and perform non-perturbative calculations starting from the first  
1066 principles, yet we still get a theoretical prediction with a good precision. Currently there exists a  
1067 number of different groups working on the PDF parametrizations and fits, constantly improving the

---

<sup>1</sup>Given example assumes only electromagnetic interaction. For the more general electroweak case the tensor structure is more complicated and there are more than two scalar structure functions [4].

1068 fits using the data coming from hadron and electron-proton colliders. Using different PDF sets may  
 1069 give different results and also helps to estimate the systematic uncertainties implied by the PDFs.  
 1070 Historically the DIS experiments at HERA electron-proton collider have allowed to perform proton  
 1071 PDFs measurements with a good level of precision in the  $x$  region up to  $x \sim 10^{-4}$  at high  $Q^2$  of up  
 1072 to  $50\,000\,GeV^2$  [13]. The HERA experiments operated until 2008, paving the path for precision  
 1073 predictions for the Drell-Yan process. Currently there are prospects for new experiments like Large  
 Hadron Electron Collider (LHeC) that would involve DIS and further improve the PDF precision [14].

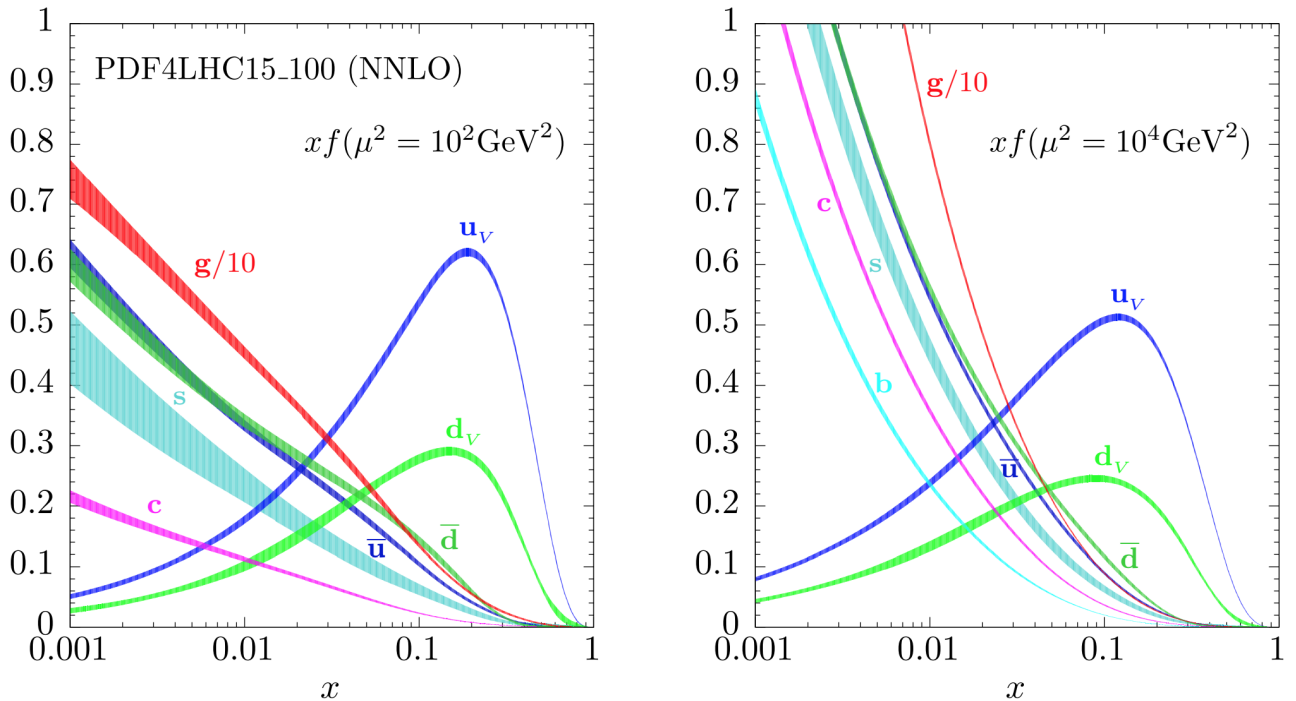


**Figure 24:** The evolution of a PDF4LHC15 NNLO Hessian set from  $Q^2 = 10^2\,GeV$  to  $Q^2 = 10^4\,GeV$  using the DGLAP. Notice the increase in the sea quark density. The PDFs include one standard deviation uncertainty band [4].

1074

## 1075 2.2.2 The Drell-Yan process

1076 The DY process happens during the high-energy hadron-hadron scattering when quark and antiquark  
 1077 annihilate to form an electroweak boson [15]. For the neutral DY process  $q\bar{q} \rightarrow Z/\gamma^* + X \rightarrow l^+l^- + X$  takes  
 1078 place. In a similar way the charged DY process can happen, generating a W boson:  $q\bar{q}' \rightarrow W^\pm + X \rightarrow$   
 1079  $l^\pm\nu + X$ . It is postulated that the DY cross-section  $\sigma^{DY}$  in a proton-proton scattering can be expressed  
 1080 through the cross-sections of the corresponding parton-parton scattering cross-section convoluted with  
 1081 the PDFs of these partons:

$$\frac{d^2\sigma^{DY}}{dydM^2} = \sum_{a,b=q,\bar{q},g} \int_{\tau_1}^1 dx_1 f_a(x_1, \mu_F^2) \int_{\tau_2}^1 dx_2 f_b(x_2, \mu_F^2) \frac{d^2\hat{\sigma}_{ab}^{DY}}{dydM^2}(x_1, x_2, y, M^2, \mu_R^2, \mu_F^2). \quad (2.6)$$

1082 In this equation  $y = \frac{1}{2} \log \frac{E+p_z}{E-p_z}$  represents rapidity,  $M^2$  is the invariant mass of the lepton pair,  $\mu_F$  and  
 1083  $\mu_R$  are factorization and renormalisation scales correspondingly. Integration limits  $\tau_{1,2} = \sqrt{\frac{Q^2}{s}} e^{\pm y}$  with  
 1084  $s$  being the centre-of-mass energy of the two incoming protons. The partonic cross-sections can be in  
 1085 turn computed perturbatively as a series expansion in  $\alpha_s$  [4]:

$$\frac{d^2 \hat{\sigma}_{ab}^{DY}}{dy dM^2}(x_1, x_2, y, M^2, \mu_R^2, \mu_F^2) = \sum_{n=0}^{\infty} \left( \frac{\alpha_s \mu_R^2}{2\pi} \right)^n \frac{d^2 \hat{\sigma}_{ab}^{(n)DY}}{dy dM^2}. \quad (2.7)$$

1086 The cross-sections  $\hat{\sigma}_{ab}^{(n)DY} \propto \alpha_s^n$  contain only the terms of order  $n$  in  $\alpha_s$ . The exact sum of the expansion  
 1087 does not depend on the  $\mu_F$  and  $\mu_R$  parameters. However, finite-order calculations demand a specific  
 1088 choice for the two parameters. One of the common choices for the DY process is putting  $\mu_F = \mu_R = M$ ,  
 1089 with  $M$  being the mass of the dilepton pair.

1090 From equation 2.6 we can see that the rapidity distribution of the vector boson explicitly depends on  
 1091 the PDFs both in terms of flavour decomposition and in the sense of a particular PDF set. Figure 25  
 1092 demonstrates different rapidity distributions for two centre-of-mass energies and two different PDF  
 1093 sets.

Let us consider partonic cross-sections, which can be constructed using an analogy to QED  $e^+e^- \rightarrow \mu^+\mu^-$

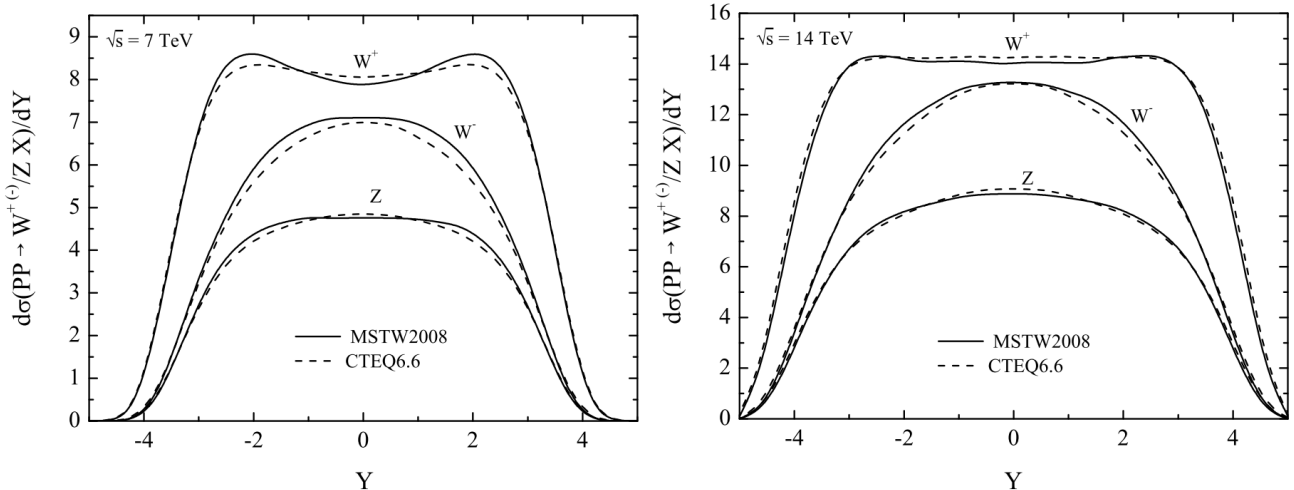


**Figure 25:** Rapidity distribution for the vector bosons using MSTW2008 and CTEQ6.6 PDF sets for the centre-of-mass energies of 7 and 14 TeV [16].

1094 - a flavour-changing process:  
 1095

$$\hat{\sigma}(q\bar{q} \rightarrow e^+e^-) = \frac{4\pi\alpha_s^2}{3s} \frac{1}{N} Q_q^2. \quad (2.8)$$

1096 Here  $Q_q^2$  is the quark charge,  $1/N$  stands for the colour factor and underlines the fact that quark and  
 1097 antiquark must have the matching colour in order to annihilate. In a similar way we can obtain the

1098 cross-section of the sub-processes of W and Z bosons production:

$$\hat{\sigma}^{q\bar{q}' \rightarrow W} = \frac{\pi}{3} \sqrt{2} G_F M_W^2 |V_{qq'}|^2 \delta(s - M_W^2), \\ \hat{\sigma}^{q\bar{q}' \rightarrow Z} = \frac{\pi}{3} \sqrt{2} G_F M_W^2 (v_q^2 + a_q^2) \delta(s - M_Z^2), \quad (2.9)$$

1099 where  $V_{qq'}$  is the element of the CKM matrix,  $v_q$  ( $a_q$ ) is a vector (axial vector) that couples the Z  
 1100 boson to the quarks. Figure 26 shows the contributions of different parton flavours into  $W^+$  and  $W^-$   
 1101 cross-sections. An assumption of narrow W resonance was used. The fact that the bosons with opposite  
 1102 charges are formed from different quarks makes a notable difference at the LHC experiments. Figure  
 1103 27 contains the comparison of the results obtained at the LHC experiments with the NNLO theoretical  
 predictions that use different PDF sets.

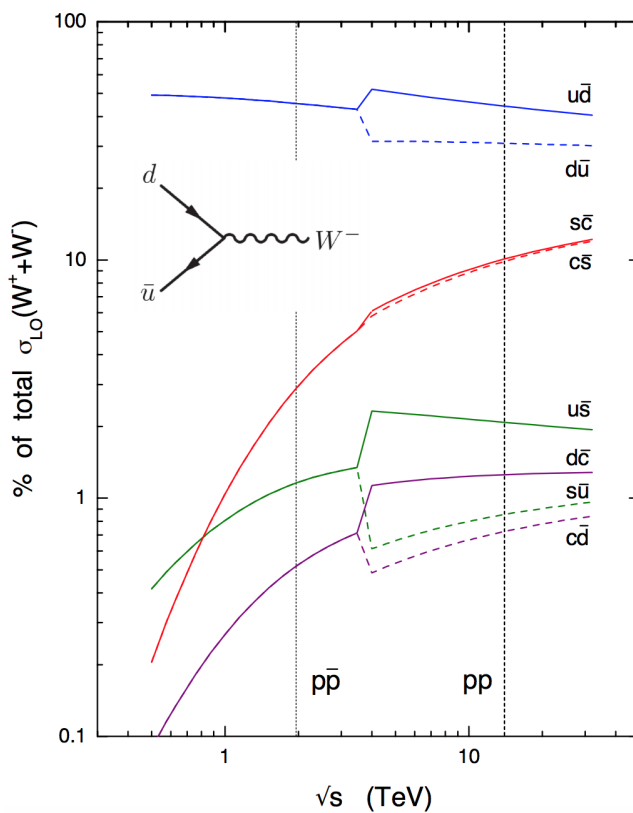
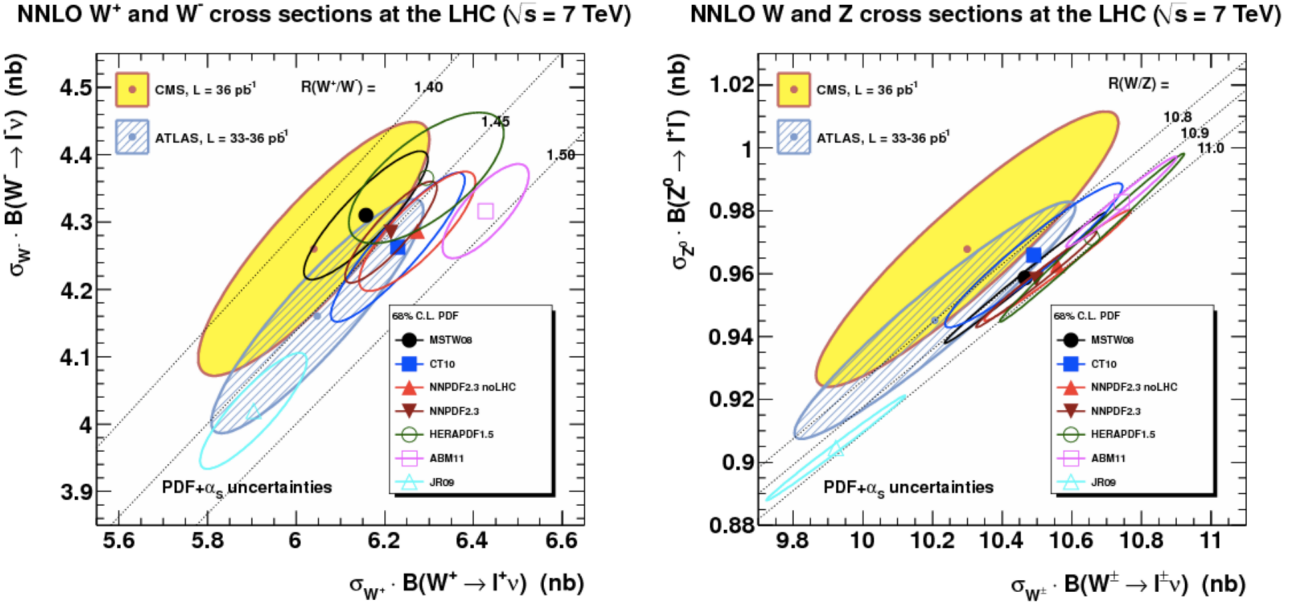


Figure 26: Parton contributions to the cross-sections of  $W^+$  and  $W^-$  bosons for LHC and Tevatron cases [17].

1104

### 1105 2.3 Transverse momentum of massive vector bosons

1106 The leading-order model of the DY process assumes the colliding partons to have their momentum  
 1107 perfectly collinear with the proton as a whole, which would mean that the vector boson  $p_T$  should  
 1108 peak at zero. However, most of the massive vector bosons produced in the DY process have a small



**Figure 27:** W and Z boson cross sections LHC at 7 TeV. ATLAS and CMS results, compared to NNLO predictions for various PDF sets [18].

yet non-zero transverse momentum,  $p_T \ll M_V$ . This occurs due to a non-perturbative effect of partons moving within the colliding protons, having an intrinsic momentum of their own. This intrinsic momentum  $< k_T > \sim \Lambda_{QCD}$  is well parametrized using a Gaussian distribution with average value of 500 [19] or 700 MeV [20], although there are ongoing efforts for a more sophisticated parametrization that would allow a better modelling of the lower part of vector boson spectrum, at  $p_T < 2$  GeV [21]. The spectrum at higher values of  $p_T$  is determined by hard perturbative parton emission(s) like  $q\bar{q} \rightarrow Vg$ ,  $qg \rightarrow Vq$ . The corresponding amplitudes can be conveniently expressed using Mandelstam variables:

$$\begin{aligned} \sum |\mathcal{M}^{q\bar{q}' \rightarrow Wg}|^2 &= \alpha_s \sqrt{2\pi G_F M_W^2} |V_{q\bar{q}}|^2 \frac{8}{9} \frac{t^2 + u^2 + 2M_W^2 s}{tu}, \\ \sum |\mathcal{M}^{qg \rightarrow Wq'}|^2 &= \alpha_s \sqrt{2\pi G_F M_W^2} |V_{q\bar{q}}|^2 \frac{1}{3} \frac{s^2 + u^2 + 2M_W^2 t}{-su}, \end{aligned} \quad (2.10)$$

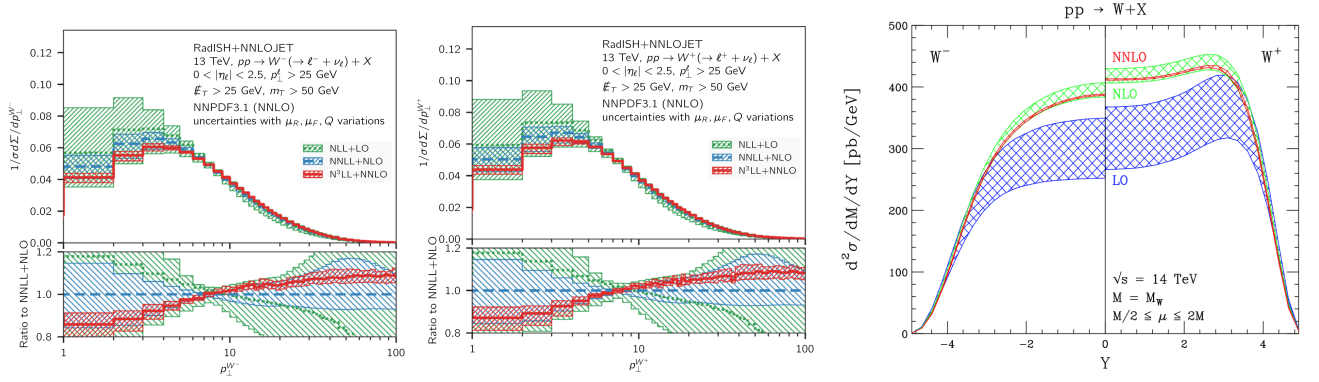
where the summation is performed over colours and spins in the final and initial states. Integrating these partonic matrix elements with the PDFs one can obtain the transverse momentum distribution  $d\sigma/dp_T$ . Further precision can be obtained by considering corrections from next-to-leading order processes  $\sim O(\alpha_s^2)$  like  $q\bar{q} \rightarrow Vgg$  - that would mainly affect the high  $p_T$  tail of the distribution. The matrix elements in 2.10 become singular when the emitted partons become soft or collinear to the initial-state partons - it is related to the poles at  $u = 0$  and  $t = 0$  in the denominator. Also for the NLO processes like  $q\bar{q} \rightarrow Vgg$  a singularity arises if the two final-state gluons are collinear. This creates a problem for the calculation of the low- $p_T$  part of the spectrum. Mathematically it is reflected in the appearance of different powers of logarithms like  $\log M_W^2/p_T^2$  in all orders of cross-section expansion in  $\alpha_s$ , which leads to divergences when  $p_T$  is small. This forces us to look for alternative approach that would take into account all the orders of the expansion.

1128 All-order resummation may be performed in a variety of approaches, one of the most popular is  
 1129 provided by parton showers. Its numerical implementation is available in a number of Monte-Carlo  
 1130 generators, PYTHIA, HERWIG and SHERPA are among the most used. It appears that for the case  
 1131 of soft and collinear gluon emission it is possible to factorize and exponentiate the logarithms in a  
 1132 *Sudakov form factor*, such that:

$$\frac{d\sigma}{dp_T^2} = \sigma \frac{d}{dp_T^2} \exp \left\{ -\frac{\alpha_s C_F}{2\pi} \log^2 \frac{M_W^2}{p_T^2} \right\},$$

$$\exp \left\{ -\frac{\alpha_s C_F}{2\pi} \log^2 \frac{M_W^2}{p_T^2} \right\} = 1 - \frac{\alpha_s}{2\pi} C_F \ln^2 \frac{M_W^2}{p_T^2} + \frac{1}{2!} \left( \frac{\alpha_s}{2\pi} \right)^2 C_F^2 \ln^4 \frac{M_W^2}{p_T^2} - \frac{1}{3!} \left( \frac{\alpha_s}{2\pi} \right)^3 C_F^3 \ln^6 \frac{M_W^2}{p_T^2} + \dots \quad (2.11)$$

1133 The exponential  $\exp\{G(\alpha_s, L)\}$ , where  $L = \log M_W^2/p_T^2$  is called the Sudakov form-factor. Its expansion  
 1134 by the powers of  $\alpha_s$  defines the resummation accuracy: the term  $\sim O(\alpha_s)$  is called the leading logarithm  
 1135 (LL), term with  $\sim O(\alpha_s^2)$  is the next-to-leading logarithm (NLL) and so on.  
 1136 The cross-sections obtained with the resummation methods provide a good prediction for soft and  
 1137 collinear emissions at low  $p_T \ll M_W$ . In order to get a combined cross-section for higher  $p_T$  region the  
 1138 resummed cross-section has to be *matched* with the fixed-order cross-sections of the corresponding  
 1139 power in  $\alpha_s$ . Figure ?? contains NNLO resummed predictions for the W  $p_T$  spectrum produced with  
 1140 RadISH[22]. In Chapter 9 of this thesis the spectrum generated by another resumming tool - DYRes [23],  
 is used for comparison with PowHEG and SHERPA predictions.



(a)  $W^-$  transverse momentum spectrum [24]. (b)  $W^+$  transverse momentum spectrum [24]. (c)  $W^\pm$  rapidity distribution [25].

**Figure 28:** Kinematic distributions for  $W^\pm$  with corrections.

## 1142 Bibliography

- 1143 [1] M. Awramik et al. "Precise prediction for the W boson mass in the standard model". In: *Phys.*  
1144 *Rev. D* 69 (2004), p. 053006. doi: 10.1103/PhysRevD.69.053006. arXiv: hep-ph/0311148.
- 1145 [2] M et al. Aaboud. "Measurement of the W-boson mass in pp collisions at root s=7 TeV with the  
1146 ATLAS detector". In: *European Physical Journal C: Particles and Fields* 78 (Feb. 2018).
- 1147 [3] John M. Campbell, J.W. Huston, and W.J. Stirling. "Hard Interactions of Quarks and Gluons: A  
1148 Primer for LHC Physics". In: *Rept. Prog. Phys.* 70 (2007), p. 89. doi: 10.1088/0034-4885/70/1/  
1149 R02. arXiv: hep-ph/0611148.
- 1150 [4] Jun Gao, Lucian Harland-Lang, and Juan Rojo. "The Structure of the Proton in the LHC Precision  
1151 Era". In: *Phys. Rept.* 742 (2018), pp. 1–121. doi: 10.1016/j.physrep.2018.03.002. arXiv:  
1152 1709.04922 [hep-ph].
- 1153 [5] John C. Collins, Davison E. Soper, and George F. Sterman. "Factorization of Hard Processes in  
1154 QCD". In: vol. 5. 1989, pp. 1–91. doi: 10.1142/9789814503266\\_0001. arXiv: hep-ph/0409313.
- 1155 [6] M. Breidenbach et al. "Observed Behavior of Highly Inelastic Electron-Proton Scattering". In:  
1156 *Phys. Rev. Lett.* 23 (16 Oct. 1969), pp. 935–939. doi: 10.1103/PhysRevLett.23.935. URL:  
1157 <https://link.aps.org/doi/10.1103/PhysRevLett.23.935>.
- 1158 [7] J. D. Bjorken. "Asymptotic Sum Rules at Infinite Momentum". In: *Phys. Rev.* 179 (5 Mar. 1969),  
1159 pp. 1547–1553. doi: 10.1103/PhysRev.179.1547. URL: <https://link.aps.org/doi/10.1103/PhysRev.179.1547>.
- 1160 [8] Richard P. Feynman. "Very High-Energy Collisions of Hadrons". In: *Phys. Rev. Lett.* 23 (24 Dec.  
1161 1969), pp. 1415–1417. doi: 10.1103/PhysRevLett.23.1415. URL: <https://link.aps.org/doi/10.1103/PhysRevLett.23.1415>.
- 1162 [9] L.N. Lipatov. "The parton model and perturbation theory". In: *Sov. J. Nucl. Phys.* 20 (1975),  
1163 pp. 94–102.
- 1164 [10] G. Altarelli and G. Parisi. "Asymptotic freedom in parton language". In: *Nuclear Physics B* 126.2  
1165 (1977), pp. 298–318. issn: 0550-3213. doi: [https://doi.org/10.1016/0550-3213\(77\)90384-4](https://doi.org/10.1016/0550-3213(77)90384-4).  
1166 URL: <http://www.sciencedirect.com/science/article/pii/0550321377903844>.
- 1167 [11] V.N. Gribov and L.N. Lipatov. "Deep inelastic e p scattering in perturbation theory". In: *Sov. J.*  
1168 *Nucl. Phys.* 15 (1972), pp. 438–450.
- 1169 [12] Yuri L. Dokshitzer. "Calculation of the Structure Functions for Deep Inelastic Scattering and e+  
1170 e- Annihilation by Perturbation Theory in Quantum Chromodynamics." In: *Sov. Phys. JETP* 46  
1171 (1977), pp. 641–653.
- 1172 [13] Zhiqing Zhang. "New measurement and QCD analysis of DIS data from HERA". In: *PoS*  
1173 ICHEP2012 (2013). Ed. by Antonio Limosani, p. 289. doi: 10.22323/1.174.0289. arXiv:  
1174 1302.1898 [hep-ex].

- 1177 [14] Max Klein. “Future Deep Inelastic Scattering with the LHeC”. In: *From My Vast Repertoire ...: Guido Altarelli’s Legacy*. Ed. by Aharon Levy, Stefano Forte, and Giovanni Ridolfi. 2019, pp. 303–347. doi: 10.1142/9789813238053\\_0015. arXiv: 1802.04317 [hep-ph].
- 1180 [15] Sidney D. Drell and Tung-Mow Yan. “Massive Lepton-Pair Production in Hadron-Hadron Collisions at High Energies”. In: *Phys. Rev. Lett.* 25 (5 Aug. 1970), pp. 316–320. doi: 10.1103/PhysRevLett.25.316. URL: <https://link.aps.org/doi/10.1103/PhysRevLett.25.316>.
- 1183 [16] Francis Halzen, Yu Seon Jeong, and C.S. Kim. “Charge Asymmetry of Weak Boson Production at the LHC and the Charm Content of the Proton”. In: *Phys. Rev. D* 88 (2013), p. 073013. doi: 10.1103/PhysRevD.88.073013. arXiv: 1304.0322 [hep-ph].
- 1186 [17] A D Martin et al. “Parton Distributions and the LHC: W and Z Production; rev. version”. In: *Eur. Phys. J. C* 14.hep-ph/9907231. DTP-99-64. OUTP-99-31-P. RAL-TR-99-047 (July 1999), 133–145. 30 p. doi: 10.1007/s100520000324. URL: <https://cds.cern.ch/record/392675>.
- 1189 [18] Michelangelo L. Mangano. “Production of electroweak bosons at hadron colliders: theoretical aspects”. In: vol. 26. 2016, pp. 231–253. doi: 10.1142/9789814733519\\_0013. arXiv: 1512.00220 [hep-ph].
- 1192 [19] A. Bermudez Martinez et al. “Production of Z bosons in the parton branching method”. In: *Phys. Rev. D* 100 (7 Oct. 2019), p. 074027. doi: 10.1103/PhysRevD.100.074027. URL: <https://link.aps.org/doi/10.1103/PhysRevD.100.074027>.
- 1195 [20] R.Keith Ellis, W.James Stirling, and B.R. Webber. *QCD and collider physics*. Vol. 8. Cambridge University Press, Feb. 2011. ISBN: 978-0-511-82328-2, 978-0-521-54589-1.
- 1197 [21] Francesco Hautmann, Ignazio Scimemi, and Alexey Vladimirov. “Non-perturbative contributions to vector-boson transverse momentum spectra in hadronic collisions”. In: *Physics Letters B* 806 (2020), p. 135478. ISSN: 0370-2693. doi: <https://doi.org/10.1016/j.physletb.2020.135478>. URL: <http://www.sciencedirect.com/science/article/pii/S0370269320302823>.
- 1201 [22] Stefan Kallweit et al. “Accurate single- and double-differential resummation of colour-singlet processes with MATRIX+RadISH:  $W^+W^-$  production at the LHC”. In: (Apr. 2020). arXiv: 2004.07720 [hep-ph].
- 1204 [23] Stefano Camarda et al. “DYTurbo: Fast predictions for Drell-Yan processes”. In: *Eur. Phys. J. C* 80.arXiv:1910.07049. 3 (Oct. 2019), 251. 15 p. doi: 10.1140/epjc/s10052-020-7757-5. URL: <https://cds.cern.ch/record/2698978>.
- 1207 [24] Wojciech Bizon et al. “The transverse momentum spectrum of weak gauge bosons at  $N^3 LL + NNLO$ ”. In: *Eur. Phys. J. C* 79.10 (2019), p. 868. doi: 10.1140/epjc/s10052-019-7324-0. arXiv: 1905.05171 [hep-ph].
- 1210 [25] Charalampos Anastasiou et al. “High precision QCD at hadron colliders: Electroweak gauge boson rapidity distributions at NNLO”. In: *Phys. Rev. D* 69 (2004), p. 094008. doi: 10.1103/PhysRevD.69.094008. arXiv: hep-ph/0312266.



# 3

## The Large Hadron Collider

1213

1214

### 1215 3.1 Introduction

1216 The study of elementary particles naturally demands a stable source of particles. At the dawn of  
1217 particle physics the two main sources were radioactive materials and cosmic rays. However soon  
1218 researchers became in need of a more reliable source of particles in terms of particle energy, luminosity  
1219 and experimental repeatability. This has commenced the era of particle accelerators.

1220 The first examples of particle accelerators were designed in the late 1920s and in the early 1930s. Two  
1221 different designs emerged: linear and circular. The former accelerates particles via electric field during  
1222 the single pass through the machine, while the latter uses magnetic field to make accelerated particles  
1223 go in circles allowing to re-accelerate the same beam many times. On the other hand the circular design  
1224 comprises energy losses due to Bremsstrahlung radiation.

1225 In the second half of the XX<sup>th</sup> century the accelerators gradually got bigger and bigger in both size and  
1226 centre-of-mass energy of the accelerated particles. This has allowed to create an experimental basis for  
1227 the development of modern particle physics, notably the Standard Model.

1228 Up to this day the biggest particle accelerator with the highest centre-of-mass energy is the Large  
1229 Hadron Collider (LHC). The LHC is a circular collider that lies in a tunnel of 27 km under the French-  
1230 Swiss border next to Geneva [1]. In 2012 the two biggest experiments of LHC have claimed the  
1231 discovery of the Higgs boson, the last elementary particle predicted by the Standard Model which was  
1232 not yet discovered by that time. [2], [3].

### 1233 3.2 The LHC running sequence

1234 It takes quite a journey for a proton to travel from a hydrogen tank (Fig. 31) into one of the LHC's  
1235 collision points. A resourceful system of pre-accelerators is necessary to make the proton beam ready  
1236 to get injected into one of the two LHC beam pipes. The LHC accelerator complex was not built from  
1237 scratch - it uses vast CERN infrastructure, that was built for the previous particle physics experiments.  
1238 After stripping the electrons off the atoms of hydrogen using a magnetic field the yielded protons



**Figure 31:** A hydrogen tank supplies LHC with protons [4].

1239 get accelerated to the energy of 50 MeV by the Linac 2<sup>1</sup> [5]. After that the beam gets into the Proton  
 1240 Synchrotron Booster (PSB) to be accelerated to 1.4 GeV. The next link of the pre-acceleration chain is  
 1241 the Proton Synchrotron (PS) - a true veteran among CERN accelerators that first accelerated protons in  
 1242 1959 breaking the world record in acceleration energy. Currently thanks to PSB and other modifications  
 1243 it can sustain proton beam intensity 1000 times larger than back in 1959. The PS accelerates the beam  
 1244 up to 25 GeV and conveys it further to the Super Proton Synchrotron (SPS) - the second-largest particle  
 1245 accelerator at CERN. Back in 1983 the massive electroweak bosons were discovered at the SPS but even  
 1246 now it serves as a main accelerator for the NA61/SHINE, NA62 and COMPASS experiments. The SPS  
 1247 raises the beam energy to 450 GeV and finally injects it into the LHC beam pipes (see Fig 32).  
 1248

1249 The LHC has inherited its 27 km tunnel from the predecessor, an electron-positron collider called  
 1250 Large Electron-Positron (LEP). However, all the LEP hardware has been replaced to sustain the con-  
 1251 ditions of the LHC beam. About 2/3 of the LHC circumference length is occupied by the dipole  
 1252 magnets that bend the trajectory of the proton beam to keep it within the pipe. These magnets use  
 1253 superconducting coils that conduct a current of 11080 amperes to produce a magnetic field of 8.3 Tl.  
 1254 Proton acceleration is maintained by the radio-frequency (RF) cavities (Fig. 33a). Besides the accelera-  
 1255 tion particles the RF cavities are also responsible for beam bunching i.e. separating the beam into a  
 1256 train of separated particle packs, each containing about  $10^{11}$  protons. During LHC Run 2 the bunches  
 1257 were separated by 7 meters (25 ns) with a maximum of 2556 circulating bunches. The LHC has four  
 1258 crossing points, where the two beams are crossed in order to collide protons. Naturally, the particle  
 1259 detectors are installed at these four points. Before getting directed at the crossing point the beams get  
 1260 squeezed to make their cross-section as small as  $16 \mu\text{m}^2$  (Fig 34a).

<sup>1</sup>After Run 2 the Linac 2 has been decommissioned to be succeeded by Linac 4.

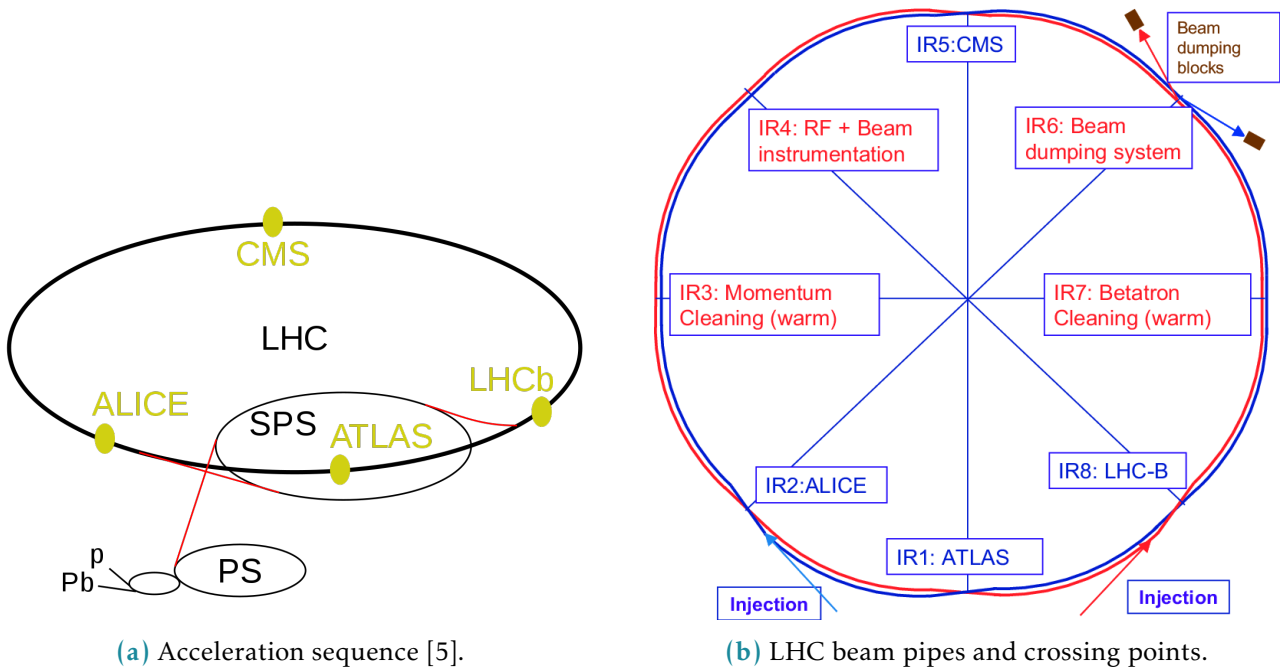


**Figure 32:** Schematic depiction of the LHC ring.

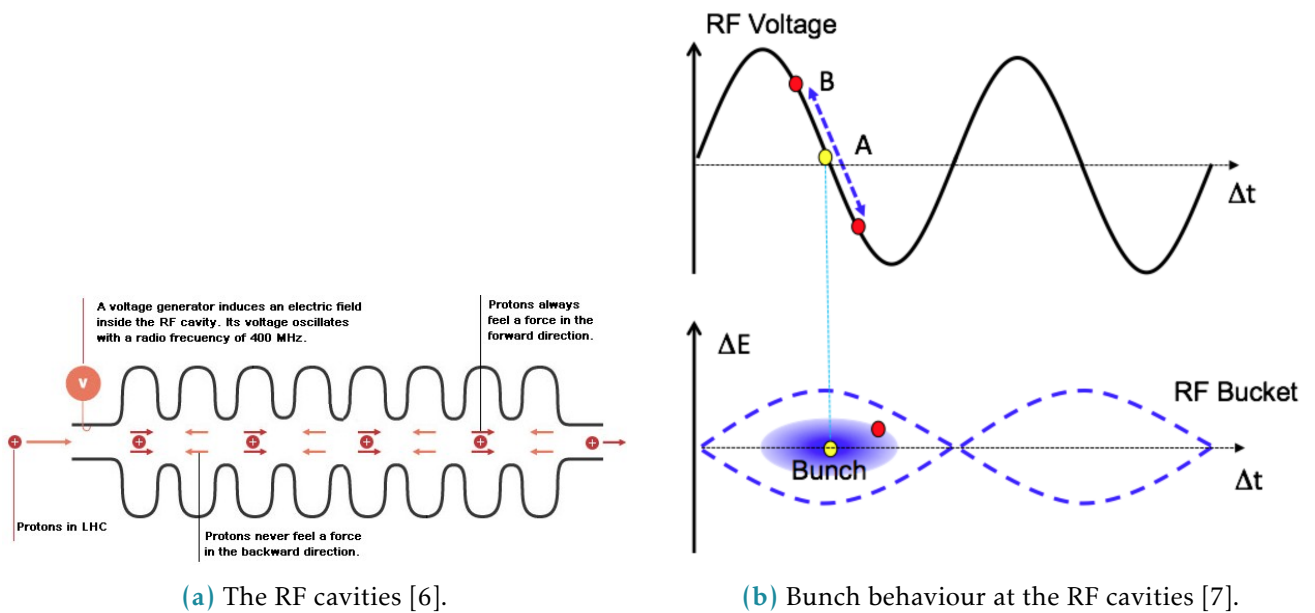
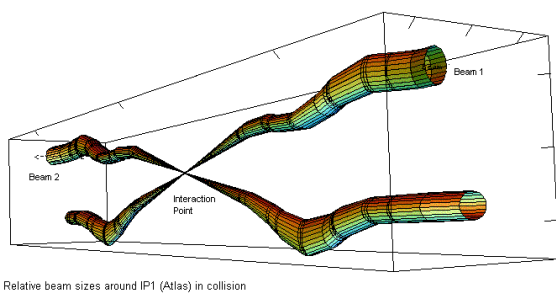
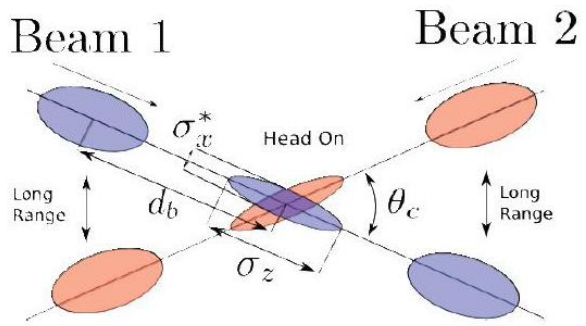


**Figure 33:** Bunching at RF cavities



(a) The two beams getting squeezed at the IP [8].



(b) Bunches at the collision point [9].

**Figure 34:** Bunch crossing at the LHC.

1261 In order to estimate the number of single proton-proton interactions in the crossing beams a value  
 1262 called instantaneous luminosity (simply called luminosity) is introduced. It is the proportionality  
 1263 factor between the number of events per second  $dR/dt$  and the cross-section  $\sigma_p$ :

$$\frac{dR}{dt} = \mathcal{L} \cdot \sigma_p.$$

1264 For the case of head-on collisions the luminosity would equal to [10]:

$$\mathcal{L} = \frac{N_1 N_2 f N_b}{4\pi \sigma_x \sigma_y}, \quad (3.1)$$

1265 with  $N_1$  and  $N_2$  being the intensities of the two colliding beams,  $f$  is the revolution frequency,  $N_b$  -  
 1266 the number of bunches per beam,  $\sigma_x, \sigma_y$  - the r.m.s. beam widths in the corresponding dimensions,  
 1267 assuming that the bunches in both beams have the same size and Gaussian profiles.

1268

1269 Head-on crossing of the beams would ensure maximal luminosity given the same beams, but on the  
 1270 other hand the measurement would suffer from unwanted beam-to-beam effects. To avoid it the beams  
 1271 at the LHC are crossed at an angle, which is called the crossing angle (see Fig. 34b). For the case of  
 1272 head-on collisions the luminosity gets a factor  $\mathcal{F}$  [10]:

$$\mathcal{L} = \frac{N_1 N_2 f N_b}{4\pi \sigma_x \sigma_y} \cdot \mathcal{F}, \quad (3.2)$$

1273 with geometric factor

$$\mathcal{F} = \frac{1}{\sqrt{1 + \left(\frac{\sigma_s}{\sigma_x} \frac{\theta_c}{2}\right)}},$$

1274 where  $\sigma_s$  is the r.m.s. of the bunch length and  $\theta_c$  is the crossing angle. Varying the parameters like  
 1275 beam intensity, bunch spacing, beam profile, crossing angle and others becomes a flexible tool for  
 1276 luminosity control. This comes in handy for different physics analysis, as some processes are rare  
 1277 and demand as much luminosity as possible (this is true, for example, for most of the Higgs studies),

Collision energy	Year	Integrated luminosity, $pb^{-1}$	Total uncertainty, %
5 TeV	2017	258	1.6
13 TeV	2017	148	2.1
13 TeV	2018	193	1.5

**Table 31:** Energy and luminosity of the special low-mu runs.

1278 whereas the others suffer from high pile-up conditions. The instantaneous luminosity integrated over a  
 1279 period of time is called the integrated luminosity:

$$\mathcal{L}_{int} = \int_0^T \mathcal{L}(t) dt, \quad (3.3)$$

1280 and is directly related to the number of observed events  $\mathcal{L}_{int} \cdot \sigma_p = N_{events}$ . A precise measurement of  
 1281 the integrated luminosity is crucial for the LHC results since the uncertainty on it impacts most of  
 1282 the analyses. A comprehensive overview on the luminosity determination at proton colliders can be  
 1283 found here [11]. Absolute luminosity measurements at the LHC are performed predominantly using  
 1284 the van-der-Meer (vdM) scan method [12], [13].

### 1285 3.3 Special low pile-up run during LHC Run 2

1286 During the Run 2 that lasted from 2015 to 2018 the ATLAS experiment has collected  $146.9 fb^{-1}$  of  
 1287 data under different bunch crossing conditions (see Fig. 35). However, the precise measurement of the  
 1288 W boson-related processes demands special conditions. High number of proton-proton collisions per  
 1289 bunch crossing leads to contamination of the final state signal with soft collisions products. This effect,  
 1290 known as pile-up, complicates object reconstruction and results in systematic uncertainties growth. For  
 1291 this reason two special runs with low number of interactions per bunch crossing have been performed  
 1292 by the LHC in 2017 and 2018 at he energies of 5 and 13 TeV. Table 31 contains information on the data  
 1293 collected at ATLAS experiment during the special low pile-up run with  $\langle \mu \rangle \approx 2$ .

1294

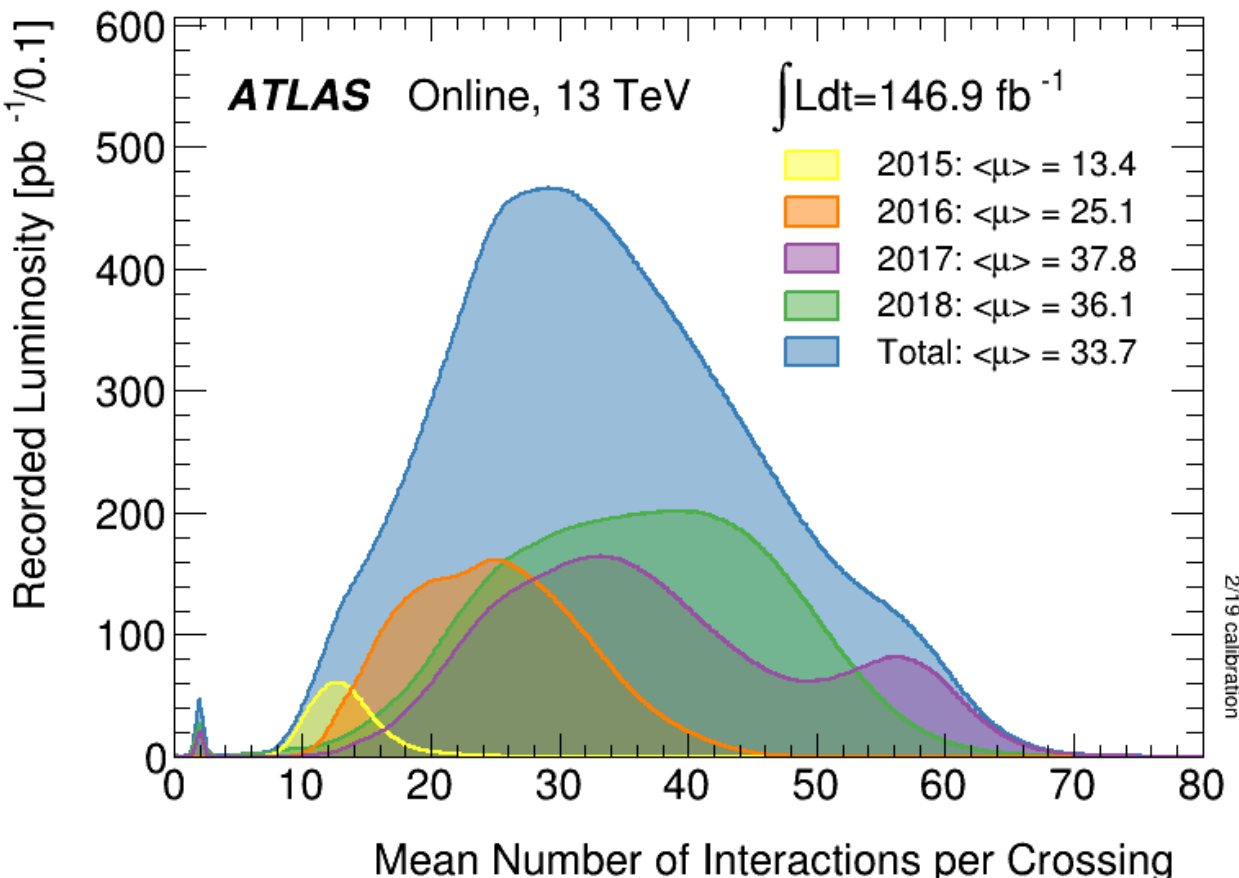


**Figure 35:** Number of Interactions per bunch crossing in ATLAS Run 2 [14]. The little bump around  $\mu \approx 2$  corresponds to special low pile-up runs.

## 1295 Bibliography

- 1296 [1] Oliver Bruning and Lucio Rossi. "The High-Luminosity Large Hadron Collider". In: *Nature Rev. Phys.* 1.CERN-ACC-2019-0039 (Mar. 2019), 1. 3 p. doi: 10.1038/s42254-019-0050-6. URL: <https://cds.cern.ch/record/2668521>.
- 1297 [2] Georges Aad et al. "Observation of a new particle in the search for the Standard Model Higgs
- 1300 boson with the ATLAS detector at the LHC". In: *Phys. Lett.* B716 (2012), pp. 1–29. doi: 10.1016/j.physletb.2012.08.020. arXiv: 1207.7214 [hep-ex].
- 1301 [3] Serguei Chatrchyan et al. "Observation of a New Boson at a Mass of 125 GeV with the CMS
- 1303 Experiment at the LHC". In: *Phys. Lett.* B716 (2012), pp. 30–61. doi: 10.1016/j.physletb.2012.
- 1304 08.021. arXiv: 1207.7235 [hep-ex].
- 1305 [4] *The source of protons*. URL: [https://www.lhc-closer.es/taking\\_a\\_closer\\_look\\_at\\_lhc/0\\_proton\\_source](https://www.lhc-closer.es/taking_a_closer_look_at_lhc/0_proton_source).
- 1306

- 1307 [5] CERN. *CERN's accelerator complex*. URL: <https://home.cern/science/accelerators/accelerator-complex>.
- 1308
- 1309 [6] *RF cavities*. URL: [https://www.lhc-closer.es/taking\\_a\\_closer\\_look\\_at\\_lhc/0\\_rf\\_cavities](https://www.lhc-closer.es/taking_a_closer_look_at_lhc/0_rf_cavities).
- 1310
- 1311 [7] Edmund J N Wilson. *An introduction to particle accelerators*. Oxford: Oxford Univ. Press, 2001. doi: 10.1093/acprof:oso/9780198508298.001.0001. URL: <http://cds.cern.ch/record/513326>.
- 1312
- 1313 [8] Riccardo De Maria, Oliver Brüning, and Rivkin Leonid. "LHC Interaction region upgrade". In: (Jan. 2008).
- 1314
- 1315 [9] LHC outreach. *CERN's accelerator complex*. URL: <https://lhc-machine-outreach.web.cern.ch/collisions.htm>.
- 1316
- 1317 [10] Werner Herr and B Muratori. "Concept of luminosity". In: (2006). doi: 10.5170/CERN-2006-002.361. URL: <https://cds.cern.ch/record/941318>.
- 1318
- 1319 [11] P Grafström and W Kozanecki. "Luminosity determination at proton colliders". In: *Prog. Part. Nucl. Phys.* 81 (2015), 97–148. 52 p. doi: 10.1016/j.ppnp.2014.11.002. URL: <http://cds.cern.ch/record/2153734>.
- 1320
- 1321
- 1322 [12] S van der Meer. *Calibration of the effective beam height in the ISR*. Tech. rep. CERN-ISR-PO-68-31. ISR-PO-68-31. Geneva: CERN, 1968. URL: <https://cds.cern.ch/record/296752>.
- 1323
- 1324 [13] Carlo Rubbia. *Measurement of the luminosity of p-overlinep collider with a (generalized) Van der Meer Method*. Tech. rep. CERN-p $\bar{p}$ -Note-38. Geneva: CERN, Nov. 1977. URL: <https://cds.cern.ch/record/1025746>.
- 1325
- 1326
- 1327 [14] The ATLAS collaboration. *Number of Interactions per Crossing*. Jan. 2018. URL: <https://twiki.cern.ch/twiki/bin/view/AtlasPublic/LuminosityPublicResultsRun2>.
- 1328



1329

1330

## The ATLAS detector

### 4.1 General description and layout

1332 The ATLAS experiment is a multipurpose detector at the LHC built, along with its peer Compact Muon  
1333 Solenoid (CMS), in order to probe the p-p, A-A and p-A collisions using the full LHC luminosity [1].  
1334 Being the largest (but not the heaviest) detector ever built for a collider experiment the ATLAS detector  
1335 is 44m length, 25m tall and weights 7000 tonnes.  
1336 The detector has a cylindrical shape and is an onion-like arrangement of several detector systems  
1337 centred at the Interaction Point (IP) as shown in fig. 41. The sub-detectors operate in the magnetic  
1338 field created by the solenoid and toroid magnets (ATLAS owes its name to the latter). Data acquisition  
1339 and recording is controlled by the Trigger and Data Acquisition (TDAQ) systems, allowing eventually  
1340 to lower the event rate to a value acceptable for the data storage. The named systems are described in  
1341 more detail in this chapter.

### 4.2 Coordinate system

1342 The ATLAS results often reference ATLAS coordinates briefly described in this subsection. The origin  
1343 of the right-handed coordinate system is placed at the IP with the z-axis directed along the beam  
1344 direction. This, in turn, defines the transverse x-y plane with the x axis pointing towards the centre of  
1345 the LHC ring and the y axis directed upwards. All transverse observables like  $p_T$  and  $E_T$  are defined in  
1346 this 2D plane. Besides the mentioned Cartesian coordinates the azimuthal angle  $\phi$  is defined in the  
1347 transverse plane around the beam axis. The polar angle  $\theta$  is the elevation angle measured from the  
1348 beam axis. The following metric quantities are also to be mentioned:  
1349

- 1350 • Pseudorapidity  $\eta = -\ln \tan(\theta/2)$ ,
- 1351 • Rapidity  $y = 1/2 \ln [(E+p_z)/(E-p_z)]$
- 1352 • The distance between particles  $\Delta R = \sqrt{\Delta\eta^2 + \Delta\phi^2}$

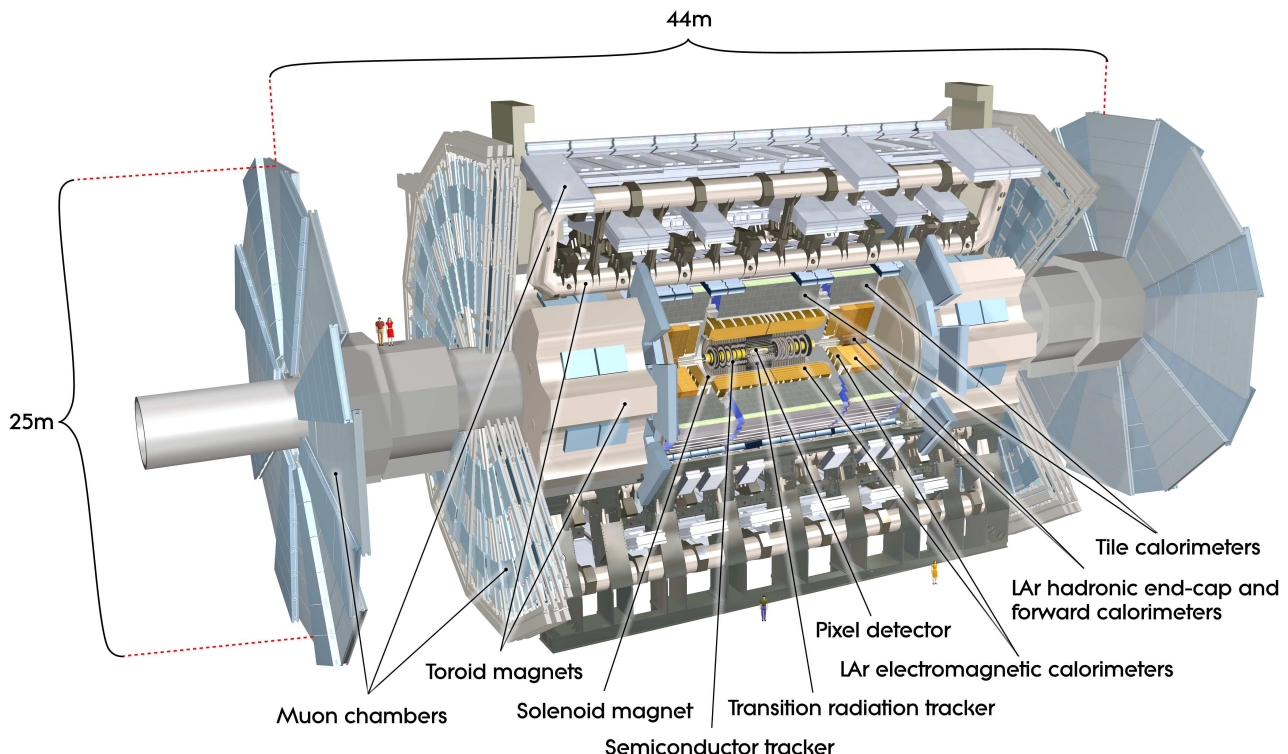


**Figure 41:** ATLAS detector general layout

### 1353 4.3 Magnet system and magnetic field

1354 ATLAS has a hybrid system of four superconducting magnets which has 22 m in diameter, 26 m in  
 1355 length and stores an energy of 1.6 GJ [2]. The windings of the magnets are schematically shown in fig.  
 1356 42. The four magnets that the magnet system comprises are the following:

- 1357 • The central solenoid is aligned with the beam axis providing a 2T axial magnetic field for the  
 1358 inner detector.
- 1359 • A barrel toroid produces a toroidal magnetic field of about 0.5T for the muon detectors in the  
 1360 barrel region.
- 1361 • Two end-cap toroids produce a toroidal magnetic field of approximately 1T for the muon detectors  
 1362 in the end-cap regions.

### 1363 4.4 Inner detector

1364 The ATLAS Inner Detector (ID) is designed to deliver pattern recognition, high-resolution momentum  
 1365 measurement [3],[4] along with primary and secondary vertex determination for charged particle tracks

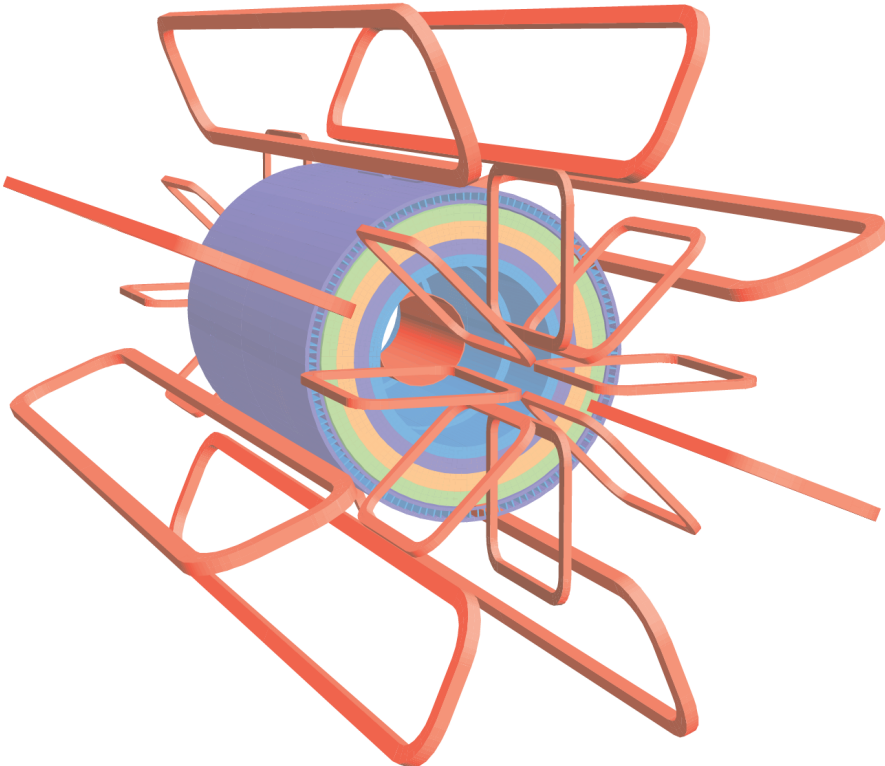


**Figure 42:** Geometry of ATLAS magnet windings

1366 above a designated  $p_T$  threshold of 0.5 GeV (in some cases being capable of going as low as 0.1 GeV)  
1367 within the pseudorapidity range  $|\eta| < 2.5$ . The inner detector provides reliable electron identification  
1368 in the rapidity range of  $|\eta| < 2.0$  for energies from 0.5 GeV to 150 GeV.

1369 The ID layout is a result of the technical requirements: it is assembled in a cylindrical envelope of 3512  
1370 mm in length and 1150 mm in radius. It is surrounded by the magnetic field of 2T imposed by the  
1371 superconducting solenoid (see section 4.3).

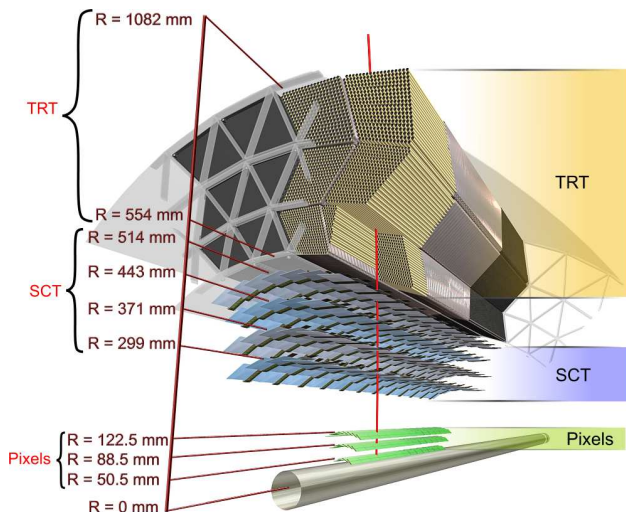
1372 Three independent sub-detectors complement each other in the inner detector (see Fig. 511a (a)):

1373 • Silicon pixel with 3 cylindrical layers for the barrel and 3 discs on each side for the end-cap. It  
1374 provides the highest granularity around the vertex region. Normally each track hits three pixel  
1375 layers. The pixel detector has about 80.4 million readout channels. Each of the 1744 identical  
1376 pixel sensors has 47232 pixels and 46080 readout channels. About 90% of the pixels have a size  
1377 of  $50 \times 400 \mu\text{m}^2$ , the remaining pixels are a bit longer:  $50 \times 600 \mu\text{m}^2$ .

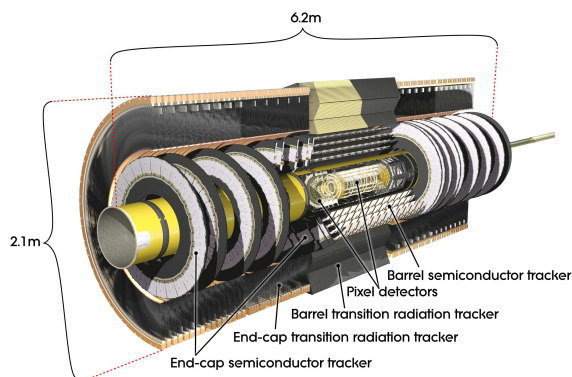
1378 • Silicon microstrip layers (SCT) with 4 cylindrical layers and 9 discs on each side for the end-cap.  
1379 A track typically crosses the strip layers in four space points. The SCT has approximately 6.3  
1380 millions readout channels from its 15912 sensors. There are 768 active strips of 12 cm length and  
1381  $80 \mu\text{m}$  width per sensor plus two bias potential strips on the sensor edges.

1382 • Transition radiation tracker (TRT) with 73 straw planes in the barrel and 160 straw planes in

1383 the end-cap. The TRT has around 351,000 readout channels and detects in average 36 hits per  
 1384 track. The straw tubes that make up the TRT module are 4 mm thick and 1.44 m long (0.37 m  
 1385 in the end-cap) and made out of polyamide films reinforced with carbon fibres. The straws are  
 1386 filled with a gas mixture of 70% Xe, 27% CO<sub>2</sub> and 3% O<sub>2</sub> and supplied with gilded tungsten  
 1387 anodes which are directly connected to the readout channels. The pixel and SCT sensors are  
 1388 highly radiation-proof and operate in the temperature range from -5°C to -10°C to minimize the  
 1389 radiation damage, while the TRT module operates at room temperature.



(a) Inner detector



(b) A perspective cut-away view of the pixel detector.

## 1390 4.5 Calorimeter system

1391 The ATLAS calorimeter system covers the rapidity range within  $|\eta| < 4.9$  and consists of several different  
 1392 detector systems. The rapidity region matched to the inner detector possesses fine granularity perfectly  
 1393 suited for high-precision measurements of photons and electrons. The remaining part's granularity  
 1394 is coarser but enough to perform hadronic jet reconstruction. The view of the ATLAS calorimeter is  
 1395 presented on fig. 44.

1396 Besides measuring the energy of travelling particles calorimeters must also contain electromagnetic  
 1397 and hadronic showers, limiting their ability to penetrate the calorimeter completely and get to the  
 1398 muon chambers. This provides a typical scale for the size of the calorimeter modules: the EMC [5] is  
 1399  $>22$  radiation lengths ( $X_0$ ) in the barrel and  $>24X_0$  in the end-caps. The hadronic calorimeter has a  
 1400 thickness of  $9.7$  interaction lengths ( $\lambda$ ) in the barrel and  $10\lambda$  in the end-cap, which is enough to keep  
 1401 the leakage level below the typical muon background. This size also provides good resolution for the  
 1402 hadron energy measurement. The detailed description of the calorimeter system can be found in table  
 1403 41. The tile calorimeter [6] uses scintillating tiles as active material alternated with steel absorbers. All  
 1404 the other calorimeter systems use liquid argon as an active medium with lead sampling.

	Barrel	End-cap	
<b>EM Calorimeter</b>			
Number of layers and $ \eta $ coverage			
Presampler	1 $ \eta  < 1.52$	1 $1.5 <  \eta  < 1.8$	
Calorimeter	3 $ \eta  < 1.35$	2 $1.375 <  \eta  < 1.5$	
Granularity $\Delta\eta \times \Delta\phi$ versus $ \eta $			
Presampler	$0.025 \times 0.1$ $ \eta  < 1.52$	$0.025 \times 0.1$ $1.5 <  \eta  < 1.8$	
Calorimeter 1st layer	$0.025 / 8 \times 0.1$ $ \eta  < 1.40$	$0.050 \times 0.1$ $1.375 <  \eta  < 1.425$	
	$0.025 \times 0.025$ $1.425 <  \eta  < 1.5$	$0.025 \times 0.1$ $1.425 <  \eta  < 1.5$	
		$0.025 / 8 \times 0.1$ $1.5 <  \eta  < 1.8$	
		$0.025 / 6 \times 0.1$ $1.8 <  \eta  < 2.0$	
		$0.025 / 4 \times 0.1$ $2.0 <  \eta  < 2.4$	
		$0.025 \times 0.1$ $2.4 <  \eta  < 2.5$	
		$0.1 \times 0.1$ $2.5 <  \eta  < 3.2$	
Calorimeter 2nd layer	$0.025 \times 0.025$ $ \eta  < 1.40$	$0.050 \times 0.1$ $1.375 <  \eta  < 1.425$	
	$0.075 \times 0.025$ $1.4 <  \eta  < 1.475$	$0.025 \times 0.025$ $1.425 <  \eta  < 2.5$	
		$0.1 \times 0.1$ $2.5 <  \eta  < 3.2$	
Calorimeter 3rd layer	$0.050 \times 0.025$ $ \eta  < 1.35$	$0.050 \times 0.025$ $1.5 <  \eta  < 2.5$	
Number of readout channels			
Presampler	7808	1536 (both sides)	
Calorimeter	101760	62208 (both sides)	
<b>LAr hadronic end-cap</b>			
$ \eta $ coverage		$1.5 <  \eta  < 3.2$	
Number of layers		4	
Granularity $\Delta\eta \times \Delta\phi$	$0.1 \times 0.1$	$1.5 <  \eta  < 2.5$	
	$0.2 \times 0.2$	$2.5 <  \eta  < 3.2$	
Readout channels		5632 (both sides)	
<b>LAr forward calorimeter</b>			
$ \eta $ coverage		$3.1 <  \eta  < 4.9$	
Number of layers		3	
Granularity $\Delta x \times \Delta y$		FCal $3.0 \times 2.6$ FCal: ~four times finer	
		$3.15 <  \eta  < 4.30$ $3.10 <  \eta  < 3.15$	
		$4.30 <  \eta  < 4.83$	
		FCal2 $3.3 \times 4.2$ FCal2: ~four times finer	
		$3.24 <  \eta  < 4.50$ $3.20 <  \eta  < 3.24$	
		$4.50 <  \eta  < 4.81$	
		FCal3 $5.4 \times 4.7$ FCal3: ~four times finer	
Readout channels		$3.32 <  \eta  < 4.60$ $3.29 <  \eta  < 3.32$	
		$4.60 <  \eta  < 4.75$	
Readout channels		3524 (both sides)	
<b>Scintillator tile calorimeter</b>			
	Barrel	Extended barrel	
$ \eta $ coverage	$ \eta  < 1.0$	$0.8 <  \eta  < 1.7$	
Number of layers	3	3	
Granularity $\Delta\eta \times \Delta\phi$	4.5. CALORIMETER SYSTEM 0.1 $0.2 \times 0.2$	47	
		$0.2 \times 0.1$	
Readout channels	5760	4092 (both sides)	

Table 41: ATLAS calorimeter in numbers

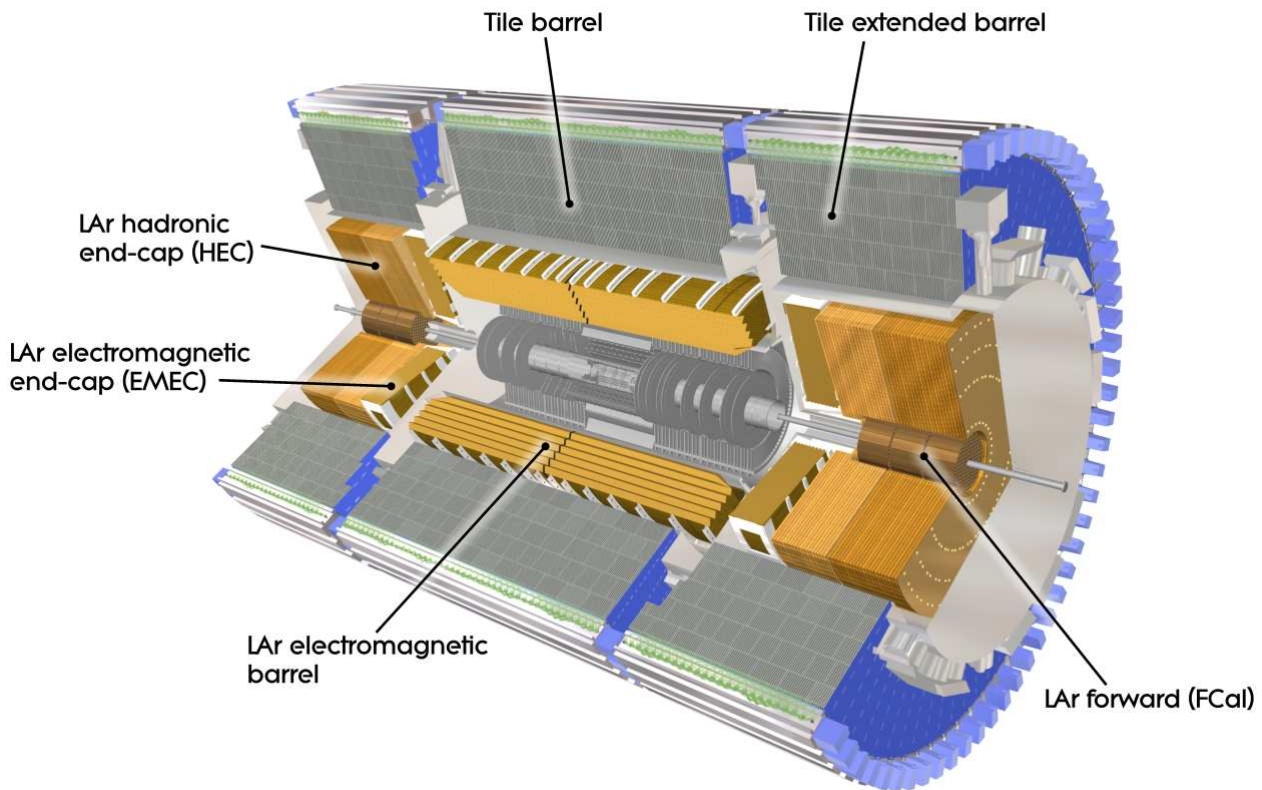


**Figure 44:** ATLAS calorimeter general layout

1405 **4.5.1 Electromagnetic calorimeter**

1406 The EMC has two submodules:

- 1407 • EMC barrel detector.
- 1408 • Electromagnetic end-cap calorimeter (EMEC) end-cap detector.

1409 The EMC barrel module consists of two identical half-barrels 3.2 meters long with inner and outer  
 1410 radii 2.8 m and 4 m respectively. There is a 4 mm gap at  $z = 0$  between the half-barrels. The second  
 1411 crack is situated between the barrel and the end-cap at  $1.37 < |\eta| < 1.52$ . The EMEC comprises two  
 1412 pairs of coaxial wheels of 63 cm thickness having inner and outer radii of 330 mm and 2098 mm  
 1413 respectively. The crack between the two wheels makes a third crack at  $|\eta| = 2.5$ . Both barrel and  
 1414 end-cap electromagnetic calorimeters are designed to have an accordion-shaped absorbers made out of  
 1415 lead plates, coated in stainless steel sheets. The readout electrodes are placed in the gaps between the  
 1416 absorbers. This type of geometry allows full coverage in  $\phi$  without cracks together with fast extraction  
 1417 of the signal from both sides of the electrodes. The orientation of the accordion waves is axial in  
 1418 the barrel and radial in the end-caps (see fig. 44). These features of the calorimeter lead to virtually

- 1419 uniform performance in the  $\phi$  dimension.
- 1420 Segmentation in  $\eta$  is very different in the layers of the calorimeter, but the second layer always has  
1421 the finest granularity because electrons and photons are supposed to leave most of their energy in the  
1422 second calorimeter layer. In order to correct for the energy losses upstream the barrel calorimeter is  
1423 preceded by a thin LAr active layer of 11 mm called presampler. For more details on  $\eta$  coverage and  
1424 granularity see table 41.

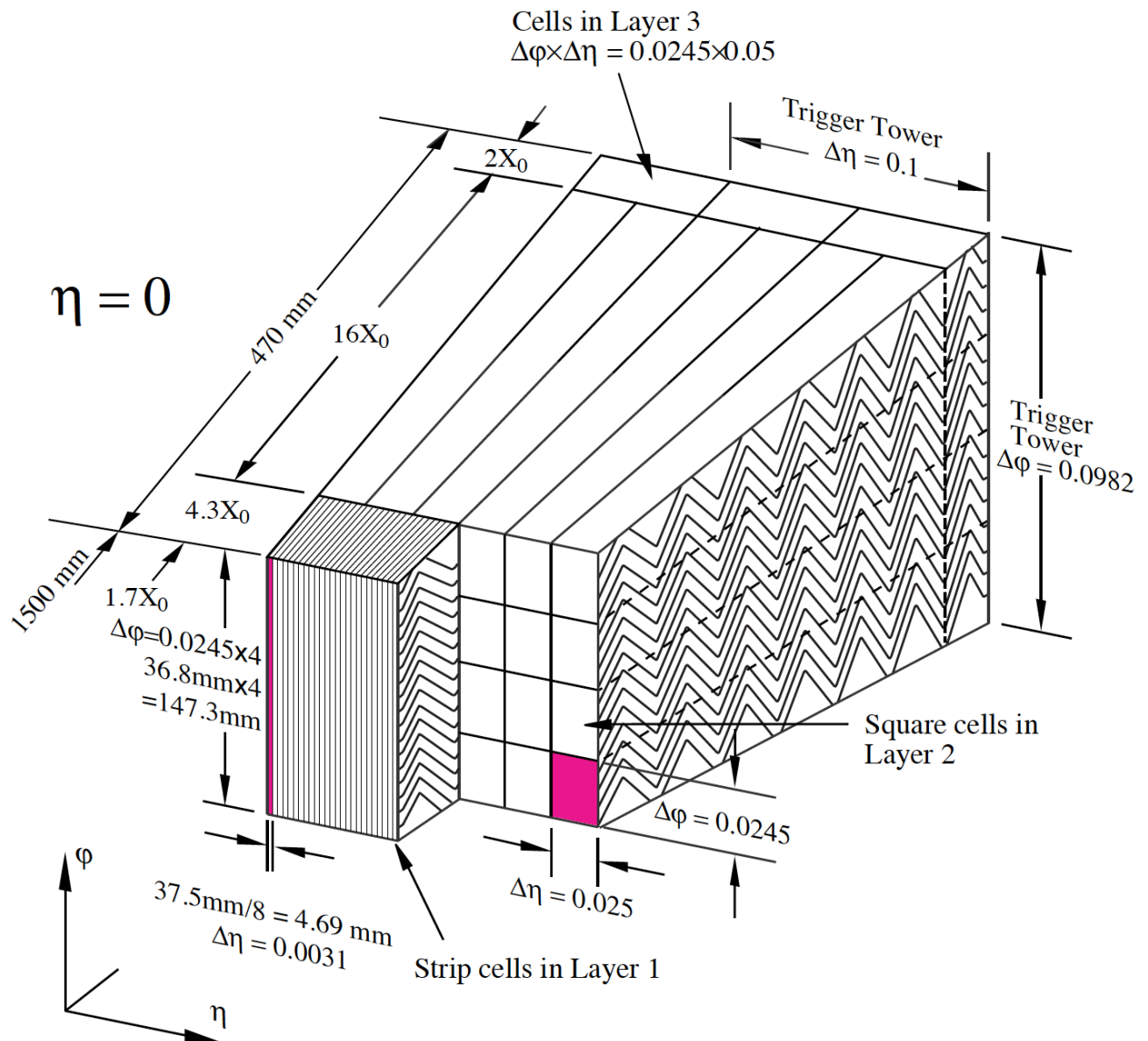
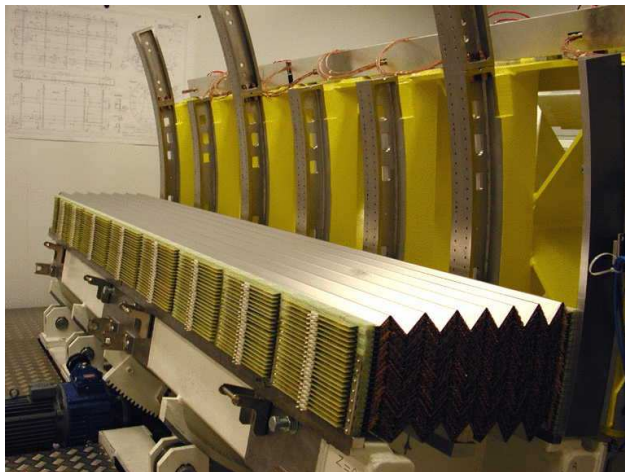


Figure 45: ATLAS EM calorimeter layers



(a) Barrel



(b) End-cap

**Figure 46:** Accordion absorbers of the EMC

#### 1425 4.5.2 Hadronic calorimeter

1426 The hadronic calorimeter (HC) is composed of three submodules:

- 1427 • HC scintillating tile detector, a steel sampled detector divided in turn into central barrel having  
1428 5.8 m in length and two extended barrels 2.6 m in length each. The extended barrels have inner  
1429 radii of 2.28 m and outer radii of 4.25 m. The tile calorimeter consists of three layers having  
1430 about 1.5, 4.1 and 1.8 interaction lengths  $\lambda$  in the barrel and 1.5, 2.6 and 3.3  $\lambda$ s in the extended  
1431 barrel.
- 1432 • Hadronic end-cap calorimeter (HEC) detector is a liquid argon calorimeter sampled with copper.  
1433 It has two pairs of independent wheels symmetrically located behind the EMEC called the front  
1434 and the rear wheel. The wheels are cylindrical, their outer radius is 2030 mm.
- 1435 • Forward calorimeter (FCal) detector modules are located about 4.7 m from the IP and are  
1436 subjected to very high particle flux and radiation. It consists of three wheels 45 cm deep each.  
1437 The first one, FCal1 is sampled with copper intended for the measurement of electromagnetic  
1438 processes. The two other wheels FCal2 and FCal3 are sampled with tungsten and designed for  
1439 the hadronic showers measurement.

1440 The number of the readout channels as well as the  $\eta$  coverage of every module and submodule is  
1441 described in the Table 41.

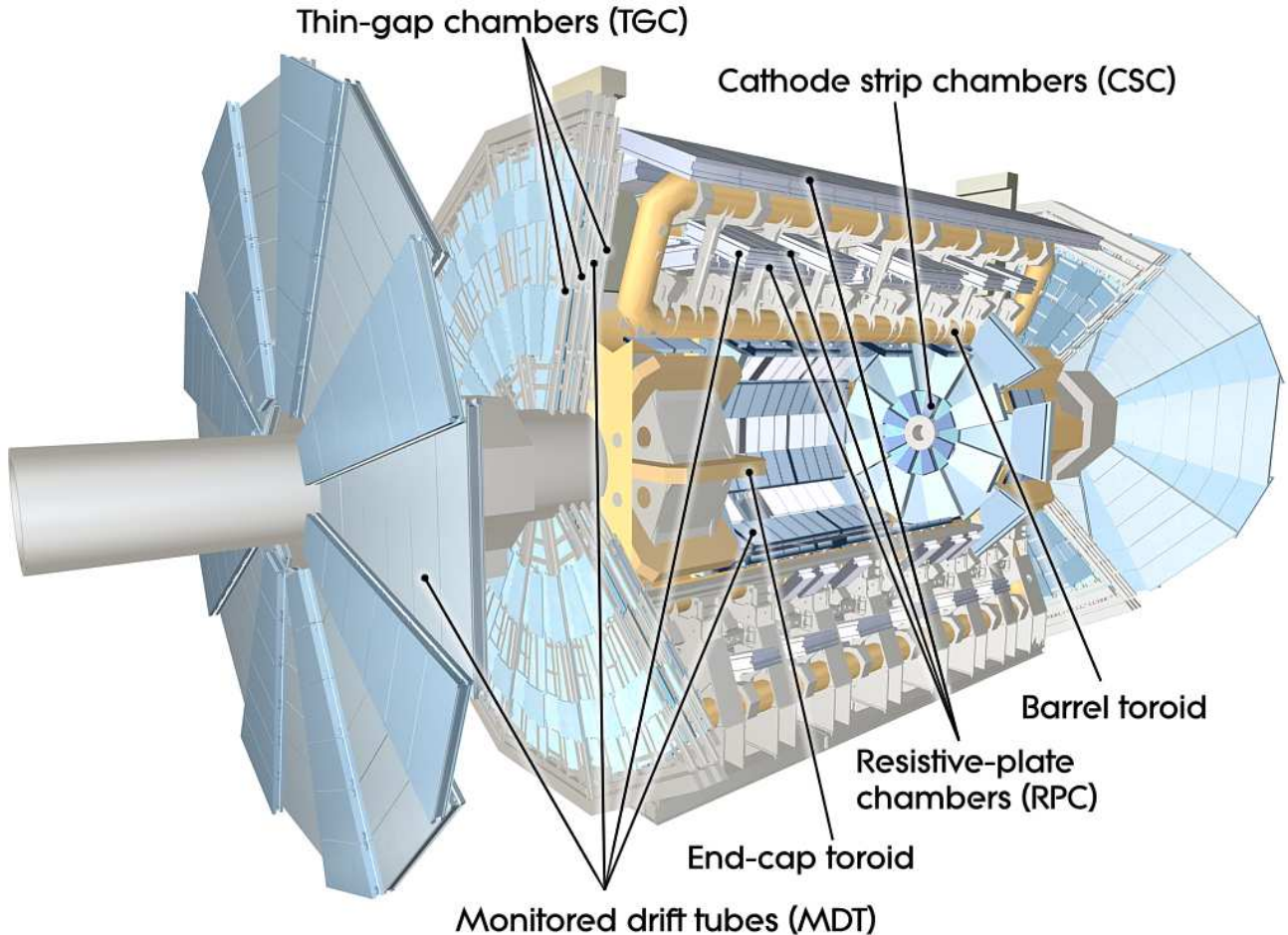


**Figure 47:** ATLAS muon system

## 1442 4.6 Muon detectors

1443 Most of the muons produced as a result of the p-p collisions are able to penetrate through the calorimeters and make it to the muon detectors where their tracks are getting measured. The spectrometer provides high-precision measurement of the muon momenta in the rapidity range of  $|\eta| < 2.7$  and approximate transverse momentum range of  $3 \text{ GeV} < p_T < 3 \text{ TeV}$ . The lower bound on the momentum is mainly due to energy losses in the calorimeter, while the upper bound is caused by the sagitta bias coming from the tracking chambers alignment. The goal  $p_T$  resolution is about 10% for a 1 TeV muon track.

1450 The muon tracks[7],[8] are bent by the toroid magnets allowing to determine muon kinematic properties. The large barrel toroid covers the rapidity range of  $|\eta| < 1.4$ , while at  $1.6 < |\eta| < 2.7$  the tracks are bent by the smaller end-cap magnets. The deflection in the transition region of  $1.4 < |\eta| < 1.6$  is provided by the barrel and end-cap fields combined.

1454 The general layout of the muon spectrometer is depicted on fig. 47, the parameters of the muon systems

1455 can be found in table 42. Just like the rest of the detector systems the muon spectrometer is split into  
1456 the barrel and the end-cap parts.

1457 The muon spectrometer possesses a fast triggering system able to trigger for muons in the rapidity  
1458 range of  $|\eta| < 2.4$ . It delivers the track information within a few tens of nanoseconds after the particle  
1459 passage which also allows to use it for the bunch-crossing identification. The trigger chambers measure  
1460 both  $\eta$  and  $\phi$  coordinates of a track of which the former is in the bending plane and the latter is in the  
1461 non-bending plane.

1462 There are two types of fast triggering detectors used in the muon spectrometer:

1463 • The Resistive Plate Chambers (RPCs) is a gaseous electrode-plate detector filled with a  $C_2H_2F_4/Iso-$   
1464  $C_4H_{10}/SF_6$  gas mixture (94.7/5/0.3). Two resistive plates of phenolic-melaminic plastic laminate  
1465 are separated by insulating spacers of 2 mm thickness. The plates contain an electric field of  
1466 about 4.9 kV/mm such that the ionizing tracks cause avalanches towards the anode. The signal is  
1467 read out through the capacitive coupling of metallic strips, mounted to the resistive plates. The  
1468 RPCs have nominal operating voltage of 9.8 kV and provide an excellent time resolution of a few  
1469 ns with a supported local rate capability of  $1000 \text{ Hz/cm}^2$

1470 • Thin Gap Chambers (TGCs) are multi-wire proportional chambers with the wire-to-cathode  
1471 distance of 1.4 mm and wire-to-wire distance of 1.8 mm and wire potential of 2900 V. The  
1472 2.8-mm gas gap is filled with highly quenching gas mixture of  $CO_2$  and  $n - C_5H_{12}$  (55/45). Small  
1473 distance between the wires allows a very good time resolution of  $<25$  ns in 99% of cases .

1474 The precision-tracking chambers measure the coordinate of a track in the bending plane which is then  
1475 matched with the second coordinate, measured by the trigger chamber.

1476 There are two types of precision tracking systems used:

1477 • The Monitored Drift Tubes (MDTs) are pressurised drift tubes with a diameter of 29.970 mm  
1478 filled with  $Ar/CO_2$  at 3 bar. Once the muon penetrates the tube it ionises the gas and the  
1479 ionised electrons are collected at the central tungsten-renium wire of  $50 \mu\text{m}$  in diameter and at a  
1480 potential of 3080 V. This type of design carries several advantages: mechanical stiffness hence  
1481 the alignment precision, reliability coming from the fact that a failure of a single tube would  
1482 not cause malfunction of the others. MDTs counting rate is limited to  $150 \text{ Hz/cm}^2$  which is not  
1483 sufficient for the innermost layer in the forward region of  $2.0 < |\eta| < 2.7$ .

1484 • Cathode Strip Chambers (CSCs) are gas detectors filled with  $Ar/CO_2$  in 80/20 proportion. The  
1485 ionised electrons are collected at the wires which are oriented in the radial direction and operate  
1486 at a potential of 1900 V. They are installed in the so-called Small Wheels and there are 16 CSCs  
1487 on either side of the ATLAS detector. . The CSCs are able to provide a counting rate of 1000  
1488  $\text{Hz/cm}^2$  which makes it a reasonable replacement for the MDTs in the region close to the beam.

1489 The precision-tracking chambers in the barrel are positioned between and on the coils of the super-  
 1490 conducting barrel toroid magnet. They form three concentric cylindrical shells around the beam axis  
 1491 at the approximate radii of 5 m, 7.5 m and 10 m. In the barrel region the RPCs were chosen for the  
 1492 fast triggering whereas the MDTs provide the precision tracking. The end-cap muon spectrometer is  
 1493 assembled in the form of large wheels perpendicular to the beam axis and located at distances about  
 1494 7.4 m, 10.8 m, 14 m and 21.5 m from the interaction point. The triggering in the end-cap is provided  
 1495 by the TGCs. Most of the precision tracking chambers are the MDTs similarly to the barrel, except for  
 1496 the forward region of  $2.0 < |\eta| < 2.7$  where the CSCs are installed in the innermost tracking layer. The  
 1497 reason for that is their higher resistance to radiation and increased particle flow which becomes an  
 1498 issue if you get closer to the beam.  
 1499 Barrel and end-cap alignment is illustrated on Fig. 48 which contains the side and transverse views of  
 the muon spectrometer.

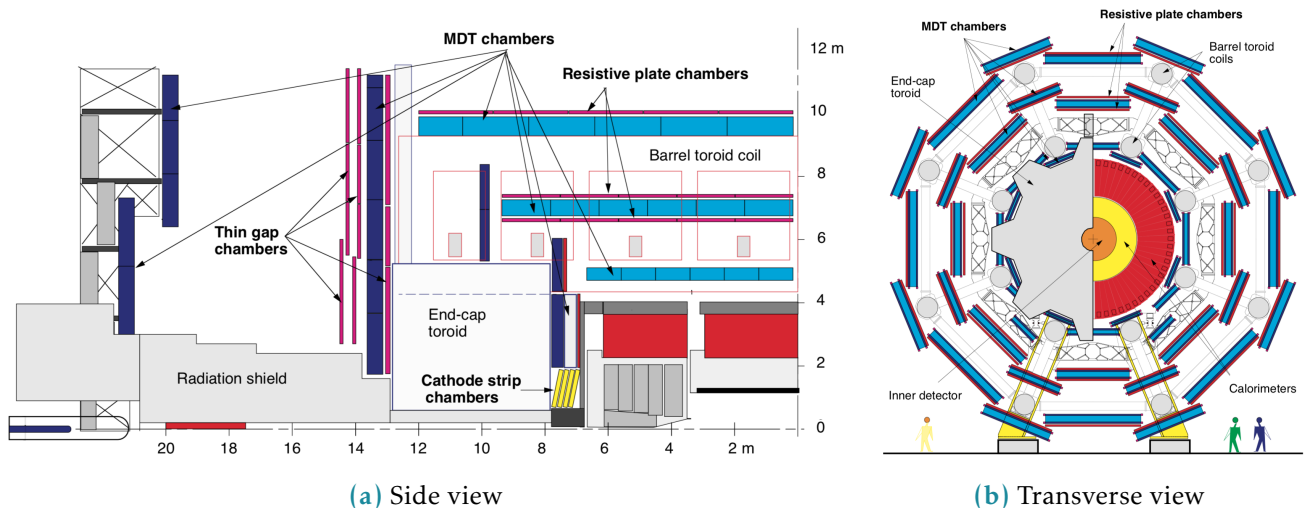


**Figure 48:** Cut views of the muon systems

1500

## 1501 4.7 Forward detectors

1502 There are three detector systems that cover the ATLAS forward region (see Fig. 49): LUminosity  
 1503 measurement using Cherenkov Integrating Detector (LUCID), Absolute Luminosity for ATLAS (ALFA)  
 1504 and Zero-Degree Calorimeter (ZDC). The measurement of luminosity is the main goal of the first two  
 1505 detectors and has fundamental importance: it provides the normalization scale for all the observed  
 1506 processes.  
 1507 LUCID[9], [10] is the main ATLAS relative luminosity monitor. The main purpose of the LUCID detec-  
 1508 tor is to detect inelastic p-p scattering in the forward region measuring the integrated luminosity and  
 1509 performing online monitoring of the instantaneous luminosity and beam conditions with uncertainty  
 1510 of about few percent. It is symmetrically installed at  $\pm 17$  m from the interaction point and at a radial

<b>Monitored drift tubes</b>	<b>MDT</b>
Coverage	$ \eta  < 2.7$ (innermost layer: $ \eta  < 2.0$ )
Number of chambers	1088 (1050)
Number of channels	339 000 (354 000)
Function	Precision tracking
<b>Cathode strip chambers</b>	<b>CSC</b>
Coverage	$2.0 <  \eta  < 2.7$
Number of chambers	32
Number of channels	31 000
Function	Precision tracking
<b>Resistive plate chambers</b>	<b>RPC</b>
Coverage	$ \eta  < 1.05$
Number of chambers	544 (606)
Number of channels	359 000 (373 000)
Function	Triggering, second coordinate
<b>Thin gap chambers</b>	<b>TGC</b>
Coverage	$1.05 <  \eta  < 2.7$
Number of chambers	3588
Number of channels	318 000
Function	Triggering, second coordinate

**Table 42:** ATLAS muon spectrometer subsystems coverage and parameters

1511 distance of about 10 cm from the beam line (resulting in  $|\eta| \approx 5.8$ ). On each side four bundles of quartz  
 1512 fibres are used as a medium producing Cherenkov radiation directing the Cherenkov light into the 16  
 1513 Photomultipliator Tubes (PMTs) placed outside the radiation shielding.

1514 The ALFA[11] detector is used to measure the absolute luminosity through elastic scattering at small  
 1515 angles. The design of the ALFA detector allows to precisely measure the track of scattered protons  
 1516 at millimetre distance from the beams. This is achieved by placing detectors in Roman Pots i.e. thin  
 1517 walled vessels which allow to operate the detectors inside the LHC beam pipe [12]. In order to perform  
 1518 such measurement we need to meet the following conditions:

1519

- 1520 • The beam has to be more parallel than normally. Special collider beam optics allowing high values  
 1521 of the amplitude function at the interaction point  $\beta^*$  together with reduced beam emittance.  
 1522 • To be sensitive to small angles the detectors have to be placed as far as possible from the  
 1523 interaction point and close to the beam. This is why the detectors are located inside the Roman  
 1524 Pots at  $\pm 240$  from the interaction point. On each side there are two Roman Pots separated by four  
 1525 meters.

1526 The Roman pot windows allow the elastically scattered protons to reach the square scintillating fibres

of 0.5 mm width which are in turn connected to multi-anode PMTs through the light-guides. The detector provides a spatial resolution of  $30 \mu\text{m}$  and allows to measure the absolute luminosity an uncertainty of 1.7% for the Run 2[13].

ZDC are used to detect forward neutrons at  $|\eta| > 8.3$  in heavy-ion collisions, which in turn allows to determine the centrality of such collisions. The detector is installed at  $\pm 140$  m from the interaction point. Every ZDC arm consists of 4 modules: one electromagnetic and three hadronic. These modules are quartz rods shielded by the tungsten plates and connected to the PMTs via the light-guides allowing to measure incending particle energy and position. The EM module has a better position resolution mapping each of 96 quartz rods into a single pixel, while the hadronic modules map a bundle of four rods into a pixel. Only one of the three hadronic modules per arm provide position-sensing rods and only the arm at -140 m has the position-sensing EM module.

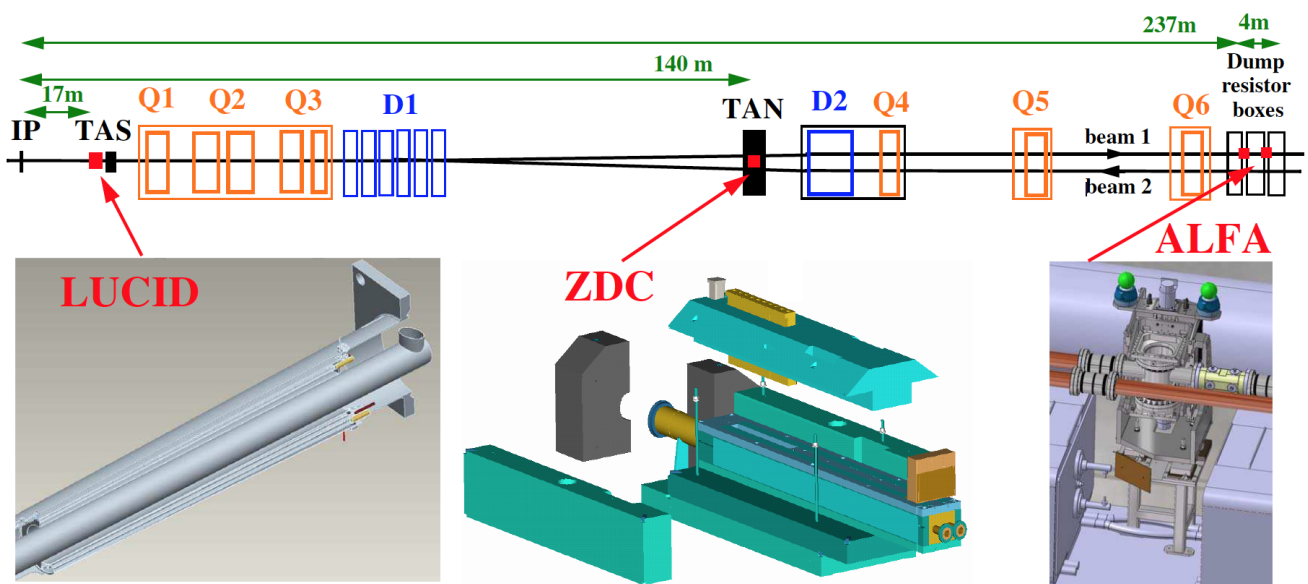


**Figure 49:** ATLAS forward detectors

1537

## 4.8 Trigger system

Considering that the bunch crossing rate at LHC is about 40 MHz and that ATLAS detector has over one million read-out channels it would never be possible to store all the raw data without significant preselection that would decrease the data rate. The selection criteria are picked to retain and store only the events which might be interesting for the LHC physics. The preselection and storage is conducted with the help of TDAQ systems.

The trigger system has three distinct levels: L1, L2 and the event filter, the two latter levels are also called High-level Trigger (HLT). Each next level refines the decisions made before and, if necessary, applies additional selection, further lowering the event rate. The data acquisition system receives and

1547 buffers the event data from the readout electronics at the L1 trigger accept rate which for Run 2 is  
1548 about 100 kHz [14]. The HLT then lowers the rate down to 1.5 kHz which is then stored for the offline  
1549 analysis.

1550 The L1 trigger looks for muons, electrons, photons and hadrons from  $\tau$ -lepton decays with high  
1551 transverse momentum, large missing and total transverse energy. The muons of interest are identified  
1552 using the muon spectrometer trigger system described in section 4.6. The rest of the particles are  
1553 selected using the information from all the calorimeters with reduced granularity. During the Run 2 an  
1554 intermediate L1Topo trigger was also added allowing to combine the information from the spectrometer  
1555 and calorimeter and extend possible trigger selections. Results from these triggers get processed by the  
1556 central trigger processor which implements the trigger menu made up of different combinations of  
1557 trigger selections. The decision latency for the L1 trigger must not exceed  $2.5 \mu\text{s}$  after the corresponding  
1558 bunch crossing.

1559 For every selected event the L1 defines one or more regions called Region of Interest (RoI) which  
1560 include the  $\eta$  and  $\phi$  coordinates of these regions for their subsequent use by the HLT. The L2 selection  
1561 is seeded by RoI and uses full granularity and precision along with other detector data available. The  
1562 trigger block diagram is presented in fig. 410.

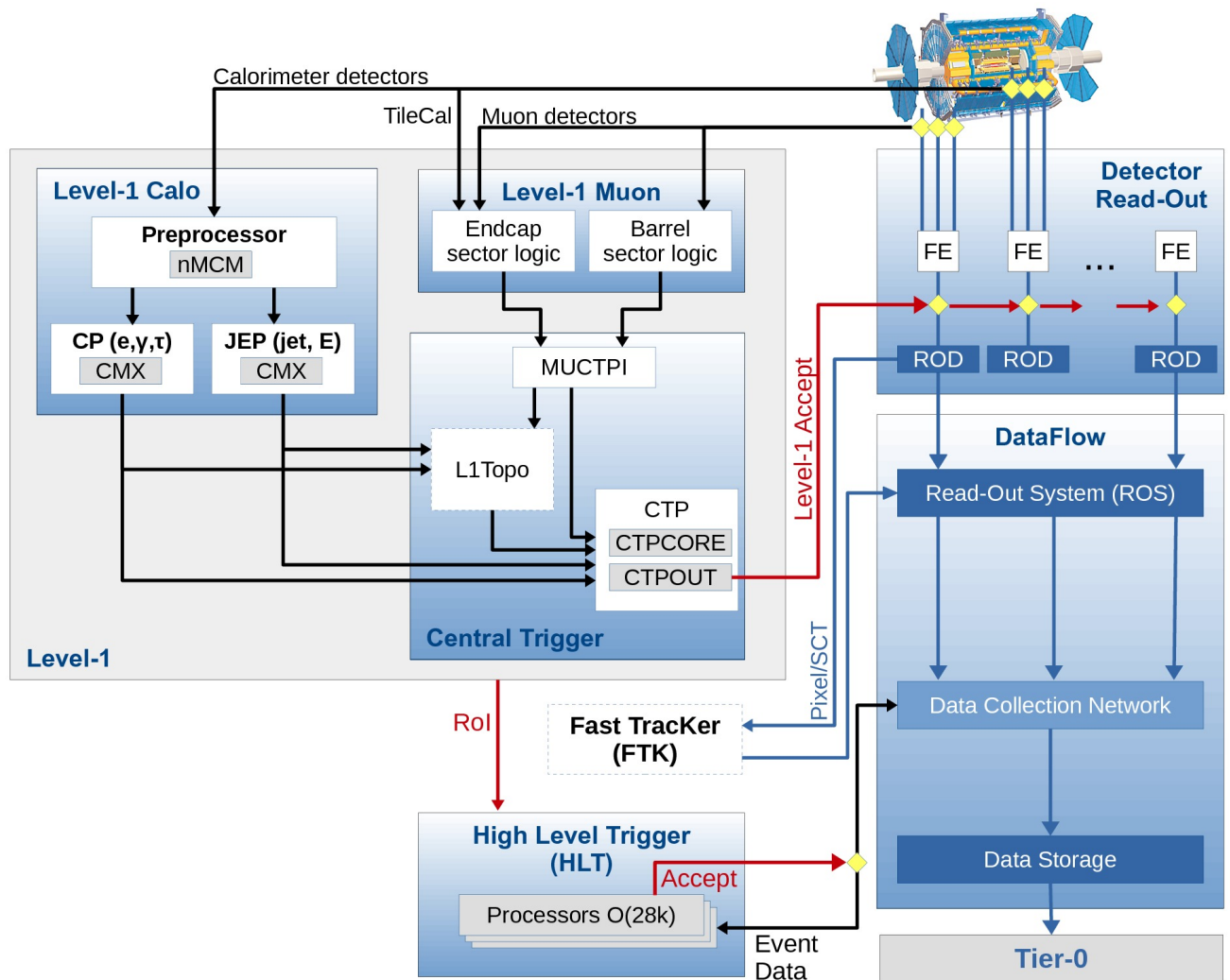


Figure 410: The scheme of ATLAS trigger systems

## 1563 Bibliography

- 1564 [1] G. Aad et al. "The ATLAS Experiment at the CERN Large Hadron Collider". In: *JINST* 3 (2008),  
1565 S08003. doi: 10.1088/1748-0221/3/08/S08003.
- 1566 [2] *ATLAS magnet system: Technical Design Report*, 1. Technical Design Report ATLAS. Geneva: CERN,  
1567 1997. URL: <https://cds.cern.ch/record/338080>.
- 1568 [3] *ATLAS inner detector: Technical Design Report*, 1. Technical Design Report ATLAS. Geneva: CERN,  
1569 1997. URL: <https://cds.cern.ch/record/331063>.
- 1570 [4] S Haywood et al. *ATLAS inner detector: Technical Design Report*, 2. Technical Design Report ATLAS.  
1571 Geneva: CERN, 1997. URL: <http://cds.cern.ch/record/331064>.

- 1572 [5] *ATLAS liquid-argon calorimeter: Technical Design Report*. Technical Design Report ATLAS. Geneva:  
1573 CERN, 1996. URL: <https://cds.cern.ch/record/331061>.
- 1574 [6] *ATLAS tile calorimeter: Technical Design Report*. Technical Design Report ATLAS. Geneva: CERN,  
1575 1996. URL: <https://cds.cern.ch/record/331062>.
- 1576 [7] *ATLAS muon spectrometer: Technical Design Report*. Technical Design Report ATLAS. Geneva:  
1577 CERN, 1997. URL: <https://cds.cern.ch/record/331068>.
- 1578 [8] ATLAS Collaboration. *Technical Design Report for the Phase-II Upgrade of the ATLAS Muon Spec-  
1579 trometer*. Tech. rep. CERN-LHCC-2017-017. ATLAS-TDR-026. Geneva: CERN, Sept. 2017. URL:  
1580 <https://cds.cern.ch/record/2285580>.
- 1581 [9] g chiodini g, n orlando n, and s spagnolo s. *ATLAS RPC time-of-flight performance*. Tech. rep.  
1582 ATL-MUON-PROC-2012-002. Geneva: CERN, Apr. 2012. URL: <https://cds.cern.ch/record/1437020>.
- 1584 [10] Marco Bruschi. *The new ATLAS/LUCID detector*. Tech. rep. ATL-FWD-PROC-2015-002. Geneva:  
1585 CERN, June 2015. URL: <https://cds.cern.ch/record/2025000>.
- 1586 [11] S. Abdel Khalek et al. “The ALFA Roman Pot Detectors of ATLAS”. In: *JINST* 11.11 (2016),  
1587 P11013. doi: 10.1088/1748-0221/11/11/P11013. arXiv: 1609.00249 [physics.ins-det].
- 1588 [12] U. Amaldi et al. “Measurements of the proton proton total cross-sections by means of Coulomb  
1589 scattering at the Cern intersecting storage rings”. In: *Phys. Lett. B* 43 (1973), pp. 231–236. doi:  
1590 10.1016/0370-2693(73)90277-3.
- 1591 [13] *Luminosity determination in pp collisions at  $\sqrt{s} = 13$  TeV using the ATLAS detector at the LHC*.  
1592 Tech. rep. ATLAS-CONF-2019-021. Geneva: CERN, June 2019. URL: <https://cds.cern.ch/record/2677054>.
- 1594 [14] William Panduro Vazquez and ATLAS Collaboration. *The ATLAS Data Acquisition system in LHC  
1595 Run 2*. Tech. rep. ATL-DAQ-PROC-2017-007. 3. Geneva: CERN, Feb. 2017. doi: 10.1088/1742-  
1596 6596/898/3/032017. URL: <https://cds.cern.ch/record/2244345>.

# 5

1597

1598

## Electromagnetic shower shapes correction in the electromagnetic calorimeter

### 1599 5.1 Introduction

1600 The design and functionality of the ATLAS electromagnetic calorimeter was described in 4.5.1. Let's  
 1601 consider a bit more in detail the physical processes happening in the EMC.

1602 In order to measure particle's energy within the calorimeter we must make the particle to loose its entire  
 1603 energy within the calorimeter. For the electrons and photons with energies over few MeV (which is the  
 1604 case for the ATLAS experiment) the primary energy loss mechanism lies in bremsstrahlung radiation  
 1605 and pair creation). The two processes complete each other, so when a high-energy electron or photon  
 1606 gets into the calorimeter, it creates an avalanche-like processus called the electromagnetic shower when  
 1607 a bremsstrahlung-radiated photons create more electron-positron pairs which in turn radiate more  
 1608 bremsstrahlung photons and so on and so forth (see fig. 51.).

1609 The longitudinal and transverse development of the shower depends on the type of the initial particle

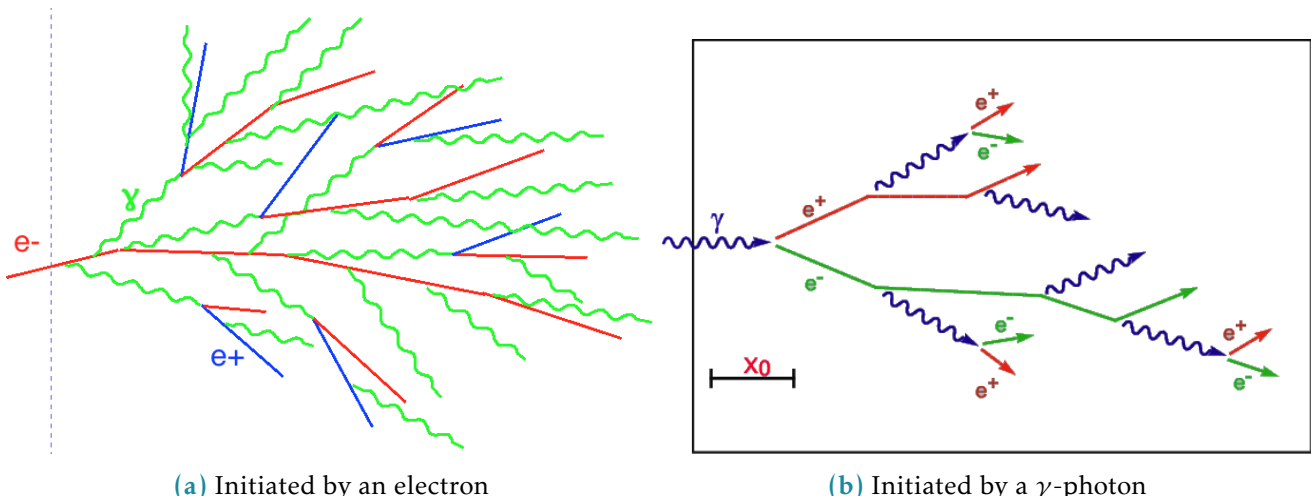
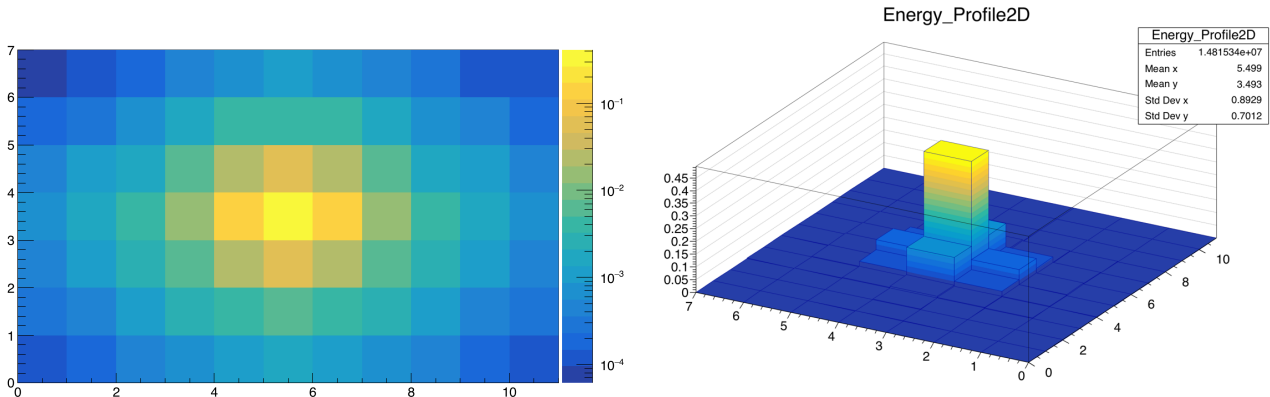


**Figure 51:** The schematic portrayal of EM shower development

1610 and on its energy. The energy is well measured by the calorimeter, but identifying the particle still  
 1611 remains a challenging task. The transverse granularity of the ATLAS calorimeter allows to resolve the  
 1612 energy distribution within the electromagnetic shower in the transverse plane. This information can

1613 later be used for particle identification.

1614 When an  $e/\gamma$  particle hits the calorimeter its footprint in the second layer of the calorimeter is visible as  
 1615 a cluster of calorimeter cells centered at the central cell having the most energy deposited (sometimes  
 1616 referred to as "the hottest cell"). Roughly 90% of shower energy is contained in the core 3x3 cells. We  
 1617 have considered a cluster of 7x11 ( $\eta \times \phi$ ) cells, which is schematically depicted on fig. 52a.

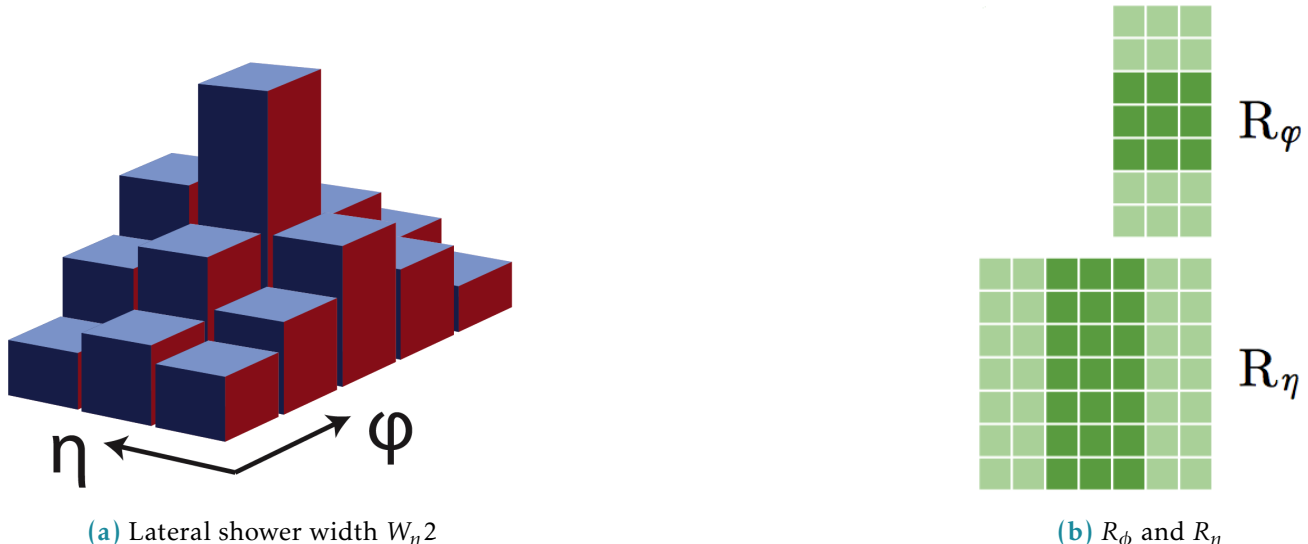


(a) Energy profile of a window of 7x11 cells in the 2nd calorimeter layer (logarithmic scale)

(b) 2D profile of the cluster

**Figure 52:** Visualisations of the 7x11 calorimeter cluster

1618 In order to characterise the energy distribution within the shower profile a number of observables  
 1619 called shower shapes are used. They are then used as an input for particle identification MVA algorithm.  
 1620 Current study focuses on the second layer of the calorimeter for which there are three shower shape  
 1621 observables described below [1]:



(a) Lateral shower width  $W_{\eta 2}$

(b)  $R_\phi$  and  $R_\eta$

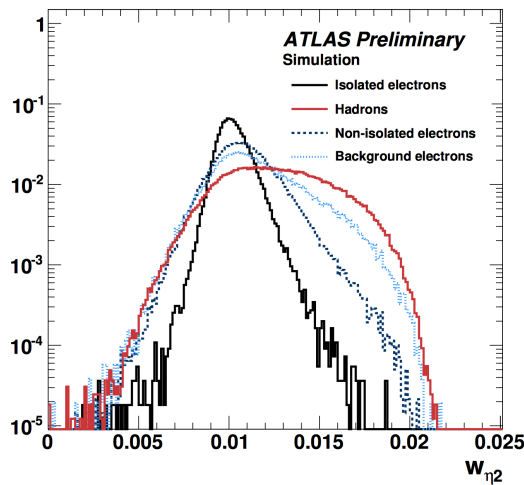
**Figure 53:** Shower shapes in the second layer of the electromagnetic calorimeter

1622 • Lateral shower width  $W_{\eta 2} = \sqrt{\sum(E_i \eta_i^2) - (\sum(E_i \eta_i)/\sum(E_i))^2}$  calculated within a window of 3x5

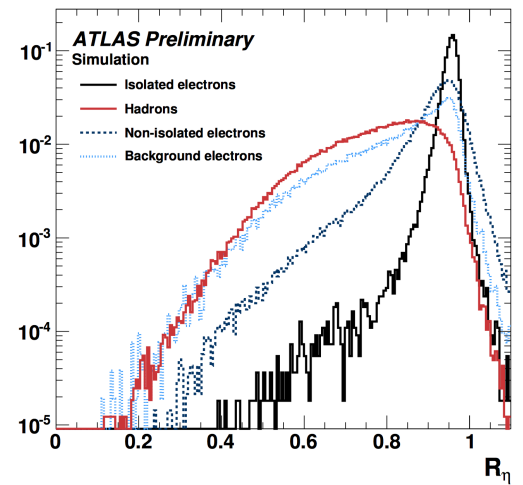
1623     cells.

- 1624     •  $R_\phi$  - ratio of the energy in 3x3 cells over the energy in 3x7 cells centered around the hottest cell.  
 1625     •  $R_\eta$  - ratio of the energy in 3x7 cells over the energy in 7x7 cells centered around the hottest cell.

1626     The shower shapes distributions for different types of particles is shown in fig. ?? - although the  
 1627     distributions overlap, combining the shower shapes information with the inputs from other detectors  
 allow to identify the particle.



(a)  $W_{\eta 2}$  distribution simulation



(b)  $R_\eta$  distribution simulation

**Figure 54:** Distribution of  $R_\eta$  in simulation (GEANT4) for electrons and jets [2].

1628

1629     Figure ?? shows how  $R_\eta$  distribution is different in jets, signal electrons and background electrons.  
 1630     Background electrons denote non-prompt electrons which are not originated from primary vertex.

1631

1632     The shower shapes appear to be extremely sensitive to the detector material modelling. A sim-  
 1633     plification in the geometry of the EMCAL absorber geometry in GEANT4 9.2 (a layered structure of  
 1634     the accordion was represented as a homogenous material) has lead to visible discrepancies in the  
 1635     shower shapes between the data and MC. This was corrected in GEANT4 9.4 significantly improving  
 1636     the agreement, although not eliminating it completely (see fig. 55). The origin for the remaining  
 1637     discrepancy is not clear.

1638

1639     Disagreement in shower shapes between the data and MC leads to discrepancies in particle ID which  
 1640     are later fixed using  $\eta$ - and  $p_T$ -dependent scale factors. Correction of the shower shapes aims to get  
 1641     the scale factors closer to unity, reducing the corresponding systematic uncertainties and improving  
 1642     the precision of the measurements with electrons in the final states.

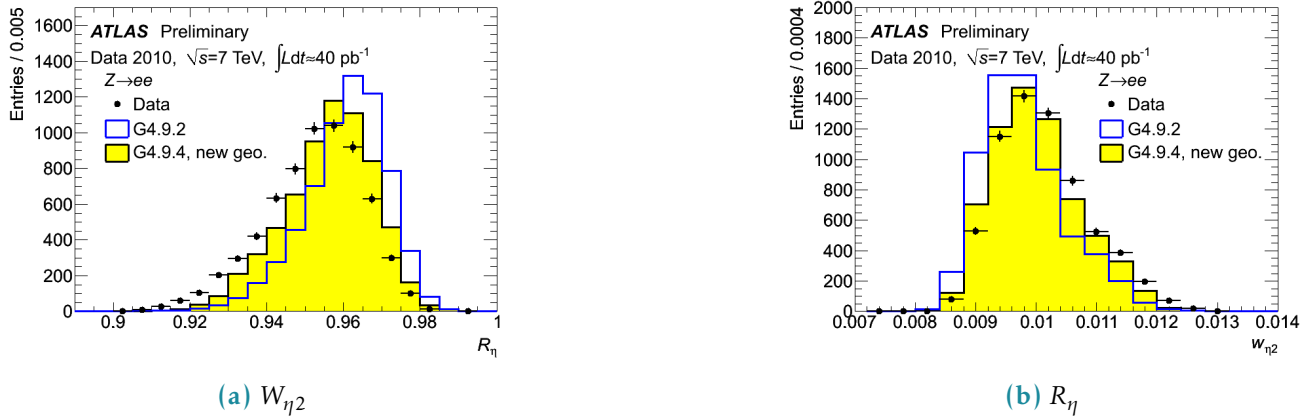


**Figure 55:** Data/MC Comparison for Calorimeter Shower Shapes of High Et Electrons [3].

## 1643 5.2 Shower shapes measurement and correction

### 1644 5.2.1 Event selection

1645 For this study we have considered electrons from the  $Z \rightarrow ee$  decay. A set of recommended single  
 1646 electron triggers was used (HLT\_e26\_lhtight\_nod0\_ivarloose, HLT\_e60\_lhmedium\_nod0,  
 1647 HLT\_e140\_lhloose\_nod0, HLT\_e300\_etcut). Each event was required to have 2 electrons at least one  
 1648 of which has  $p_T > 25$  GeV. In order to suppress the background both electrons had to pass gradient  
 1649 isolation. Z invariant mass cut was applied with a window of 80 – 120GeV. To avoid identification bias  
 1650 from triggering the tag and probe approach was used with only probe electrons taken into consideration  
 1651 [4]. The electron cluster in the second calorimeter layer was required to contain information from 77  
 1652 calorimeter cells. No pile-up reweighting has been applied. Datasets of 264786295 events in data (2017  
 1653 proton-proton collisions) and 79340000 events in MC (Powheg+Pythia8) were used.

### 1654 5.2.2 Data/MC discrepancies

1655 Our consideration begins with the energy deposit of an electron in the second layer of the calorimeter.  
 1656 A window of 7 cells in  $\eta$  and 11 cells in  $\phi$  is centered around the cell with the highest energy.

1657 Shower shapes were considered in 14  $\eta$  bins in the range between  $|\eta| = (0, 2.4)$  in order to investigate  
 1658 how the discrepancy depends on  $\eta$ .

1659 The  $\eta$ -dependent shower shapes in data are wider than the MC and show a larger discrepancy in the  
 1660 endcap ( $|\eta| = (1.52, 2.4)$ ). For  $\phi$  dimension the situation is the opposite: MC is wider than the data and  
 1661 the barrel ( $|\eta| = (0, 1.52)$ ) shows larger discrepancy. Figures ??, ??, ?? contain examples of shower shapes  
 1662 in different eta bins.

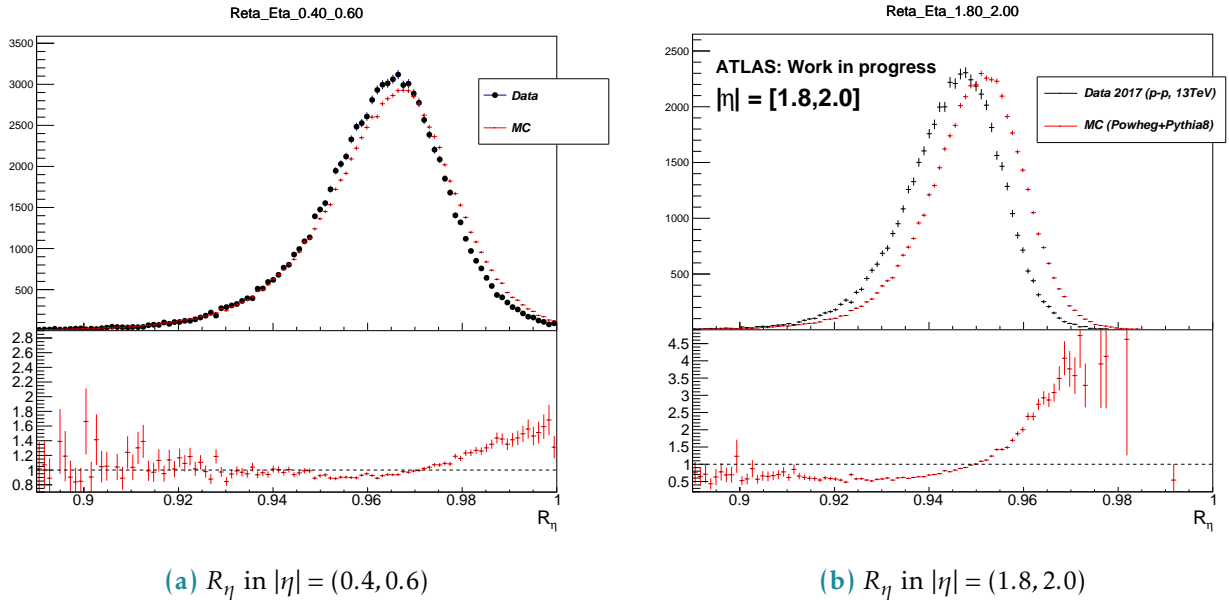


**Figure 56:**  $R_\eta$  in the barrel and in the end-cap, Data vs MC

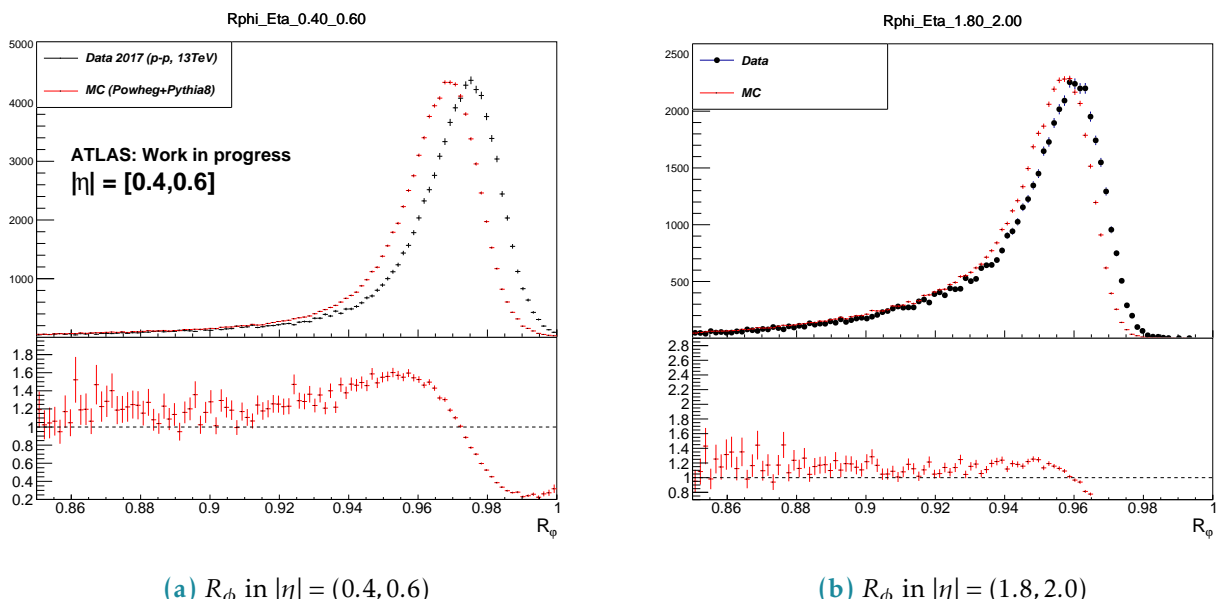


**Figure 57:**  $R_\phi$  in the barrel and in the end-cap, Data vs MC

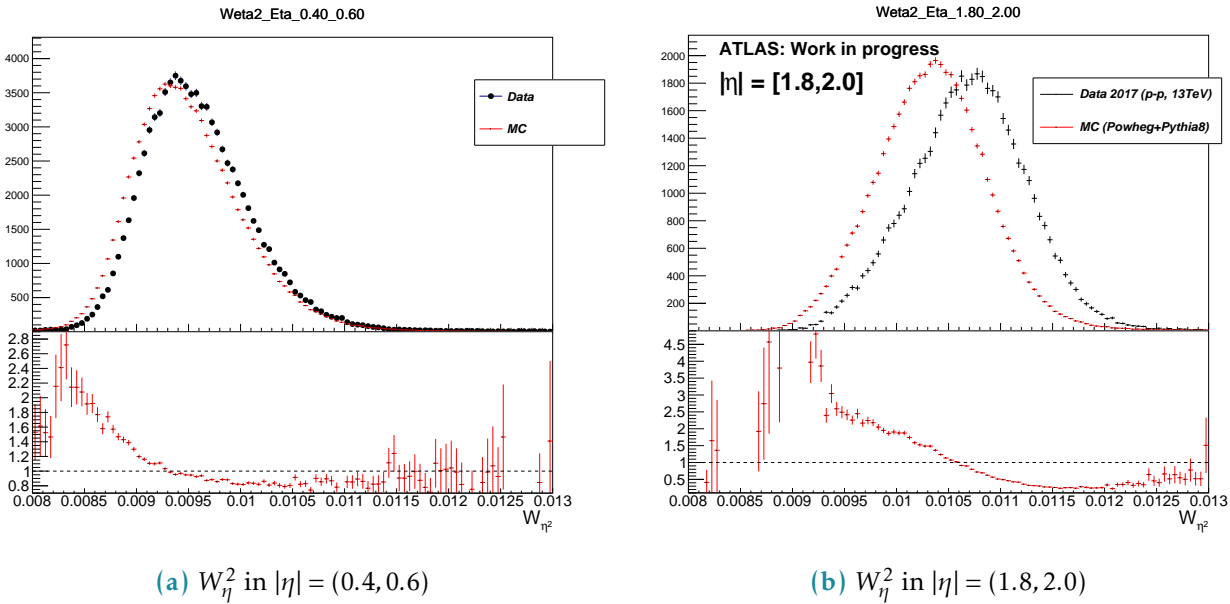


**Figure 58:**  $W_\eta^2$  in the barrel and in the end-cap, Data vs MC

### 1663 5.2.3 The correction procedure

#### 1664 The correction matrix

1665 The correction procedure is based on the redistribution of energy between the cluster cells in MC so  
 1666 that the distribution becomes consistent with the data. For every  $\eta$  bin a correction matrix is derived in  
 1667 the following way:

$$M_i^{Correction} = \frac{E_i^{Data}}{\sum E^{Data}} - \frac{E_i^{MC}}{\sum E^{MC}}$$

1668  $\sum_i M_i^{Correction} = 0, i = 1..77.$

1669  $E_i^{Data}, E_i^{MC}$  - matrix elements of the averaged energy profiles. The correction is then applied to the  
 1670 electron cluster cells on event-by-event basis:

$$E_i^{Reweighted} = E_i^{Non-reweighted} (1 + M_i^{Correction}).$$

1671 This redistributes the energy among the cells keeping the total energy exactly the same.

#### 1672 Bremsstrahlung tails

1673 The magnetic field directed along the  $\phi$  dimension leads to a significant asymmetry in energy deposits  
 1674 for electrons and positrons (figure ??).

1675 Considering the fact that the reweighting is intended to correct for the data/MC discrepancies  
 1676 themselves and not for the bremsstrahlung effect it makes sense to develop the bremsstrahlung-free  
 1677 correction function based on  $e^+$  and  $e^-$  correction matrices. The principle is schematically explained on

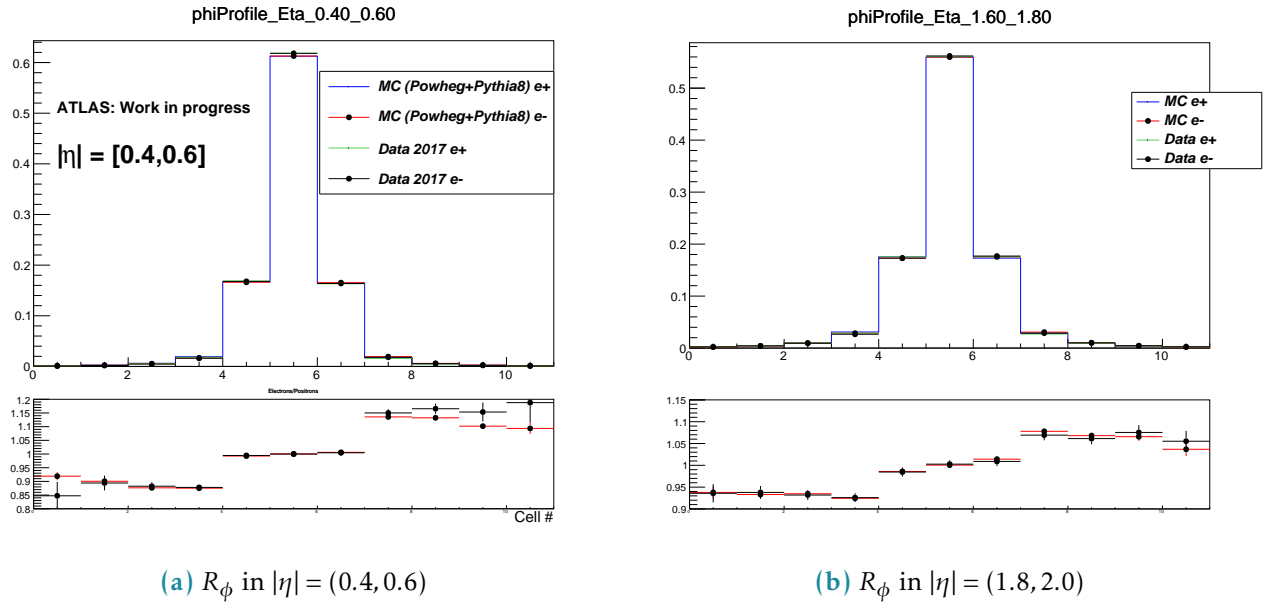


**Figure 59:**  $R_\phi$  in the barrel and in the end-cap, Data vs MC

1678 figure 510.

Good agreement of data and MC description of  $e^+$  and  $e^-$  asymmetry gives a hint that the material

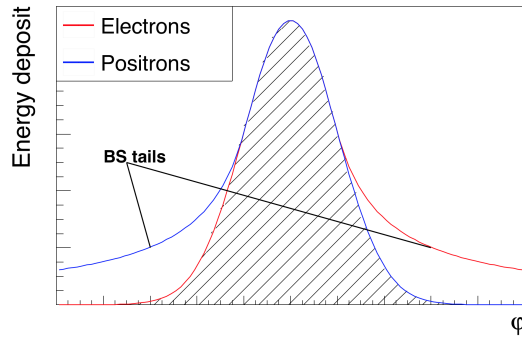


**Figure 510:** Schematic energy profile in  $\phi$  dimension. Bremsstrahlung tails subtraction based on  $e^+$  and  $e^-$  energy profiles.

1679

1680 mismodelling cannot be the main source of the data/MC disagreement.

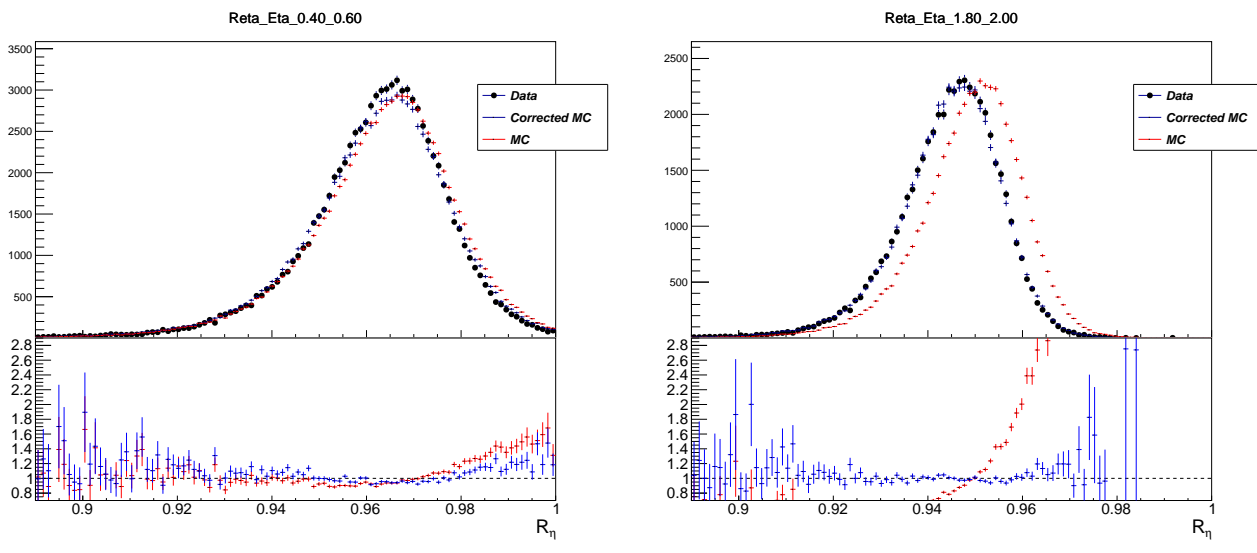
1681

### 1682 5.3 Results

1683 Figures 511, 512, 513 show the effect of the correction. The shower shapes in MC become very close to  
1684 the data, correcting a significant discrepancy.

1685 Figures 514 contain shower shapes vs  $p_T$  integrated over  $\eta$ . They demonstrate that the correction does

1686 not depend on the  $p_T$  which allows to expect the decreased systematic uncertainties for  $p_T$  regions  
 1687 distant from 40 – 50 GeV.  
 1688 Finally, figure 515 shows the effect of the correction on electron ID efficiency. We can see a visible  
 1689 improvement, notably in the endcap region. Nevertheless the barrel region shows little improvement.  
 1690 It can be explained by the fact that electron ID MVA relies on many variables while only a number of  
 1691 them were corrected during current study.  
 1692 The proposed method is getting integrated into ATLAS Athena framework as an option and is planned  
 1693 to be used as a baseline for Run 3.



(a) Reweighted  $R_\eta$  in  $|\eta| = (0.4, 0.6)$ .

(b) Reweighted  $R_\eta$  in  $|\eta| = (1.8, 2.0)$ .

**Figure 511:**  $R_\eta$  in the barrel and in the end-cap

## 1694 5.4 Appendix: control plots

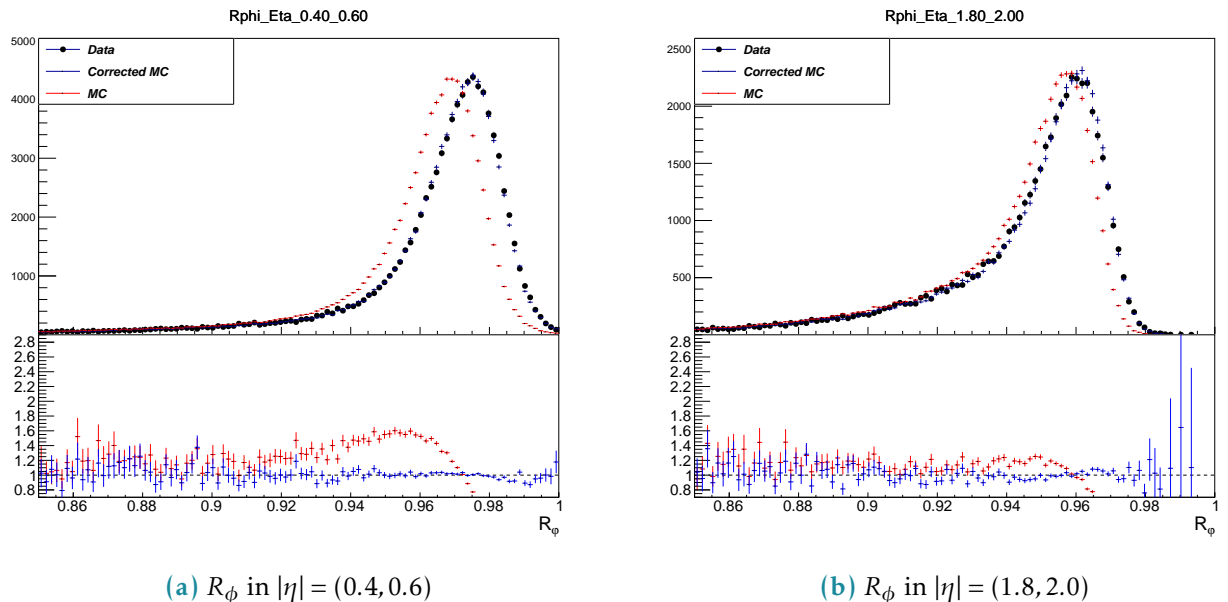


**Figure 512:**  $R_\phi$  in the barrel and in the end-cap, Data, MC, reweighted MC

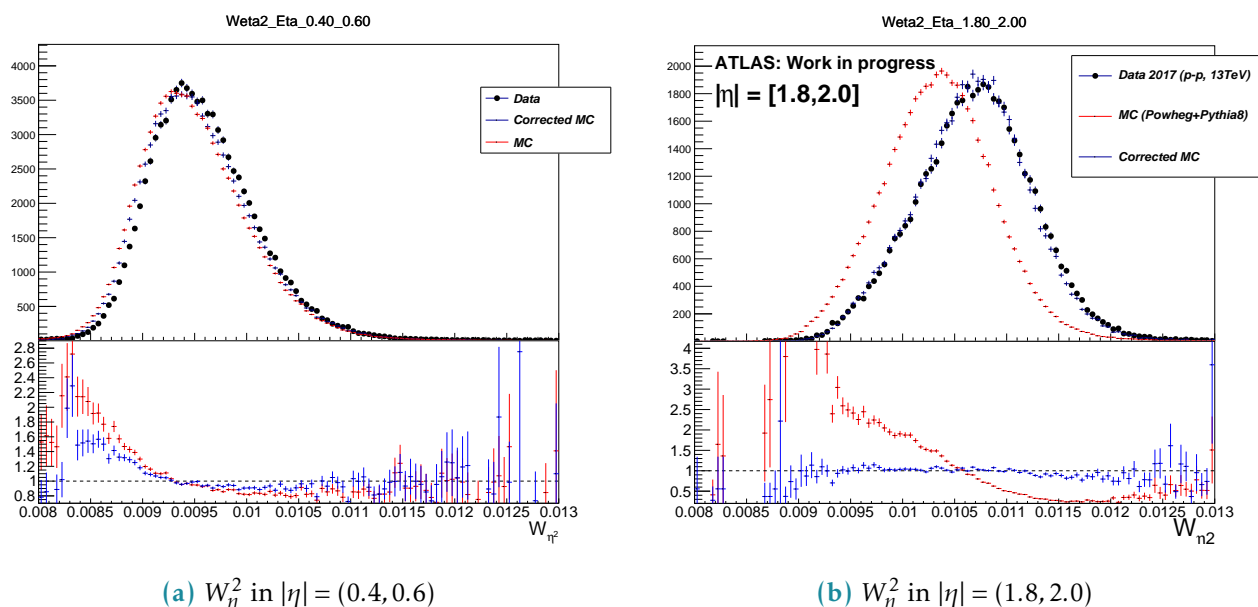


**Figure 513:**  $W_\eta^2$  in the barrel and in the end-cap, Data, MC, reweighted MC

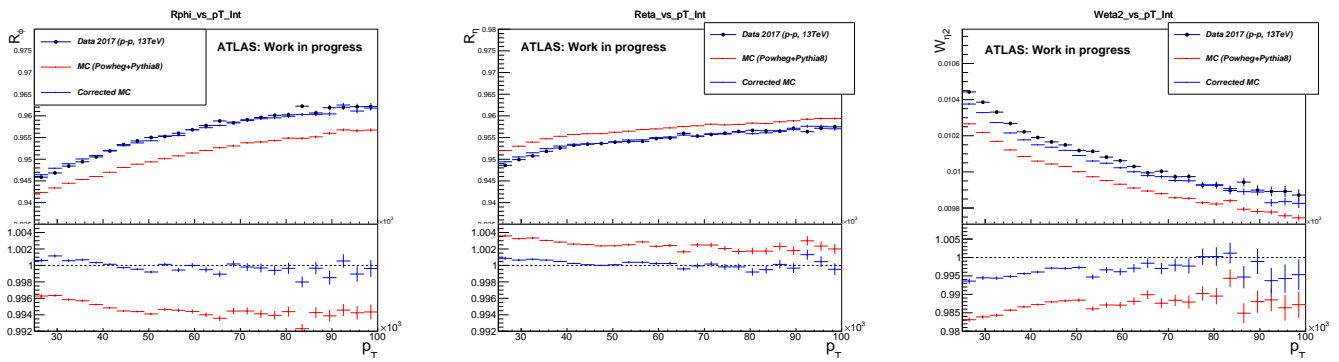


**Figure 514:** Distributions integrated over  $p_T$  (a)  $R_\phi$ ; (b)  $R_\eta$ ; (c)  $W_{\eta 2}$ .

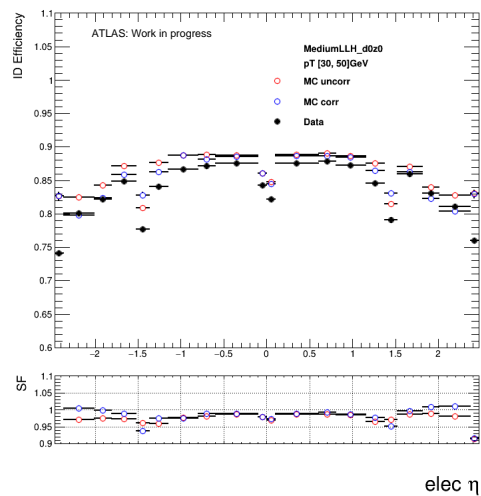


**Figure 515:** Electron identification efficiency as a function of the electron pseudo-rapidity

## 1695 Bibliography

- 1696 [1] “Electron and photon performance measurements with the ATLAS detector using the 2015-2017  
1697 LHC proton-proton collision data”. In: *JINST* 14.arXiv:1908.00005. 12 (Aug. 2019). 31 figures,  
1698 3 tables. All figures including auxiliary figures are available at <https://atlas.web.cern.ch/Atlas/GROUPS/PHYSICS/PAPERS/EGAM-2018-01>, P12006. 70 p. doi: 10.1088/1748-0221/14/12/P12006. URL: <https://cds.cern.ch/record/2684552>.
- 1701 [2] *Expected electron performance in the ATLAS experiment*. Tech. rep. ATL-PHYS-PUB-2011-006.  
1702 Geneva: CERN, Apr. 2011. URL: <http://cds.cern.ch/record/1345327>.
- 1703 [3] *Data/MC Comparison for Calorimeter Shower Shapes of High Et Electrons*. Tech. rep. ATL-COM-  
1704 PHYS-2011-1299. Geneva: CERN. URL: <https://atlas.web.cern.ch/Atlas/GROUPS/PHYSICS/EGAMMA/PublicPlots/2011005/ATL-COM-PHYS-2011-1299/index.html>.

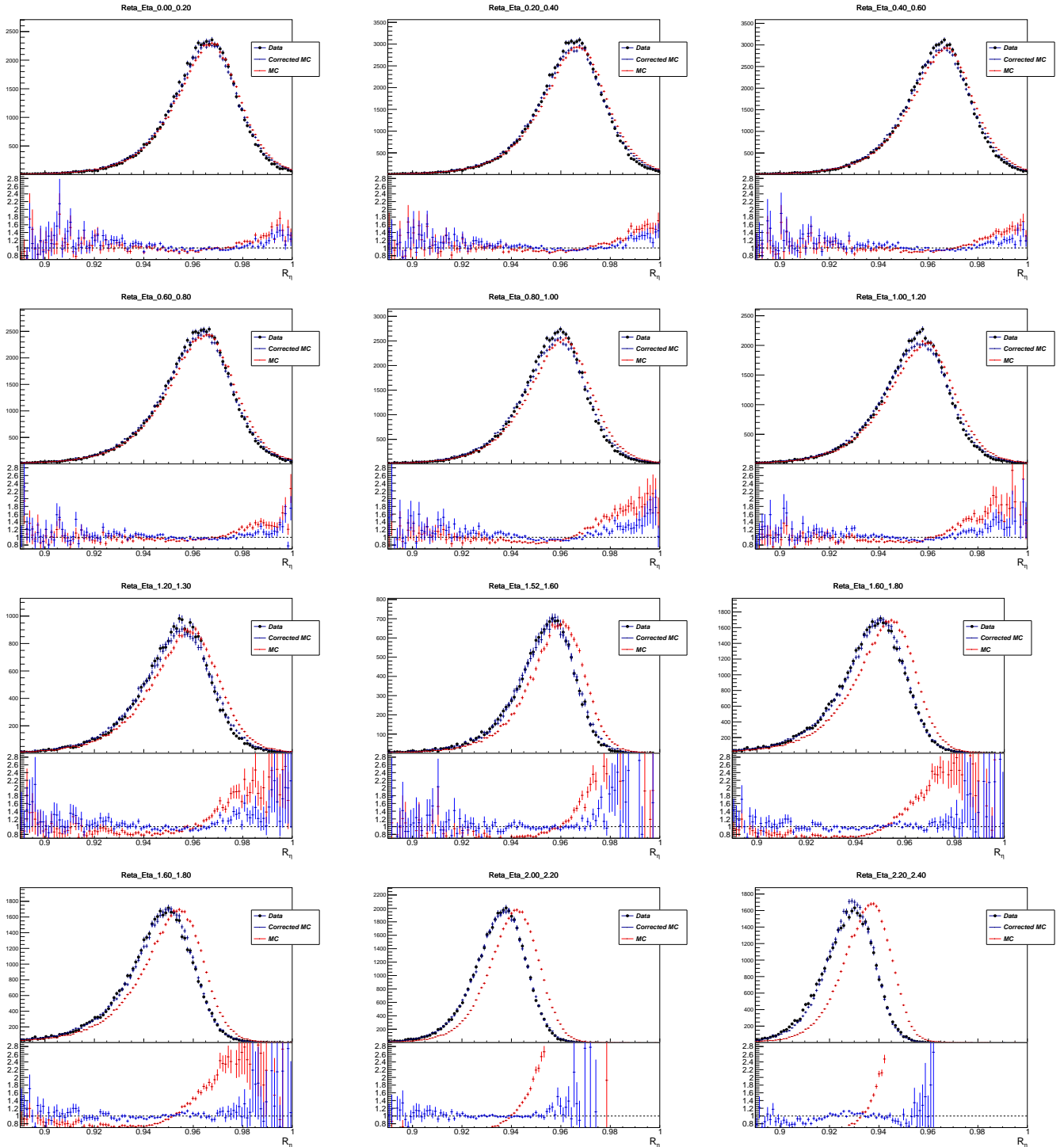
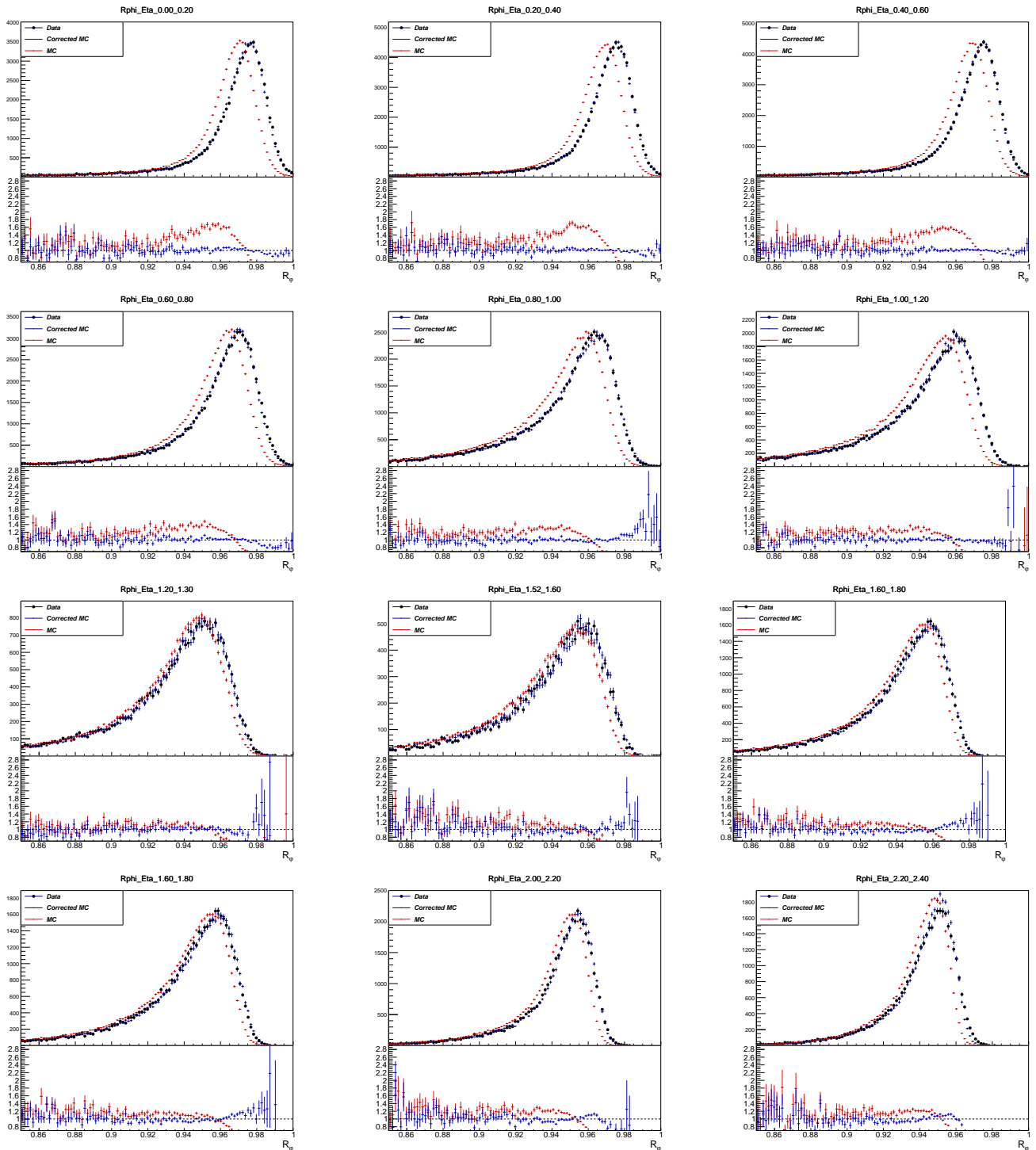


Figure 516: Reta 2

- 1706 [4] “Electron reconstruction and identification efficiency measurements with the ATLAS detector  
 1707 using the 2011 LHC proton-proton collision data. Electron reconstruction and identification effi-  
 1708 ciency measurements with the ATLAS detector using the 2011 LHC proton-proton collision data”.

## Mesure de la masse du boson W avec le détecteur ATLAS au LHC



**Figure 517:** Rphi in all eta slices

1709 In: *Eur. Phys. J. C* CERN-PH-EP-2014-040. CERN-PH-EP-2014-040 (Apr. 2014). Comments: 38  
 1710 pages plus author list (62 pages total), 20 figures, 4 tables, submitted to JHEP, All figures includ-  
 1711 ing auxiliary figures are available at <https://atlas.web.cern.ch/Atlas/GROUPS/PHYSICS/PA>

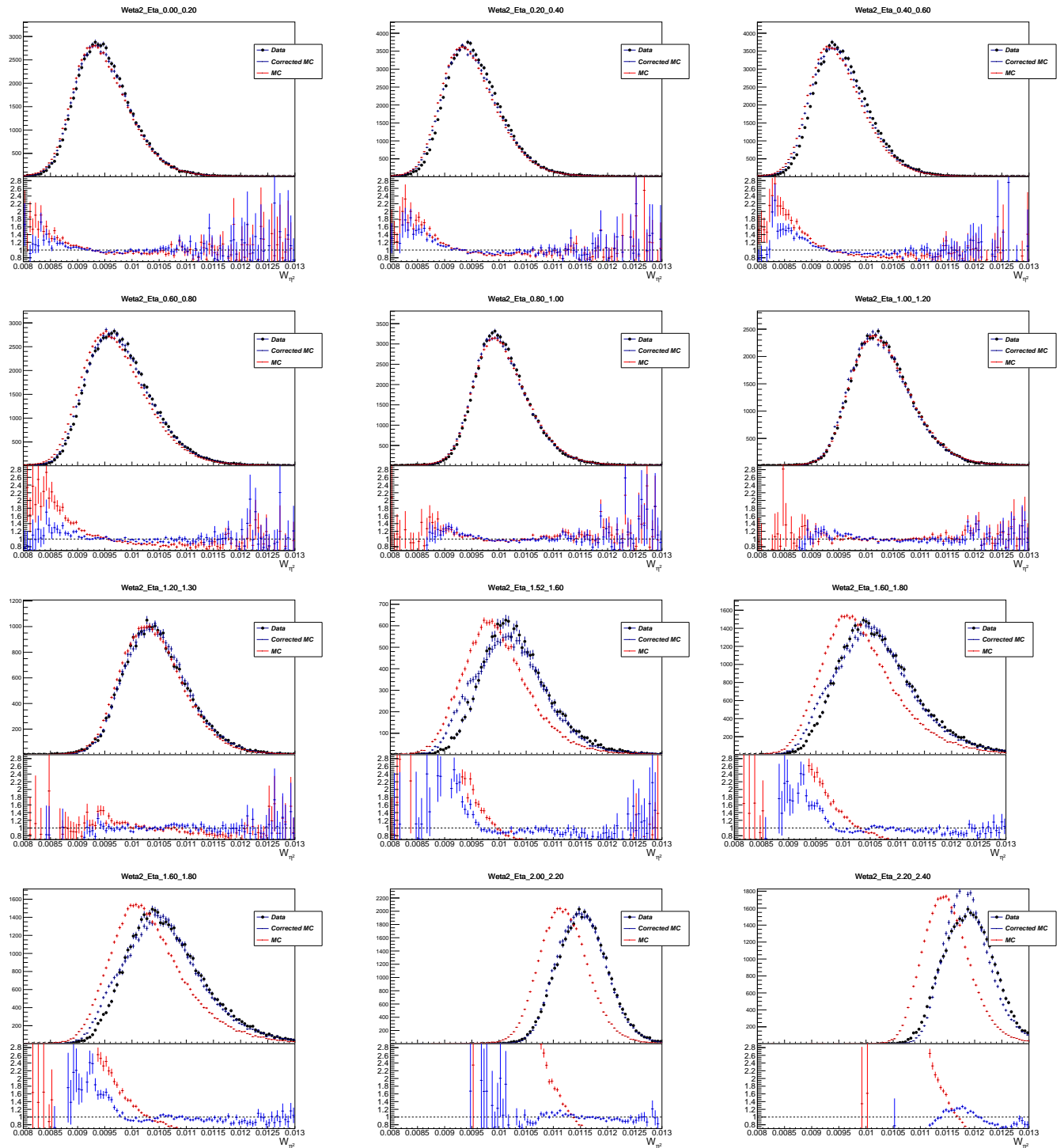


Figure 518: Reta 2

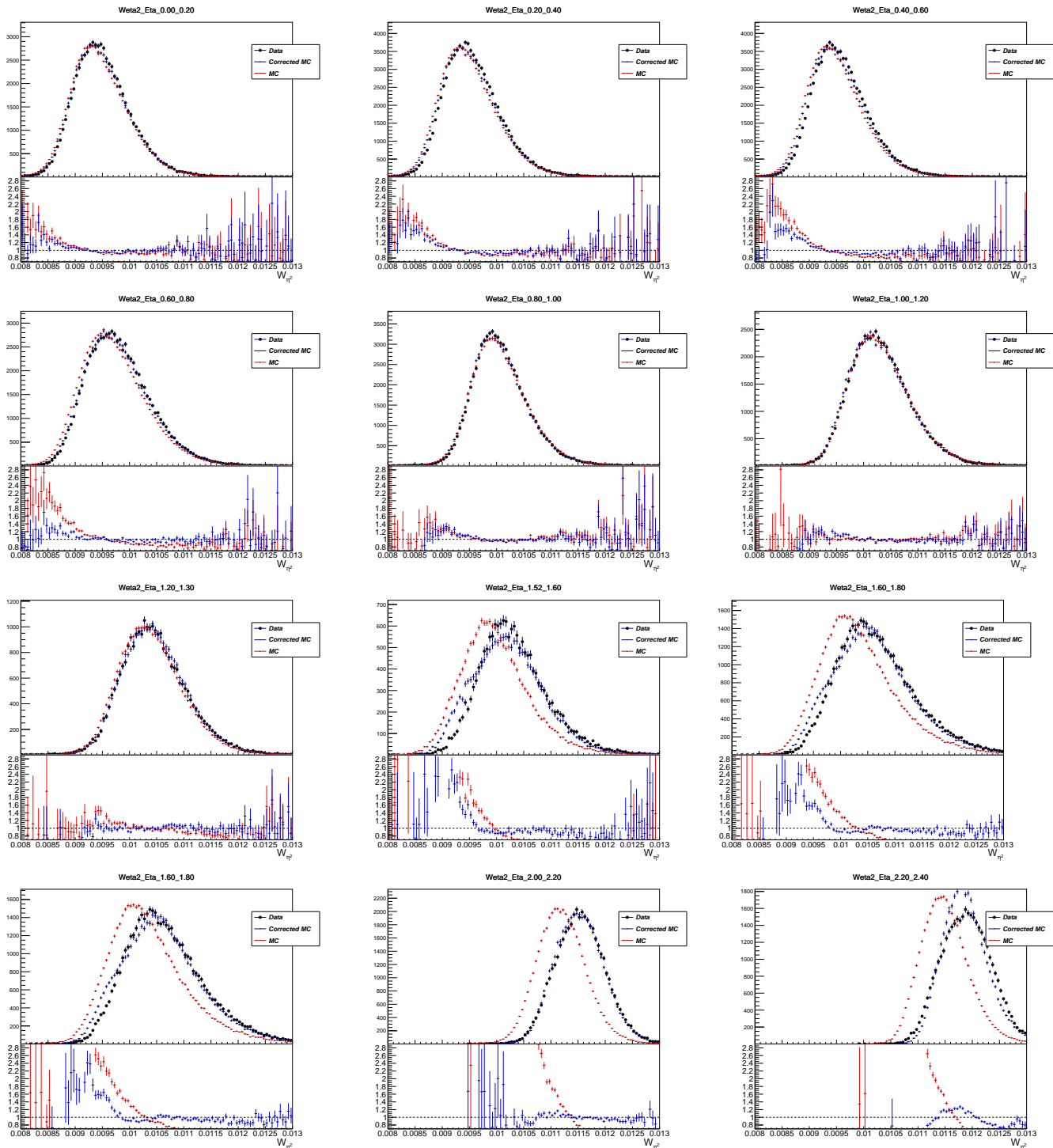


Figure 519: Reta 2

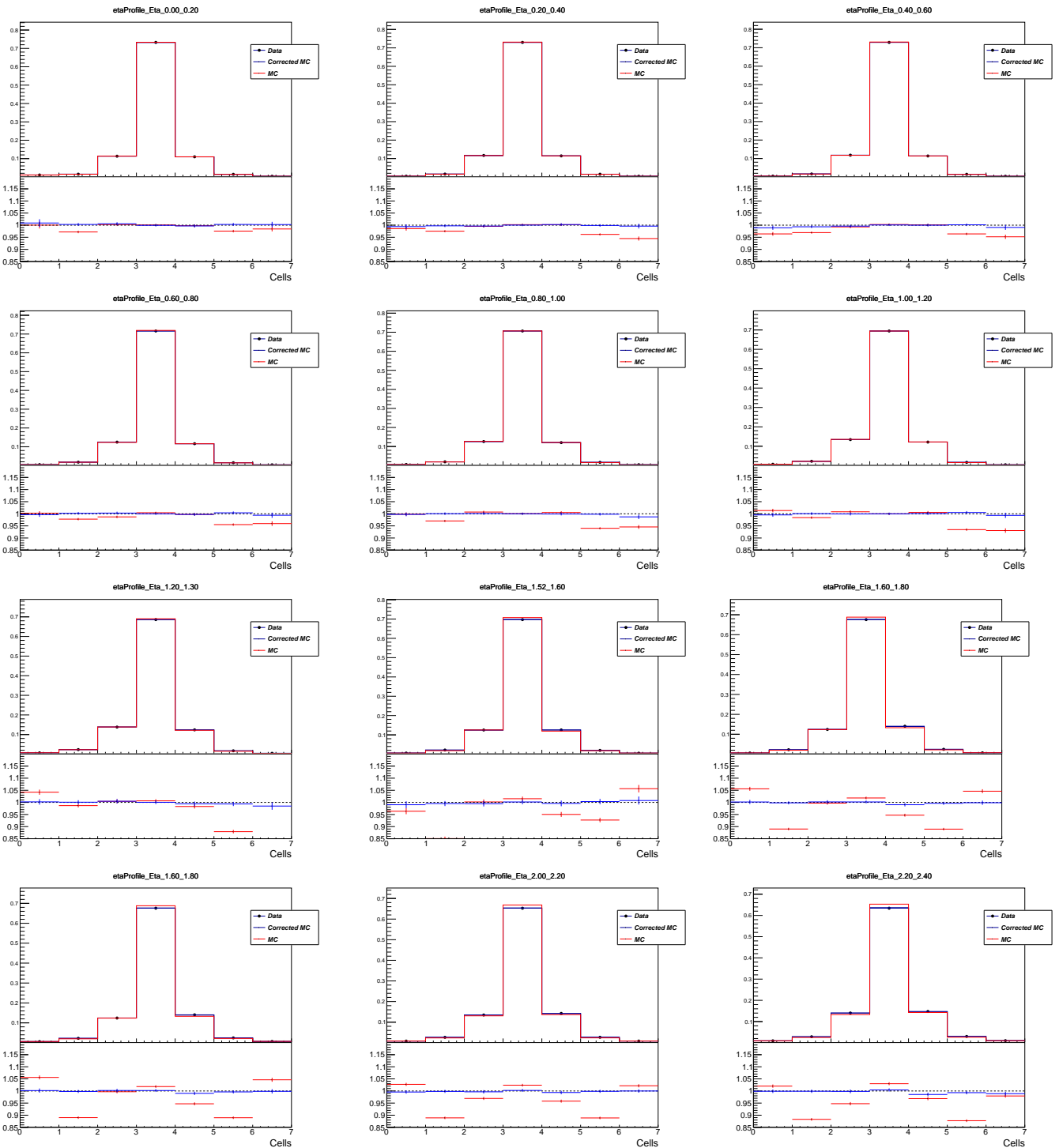
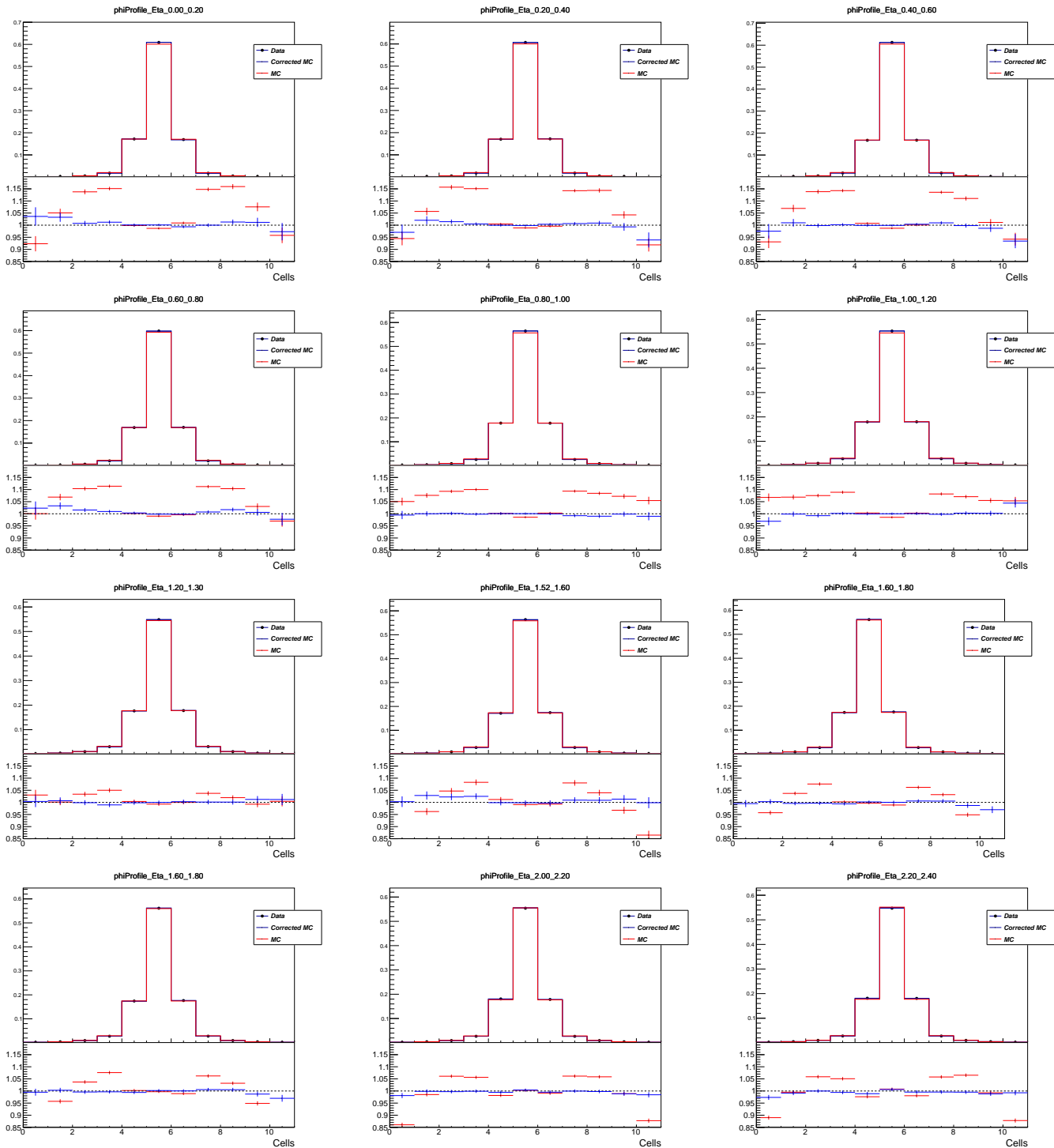


Figure 520: Reta 2



**Figure 521:** Reta 2

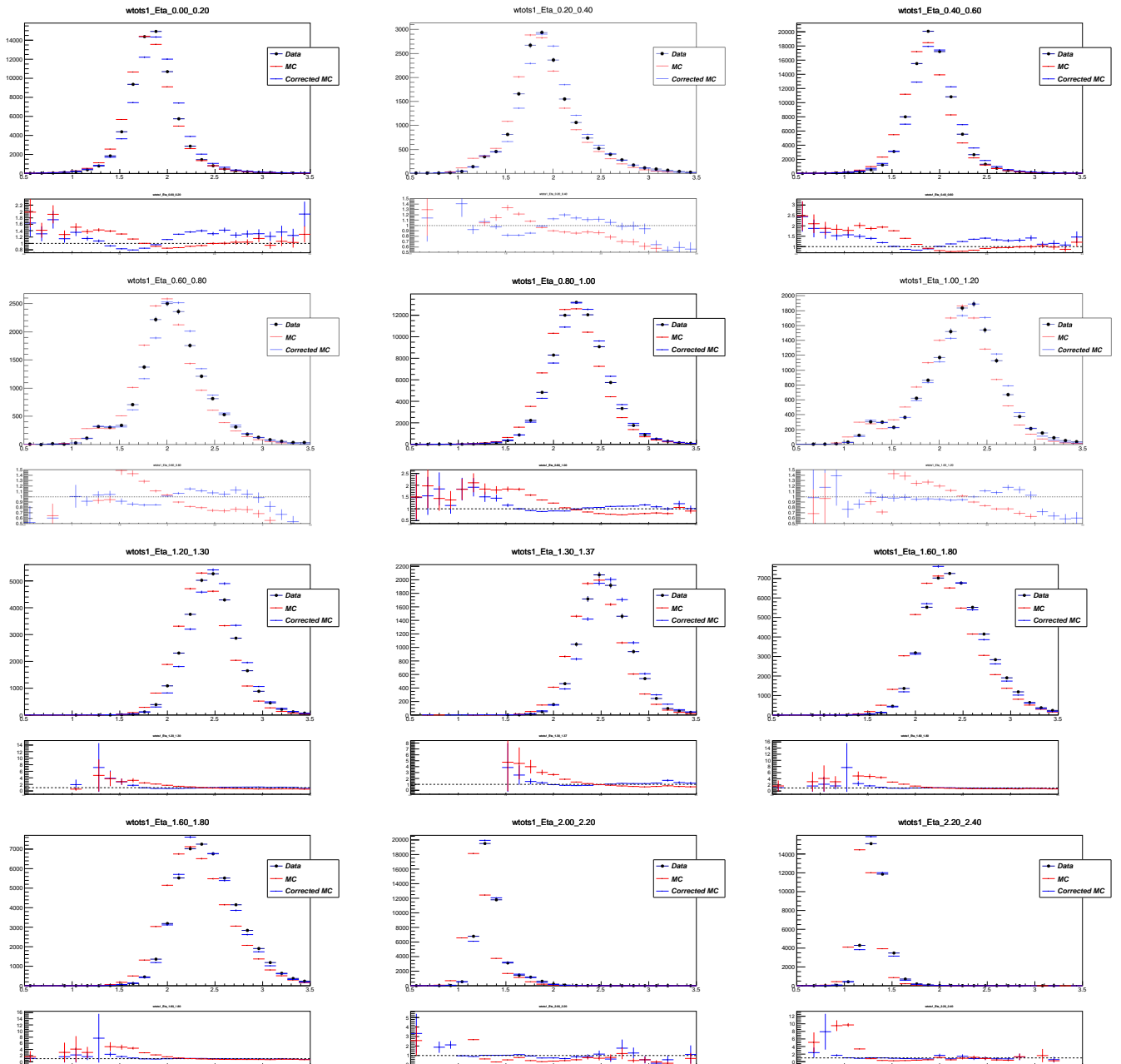


Figure 522: Reta 2



# 6

## Event reconstruction

1714

1715

### 6.1 Charged particles track reconstruction

1716 A track  $q$  is formed based on the information from the ID and is represented by five parameters:  
1717  $q = (d_0, z_0, \phi, \theta, q/p)$ , where  $d_0$  is the distance from the track to the Z axis (transverse impact parameter),  
1718  $z_0$  is the Z coordinate of the perpendicular dropped from the track onto the Z axis (longitudinal impact  
1719 parameter) (see fig. 61),  $\phi$  and  $\theta$  are the azimuthal and polar angles correspondingly and  $q/p$  is the  
1720 charge to momentum ratio of the particle. The process for track reconstruction is the same for lepton  
1721 and charged hadron candidates.  
1722

To form tracks using the detector response information the following steps are performed [2]:

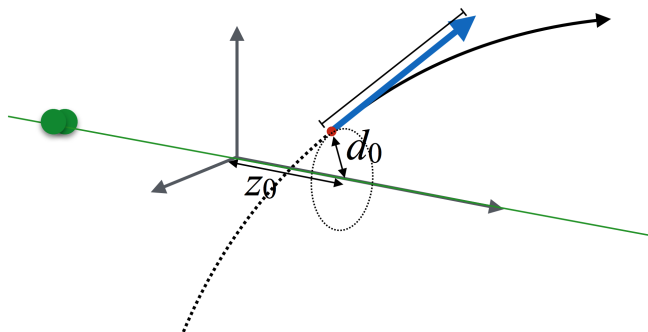


Figure 61: Impact parameters  $z_0$  and  $d_0$  [1].

1723

- 1724 • **Clustering** single hits in the pixel and SCT detectors. Neighbouring hits are combined to form a  
1725 single cluster, clusters are then transformed into *space points* that have having 3D coordinates. A  
1726 cluster may be identified as a single-particle cluster or as merged cluster, created by two or more  
1727 particles. Identification of a cluster as a merged one and separation of energy deposits between  
1728 the particles (possible only for two particles) is performed by means of a Neural Network (NN)  
1729 algorithm.
- 1730 • **Forming seeds** out of the space points. To form a seed three space-points originating from unique  
1731 layers of the silicon detectors (pixel or SCT) are used. All possible combinations of seeds are  
1732 formed at this stage. For every seed a crude estimate of the track parameters is performed.

- 1733 • **Track candidates** are formed out of the seeds by extending them within the silicon sub-detectors  
1734 following the most likely path. A combinatorial Kalman filter [3] is used to build the track  
1735 candidates. The purity of the seeds depends significantly on the sub-detector that recorded the  
1736 corresponding space-points. SCT-only seeds are considered the most reliable, followed by the  
1737 seeds that origin only from the pixel detector space-points, and the least reliable are the seeds  
1738 originating from both of these sub-detectors - that determines the order of seed consideration  
1739 when composing track candidates.

1740 Some fraction of the seeds that meet the necessary requirements become track candidates, the  
1741 rest are discarded. A seed may be used for more than one track candidate if more than one  
1742 space-point extension exists on the same layer.

- 1743 • **Ambiguity solving** is the next step necessary to eliminate incorrectly assigned space-points or  
1744 resolve conflicting track candidates that have an overlapping space-point. At this stage the track  
1745 candidates are assigned a *track score*. The track score depends on the number of clusters associated  
1746 to the track and which sub-detector these clusters originate from, the existence of holes (the  
1747 absence of a cluster associated to a detector layer crossed by the track), the quality of the  $\chi^2$  fit of  
1748 the track and track momentum.

1749 The tracks are ordered by their track score and consequently fed to the ambiguity resolving  
1750 sequence. A track must pass a number of kinematic cuts, impact parameters cuts, number of  
1751 holes, number of clusters and shared clusters cuts, otherwise the track candidate is rejected. If  
1752 a track candidate has no shared clusters with other candidates it is accepted after that. If there  
1753 are merged clusters then it is up to the NN to either accept the track, reject it or eliminate a  
1754 space-point and recycle the updated track candidate (see Fig. 62a).

- 1755 • **TRT extension** means matching of the track, composed using the information from silicon sub-  
1756 detectors to the trace in the TRT tracker. This allows to improve momentum measurement  
1757 benefiting from extended track length.
- 1758 • Final high-resolution **track fit** is performed using all available information. Position and un-  
1759 certainty of each cluster are determined by an additional NN allowing for more precise track  
1760 parameters. The curvature of the particle track also serves for charge sign identification.

## 1761 6.2 Determining the primary vertex of the event

1762 Primary vertex determination is crucial for physics analyses for many reasons. One of them is the  
1763 necessity to separate particles originating from hard events from pile-up. Another reason is to keep  
1764 track of long-lived decay chains and distinguish between prompt and non-prompt particles. Flavour  
1765 tagging, background suppression and decay reconstruction also rely heavily on the primary vertex  
1766 determination.

1767 After reconstructing the tracks of individual particles the obtained information is used to reconstruct

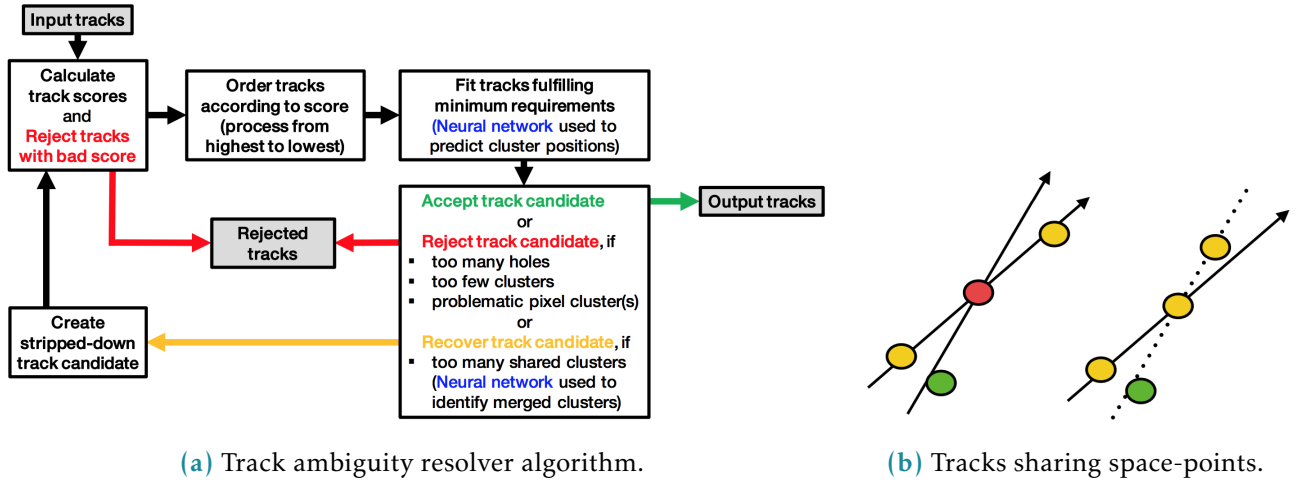


**Figure 62:** Ambiguity solving process [2].

1768 the Primary Vertex (PV) of the event [4]. The procedure relies on the reconstructed tracks and goes as  
 1769 follows:

- 1770 • A seed from the first vertex is selected. The transverse position of the seed is taken as the centre  
 1771 of the beam spot. The z-coordinate of the seed is calculated as the mode of  $z_0$  coordinates of the  
 1772 tracks.
- 1773 • Using the seed and the available tracks an iterative fit is performed in order to find the best  
 1774 position for the PV. In each iteration the tracks that are less compatible with the vertex are  
 1775 down-weighted and the vertex position gets recomputed. With every iteration the spread in the  
 1776 weight increases, separating track set into compatible tracks that mostly determine the vertex  
 1777 position and incompatible tracks that have little weight and therefore very little influence on the  
 1778 track position.
- 1779 • After the fit is done compatible tracks remain assigned to the vertex, while incompatible tracks  
 1780 are removed from it. These incompatible tracks can be used in the determination of a different  
 1781 vertex.
- 1782 • The procedure is repeated with the remaining tracks of the event.
- 1783 • The primary vertex is a vertex with the highest sum of the assigned tracks transverse momenta  
 1784  $\sum_{\text{tracks}} p_T^2$ .

1785 For the upcoming Run 3 of the LHC certain improvements and modifications are foreseen [5].

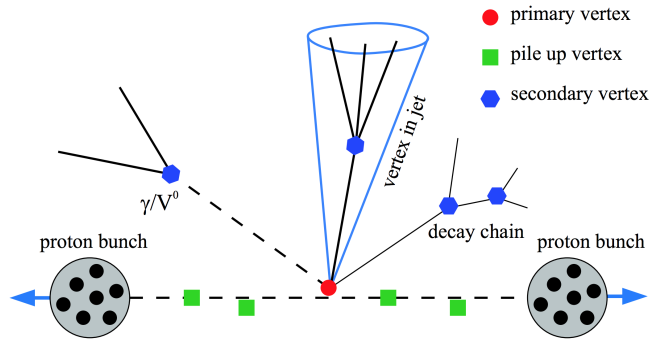


**Figure 63:** Primary, secondary and pile-up vertices [6].

## 1786 6.3 Muon reconstruction and identification

1787 Muon reconstruction relies primarily on the information from the ID (the muon track) and the Muon  
 1788 Spectrometer (MS), sometimes also using additional information from the calorimeter. At the first  
 1789 stage a muon is independently reconstructed in the tracker and in the spectrometer, and then the two  
 1790 reconstructed tracks are combined to compose a muon track used in the physics analyses [7]. Track  
 1791 reconstruction is described in section 6.1.

### 1792 6.3.1 Muon reconstruction

1793 Muon reconstruction in the muon spectrometer begins with a search for hit patterns in each muon  
 1794 chamber and forming of the segments. Using the Hough transform [8] the hits in each MDT chamber  
 1795 and nearby trigger chamber are aligned on trajectories in the bending plane. The orthogonal coordinate  
 1796 is measured with RPC and TGC detectors. A separate combinatorial search is conducted in the CSC  
 1797 detectors in  $\phi$  and  $\eta$  detector planes.

1798 Then the track candidates are built by fitting hits from different layers. This algorithm starts a  
 1799 combinatorial search first using the segments from the middle layers as seeds, as there are more trigger  
 1800 hits in the middle layer. The search is later extended to include the segments from other layers as seeds.  
 1801 Segment selection criteria are based on hit multiplicity and fit quality. The segments are matched using  
 1802 their relative positions and angles. In all the regions, except barrel-endcap transition region, at least  
 1803 two matching segments are needed to build a track (one segment is enough in the transition region).  
 1804 A single segment can be used by two or more track candidates. An overlap removal algorithm decides  
 1805 to which track should a segment belong or shares a segment between two tracks. A global  $\chi^2$  fit is used  
 1806 to fit all the hits associated to every track. If the  $\chi^2$  fit meets the designated criteria then the track is  
 1807 accepted. If a hit impair the  $\chi^2$  fit significantly, then this hit may be removed and the fit is repeated.  
 1808 On the other hand, new hits may be recovered if they fit the track candidate trajectory.  
 1809 Accurate fitting of the track trajectory is extremely important for the measurement of muon momentum.  
 1810 A quantity called *sagitta* is measured by the MS (see Fig. 64). Knowing the length  $L$  and the sagitta  $S$

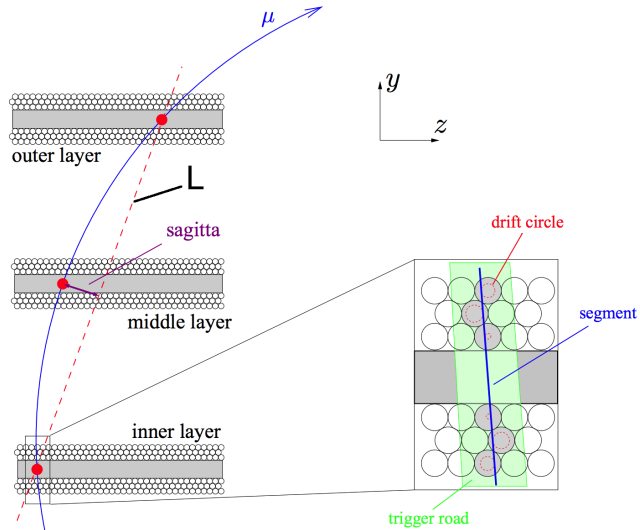


**Figure 64:** Sagitta used for the determination of the muon momentum [9].

1811 we can determine the momentum:

$$p = \frac{BL^2}{8S}, \quad (6.1)$$

1812 where  $B$  is the magnetic field strength.

1813 After the muon gets reconstructed in every detector system separately, the obtained information is  
1814 combined to form a reconstructed muon object. Depending on the detectors used for the combined  
1815 reconstruction there are *four types of muons* defined (see Fig. 65):

- 1816 • **Combined (CB) muon** is formed from a global refit of the tracks reconstructed independently  
1817 in the ID and in the MS. During this global refit the hits from both detectors are used and also  
1818 new hits may be added. Normally the outside-in pattern is used, when MS track is extrapolated  
1819 inwards to match ID track. Inverse inside-out procedure is used as a complementary approach.
- 1820 • **Segment-tagged (ST) muon** is a particle with an ID track that was extrapolated to the MS and  
1821 associated with at least one local track segment in the MDT or CSC chambers. Normally these  
1822 are muons with low  $p_T$  or their trajectory crosses regions with reduced MS acceptance.
- 1823 • **Calorimeter-tagged (CT) muon** has a valid ID track that can be associated to an energy deposit  
1824 in the calorimeter compatible with minimum-ionizing particle. The CT muons have the lowest  
1825 purity among the muon types although they provide acceptance where the MS coverage may be  
1826 absent, like the very central region with  $|\eta| \leq 0.1$  for  $15 < p_T < 100$  GeV.
- 1827 • **Extrapolated (ME) muon** (standalone muon) trajectory is reconstructed base only on the MS  
1828 track and a loose requirement to match the IP. ME muons allow to extend the muon acceptance  
1829 to the region which is not covered by the ID, namely  $2.5 < |\eta| < 2.7$ .

1830 In case of overlap between different muon types the preference is given to CB muons, then to ST and then to CT muons. ME muons overlaps are resolved based on the MS track quality.

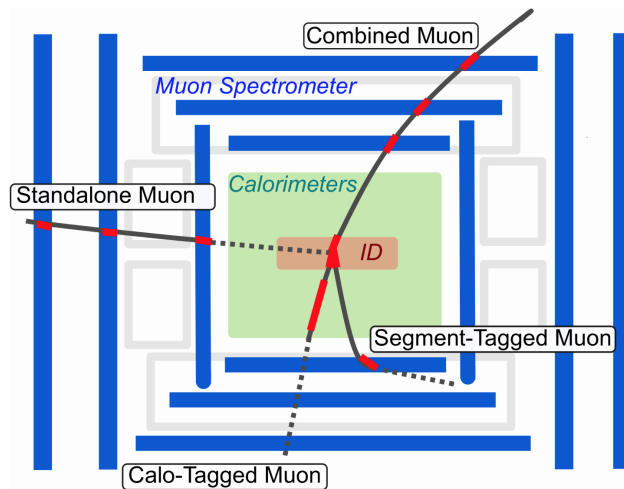


**Figure 65:** Four types of reconstructed muons ??.

1831

### 1832 6.3.2 Muon identification

1833 Muon identification is a set of measures to ensure that the registered particle has indeed the character-  
 1834 istics of a muon and to identify the mechanism of its production. Muons created in the course of decay  
 1835 of a short-lived particle (e.g. a massive boson) are called *prompt muons*, while those originating from  
 1836 hadron or tau decays are called *non-prompt*. Muon identification plays an important role in background  
 1837 suppression and guaranteeing a robust momentum measurement.

1838 Muons that are created during the in-flight decay of the charged hadrons in the ID usually have a  
 1839 distinctive "kink" topology in their reconstructed track. This results in a decreased quality of the  
 1840 resulting track fit and the incompatibility between the results of momentum measurement in the ID  
 1841 and MS. Muons originating from W boson decays are called *signal*, while those coming from hadron  
 1842 decays are called *background*. For CB muons the three main identification variables are the following:

1843 • *q/p significance* is defined as  $\frac{|(q/p)_{ID} - (q/p)_{MS}|}{\sqrt{\sigma^2(q/p)_{ID} + \sigma^2(q/p)_{MS}}}$  - an absolute difference between *q/p* measured in  
 1844 the two detectors over the combined uncertainty.

1845 • Relative transverse momentum difference  $\rho = \frac{|p_T^{ID} - p_T^{MS}|}{p_T^{combined}}$ .

1846 • Normalized  $\chi^2$  fit of the combined track.

1847 Robust momentum measurement is ensured by specific requirements to the number of hits in the ID  
 1848 and MS. A number of muon identification selections (working points) is developed to address specific  
 1849 analyses.

**1850 6.3.3 Muon isolation**

1851 Isolated muons are a defining signature of massive boson decays. In the decays of W, Z and Higgs  
1852 bosons muons are created separated from the rest of the particles. Quantitative measurement of  
1853 detector activity around a muon candidate is called *muon isolation* and serves as an invaluable tool  
1854 for background suppression. Muon isolation is assessed through two observables: one is track-based,  
1855 another is calorimeter-based.

1856 The track-based observable  $p_T^{varcone20}$  is defined as a scalar sum of all the particles with  $p_T > 1$  GeV in a  
1857 cone  $\Delta R = \min(10\text{GeV}/p_T^\mu, 0.2)$  around the muon with transverse momentum  $p_T^\mu$  excluding the proper  
1858 track of the muon. The  $p_T$  dependence helps this definition to perform better for the muons created in  
1859 the decay of the particles with high transverse momentum.

1860 The calorimeter-based isolation observable  $E_T^{topocone20}$  is defined as the sum of the transverse energy of  
1861 all the topological clusters in a cone of a size  $\Delta R = 0.2$  around the muon after subtracting the proper  
1862 muon energy deposit and correcting for the pile-up effects.

1863 In both cases the size of the cone may be varied, normally in the range between 0.2 and 0.4, depending  
1864 on the analysis needs. Isolation criteria are typically defined using the relative isolation variables, using  
1865 the ratio of  $p_T^{varcone20}$  and  $E_T^{topocone20}$  to the transverse momentum. A number of working points exist,  
1866 each having a certain requirements for one or both of the isolation variables.

**1867 6.4 Electron reconstruction and identification****1868 6.4.1 Electron reconstruction**

1869 Electron reconstruction starts with two separate parts: track reconstruction in the ID and cluster  
1870 reconstruction in the calorimeter, which are then matched to each other in order to make an electron  
1871 candidate [10]. During Run 2 two algorithms were used for the cluster reconstruction, both of them are  
1872 described below.

1873

**1874 Sliding window**

1875 It must be mentioned that this method is deprecated and starting from 2017 is replaced by the  
1876 topocluster method described in the next section. The EMC is divided into a grid of 200x256 towers in  
1877  $\eta \times \phi$  plane, each tower having a size of  $\Delta\eta \times \Delta\phi = 0.025 \times 0.025$ , reproducing the granularity of the  
1878 second layer in the EMC. Energy deposits in all available calorimeter layers (first, second and third  
1879 layers of the EMC in the region  $|\eta| < 2.47$  and the presampler in the region  $|\eta| < 1.8$ ) are approximately  
1880 calibrated at the EM scale and summed up for each tower. If the cumulative energy deposit in a certain  
1881 tower exceeds 2.5 GeV then this tower is used as a seed. Then for every seed a sliding window algorithm  
1882 of size  $3 \times 5$  is used [11], forming a cluster around every seed.

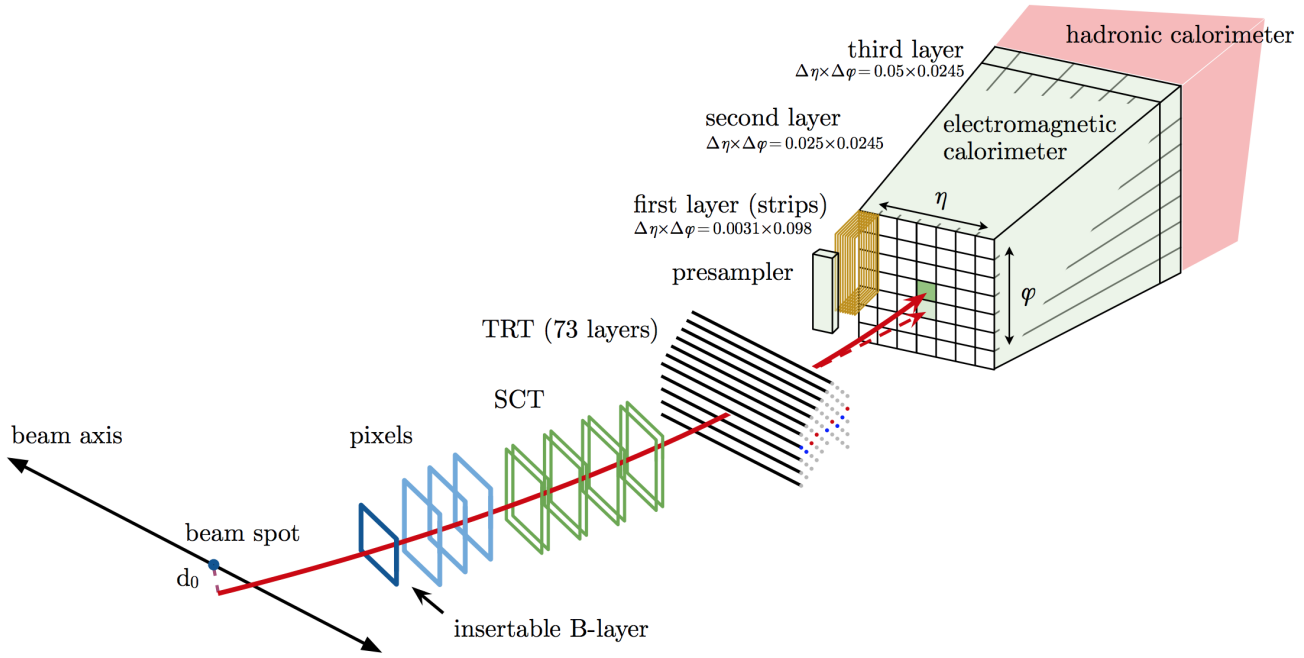


**Figure 66:** The path of an electron through the detector is shown by solid red line. The dashed red line denotes the trajectory of a photon, produced as a Bremsstrahlung radiation in the TRT [10].

1883 It happens that two seed-cluster candidates are found in close proximity. When their towers overlap  
 1884 within an area of  $\eta \times \phi = 5 \times 9$  in units of  $0.025 \times 0.025$  the two clusters are considered overlapping. In  
 1885 this case two options are possible:

- 1886 • If the transverse energies of the two clusters are more than 10% different then the cluster with  
 1887 higher  $E_T$  is retained.  
 1888 • If the difference in the transverse energies is within 10% then the cluster with higher value of the  
 1889  $E_T$  in the central tower is kept.

1890 After the overlap is resolved the duplicate cluster is removed.

1891

#### 1892 Topocluster reconstruction

1893 The algorithm for topocluster reconstruction [12], [13] starts with composing proto-clusters in the  
 1894 calorimeter using the noise threshold:

$$\zeta_{cell}^{EM} = \frac{E_{cell}^{EM}}{\sigma_{noise,cell}^{EM}}, \quad (6.2)$$

1895 where  $E_{cell}^{EM}$  is the cell energy at the EM scale and  $\sigma_{noise,cell}^{EM}$  is the expected cell noise. The latter comprises  
 1896 the electronic and the pile-up noise estimate based on the expected instantaneous luminosity. The

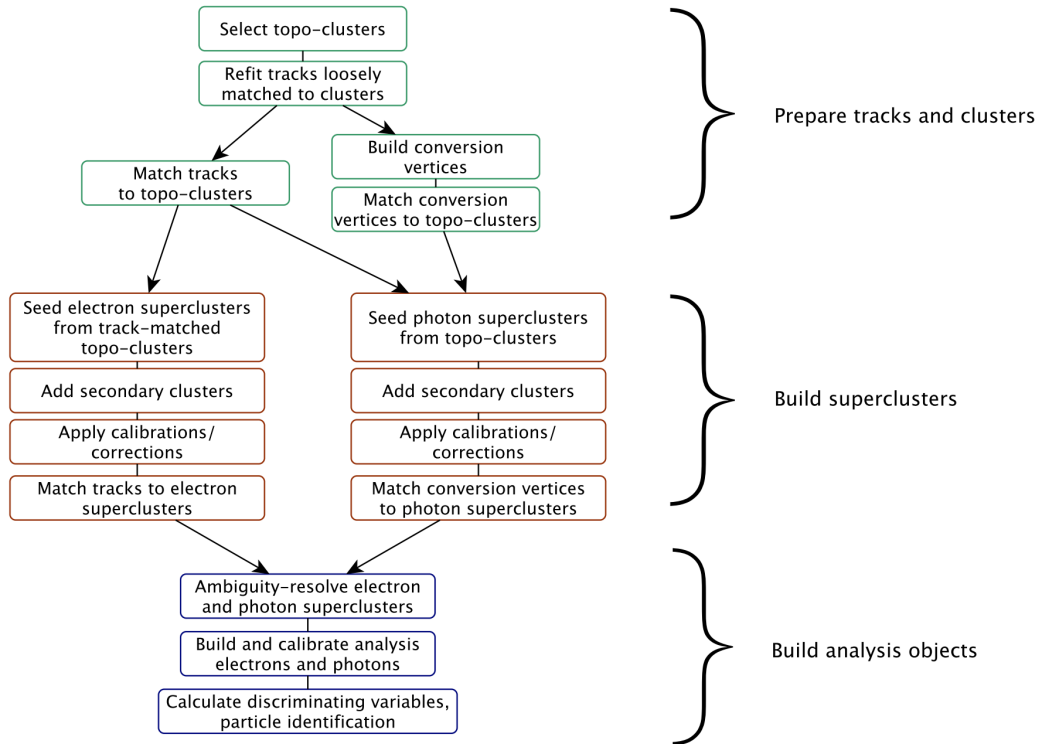


Figure 67: The algorithm scheme for topocluster reconstruction.

proto-cluster is formed around a cell with  $|\zeta_{cell}^{EM}| \geq 4$ . Then the neighbouring cells are added to the proto-cluster. If an added cell passes the requirement of  $|\zeta_{cell}^{EM}| \geq 2$  then it serves as a seed for the next iteration, collecting all of its neighbours to the proto-cluster. If the two proto-clusters share a cell with  $|\zeta_{cell}^{EM}| \geq 2$  then these proto-clusters are merged together. Proto-clusters with two local maxima are split into two clusters. For a proto-cluster to be considered as the EM topocluster it must have at least 50% of its energy being contained in the EMC. At the stage of track reconstruction the tracks are first extended and fitted with the global  $\chi^2$  fitter using the pion hypothesis [14]. If it fails, then a more complicated pattern reconstruction algorithm based on Kalman filter is used [15]. This algorithm uses the electron hypothesis and allows up to 30% energy loss at each material surface. Then the tracks are loosely matched to the EM clusters if they meet one of the following criteria:

- The tracks extrapolated to the second layer of the EMC are consistent in  $\phi$  and  $\eta$  (matching in  $\eta$  is not required for TRT-only tracks).
  - The extrapolated tracks are consistent in  $\phi$  (with a bit tighter requirements) and  $\eta$  after rescaling the track momentum to cluster momentum.
- Matching in  $\phi$  coordinate assumes charge asymmetry to account for different direction of possible Bremsstrahlung radiation for positive and negative particles. Then the loosely matched tracks that have at least four silicon hits are refitted using the optimized Gaussian-sum filter (GSF) [16], that allows to

1914 better take into account the energy losses in solid material.

1915

### 1916 Track-cluster matching

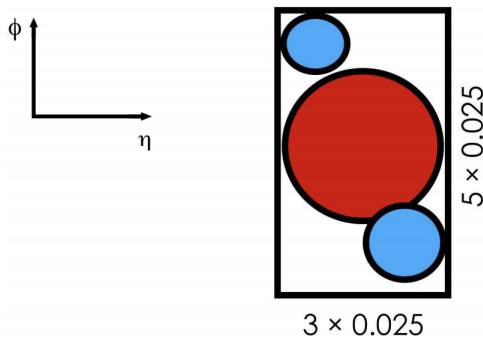
1917 Once the track is fitted with the GSF algorithm the final matching with the cluster is performed using  
 1918 tighter matching requirements between the track and the cluster barycentre. If matching criteria are  
 1919 met with two or more tracks then the ambiguity resolving algorithm is used. This algorithm takes into  
 1920 account a number of parameters like the distance between the cluster barycentre and the track in  $\phi$   
 1921 and  $\eta$ , number of hits in the silicon detector and in the innermost silicon layer, association to photon  
 1922 conversion vertex,  $E/p$  ratio and  $p_T$ . This allows to exclude converted photons as electron candidates  
 1923 and also helps to maintain high photon reconstruction efficiency. After track-cluster matching the  
 1924 electron cluster is extended around the seed to  $3 \times 7$  in the barrel region or  $5 \times 5$  in the end-cap region  
 1925 by adding one row of the cells on each side.

1926

### 1927 Supercluster reconstruction

#### All $e^\pm, \gamma$ :

Add all clusters within  $3 \times 5$  window around seed cluster.



#### Electrons only:

Seed, secondary cluster  
**match the same track.**

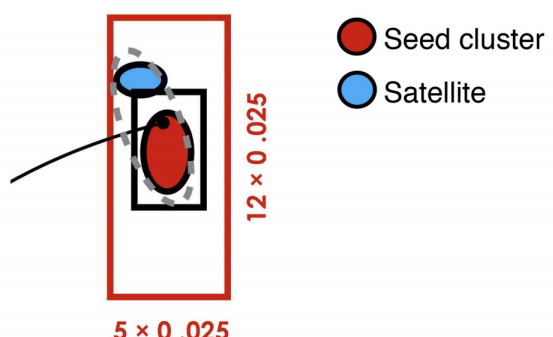


**Figure 68:** Supercluster reconstruction for electrons. Seed clusters are shown in red, satellite clusters in blue.

1928 The composition of an electron supercluster is performed in two stages: first, the candidate EM  
 1929 topocluster is tested to be used as a seed for the supercluster. In the second stage the nearby EM  
 1930 topoclusters can be identified as satellite clusters, emerging from Bremsstrahlung radiation or topoclus-  
 1931 ter splitting.

1932 First the EM topoclusters are sorted by their  $E_T$  in descending order. For the cluster to be considered  
 1933 a seed it must have  $E_T > 1$  GeV, must be matched to a track with at least four hits in the silicon

1934 detectors and should not be assigned as a satellite cluster to any other seed. If these requirements  
 1935 are met then the algorithm described in Fig. 68 is started. First, all topoclusters within a window of  
 1936  $\Delta\eta \times \Delta\phi = 0.075 \times 0.125$  around the seed cluster barycentre are added as satellite cluster, as they most  
 1937 probably represent secondary EM showers coming from the same initial electron. Also, if a cluster  
 1938 within  $\Delta\eta \times \Delta\phi = 0.125 \times 0.3$  window around the seed cluster barycentre share the "best-matched" track  
 1939 with the seed cluster - it is also added as a satellite. Finally the energy of the reconstructed cluster  
 1940 must be calibrated. The calibration is performed using a multivariate technique based on data and  
 1941 MC samples using  $Z \rightarrow ee$  events [17], [18]. The shower shapes and other discriminating variables are  
 1942 computed at this stage.

1943 **6.4.2 Electron identification**

1944 Prompt electrons in the central region of the ATLAS detector ( $|\eta| < 2.47$ ) are selected using a likelihood-  
 1945 based (LH) identification. The LH uses a number of inputs from ID and calorimeter detectors, as well  
 1946 as combined information from both detectors (see Table 1 in [10]). The probability density functions  
 1947 (pdfs) for the likelihoods of Run 2 were obtained using the simulated events.  
 1948 The electron LH is based on the products of n pdfs P for signal  $L_S$  and background  $L_B$ :

$$L_{S(B)}(\mathbf{x}) = \prod_{i=1}^n P_{S(B)}^i(x_i), \quad (6.3)$$

1949 where  $\mathbf{x}$  is the vector of the LH input parameters,  $P_S^i$  and  $P_B^i$  are the pdf values for parameter  $i$  at  
 1950 value  $x_i$  for signal and background respectively. The LH operates at a number of working points,  
 1951 the higher the likelihood - the lower is the efficiency. For example, the efficiencies for identifying a  
 1952 prompt electron with  $E_T = 40$  GeV for Loose, Medium and Tight working points are 93%, 88% and  
 1953 80% respectively. Prompt electrons are assumed to come from the signal, while background includes  
 1954 the jets that mimic the prompt electrons, electrons from photon conversions and non-prompt electrons  
 1955 from hadron decays. For each electron candidate a discriminant  $d_L$  is composed:

$$d_L = \frac{L_S}{L_S + L_B}, \quad (6.4)$$

1956 that defines the electron likelihood identification. This discriminant  $d_L$  has a sharp peak at unity for  
 1957 the signal and at zero for the background, which is not very convenient for picking working points.  
 1958 That is why the discriminant distribution is transformed using the inverse sigmoid function:

$$d'_L = -\tau^{-1} \ln(d_L^{-1} - 1), \quad (6.5)$$

1959 where  $\tau = 15$ . Each operating point is assigned with a  $d'_L$  value - if a discriminant exceeds this value for  
 1960 a given electron then this electron is considered signal.  
 1961 There are two advantages of using likelihood-based approach comparing to selection-criteria-based  
 1962 ("cut-based") identification:

- The drawback of a cut-based approach is that if an electron fails to pass one of the cuts - it is definitely removed from the selection, while in the LH approach it is still possible for this electron to pass the selection thanks to other parameters. This quality promotes the selection efficiency.
  - In case of a significant overlap in signal and background distribution of a certain parameter using it in a cut-based identification would entail large losses in efficiency. In the likelihood-based identification this parameter may be added without penalty.
- The likelihood input parameters were obtained from the simulated events, which means that real distributions in data may differ due to various mismodelling effects. These effects must be corrected in order to get an accurate and efficient identification. Mismodelling may depend on coordinates or energy. Chapter 5 of this dissertation is dedicated to the correction of electromagnetic shower shapes in the calorimeter, which are among the likelihood input parameters.

#### 6.4.3 Electron isolation

Electron isolation plays a very important role in background suppression in physics analyses. Since electrons are reconstructed using the information from two different detectors - two different isolation definitions are possible, track-based and calorimeter-based. Let's first consider calorimeter-based isolation.

As depicted in Fig. 69 the raw isolation energy  $E_{isol}^{T,raw}$  includes the energy of all the topoclusters,

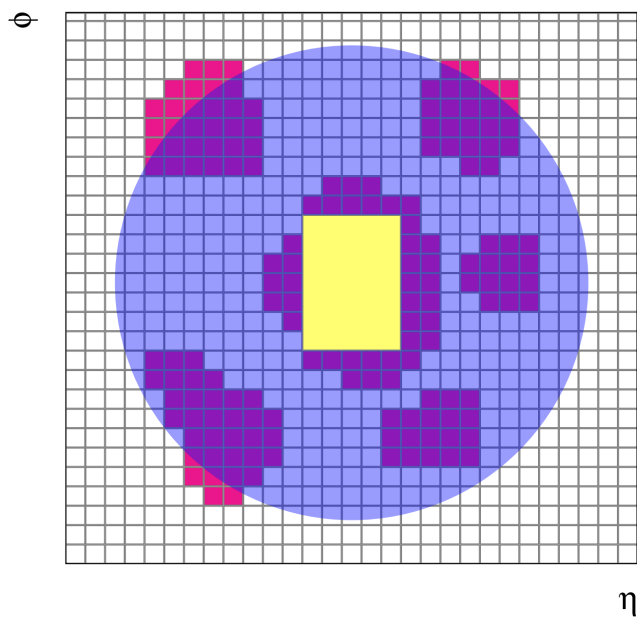


**Figure 69:** The isolation cone is centred at the candidate electron. All topological clusters, shown in red, are included in the raw isolation variable. The  $5 \times 7$  cells included into core subtraction method are marked in yellow [13].

1979  
 1980 barycentres of which fall within the isolation radius  $\Delta R$ . It also includes core energy of the electron  
 1981 candidate  $E_{isol}^{T,core}$  which comprises the  $5 \times 7$  cells within the area of  $\Delta\eta \times \Delta\phi = 0.125 \times 0.175$ . The fixed  
 1982 size of the core ensures simplicity and stability, although it may happen that the topocluster is larger  
 1983 than the size of the core resulting in attributing the proper energy of the electron to the outside activity.  
 1984 This leakage effect is corrected for using no pile-up simulated events, parametrizing the leakage with a  
 1985 Crystal Ball function as a function of the transverse energy  $E_{T,leakage} = E_{T,leakage}(E_T)$ .  
 1986 Another effect that must be corrected for is the pile-up and underlying event contribution. This  
 1987 contribution is estimated from the ambient energy density [19]. In every event all positive-energy  
 1988 topological clusters are taken into account in the entire range of calorimeter acceptance  $|\eta| < 5$  using  
 1989 the  $k_t$  jet clustering algorithm with a radius parameter  $R = 0.5$  and no jet  $p_T$  threshold. Then for every  
 1990 jet its area  $A$  is estimated and the jet energy density  $\rho = p_T/A$  is computed. Using the information on  
 1991 the jet energy density together with the location of every jet one can obtain the median energy density  
 1992  $\rho_{median}(\eta)$  - a rapidity-dependent estimate of jet densities for every event. Then the pile-up correction  
 1993 can be evaluated in the following way:

$$E_{T,pile-up}(\eta) = \rho_{median}(\eta) \times (\pi \Delta R^2 - A_{core}), \quad (6.6)$$

1994 where  $\Delta R$  is the radius of the isolation cone, and  $A_{core}$  is the area of the subtracted signal core. Finally  
 1995 the calorimeter isolation variable may be defined as follows:

$$E_{T,cone}^{isol} = E_{T,raw}^{isol} - E_{T,core} - E_{T,leakage} - E_{T,pile-up}. \quad (6.7)$$

1996 The track-based isolation includes all tracks with  $p_T > 1$  GeV, within the fiducial region of the ID, that  
 1997 satisfy basic track quality requirements. Pile-up is mitigated by requiring that  $|z_0 \sin \theta| < 3$  mm, to  
 1998 ensure that the track originates from the primary vertex. The track-based isolation is composed of all  
 1999 the tracks that fall within the radius  $\Delta R$  excluding the candidate electron track.  
 2000 The own contribution of the candidate track into the isolation must also include possible Bremsstrahlung  
 2001 radiation emitted by the candidate electron. For that reason the tracks are extrapolated to the second  
 2002 layer of the EMC and if they fall within a window of  $\Delta\eta \times \Delta\phi = 0.05 \times 0.1$  around the cluster position.  
 2003 The resulting variable is called  $p_T^{isol}$ .  
 2004 The track-based isolation allows to use variable-size cone, making the cone smaller for boosted particles.  
 2005 The cone size for the  $p_{T,var}^{isol}$  would be:

$$\Delta R = \min\left(\frac{10\text{GeV}}{p_T[\text{GeV}]}, R_{max}\right), \quad (6.8)$$

2006 where  $R_{max}$  is the maximum cone size and may vary depending on the analysis needs, typically between  
 2007 0.2 and 0.4.

2008 **6.5 Particle flow objects**

2009 The measurement of hadronic objects and particle showers remains a complicated task due to the large  
 2010 variety of particle types and properties they posses and because of the large energy/momentum span of  
 2011 the measured objects. For the low-energy charged particles the ID shows better momentum resolution  
 2012 and angular resolution. On the other hand, the calorimeter shows better performance at high energy  
 2013 and is also capable of detecting neutral particles. The idea behind the Particle Flow (PF) algorithm [20]  
 2014 is to combine the information from the two detectors to obtain the best result possible. To properly  
 2015 take into account every particle it has to be ensured that every particle detected in both detectors is  
 2016 counted only once. This means that for a charged particle its deposit in the calorimeter must be found  
 2017 and subtracted. The Particle Flow Object (PFO) reconstruction process is schematically presented in  
 Fig. 610. The process starts with getting *tight* tracks from the ID, meaning these tracks must have at

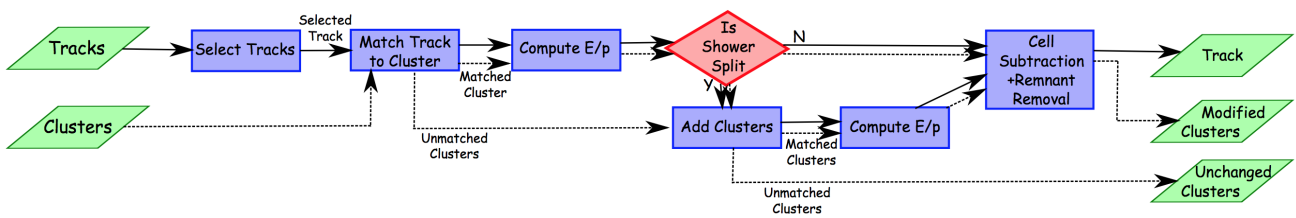


**Figure 610:** The algorithm scheme for particle flow object reconstruction [20].

2018 least nine hits in the silicon detectors and no holes n the pixel detector. The tracks must have  $|\eta| < 2.5$   
 2019 and  $0.5 < p_T < 40$  GeV, corresponding to the kinematic region where tracks offer better resolution than  
 2020 the calorimeter. The tracks associated to leptons are removed.  
 2022 The calorimeter topoclusters reconstructed like it was described in section 6.4.1 and calibrated using  
 2023 the EM scale are matched to the tracks based on their spacial position and measured momentum. First  
 2024 the ranked based on a distance metric:

$$\Delta R' = \sqrt{\left(\frac{\Delta\phi}{\sigma_\phi}\right)^2 + \left(\frac{\Delta\eta}{\sigma_\eta}\right)^2}, \quad (6.9)$$

2025 where  $\Delta\phi$  and  $\Delta\eta$  are the angular distances between the topocluster barycentres and the track,  $\sigma_\phi$   
 2026 and  $\sigma_\eta$  are uncertainties in topocluster width. Preliminary matching is reached by requiring that  
 2027  $E^{clus}/p^{trk} > 0.1$ , where  $E^{clus}$  is the cluster energy and  $p^{trk}$  is the track momentum.  
 2028 It often happens, that energy deposit of a particle is split between two (most often) or more clusters.  
 2029 Then a split shower recovery procedure is initiated, looking for matching clusters in the radius of  
 2030  $\Delta R = 0.2$  around the track extrapolated to the second layer of the EMC. Then it is estimated if the  
 2031 energy of the track and the energy of the associated topocluster is consistent. If it is the case then the  
 2032 topoclusters matched to the tracks are removed.  
 2033 Eventually two particle collections are obtained: a collection of charged particle flow objects (cPFOs)  
 2034 each with an associated track and neutral particle flow objects (nPFOs) with a calorimeter deposit. The

2035 former must also match the primary vertex, having  $|z_0 \times \sin \theta| < 2$  mm. The full procedure is described  
2036 in detail in [20].

2037 **Bibliography**

- 2038 [1] “Performance of the ATLAS Silicon Pattern Recognition Algorithm in Data and Simulation at  
2039  $\sqrt{s} = 7 \text{ TeV}$ ”. In: (July 2010).
- 2040 [2] M. Aaboud et al. “Performance of the ATLAS Track Reconstruction Algorithms in Dense Envi-  
2041 ronments in LHC Run 2”. In: *Eur. Phys. J. C* 77.10 (2017), p. 673. doi: 10.1140/epjc/s10052-  
2042 017-5225-7. arXiv: 1704.07983 [hep-ex].
- 2043 [3] R. Fruhwirth. “Application of Kalman filtering to track and vertex fitting”. In: *Nucl. Instrum.*  
2044 *Meth. A* 262 (1987), pp. 444–450. doi: 10.1016/0168-9002(87)90887-4.
- 2045 [4] S. Boutle et al. “Primary vertex reconstruction at the ATLAS experiment”. In: *J. Phys. Conf. Ser.*  
2046 898.4 (2017). Ed. by Richard Mount and Craig Tull, p. 042056. doi: 10.1088/1742-6596/898/4/  
2047 042056.
- 2048 [5] *Development of ATLAS Primary Vertex Reconstruction for LHC Run 3*. Tech. rep. ATL-PHYS-PUB-  
2049 2019-015. Geneva: CERN, Apr. 2019. url: <https://cds.cern.ch/record/2670380>.
- 2050 [6] E. Bouhova-Thacker et al. “Vertex reconstruction in the ATLAS experiment at the LHC”. In: *2008*  
2051 *IEEE Nuclear Science Symposium and Medical Imaging Conference and 16th International Workshop*  
2052 *on Room-Temperature Semiconductor X-Ray and Gamma-Ray Detectors*. 2008, pp. 1720–1727. doi:  
2053 10.1109/NSSMIC.2008.4774734.
- 2054 [7] Georges Aad et al. “Muon reconstruction performance of the ATLAS detector in proton–proton  
2055 collision data at  $\sqrt{s} = 13 \text{ TeV}$ ”. In: *Eur. Phys. J. C* 76.5 (2016), p. 292. doi: 10.1140/epjc/s10052-  
2056 016-4120-y. arXiv: 1603.05598 [hep-ex].
- 2057 [8] J. Illingworth and J. Kittler. “A survey of the hough transform”. In: *Computer Vision, Graphics,*  
2058 *and Image Processing* 44.1 (1988), pp. 87–116. issn: 0734-189X. doi: [https://doi.org/10.1016/S0734-189X\(88\)80033-1](https://doi.org/10.1016/S0734-189X(88)80033-1). url: <http://www.sciencedirect.com/science/article/pii/S0734189X88800331>.
- 2061 [9] Steffen Kaiser. “Search for the Higgs Boson in the Process  $pp \rightarrow Hqq, H \rightarrow WW$  with the ATLAS  
2062 Detector”. PhD thesis. Munich, Technische Universitaet Muenchen, 2010.
- 2063 [10] Morad Aaboud et al. “Electron reconstruction and identification in the ATLAS experiment using  
2064 the 2015 and 2016 LHC proton-proton collision data at  $\sqrt{s} = 13 \text{ TeV}$ ”. In: *Eur. Phys. J. C* 79.8  
2065 (2019), p. 639. doi: 10.1140/epjc/s10052-019-7140-6. arXiv: 1902.04655 [physics.ins-  
2066 det].
- 2067 [11] W Lampl et al. *Calorimeter Clustering Algorithms: Description and Performance*. Tech. rep. ATL-  
2068 LARG-PUB-2008-002. ATL-COM-LARG-2008-003. Geneva: CERN, Apr. 2008. url: <https://cds.cern.ch/record/1099735>.

- 2070 [12] Georges et al. Aad. “Topological cell clustering in the ATLAS calorimeters and its performance in  
2071 LHC Run 1. Topological cell clustering in the ATLAS calorimeters and its performance in LHC  
2072 Run 1”. In: *Eur. Phys. J. C* 77.CERN-PH-EP-2015-304 (Mar. 2016). Comments: 64 pages plus  
2073 author list + cover page (87 pages in total), 41 figures, 3 tables, submitted to EPJC. All figures in  
2074 including auxiliary figures are available at <http://atlas.web.cern.ch/Atlas/GROUPS/PHYSICS/PAPERS/PERF-2014-07/>, 490. 87 p. doi: 10.1140/epjc/s10052-017-5004-5. url: <https://cds.cern.ch/record/2138166>.
- 2077 [13] Georges Aad et al. “Electron and photon performance measurements with the ATLAS detector  
2078 using the 2015–2017 LHC proton-proton collision data”. In: *JINST* 14.12 (2019), P12006. doi:  
2079 10.1088/1748-0221/14/12/P12006. arXiv: 1908.00005 [hep-ex].
- 2080 [14] Thijs G. Cornelissen et al. “The global chi\*\*2 track fitter in ATLAS”. In: *J. Phys. Conf. Ser.* 119  
2081 (2008). Ed. by Randall Sobie, Reda Tafirout, and Jana Thomson, p. 032013. doi: 10.1088/1742-  
2082 6596/119/3/032013.
- 2083 [15] T Cornelissen et al. *Concepts, Design and Implementation of the ATLAS New Tracking (NEWT)*.  
2084 Tech. rep. ATL-SOFT-PUB-2007-007. ATL-COM-SOFT-2007-002. Geneva: CERN, Mar. 2007.  
2085 url: <https://cds.cern.ch/record/1020106>.
- 2086 [16] *Improved electron reconstruction in ATLAS using the Gaussian Sum Filter-based model for bremsstrahlung*.  
2087 Tech. rep. ATLAS-CONF-2012-047. Geneva: CERN, May 2012. url: <https://cds.cern.ch/record/1449796>.
- 2089 [17] Morad Aaboud et al. “Electron and photon energy calibration with the ATLAS detector using  
2090 2015–2016 LHC proton-proton collision data”. In: *JINST* 14.03 (2019), P03017. doi: 10.1088/  
2091 1748-0221/14/03/P03017. arXiv: 1812.03848 [hep-ex].
- 2092 [18] Morad Aaboud et al. “Measurement of the photon identification efficiencies with the ATLAS  
2093 detector using LHC Run 2 data collected in 2015 and 2016”. In: *Eur. Phys. J. C* 79.3 (2019), p. 205.  
2094 doi: 10.1140/epjc/s10052-019-6650-6. arXiv: 1810.05087 [hep-ex].
- 2095 [19] Matteo Cacciari and Gavin P. Salam. “Pileup subtraction using jet areas”. In: *Phys. Lett. B* 659  
2096 (2008), pp. 119–126. doi: 10.1016/j.physletb.2007.09.077. arXiv: 0707.1378 [hep-ph].
- 2097 [20] Morad et al. Aaboud. “Jet reconstruction and performance using particle flow with the ATLAS  
2098 Detector. Jet reconstruction and performance using particle flow with the ATLAS Detector”. In:  
2099 *Eur. Phys. J. C* 77.CERN-EP-2017-024. 7 (Mar. 2017). 67 pages in total, author list starting page 51,  
2100 37 figures, 1 table, final version published in Eur. Phys. J C, all figures including auxiliary figures  
2101 are available at <http://atlas.web.cern.ch/Atlas/GROUPS/PHYSICS/PAPERS/PERF-2015-09/>,  
2102 466. 67 p. doi: 10.1140/epjc/s10052-017-5031-2. url: <https://cds.cern.ch/record/2257597>.



# 7

2104

2105

## Calibrations and corrections

### 2106 7.1 Electron corrections

2107 This section describes the electron calibrations and corrections used in  $p_T^W$  analysis. They were derived  
 2108 from the low- $\mu$  special run data collected in 2017 and 2018 at 5 and 13 TeV and the dedicated Monte-  
 2109 Carlo (MC) samples [1], as well as from the standard ATLAS high pileup data collected during the Run  
 2110 2.

#### 2111 7.1.1 Energy scale and resolution correction

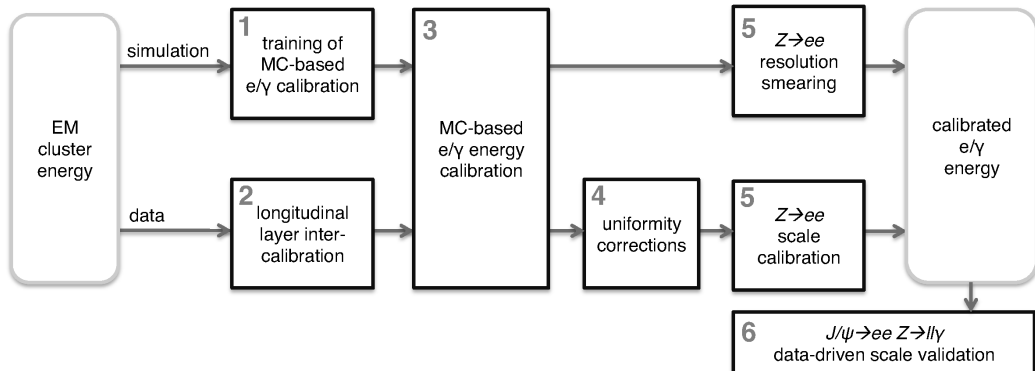


Figure 71: Schematic overview of energy response calibration procedure for electrons and photons.

2112 In order to obtain the energy scale and resolution corrections, electrons from  $Z \rightarrow ee$  process were  
 2113 used. The selection criteria were the same for data and MC simulation. For high- $\mu$ , electron candidates  
 2114 must pass the corresponding triggers and are required to have  $p_T > 27\text{ GeV}$  and  $|\eta| < 2.47$ , satisfying  
 2115 the medium LH ID criteria and loose isolation criteria as described in Ref. [2]. In the low pile-up  
 2116 case electron the requirements are loosened: the candidates must pass the triggers requiring to have  
 2117  $p_T > 15$  and satisfy loose isolation criteria. The full description for the selection criteria for low pile-up  
 2118 electrons is provided in Section 8. The energy scale correction follows the method described in detail  
 2119 in Ref. [3] and schematically described in Fig. 71. The energy in both data and MC is corrected using

---

-2.47	-2.4	-2.1	-1.8	-1.55	-1.37	-1.2	-1	-0.8	-0.6	-0.4	-0.2	0	0.2	0.4	0.6	0.8	1	1.2	1.37	1.55	1.8	2.1	2.4	2.47
-------	------	------	------	-------	-------	------	----	------	------	------	------	---	-----	-----	-----	-----	---	-----	------	------	-----	-----	-----	------

---

**Table 71:** Values of  $\eta_{\text{calo}}$  bin frontiers for energy scale factors for low pile-up runs [5].

2120 the MVA-based algorithm, then the data is corrected for pile-up and uniformity. The energy response  
 2121 in data is calibrated using the  $Z \rightarrow ee$  peak to match exactly the  $Z$  resonance in the simulation. Two  
 2122 correction factors are introduced: the energy scale factor  $\alpha$  and the constant term  $c'$ . The correction  
 2123 factors are extracted using the template method described in Ref. [4]:

- The calorimeter is split into  $i$  slices in  $\eta$  and for each slice the energy response in data is corrected in the following way:

$$E^{\text{data,corr}} = E^{\text{MC}} = E^{\text{data,uncorr}} / (1 + \alpha_i),$$

2124 where  $E^{\text{data,uncorr}}$  and  $E^{\text{MC}}$  are the energy response in data and MC respectively,  $\alpha_i$  is the energy  
 2125 correction factor for the  $i^{\text{th}}$  calorimeter slice in  $\eta$ .

- The relative energy measurement resolution can be represented as a quadratic sum of three uncorrelated terms:

$$\frac{\sigma(E)}{E} = \frac{a}{\sqrt{E}} \oplus \frac{b}{E} \oplus c,$$

where  $b$  term stands for electron and pile-up noise term,  $a$  is the stochastic term related to the development of the electromagnetic shower and  $c$  is constant. The constant term  $c$  includes all corrections that do not depend on the energy (e.g. non-uniformities, mechanical imperfections, temperature gradients) and is normally within 1% in the barrel and about 1-2% in the end-cap. In order to widen the MC mass peak and match it to the data in each rapidity bin an additional constant term  $c'$  is added:

$$\left( \frac{\sigma(E)}{E} \right)_i^{\text{data}} = \left( \frac{\sigma(E)}{E} \right)_i^{\text{MC}} \oplus c'_i.$$

2126 Normally in the standard high-pileup data, the energy scale factors corrections are obtained in 68  $\eta$   
 2127 bins. For the low pile-up runs wider bins were also considered due to smaller number of  $Z \rightarrow ee$  events.  
 2128 Figure 72 demonstrates the need for wider bins, as 68 bins result in high uncertainty, especially in the  
 2129 endcap.

2130 Two binnings were considered:

- 48 bins with smaller bins in the barrel and wider bins in the endcap
- 24 bins of equal size, as shown in Table 71.

2133 As can be seen from Fig. 72, the statistical instability for the endcap bins is significantly reduced if  
 2134 wider bins are used. Since the  $\alpha$  factors are quite similar in 48 and 24 bin cases, the latter is chosen as  
 2135 the baseline.

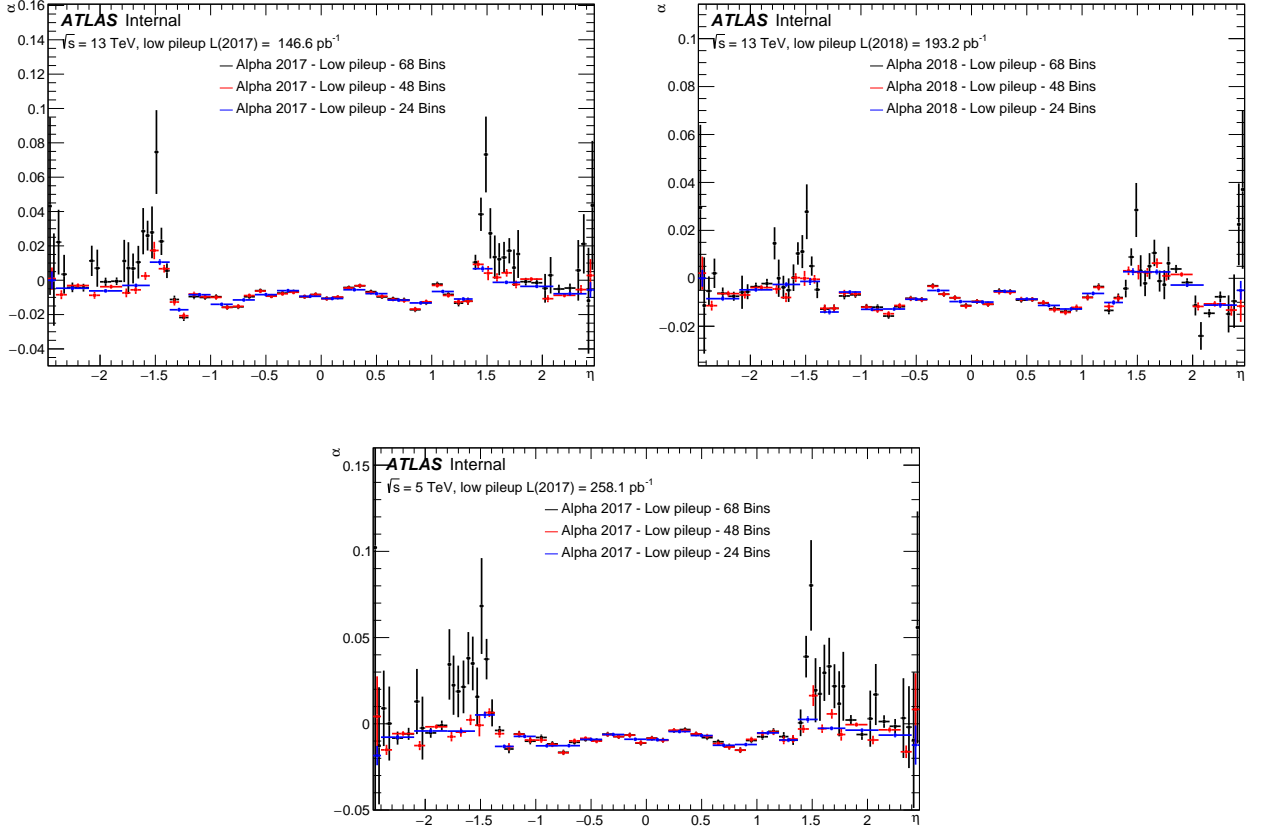


**Figure 72:** Energy scale factors  $\alpha$  for low pile-up runs of 2017 (left), 2018 (right) and 2017 at 5TeV (bottom) using 68, 48 and 24  $\eta$  bins. It can be seen, that the extraction is unstable in case of 68 bins, resulting in  $\alpha$  factors with very large uncertainties [5].

2136     The extracted constant  $c'_i$  correction term is presented in Fig. 73. The constant term  $c'$  depends on  
 2137     the data taking conditions and pile-up, so its extrapolation from a dataset obtained under different  
 2138     conditions appears problematic. This issue is discussed in Ref. [6].

2139     This correction entails experimental uncertainty, caused primarily by the statistical uncertainty of  
 2140      $\alpha_i$  and  $c'_i$  factors measurement, other uncertainties are significantly smaller and therefore neglected.  
 2141     The comparison between the data and MC invariant mass distributions around the  $Z \rightarrow ee$  peak are  
 2142     presented in Figure 74 and Fig. 75. The agreement is satisfactory and within the uncertainty.

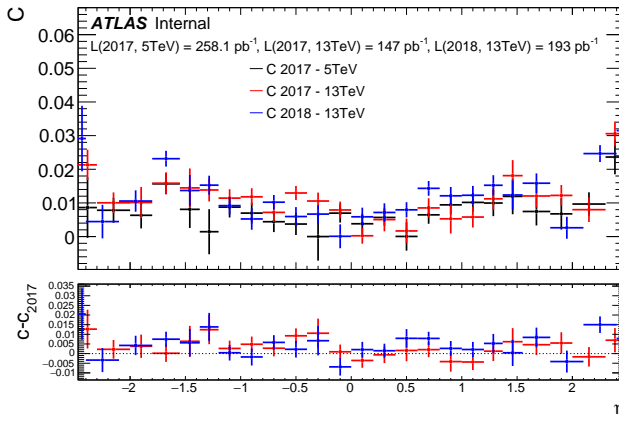


**Figure 73:** Additional constant term  $c'_i$  for low pile-up runs of 2017 (13 TeV), 2018 (13 TeV) and 2017 at 5 TeV using 24 bins. The lower panel shows the difference of  $c'_i$  to the 2017 5 TeV run [5].

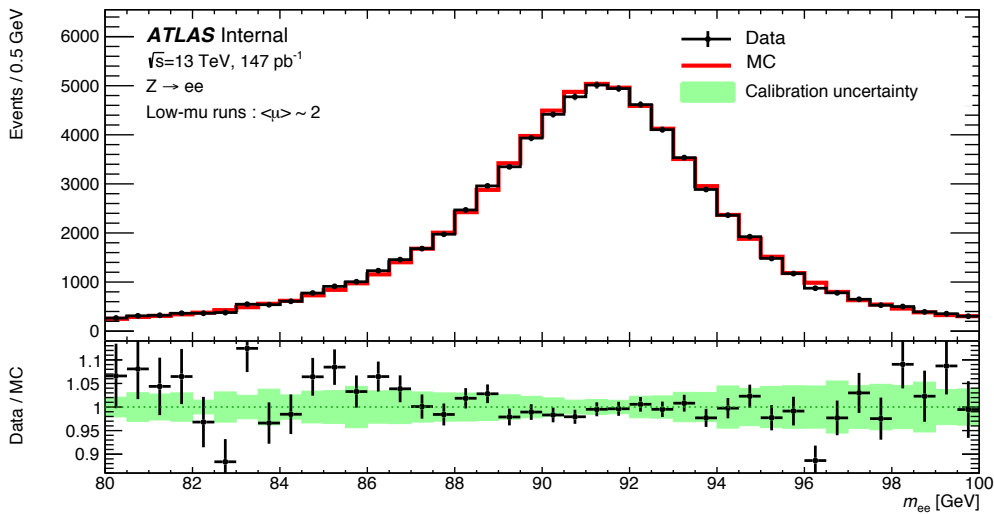


**Figure 74:** The invariant mass distribution around the Z-mass for low pile-up Data for 2017 (13 TeV) [5]

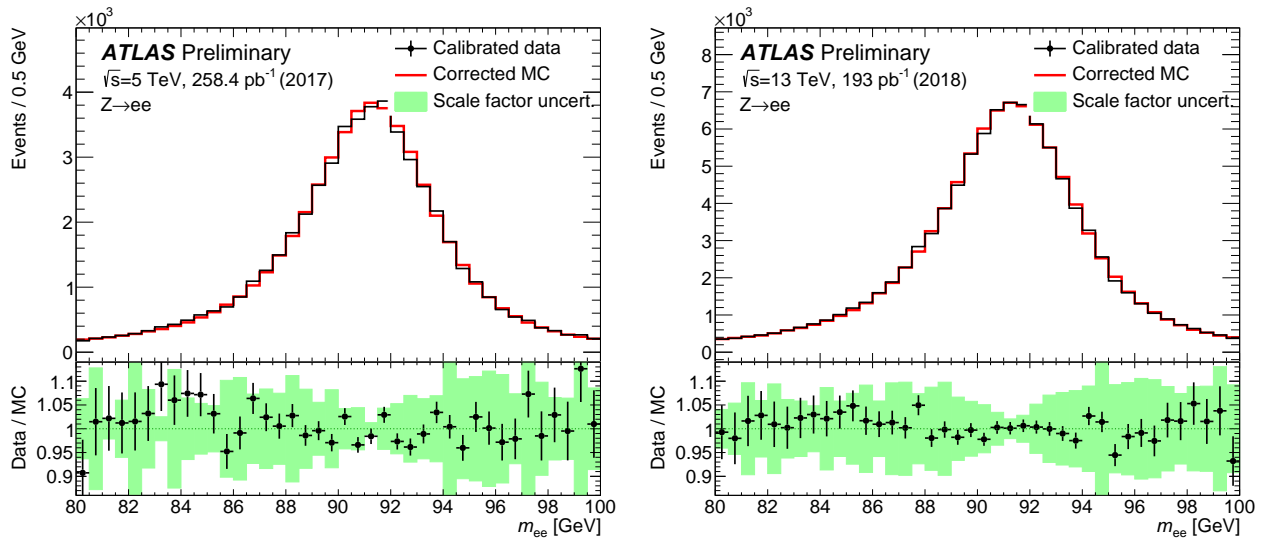


**Figure 75:** The invariant mass distribution around the Z-mass for low-pileup data for the  $\sqrt{s} = 5$  TeV data taken in 2017 (a) and the  $\sqrt{s} = 13$  TeV 2018 data (b) [5].

2143 **7.1.2 Electron selection efficiency**

The electrons used in the analysis are selected based on the corresponding requirements to the quality of their reconstruction, kinematic characteristics, and passing certain identification, isolation and trigger matching criteria. A tag-and-probe method is used to measure efficiencies in data and MC simulation, which may be different due to various aspects of physics and detector modelling (some of them are addressed in Chapter 5 of the current thesis). In order to match the MC simulation and the data in each of the aforementioned aspects the corresponding scale factor (SF)s are introduced. The SF is defined as the ratio of the data efficiency to MC efficiency:

$$SF_{(a)} = \frac{\epsilon_{(a)}^{data}}{\epsilon_{(a)}^{MC}},$$

where  $\epsilon$  stand for efficiency and index  $a$  stands for reconstruction, ID, isolation or trigger. The SF extraction allows for better agreement between data and simulation, but also brings uncertainties. The total efficiency correction is used as an event weight during the analysis:

$$W_{event}^{W \rightarrow e\nu} = SF_{reco} \cdot SF_{trig} \cdot SF_{ID} \cdot SF_{iso}.$$

2144 The tag-and-probe method used for the measurement of electron efficiencies includes the following  
2145 steps:

- 2146 • A kinematic selection is applied to  $Z \rightarrow ee$  events (Cut1).
- 2147 • A tight selection (Cut2) is applied to one of the two electrons along with matching it to the  
2148 single-electron trigger. From now on this electron is called the *tag*.
- 2149 • The other electron is called the *probe* and is used to probe the picked efficiency.
- 2150 • Selections Cut1 and Cut2 are varied in order to evaluate the stability of the method.

2151 The details are presented in Refs. [2, 7, 8].

2152 **Reconstruction efficiency**

2153 The fraction of electromagnetic clusters that are matched with the charged particle track from the ID  
2154 that satisfy the quality requirements define the reconstruction efficiency. An additional "PassTrack-  
2155 Quality" requirement of having at least 1 hit in the pixel detector and and least 7 hits in the silicon  
2156 detectors is imposed on the track of successfully reconstructed electrons.  
2157 So the electron reconstruction efficiency is calculated as:

$$\epsilon^{reco}(p_T, \eta) = \frac{N_{pass} - N_{pass}^{bkg}}{N_{pass} - N_{pass}^{bkg} + N_{fail} - N_{fail}^{bkg} + N_{photon} - N_{fit}}. \quad (7.1)$$

2158  $N_{pass(fail)}$  stands for the number of electrons passing (failing) the "PassTrackQuality" criterion. The  
 2159 background electron candidates  $N_{pass(fail)}^{bkg}$  are obtained from the template fits of the background on  
 2160 subsets that pass (fail) the "PassTrackQuality" criterion. The number of electrons that are reconstructed  
 2161 as photons is denoted by  $N_{photon}$ . The non-electron background that is reconstructed as photons is  
 2162 estimated from analytical fit in the control region away from the  $Z \rightarrow ee$  resonance and is called  $N_{fit}$ .  
 2163 An extrapolation of  $SF_{reco}$  from the high- $\mu$  data is used as a baseline for the reconstruction scale factors  
 2164 measurement. The benefits of higher statistics available in high- $\mu$  dataset outweigh the losses imposed  
 2165 by the extrapolation and provide lower uncertainty comparing to the SFs measured with low pileup  
 2166 dataset (see Fig. 77).  
 2167 The extrapolation procedure takes into account the two main differences between the high-mu and low-  
 2168 mu datasets, namely the dependence of the efficiency on the  $N_{Vtx}$  per event and a different topocluster  
 2169 threshold. Fig. 76 shows that the dependence on the number of vertices per event is well modelled by  
 2170 the MC simulation and can be extrapolated using a fit. The dependence on the topocluster threshold  
 2171 was found negligibly small.

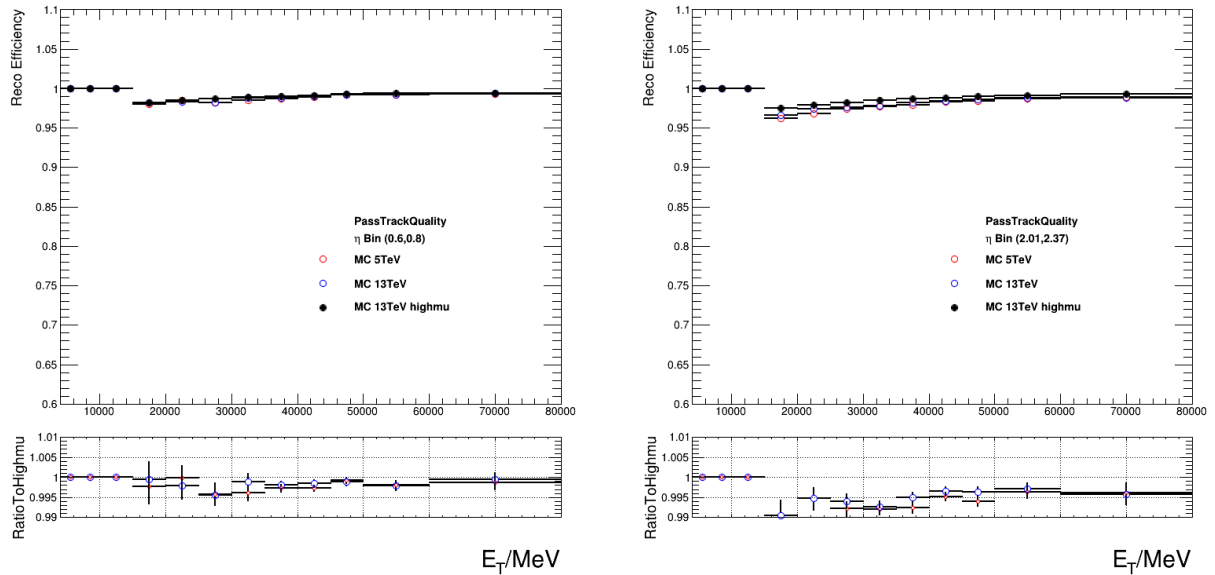


**Figure 76:** Electron reconstruction efficiencies compared for low-pileup and high-pileup MC16 in  $\eta$  range [0.60-0.80] (left) and [2.01-2.37] (right). The statistical uncertainties are shown [5].

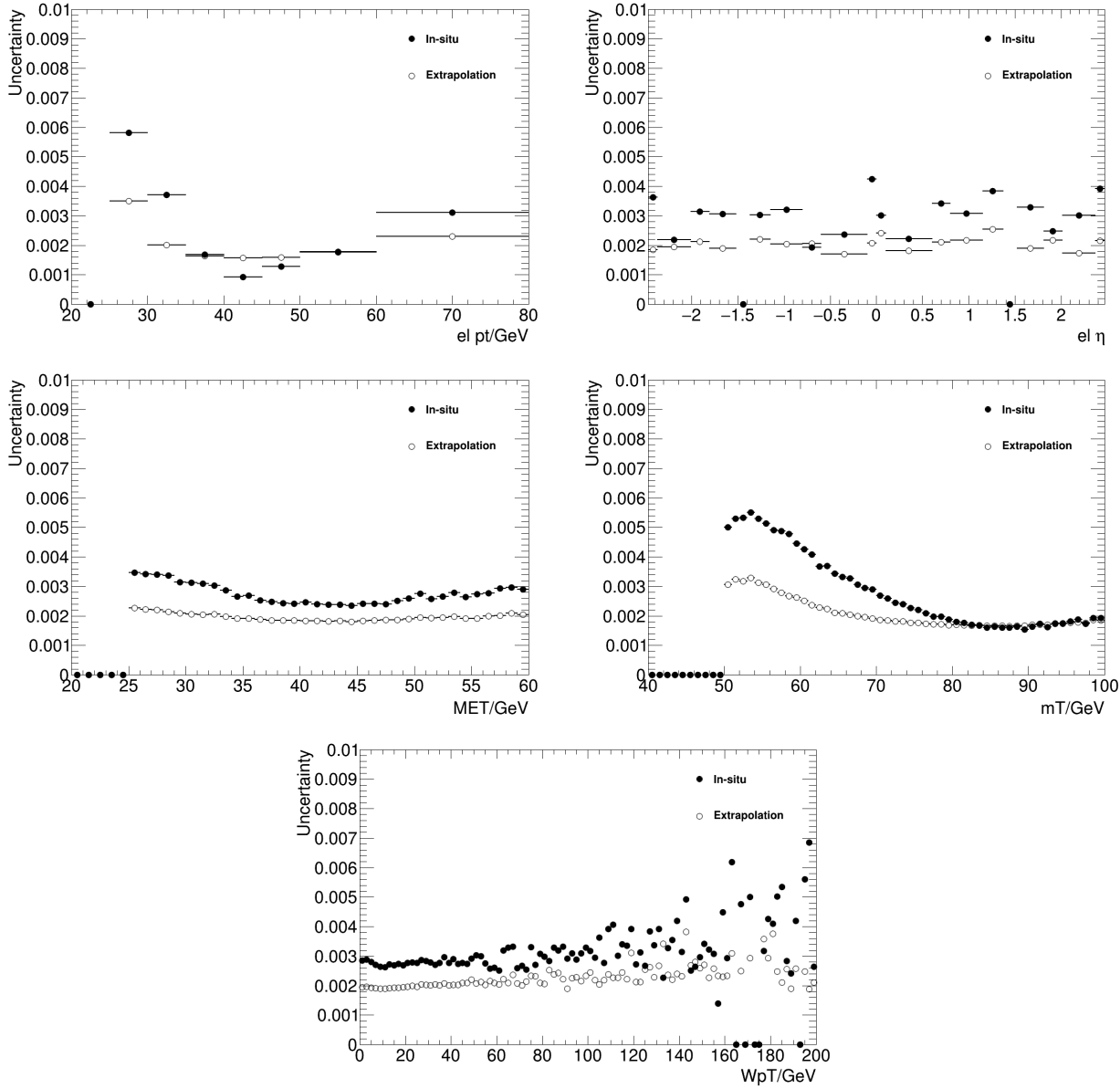


**Figure 77:** Comparison of the uncertainties due to electron reconstruction, contrasting the high- $\mu$ -extrapolated and in-situ-measured SF uncertainties in a  $W^+ \rightarrow e^+\nu$  selection at 13 TeV as function of typical kinematic variables [5].

## 2172 Identification efficiency

2173 The fraction of reconstructed electrons that pass a given working point define the electron identifi-  
 2174 cation efficiency. The low pile-up  $W \rightarrow ev$  measurement uses the "Medium LH" working point. The  
 2175 methodology is described in Ref. [7] and includes the combination of two background subtraction  
 2176 methods:  $Zmass$  and  $Ziso$ .  
 2177 In the  $Zmass$  method the background is estimated using a template method normalized in  $m_{ee}$  side  
 2178 bands. The tag is required to be trigger-matched, pass ID and isolation cuts and have  $p_T > 20$  GeV. The  
 2179 probe has to pass the "PassTrackQuality" and the electron/photon ambiguity resolver, have  $p_T > 15$   
 2180 GeV and be separated from jets with  $p_T^{jet} > 20$  GeV by  $\Delta R > 0.4$ .  
 2181 An alternative method,  $Ziso$ , uses the calorimeter energy isolation  $E_T^{cone}$  of the probe electron to  
 2182 discriminate between background and signal. Signal electrons are expected to have better isolation  
 2183 than the background. On top of the requirements used for the  $Zmass$  method the tag and probe pair  
 2184 is required to have opposite sign and to fit into mass window of 15 GeV around the Z boson mass.  
 2185 The background template shape is constructed from the probe electrons that have the same charge  
 2186 as the tag, pass the track quality criteria but fail the shower shape cuts or fail the cut-based loose  
 2187 identification. The fraction of real electrons that pass the described selection is modelled with MC  
 2188 and subtracted from the template. The background template uses the tail region of probe isolation  
 2189 distribution  $E_T^{cone0.3}/25\text{GeV} > 0.5$  is scaled to the data luminosity. An example of the probe isolation  
 2190 estimate for the numerator and denominator in eq. 7.1 in the region  $25 < E_T < 30$  and  $0.8 < \eta < 1.15$  is  
 2191 presented in Fig. 78.

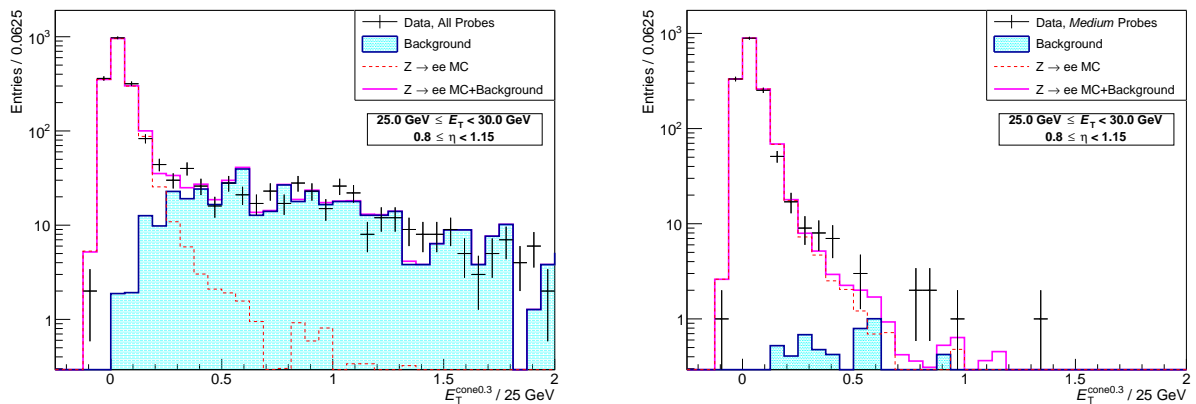


**Figure 78:**  $E_T^{cone0.3}/25\text{GeV}$  isolation distribution of probe electrons in the  $ZIso$ -method using 13 TeV  $339\text{ pb}^{-1}$  low-pileup data. Left the denominator and right the numerator distributions are shown, with the data as crosses, the signal  $Z \rightarrow ee$  expectation as open line and the background estimate as cyan area (template normalised at high values) [5].

2192 The SF to be used in the analysis is constructed out of both methods. The combination of the results  
 2193 takes into account the high degree of correlation between the two methods and includes the following  
 2194 steps:

- 2195 • the final SF is defined as an arithmetic mean of the two methods over all systematic variations;
- 2196 • the statistical uncertainty is calculated as the average of the statistical uncertainties of the  
2197 variations;
- 2198 • a covariance matrix is composed from all variations of the two methods and then decomposed  
2199 into correlated and uncorrelated parts, providing the systematic uncertainty.

2200 The combined results are presented in Fig. 79 and show similar results between both methods and the  
2201 combination. The SFs obtained from 5 and 13 TeV data samples were not combined due to significant  
2202 differences in measured efficiency.

### 2203 Isolation efficiency

2204 The electron isolation efficiency is the fraction of reconstructed and MediumLLH-identified electrons  
2205 that pass a designated isolation requirement. For this analysis the isolation requirement is chosen to be  
2206  $p_{T\text{varcone}}^{20}/p_T^e < 0.1$ . The results are presented in Fig. 710 and show that the efficiency is very high.  
2207 The SFs for 5 and 13 TeV are not combined and used separately.

### 2208 Trigger efficiency

2209 During the data-taking at low pile-up the unprescaled trigger `HLT_e15_1h1loose_nod0_L1EM12` was  
2210 used. Thanks to the ID and isolation requirements for both tag and probe electrons, the background is  
2211 negligible in the trigger efficiency measurement. The measurement results are shown in Fig. 711 and  
2212 demonstrate relatively high efficiency in most of the regions. The scale factors are also very close to  
2213 unity. No combination was performed between 5 and 13 TeV results.

### 2214 7.1.3 SF uncertainties propagation

2215 The main source of uncertainty for the measurement of the SFs is coming from the background. The  
2216 uncertainties are estimated by varying the parameters that contribute to background suppression.  
2217 These parameters include the following variations:

- 2218 • The Zmass window technique is used in the identification, isolation and trigger efficiencies  
2219 measurement. The size of the Zmass window was varied in a range of 10, 15 and 20 GeV. This  
2220 variation dominates at higher values of  $p_T$ .
- 2221 • The tag identification and isolation criteria were varied between Medium ID + calorimeter  
2222 isolation, TightLLH and Tight ID + calorimeter isolation.

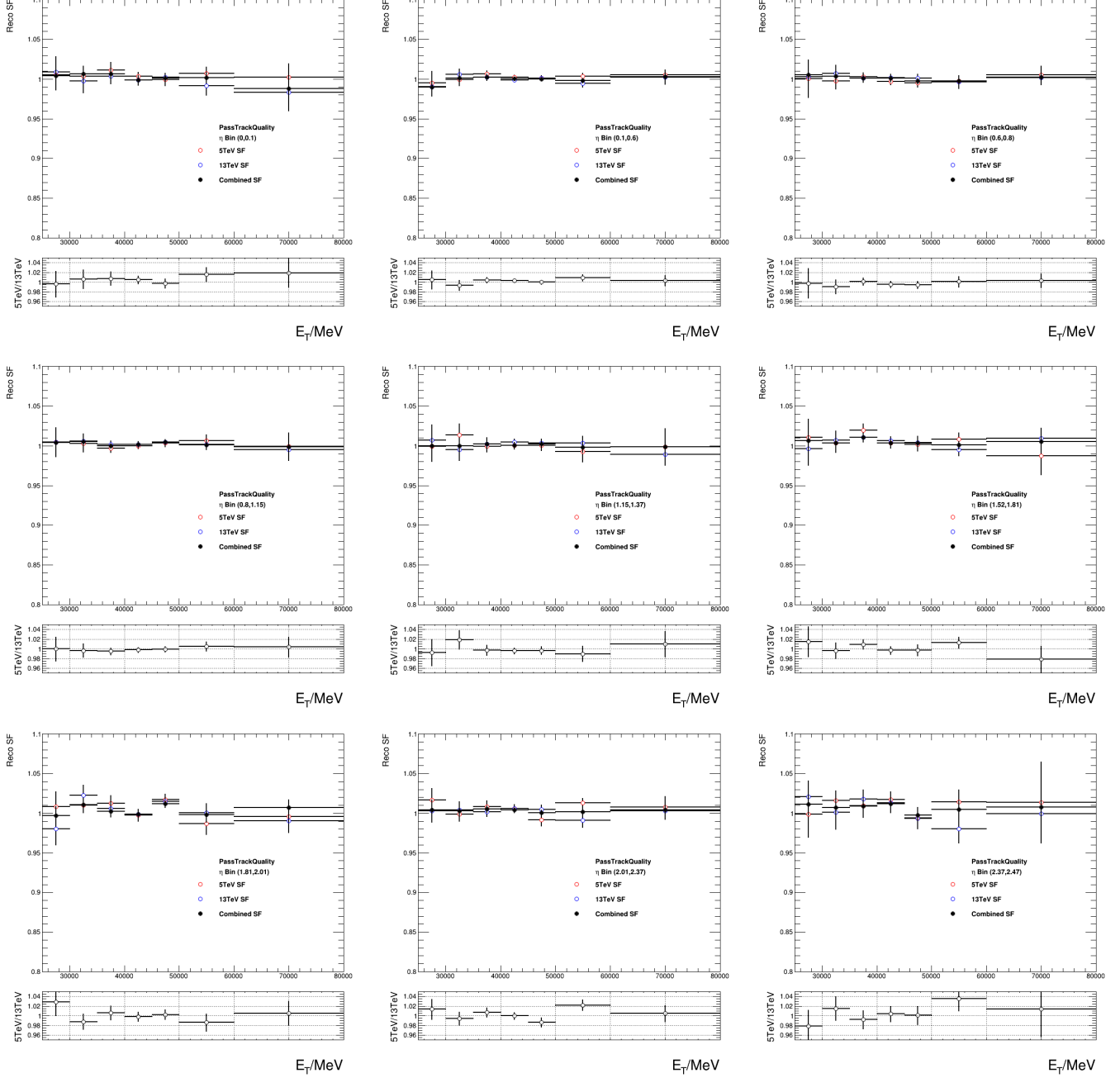


**Figure 79:** Comparison of electron reconstruction SFs with 5 TeV and 13 TeV data as well as the 5+13 TeV combination in nine  $\eta$  ranges as written in the plot legend, from most central  $\eta = 0 - 0.1$  (top left) to most forward  $\eta = 2.37 - 2.47$  (bottom right). The bottom panel shows the ratio of 5 TeV and 13 TeV SFs. The total uncertainties are shown [5].

## Mesure de la masse du boson W avec le détecteur ATLAS au LHC

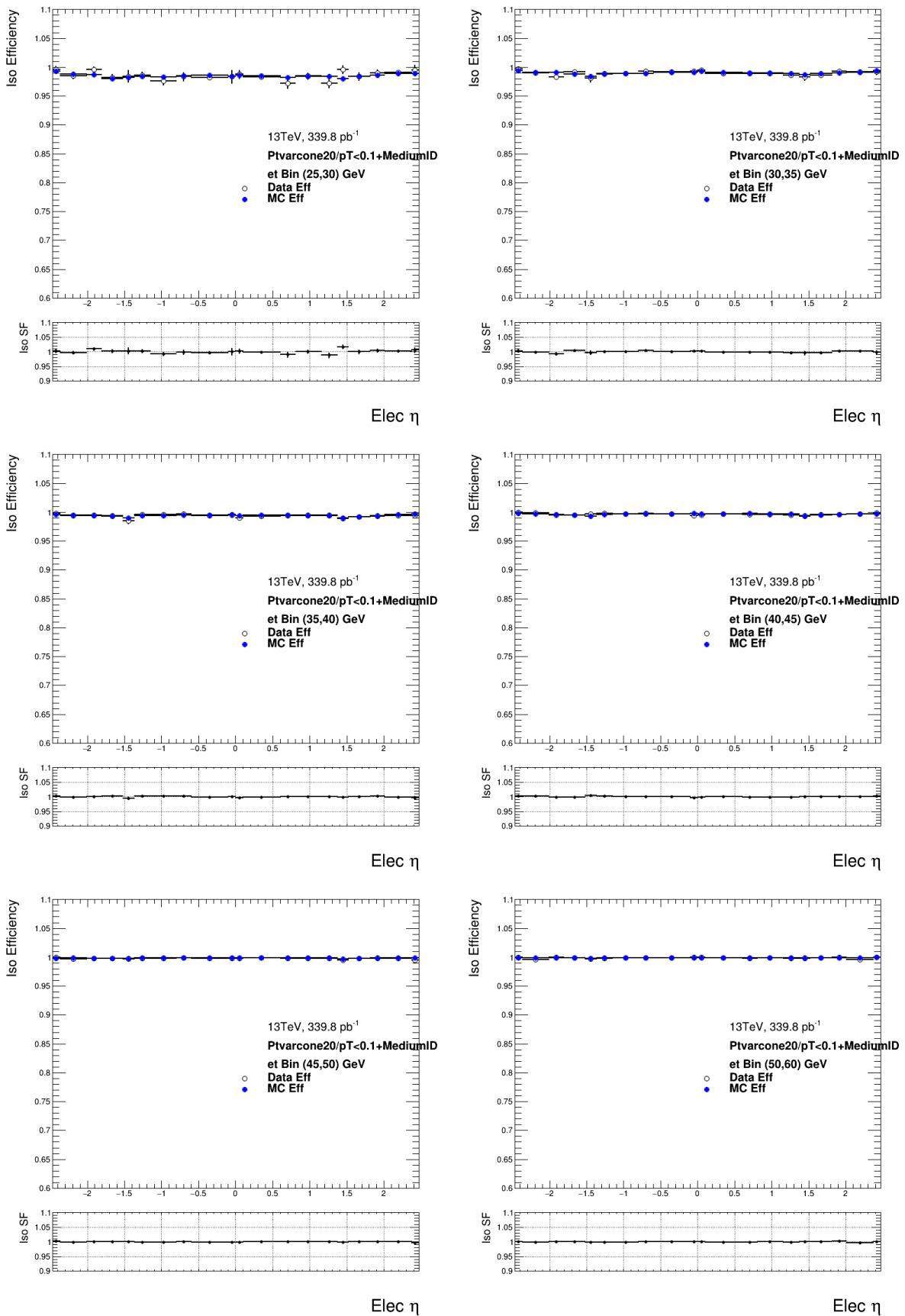


**Figure 710:** Electron isolation efficiencies (top panels) and scale factors (lower panels) for the  $ptvarcone20/p_T^e < 0.1$  working point using 13 TeV 339 pb<sup>-1</sup> low-pileup data as function of  $\eta$  in bins of  $p_T$  [5].

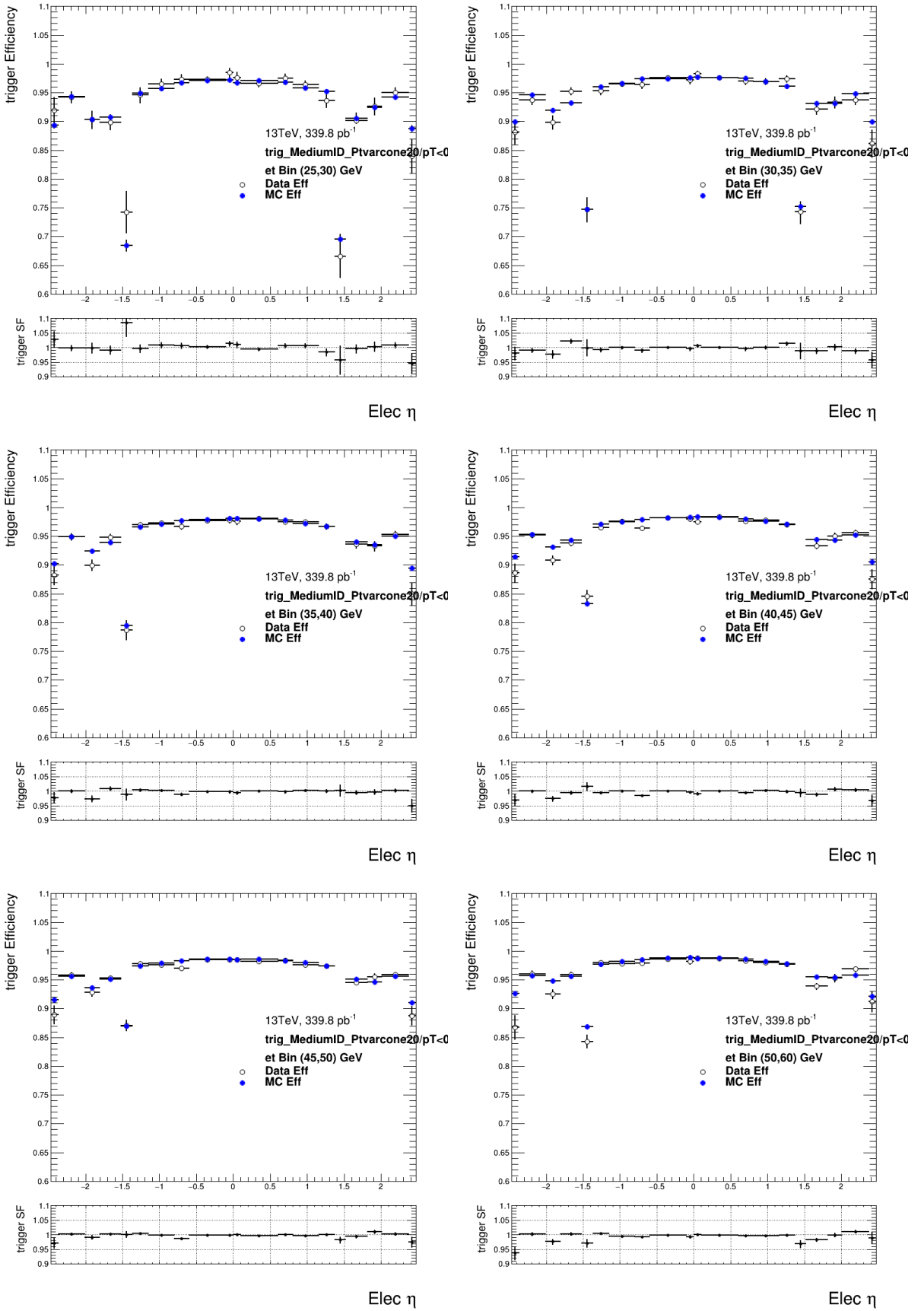
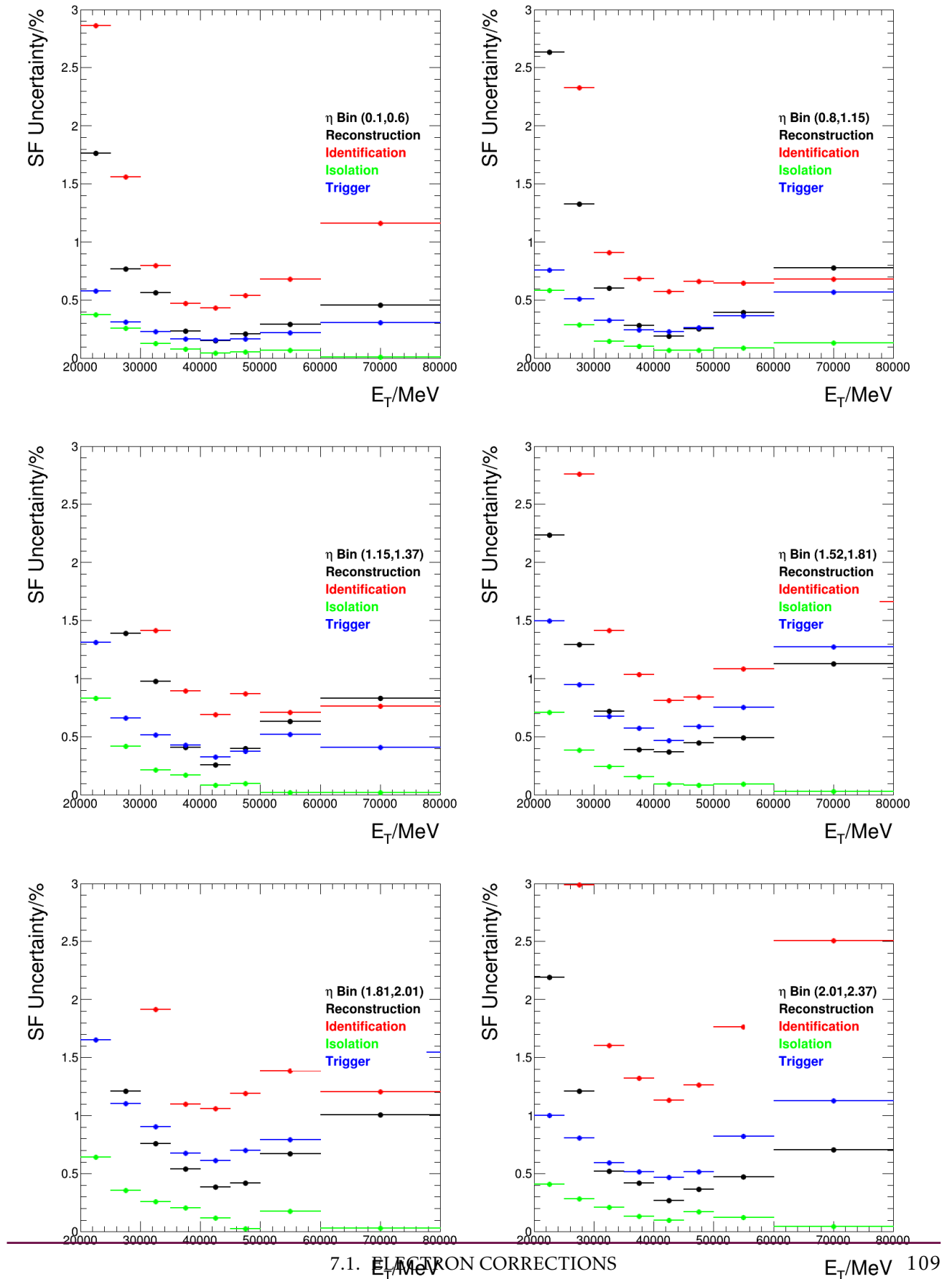


**Figure 711:** Electron trigger efficiency and scale factors (lower panels) as function of  $\eta$  in bins of  $p_T$  [5].

ELECTRON CORRECTIONS AND  
107

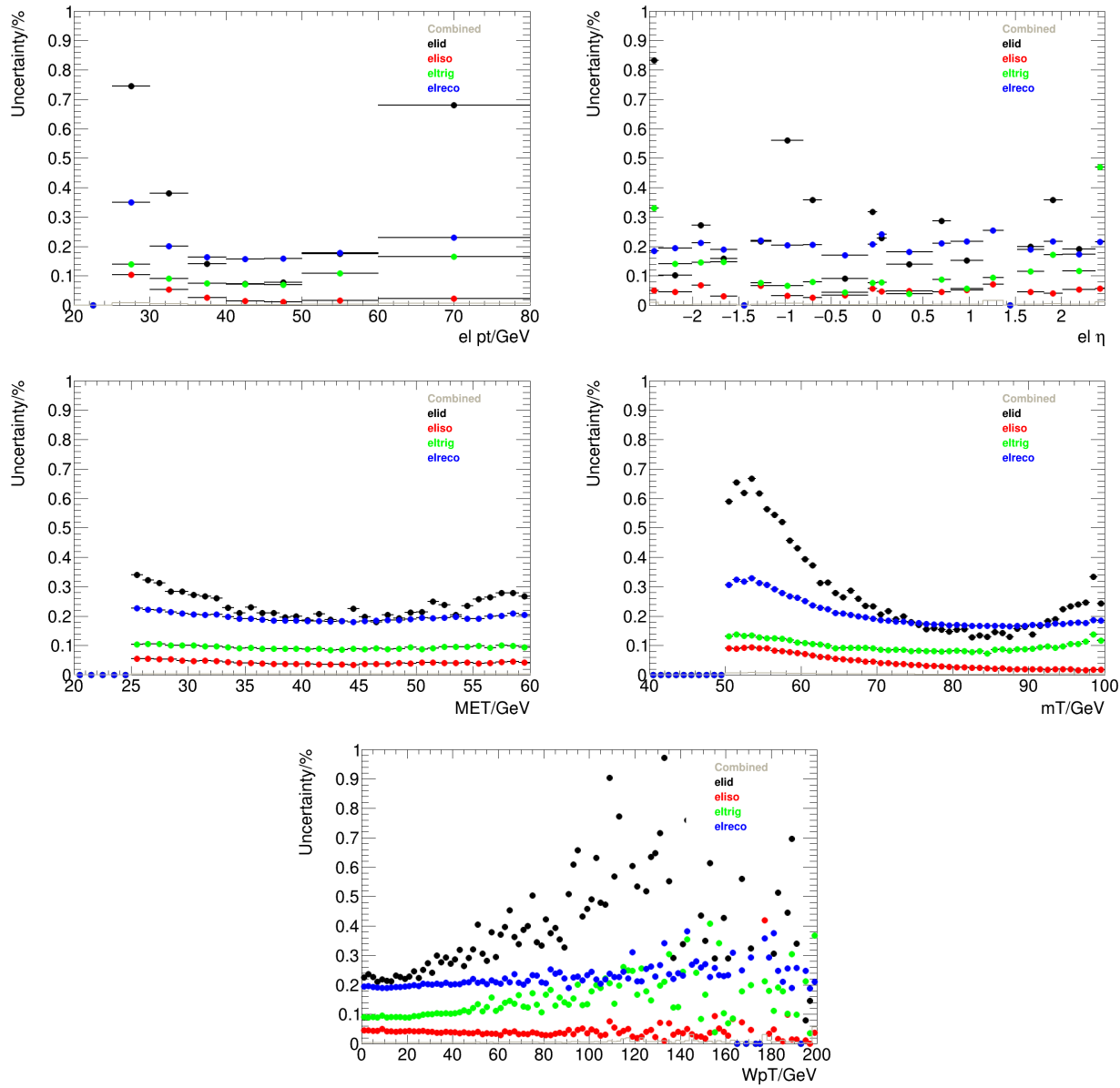
- The background template has a major influence on the estimate of signal contamination, especially at  $p_T < 30$  GeV. In addition to the nominal range of template extraction in  $120 < m_{ee} < 250$  GeV the templates are also normalized using the region of  $60 < m_{ee} < 70$  GeV.
- The side band range is varied for the reconstruction efficiency measurement.
- The isolation criteria are varied in the measurement of ID efficiency:  $E_T^{cone0.3}/25$  GeV is varied between 0.4, 0.5 and 0.6, also a larger cone isolation around the probe electron was used -  $E_T^{cone0.4}/25$  GeV.

Figure 712 shows the total relative uncertainties of the electron scale factors at 13 TeV in different  $\eta$  bins. Contributions from reconstruction and identification are the dominant ones. The uncertainties are propagated to the observables using the co-called Full correlation model (see Ref. [8]). The idea of the method is to split the sources of SF uncertainty into uncorrelated and correlated sources. Uncorrelated sources are of statistical nature and mostly related to the number of  $Z \rightarrow ee$  pairs in different bins if  $p_T$  and  $\eta$  used for SF extraction. Correlated sources of systematic uncertainty arise from the flaws of background subtraction. The Full correlation model includes about 10 sources of systematic uncertainty and around  $200 p_T \times \eta$  bins as sources of statistical uncertainty and allows to propagate these uncertainties to the observables. Figures 713 and 714 contain the results of error propagation to several observable distributions for 13 and 5 TeV respectively. Again, identification and reconstruction uncertainties have the largest contribution to the total SF uncertainty.



7.1. ELECTRON CORRECTIONS

**Figure 712:** Total relative uncertainties of electron scale factors at 13 TeV measured with tag-and-probe method [5].



**Figure 713:** Contributions to the electron uncertainties related to efficiency SF (reconstruction, identification, isolation and trigger) in a  $W^+ \rightarrow e^+\nu$  selection at 13 TeV as function of typical kinematic variables [5].

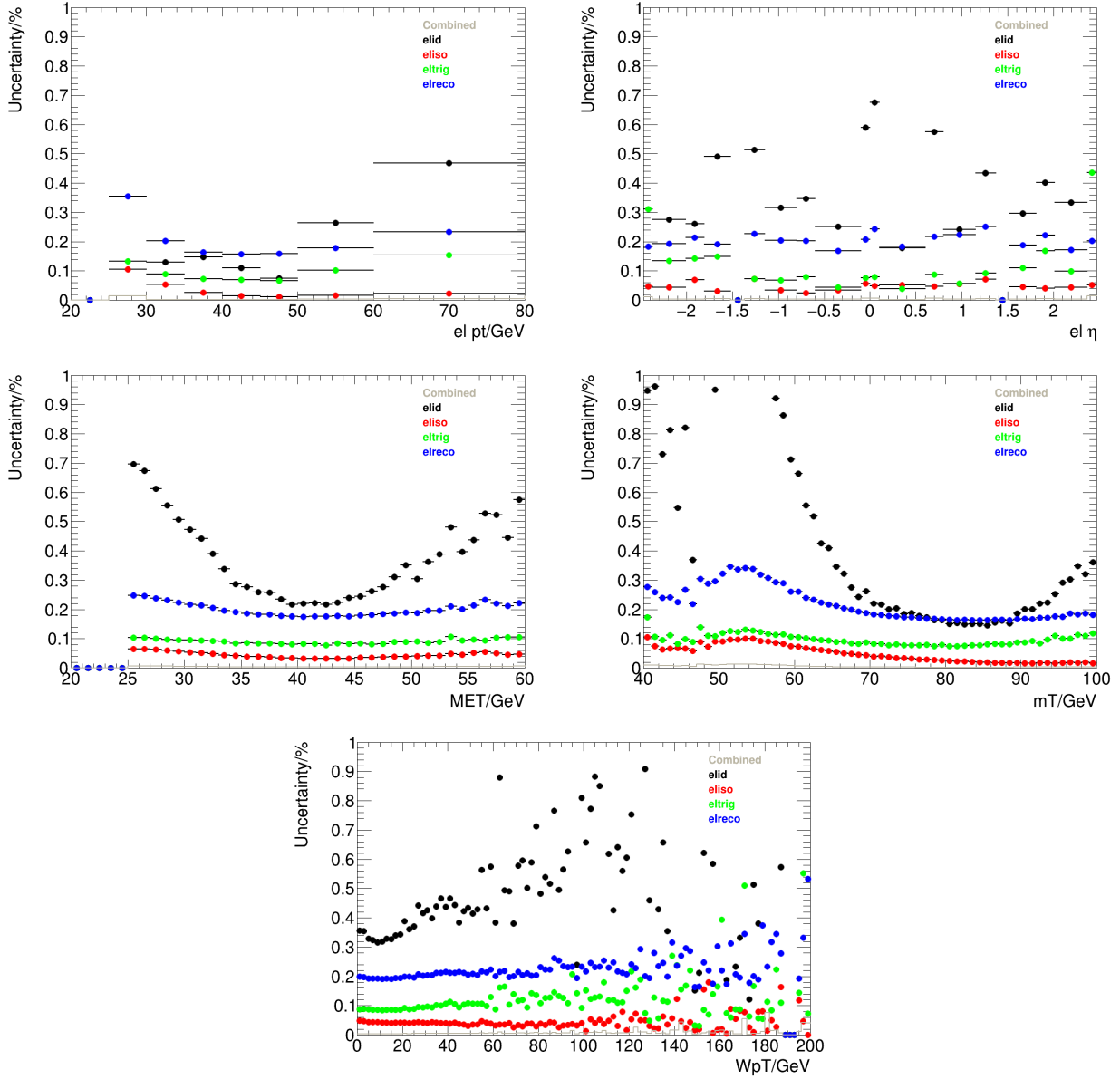


**Figure 714:** Contributions to the electron uncertainties related to efficiency SF (reconstruction, identification, isolation and trigger) in a  $W^+ \rightarrow e^+ \nu$  selection at 5 TeV as function of typical kinematic variables [5].

---

## 2241 7.2 Muon corrections

2242 Muon corrections are in many aspects similar to the electron corrections described in the previous  
 2243 section. Calibrations are used in order to match the momentum response in the data and in the MC  
 2244 simulation.

### 2245 7.2.1 Muon momentum calibration

2246 The muon momentum calibration comprises corrections to the momentum scale and resolution. At  
 2247 first the ID and MS tracks are reconstructed and corrected separately, and then the two corrections are  
 2248 propagated to correct the CB muon tracks. Low energy muons with  $5 < p_T < 30$  GeV are calibrated using  
 2249 the  $J/\psi \rightarrow \mu\mu$  resonance, while in higher energy region of  $22 < p_T < 300$  GeV the  $Z \rightarrow \mu\mu$  resonance is  
 2250 used. The statistical uncertainties are directly linked to the number of  $Z$  and  $J/\psi$  candidates in the data  
 2251 samples:

- 2252 • 5.02 TeV data (2017, period M): 660k  $J/\psi$  candidates, 75k  $Z$  candidates
- 2253 • 13 TeV data (2017, period N): 1.1M  $J/\psi$  candidates, 100k  $Z$  candidates
- 2254 • 13 TeV data (2018, periods G4 and J): 1.5M  $J/\psi$  candidates, 130k  $Z$  candidates

2255 The corrected transverse momentum  $p_T^{corr,Det}$  (where  $Det$  may stand for ID or MS) is described by the  
 2256 following equation [9]:

$$p_T^{corr,Det} = \frac{p_T^{MC,Det} + \sum_{n=0}^1 s_n^{Det}(\eta, \phi) (p_T^{MC,Det})^n}{1 + \sum_{m=0}^2 \Delta r_m^{Det}(\eta, \phi) (p_T^{MC,Det})^{m-1} g_m}, \quad (7.2)$$

2257 where  $p_T^{MC,Det}$  is the uncorrected  $p_T$  in MC simulation,  $g_m$  are normally distributed random variables  
 2258 with zero mean and unit width,  $s_n^{Det}$  and  $\Delta r_m^{Det}$  are the momentum resolution smearing and scale  
 2259 correction factors applied in the specific  $(\eta, \phi)$  detector region respectively. The  $Z$  and  $J/\psi$  peaks are  
 2260 fitted with a function that is a sum of a Crystal Ball function (that fits the mass peak), a Gaussian  
 2261 (that accounts for effects like multiple scattering) and an exponential that fits the backgrounds. The  
 2262 examples of such fits are presented at Fig. 715.

2263

2264 The measured correction parameters for  $Z$  and  $J/\psi$  peaks for 5 and 13 TeV are presented in Fig. 716,  
 2265 717, 718 and 719. The calibration and resolution corrections were obtained at high pile-up conditions  
 2266 and validated in  $Z$  and  $J/\psi$  for low pile-up.

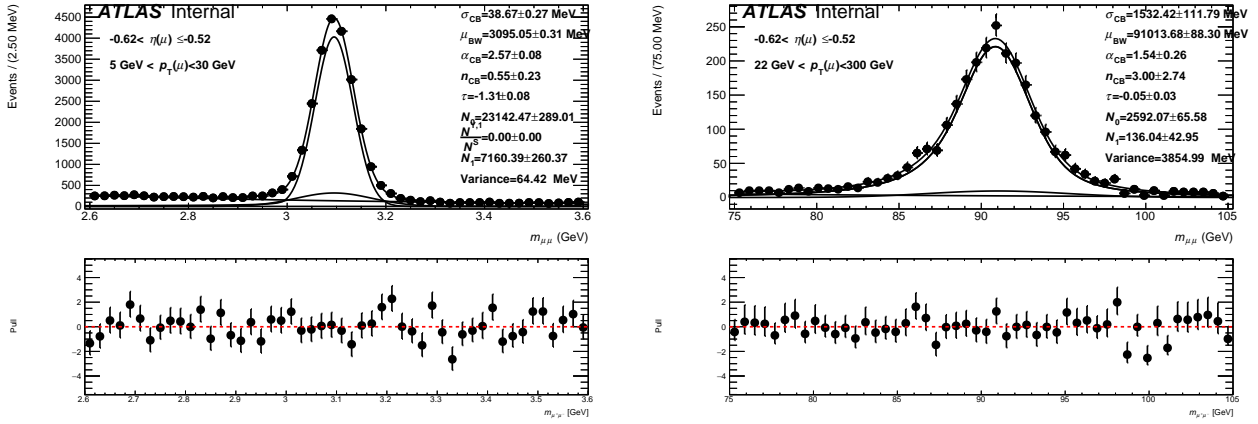


**Figure 715:** Example fits to  $J/\psi \rightarrow \mu\mu$  (left) and  $Z \rightarrow \mu\mu$  (right) mass peaks for pairs with leading muon pseudorapidity in the range  $-0.62 < \eta < -0.52$  in low-pile-up 2017 13 TeV data [10].

### 7.2.2 Correction for charge-dependent momentum bias

Misalignment in ID, MS or between the two systems can lead to a charge-dependent bias (also called *sagitta bias*) of muon reconstructed momentum. Its effect can be parametrized as follows:

$$p_T^{meas} = \frac{p_T^{reco}}{1 + q \cdot \delta_{sagitta} \cdot p_T^{reco}}, \quad (7.3)$$

where  $p_T^{meas}$  is the measured momentum that contains a bias,  $p_T^{reco}$  is the unbiased reconstructed momentum and the bias to be corrected is denoted as  $\delta_{sagitta}$ .

The sagitta correction is obtained as a function of  $\eta$ . There exist three methods of sagitta bias determination:

- The ID alignment and momentum measurement can be tested with electrons which have additional information from the charge-independent calorimeter. Using  $Z \rightarrow ee$  and/or  $W \rightarrow e\nu$  events it is possible to determine the charge bias of an electron track:

$$\delta_{sagitta} = \frac{\langle E/p_{track} \rangle^+ - \langle E/p_{track} \rangle^-}{2 \langle p_T^{calo} \rangle}, \quad (7.4)$$

where  $p_{track}$  is the momentum measured in the ID, E is the energy measured in the EMC, from which we can get the  $p_T^{calo} = E \cdot \sin \theta$  transverse momentum. The  $\langle \rangle$  brackets denote the averaging in  $\eta$  bins.

- The  $p_T(\mu)$  method is used by muon combined performance (MCP) and alignment groups in high- $\mu$  data compares the muons and anti-muons spectra in  $Z \rightarrow \mu\mu$  events. It compares the  $p_T^{\mu+}$  and  $p_T^{\mu-}$  distributions in data and MC and interprets the discrepancy as a charge-dependent misalignment.

- 2284 • The Z-mass method uses the Z mass peak. This is the main method used by MCP and alignment  
2285 groups, the results are denoted as  $M_{\mu\mu}\text{-}MCP$  and  $M_{\mu\mu}\text{-}Align$  on the plots (see [11]). The sagitta  
2286 bias is calculated iteratively minimizing the difference between the reconstructed and expected  
2287 position of the  $Z \rightarrow \mu\mu$  mass peak position. This method catches the rapidity dependence of the  
2288 sagitta bias, but is sensitive to overall offset.
- 2289 The results of these methods are presented in Fig. 720. The sagitta bias in low-pile-up data was found  
2290 to be 10 times higher than in the MC simulation. Further results in the measurement rely on the  
2291 following method: the differences between the data and MC are averaged over  $\eta$  using a fit, and also  
2292 introduce a global offset. The results are shown in Fig. 721.

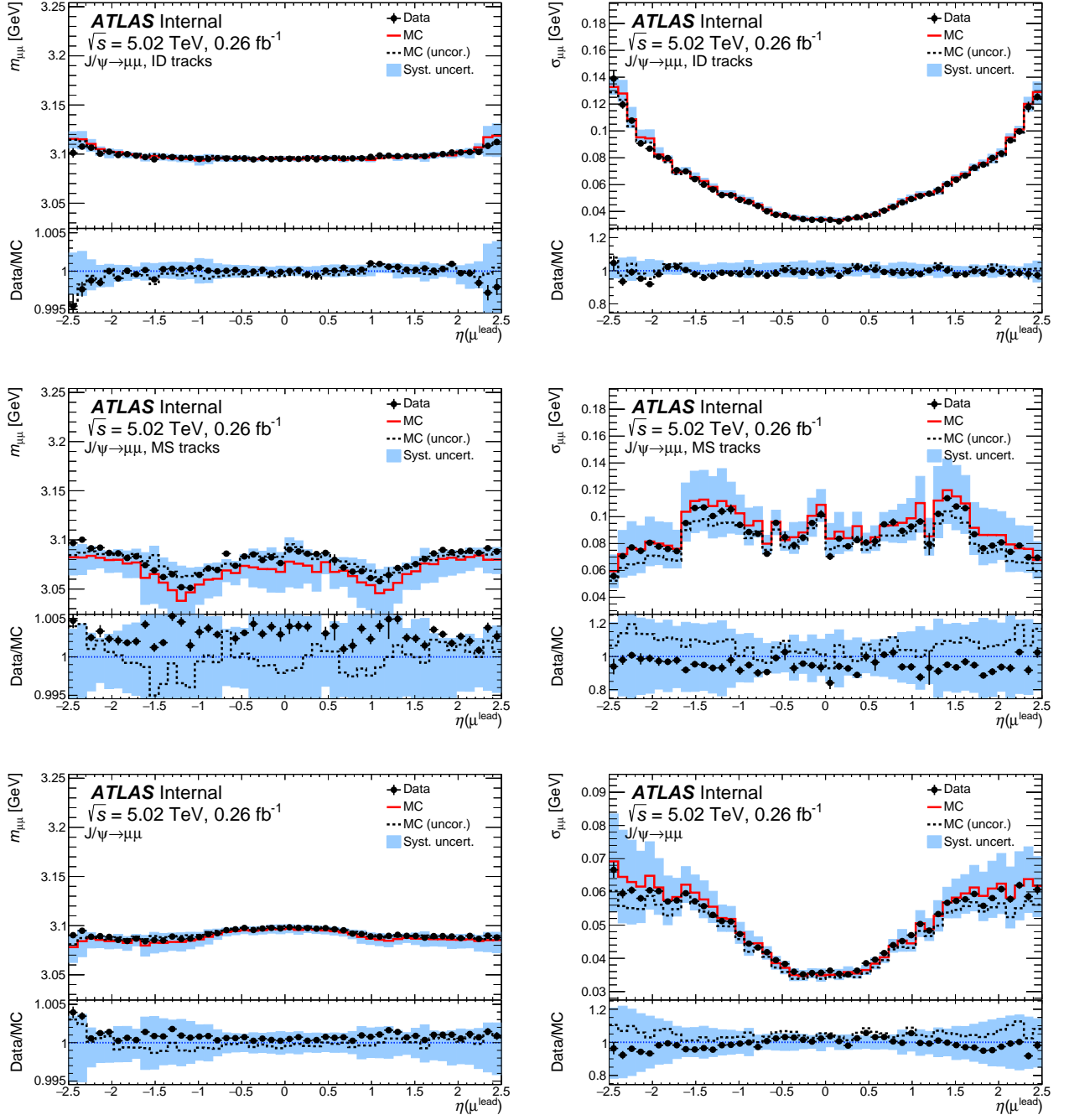


**Figure 716:** Mean (left) and width (right) of the  $J/\psi \rightarrow \mu\mu$  mass peak as a function of the leading muon  $\eta$  in 5.02 TeV data and MC. The mean and width are extracted from Crystal Ball components of the fits. In case of the simulation, both the uncorrected (dashed histogram) and corrected parameters (solid histogram) are shown. The fit results are presented for mass peaks constructed using kinematics of the muon ID tracks (top), ME tracks (middle) or CB tracks (bottom). The bottom panels in each plot show the data/MC ratio for uncorrected (dashed histogram) and corrected simulation (points) [10].

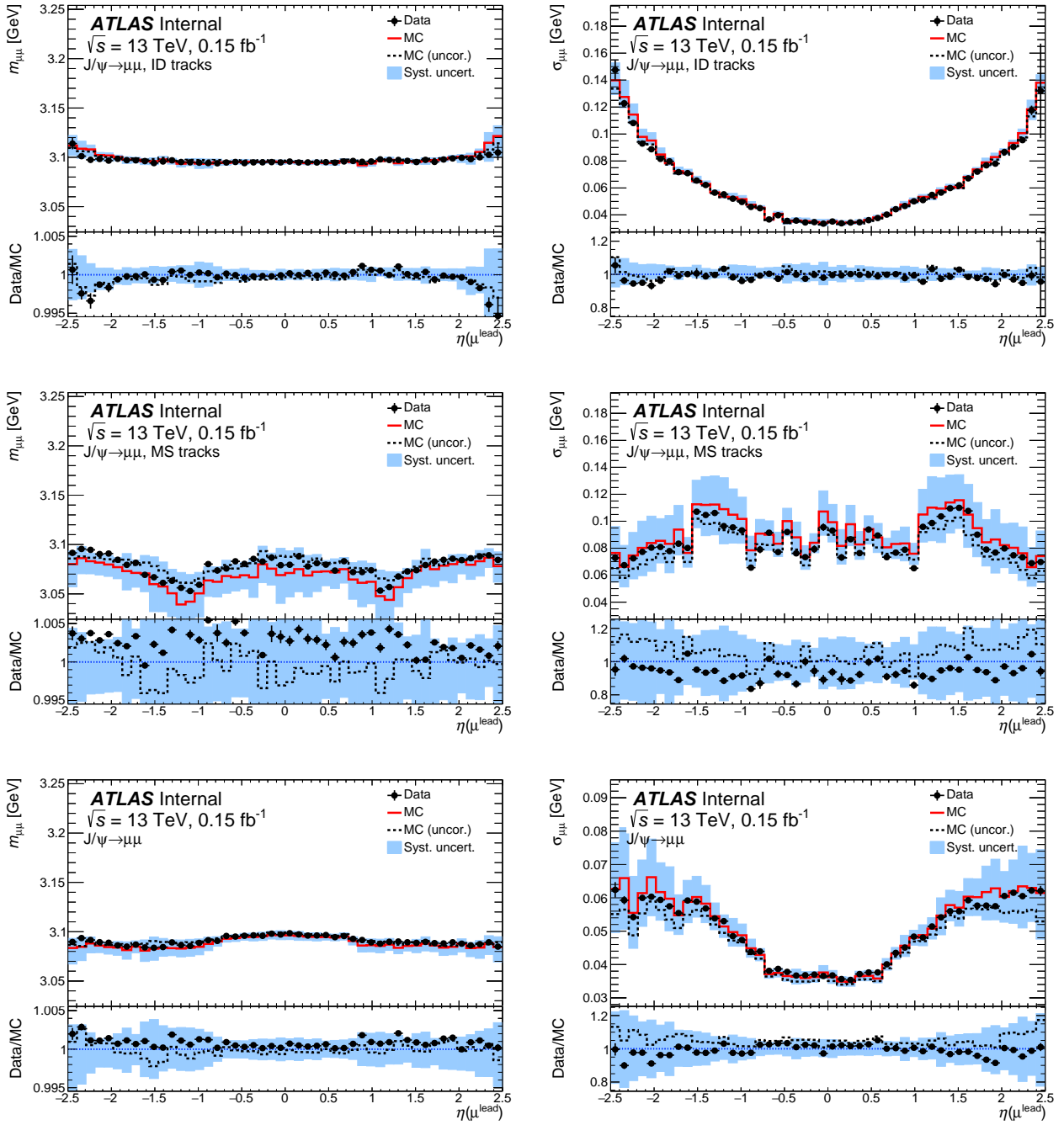


**Figure 717:** Mean (left) and width (right) of the  $J/\psi \rightarrow \mu\mu$  mass peak as a function of the leading muon  $\eta$  in 2017 13 TeV data and MC at low pile-up. The mean and width are extracted from Crystal Ball components of the fits. In case of the simulation, both the uncorrected (dashed histogram) and corrected parameters (solid histogram) are shown. The fit results are presented for mass peaks constructed using kinematics of the muon ID tracks (top), ME tracks (middle) or CB tracks (bottom). The bottom panels in each plot show the data/MC ratio for uncorrected (dashed histogram) and corrected simulation (points) [10].

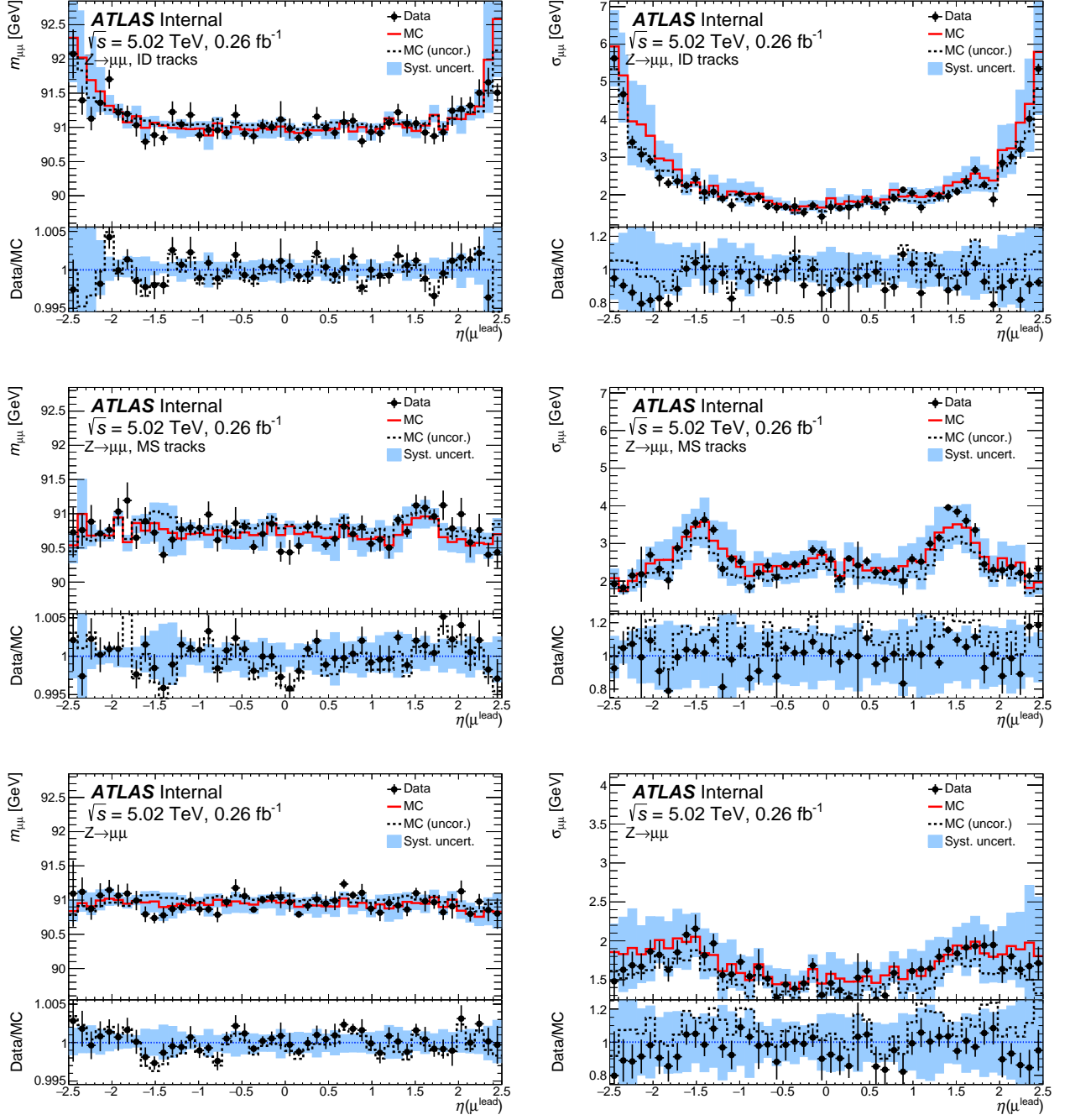


**Figure 718:** Mean (left) and width (right) of the  $Z \rightarrow \mu\mu$  mass peak as a function of the leading muon  $\eta$  in 5.02 TeV data and MC. The mean and width are extracted from Crystal Ball components of the fits. In case of the simulation, both the uncorrected (dashed histogram) and corrected parameters (solid histogram) are shown. The fit results are presented for mass peaks constructed using kinematics of the muon ID tracks (top), ME tracks (middle) or CB tracks (bottom). The bottom panels in each plot show the data/MC ratio for uncorrected (dashed histogram) and corrected simulation (points) [10].

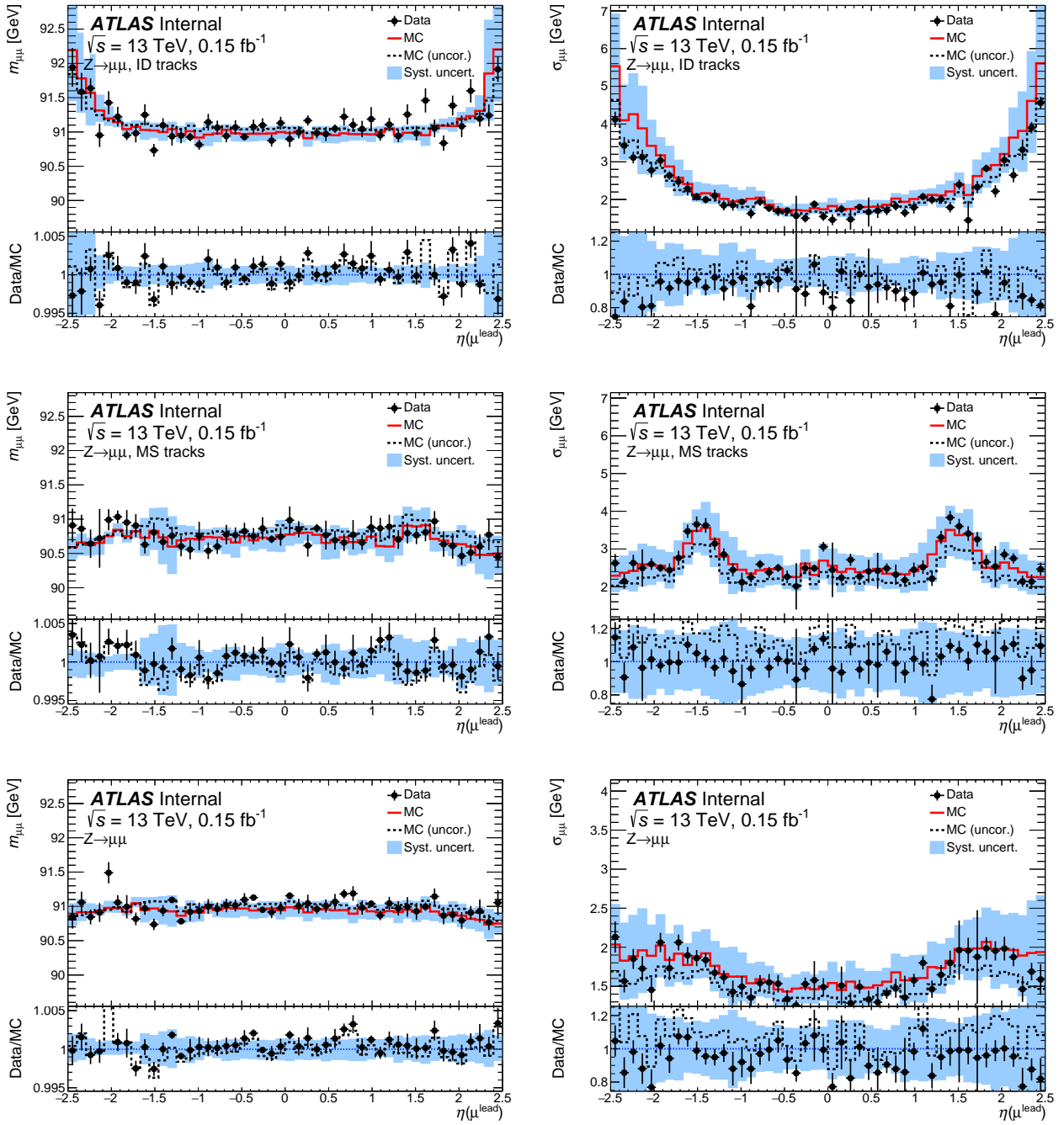


**Figure 719:** Mean (left) and width (right) of the  $Z \rightarrow \mu\mu$  mass peak as a function of the leading muon  $\eta$  in 2017 13 TeV data and MC at low pile-up. The mean and width are extracted from Crystal Ball components of the fits. In case of the simulation, both the uncorrected (dashed histogram) and corrected parameters (solid histogram) are shown. The fit results are presented for mass peaks constructed using kinematics of the muon ID tracks (top), ME tracks (middle) or CB tracks (bottom). The bottom panels in each plot show the data/MC ratio for uncorrected (dashed histogram) and corrected simulation (points) [10].

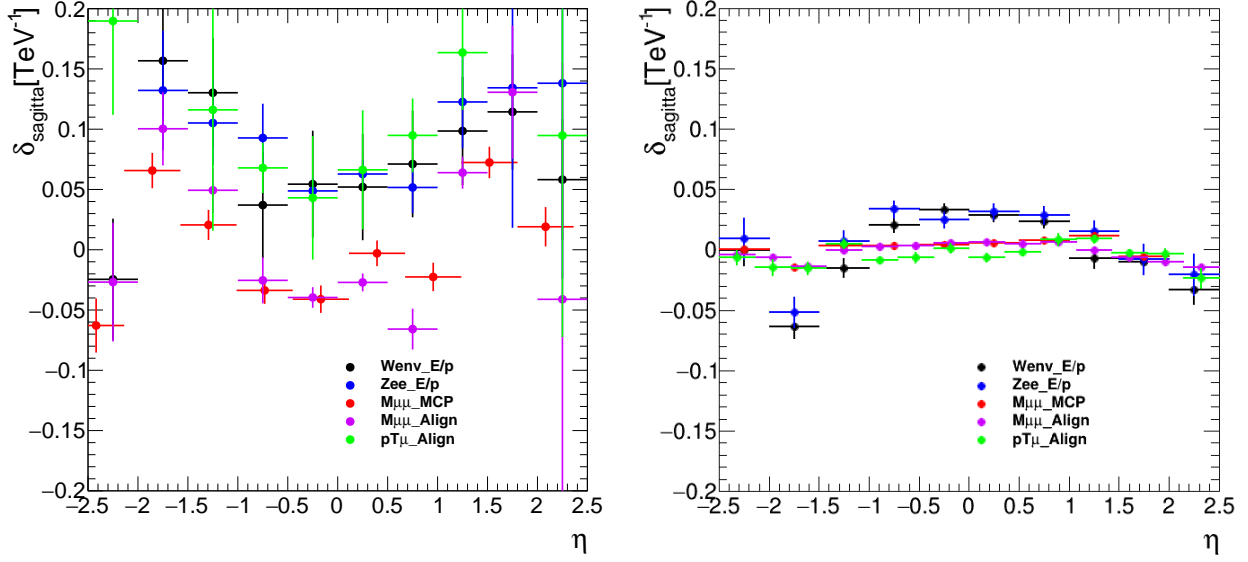


**Figure 720:** Sagitta bias corrections derived for 2017 low-pile-up data (left) and simulation (right) at  $\sqrt{s} = 13$  TeV. The corrections are evaluated with two  $Z$ -mass methods (“ $M\mu\mu$ \_MCP” and “ $M\mu\mu$ \_Align”), the  $E/p$  method applied to  $W \rightarrow e\nu$  (“ $W_{\text{env}}\text{E}/p$ ”) and  $Z \rightarrow ee$  (“ $Z_{\text{ee}}\text{E}/p$ ”) events, and the  $p_T(\mu)$  method, all of which are discussed in the text [10].

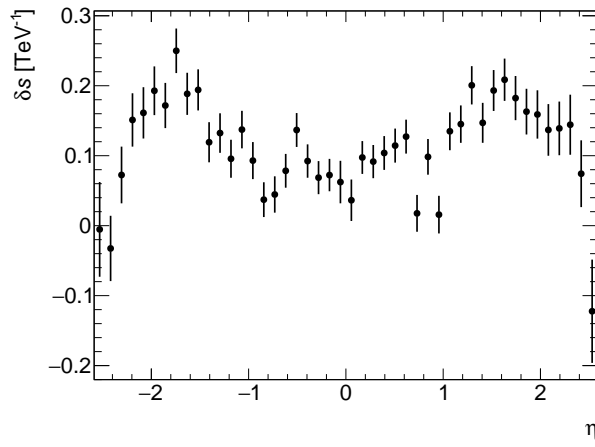


**Figure 721:** Sagitta bias correction based on 2017 low-pile-up data at  $\sqrt{s} = 13$  TeV. The statistical uncertainty (combined from uncertainties of the  $\eta$ -dependent correction and the global offset correction) is represented by error bars [10].

2293 **7.2.3 Muon efficiency measurements**

2294 Just like in the case of electrons, muons have to pass a number of quality criteria in order to be used in  
2295 the analysis:

- 2296 • Reconstruction and identification: the muon is successfully reconstructed and its ID and MS  
2297 tracks as well as EMC deposit are matched. The *medium* identification criterion is adopted for the  
2298 low- $\mu$  analysis. Only CB and ME muons with loose requirements between the tracks from ID and  
2299 MS are used. The value of  $q/p$  significance is required to be  $< 7$ .
- 2300 • Isolation: track isolation requirement of  $p_T^{varcone20}/p_T < 0.1$  was selected as an isolation criterion.
- 2301 • Trigger: the muons were required to pass the *HLT\_mu14* trigger.
- 2302 • Track-to-vertex association (TTVA) includes requirement for the muon track to match the primary  
2303 vertex. The muon objects are required to pass  $|z_0|\sin\theta < 0.5$  mm and  $d_0/\sigma(d_0) < 3$  requirements.

Just like in the case of electrons, possible discrepancies between the data and MC are corrected using the scale factors, which are in turn measured using the tag-and-probe method described in [12]. The product of the scale factors define the event weight:

$$W_{event}^{W \rightarrow e\nu} = SF_{reco/ID} \cdot SF_{trig} \cdot SF_{TTVA} \cdot SF_{iso}.$$

2304 All muon efficiencies and scale factors used in current analysis are measured in-situ using the low- $\mu$   
2305 datasets at 5 and 13 TeV by the MCP group. The results for their measurements are presented in Fig.  
2306 722, 723, 724 and 725.

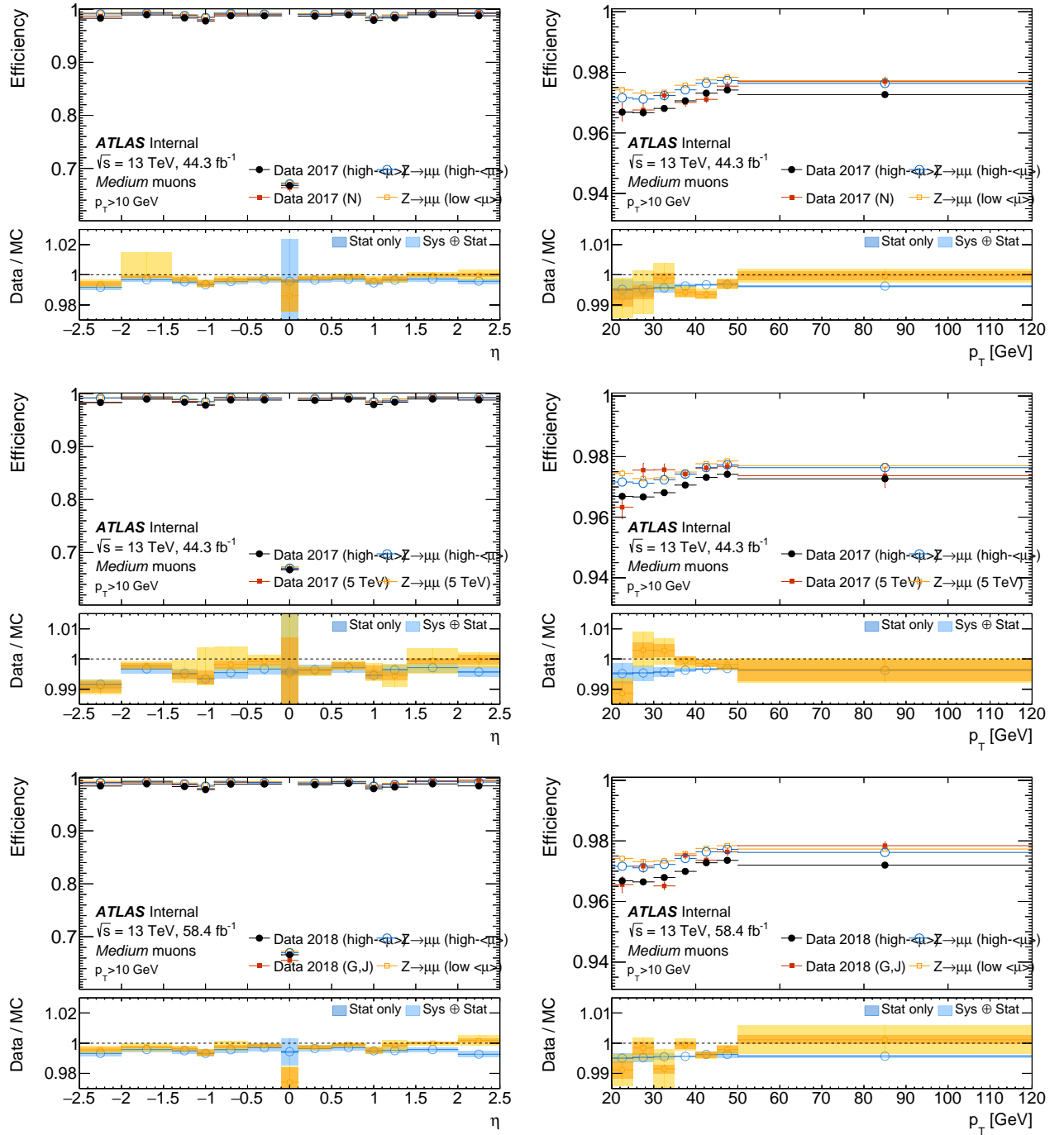


**Figure 722:** Comparison of reconstruction efficiencies for Medium muons using the low- $\mu$  runs of 2017 and 2018 at a centre-of-mass energy of  $\sqrt{s} = 13 \text{ TeV}$  and  $\sqrt{s} = 5 \text{ TeV}$ . Efficiencies are shown as a function of muon  $\eta, p_T$ . Red (orange) points correspond to low- $\mu$  data (MC), while the black (blue) points are high- $\mu$  data (MC). The bottom panels show the data/MC ratio for the low- $\mu$  (orange) and high- $\mu$  (blue) sets with statistical and total uncertainties [10].

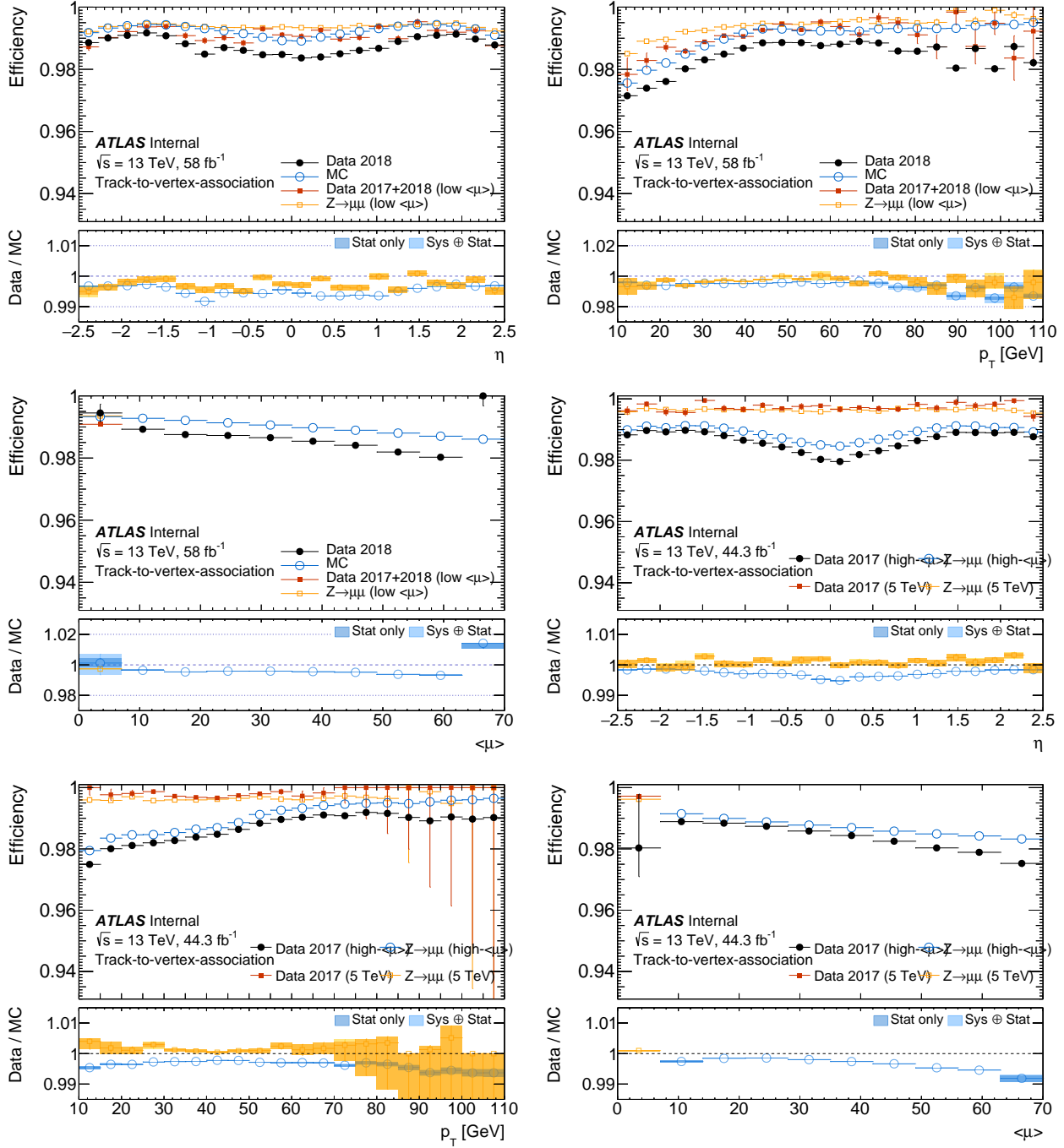


**Figure 723:** Comparison of TTVA efficiencies for Medium muons using the low- $\mu$  runs of 2017+18 at  $\sqrt{s} = 13$  TeV (top row) and low- $\mu$  runs of 2017 at  $\sqrt{s} = 5$  TeV (lower row). The low- $\mu$  results compared to a high- $\mu$  data set as specified in the plot legend. Efficiencies are shown as function of muon  $\eta$  (left) and  $p_T$  (middle) and the mean number of interactions  $\langle \mu \rangle$  (right). Red (orange) points correspond to low- $\mu$  data (MC), while the black (blue) points are high- $\mu$  data (MC). The bottom panels show the data/MC ratio for the low- $\mu$  (orange) and high- $\mu$  (blue) sets with statistical and total uncertainties [10].

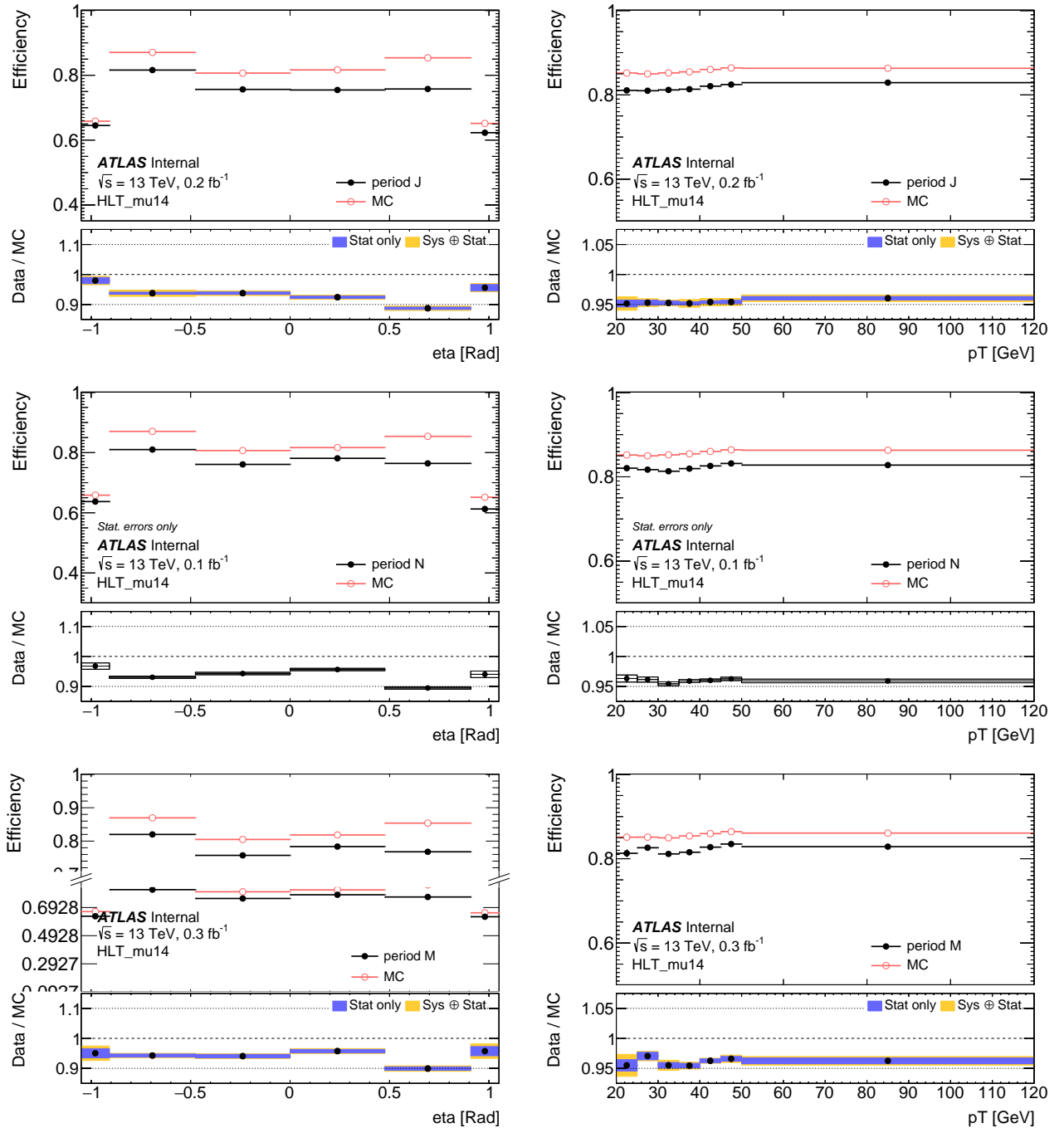


**Figure 724:** 1D trigger efficiency and systematic uncertainty in data and MC, 5 and 13 TeV from 2017 and 2018 for probes from the eta barrel region and inclusive  $\phi$ ,  $p_T$  distributions. Trigger sectors in the barrel and endcap regions are different, only the barrel trigger is shown here. The bin edges correspond to physical edges of the trigger sectors [10].

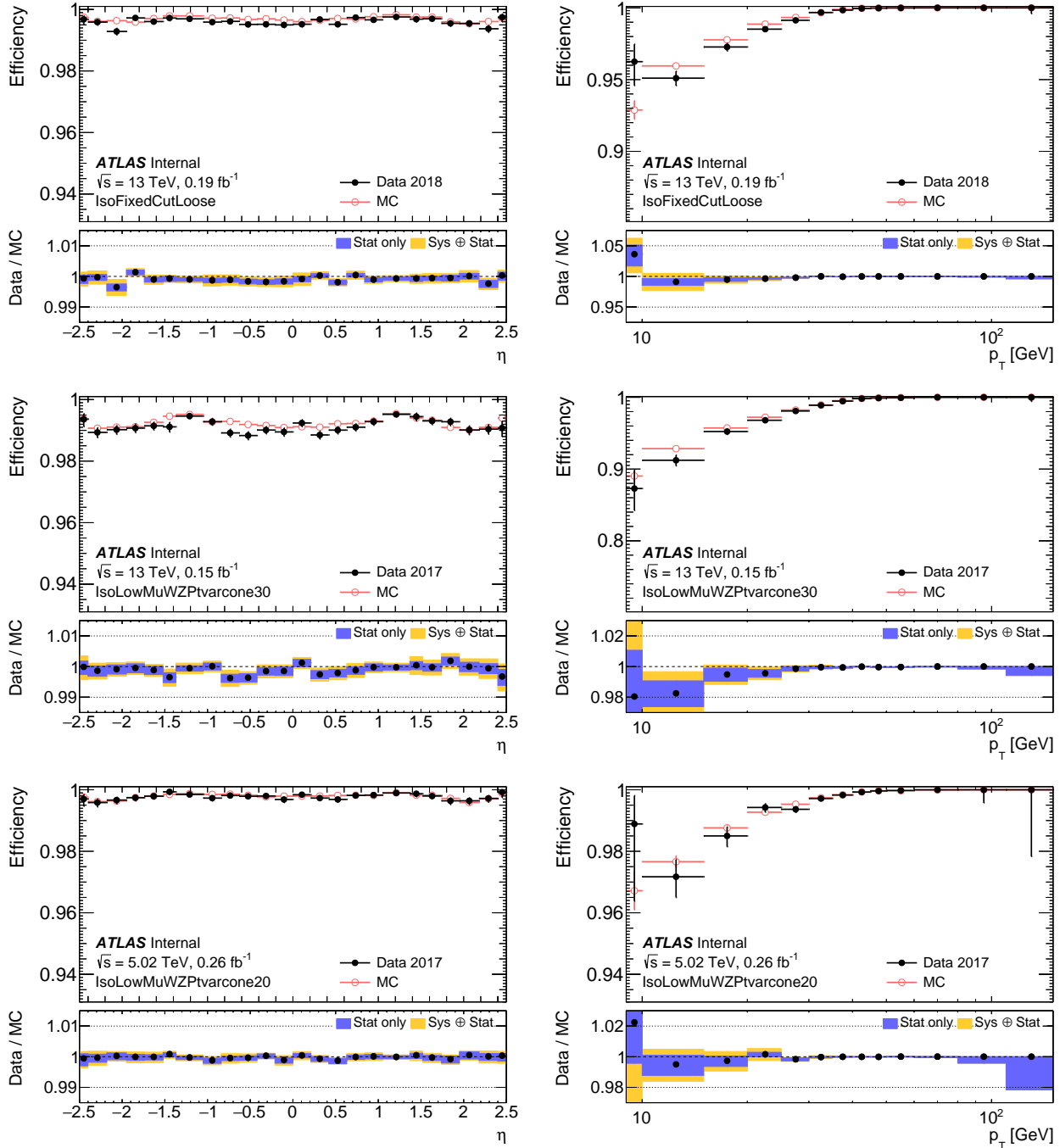


**Figure 725:** Efficiencies for Ptvarcone20 isolation selections measured in 2017 and 2018 data and MC 13 TeV and 5 TeV as a function of muon  $\eta$  (left) and  $p_T$  (right). The bottom panels show the data/MC scale factors with statistical uncertainties represented by blue boxes, while a sum in quadrature of statistical and systematic uncertainties is represented by orange boxes [10].

### 2307 7.3 Hadronic recoil calibration

2308 The study of the W boson kinematics by its leptonic decay products  $W^\pm \rightarrow l^\pm \nu$  is complicated first  
 2309 of all due to the escaping neutrino that carries away substantial information. However, the W boson  
 2310 transverse momentum can still be measured. As it was shown in Chapter 5, the largest part of the W  
 2311 boson  $p_T$  is coming from the initial state radiation. The energy of the created parton shower can be  
 2312 defined as follows:

$$2313 \quad p_T^V = p_T^\ell + p_T^\nu = - \sum_{i=\text{ISR}q,g} \vec{p}_{Ti} = -\vec{u}_T, \quad (7.5)$$

2313 where  $\vec{p}_T^V$ ,  $\vec{p}_T^\ell$  and  $\vec{p}_T^\nu$  are the transverse momenta of the vector boson, lepton and neutrino respectively.  
 2314 The vector sum of all the partons from the ISR is called the *hadronic recoil*:  $\sum_{i=\text{ISR}q,g} \vec{p}_{Ti} = \vec{u}_T$ . Then the  
 2315 missing transverse momentum  $E_T^{\text{miss}}$  of the escaping neutrino can be defined as:

$$2316 \quad E_T^{\text{miss}} = \vec{p}_T^\nu = -(\vec{u}_T + \vec{p}_T^\ell). \quad (7.6)$$

2316 The Hadronic Recoil (HR) reconstruction uses the Particle Flow Objects (PFO), which were defined  
 2317 and described in Section 6.5. It is important to exclude lepton(s) from the HR of a W(Z) event to avoid  
 2318 double counting. A cone of  $\Delta R < 0.2$  is removed around the lepton(s) and is replaced by a same-size  
 2319 cone taken in the same  $\eta$  and  $\phi$  region, but  $\Delta R > 0.4$  away from any lepton in order to obtain the  
 2320 unbiased pile-up and UE estimate. Only the leptons above  $p_T > 10\text{GeV}$  and passing fiducial cuts in  $\eta$   
 2321 and ID requirements are removed from the HR.

2322 Another important quantity for the HR is the  $\sum E_T$  - a scalar sum of the transverse energies of all  
 2323 the PFO. The  $\sum E_T$  represents the total event activity, there is a relation between the  $\sum E_T$  magnitude  
 2324 and  $u_T$  resolution. The underlying event activity, pile-up and soft emissions can be characterized  
 2325 by introducing another quantity:  $\sum \bar{E}_T = \sum E_T - u_T$ , which has the meaning of  $\sum E_T$  with hard activity  
 2326 subtracted.

2327 For the calibration of the HR it is better to introduce quantities that are defined in a natural physical  
 2328 way. The vector boson transverse momentum provides a natural axis which is convenient to use for the  
 2329 2-component decomposition of the  $u_T$  vector. The  $u_T$  component parallel to the vector boson  $p_T$ :

$$2330 \quad u_{||} = \frac{\vec{p}_T^V \cdot \vec{u}_T}{p_T^V}, \quad (7.7)$$

2330 and a perpendicular component:

$$2331 \quad u_{\perp} = \frac{|\vec{p}_T^V \times \vec{u}_T|}{p_T^V}. \quad (7.8)$$

2331 Ideally we would like to have  $u_{||} = p_T^V$  and  $u_{\perp} = 0$ , but due to detector effects it is never the case. The  
 2332 perpendicular component  $u_{\perp}$  can be thought of as the HR resolution, while  $u_{||}$  has a physical meaning  
 2333 of the recoil scale. Another important quantity is called the *bias*:

$$2334 \quad b = u_{||} + p_T^V, \quad (7.9)$$

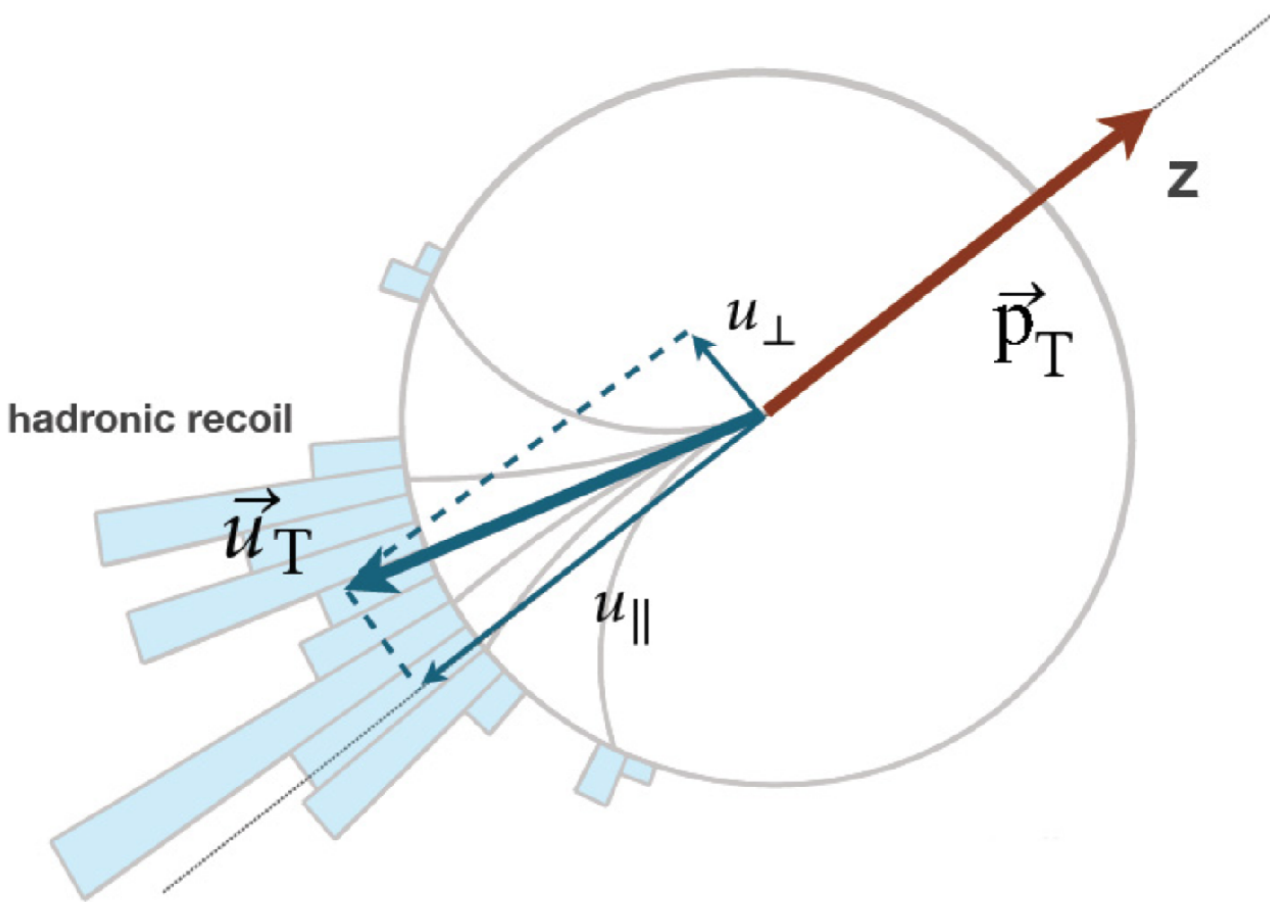


**Figure 726:** The hadronic recoil vector in the transverse plane and its components with respect to vector boson  $p_T$  [13].

which is expected to be centred around zero. In data, of course, we don't know the  $p_T^V$  of the truth boson. However, in Z decay events we can use the dilepton transverse momentum  $p_T^{\ell\ell}$  as an axis for  $u_\perp$  and  $u_\parallel$  decomposition - considering the difference in  $u_T$  resolution between  $p_T^V$  and  $p_T^{\ell\ell}$  is negligible. In W data events it is only possible to use  $p_T^l$  for  $u_T$  decomposition.

### 7.3.1 SET- $u_T$ reweighting

Despite the fact that the two electroweak bosons, W and Z, share lot of similarities, there are also small but notable differences in valence quark content and PDFs, energy scale, etc. This leads to differences in underlying event and  $p_T^V$  spectra, which manifest themselves in the observables like  $\Sigma E_T$  and  $\Sigma \bar{E}_T$ . For the high-precision measurements it is important to ensure that these quantities as well as their correlations are modelled properly. It is also important to match these correlations in data and MC simulations. Figure 727 demonstrates that the baseline PowHEGMC simulations lead to a significant mismodelling of the  $\Sigma \bar{E}_T$ - $p_T^Z$  correlation, while SHERPA shows much better agreement with the data

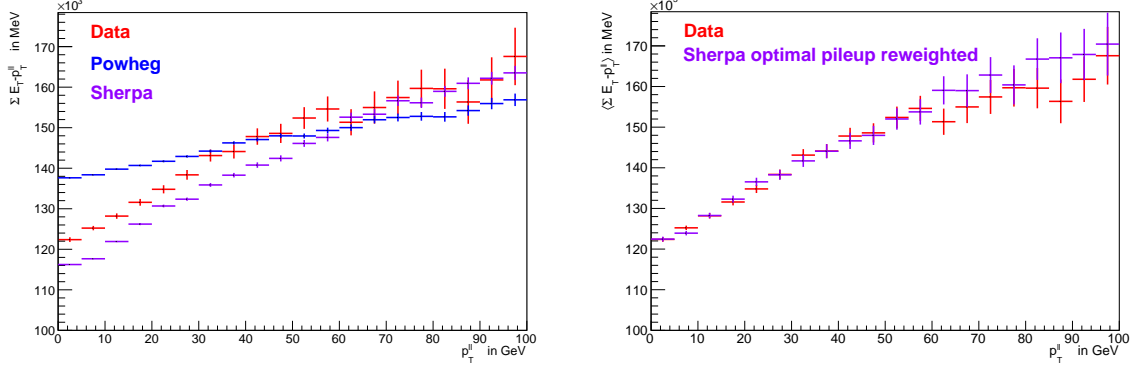


**Figure 727:** Comparison of the  $\Sigma E_T - p_T^{\ell\ell}$  description in data of the two MC samples Powheg and SHERPA at 13 TeV, showing  $\Sigma E_T - p_T^{\ell\ell}$  inclusively (left). Figure on the right shows the comparison of SHERPA to the data after a dedicated pileup reweighting [13].

from the very beginning. After applying a special pile-up reweighting of SHERPA samples a very good agreement with the data is achieved.

In order to obtain proper distributions in the MC samples, a three-step reweighting procedure is implemented.

First weight is obtained by from the 2D  $\Sigma \bar{E}_T - p_T^V$  distributions ratio in Data and MC:

$$w_{2D}^Z(\Sigma \bar{E}_T, p_T^{\ell\ell}) = \frac{h^{\text{data}, Z}(\Sigma \bar{E}_T, p_T^{\ell\ell})}{h^{\text{MC}, Z}(\Sigma \bar{E}_T, p_T^{\ell\ell})}, \quad (7.10)$$

where the following binning is used:

- $p_T^{\ell\ell}$  (13 TeV) =  $[0, 2, 3, 4, 5, 6, 7, 8, 9, 10, 12, 16, 20, 25, 30, 40, 50, 55, 65, 80, 100, 200, \infty]$  GeV
- $p_T^{\ell\ell}$  (5 TeV) =  $[0, 2, 3, 4, 5, 6, 7, 8, 9, 10, 12, 16, 20, 25, 27, 30, 40, 45, 50, 60, 70, 100, 200, \infty]$  GeV
- $\Sigma \bar{E}_T$  (13 TeV) =  $[0, 10, 20, 30, \dots, 380, \infty]$  GeV
- $\Sigma \bar{E}_T$  (5 TeV) =  $[0, 10, 20, 30, \dots, 280, \infty]$  GeV

This reweighting is obtained from the  $Z \rightarrow \mu\mu$  and  $Z \rightarrow ee$  events for 5 and 13 TeV datasets and applied to W Monte-Carlo samples. In W events the  $p_T^V$  is used instead of  $p_T^{\ell\ell}$  for obvious reasons. This reweighting assures very good agreement for the Z events, but perfect agreement is not guaranteed for the W events. For this reason a second reweighting is derived from the data:  $\Sigma \bar{E}_T$  weight is extracted in bins of  $u_T$  of 4 GeV width and applied to W MC events on top of the first 2D reweighting:

$$w_{j, \text{sliced}}^{W^\pm}(\Sigma \bar{E}_T) = \frac{h_j^{\text{data}, W^\pm}(\Sigma \bar{E}_T)}{h_j^{\text{MC}, W^\pm, \text{Z2Dmod}}(\Sigma \bar{E}_T)}, \quad (7.11)$$

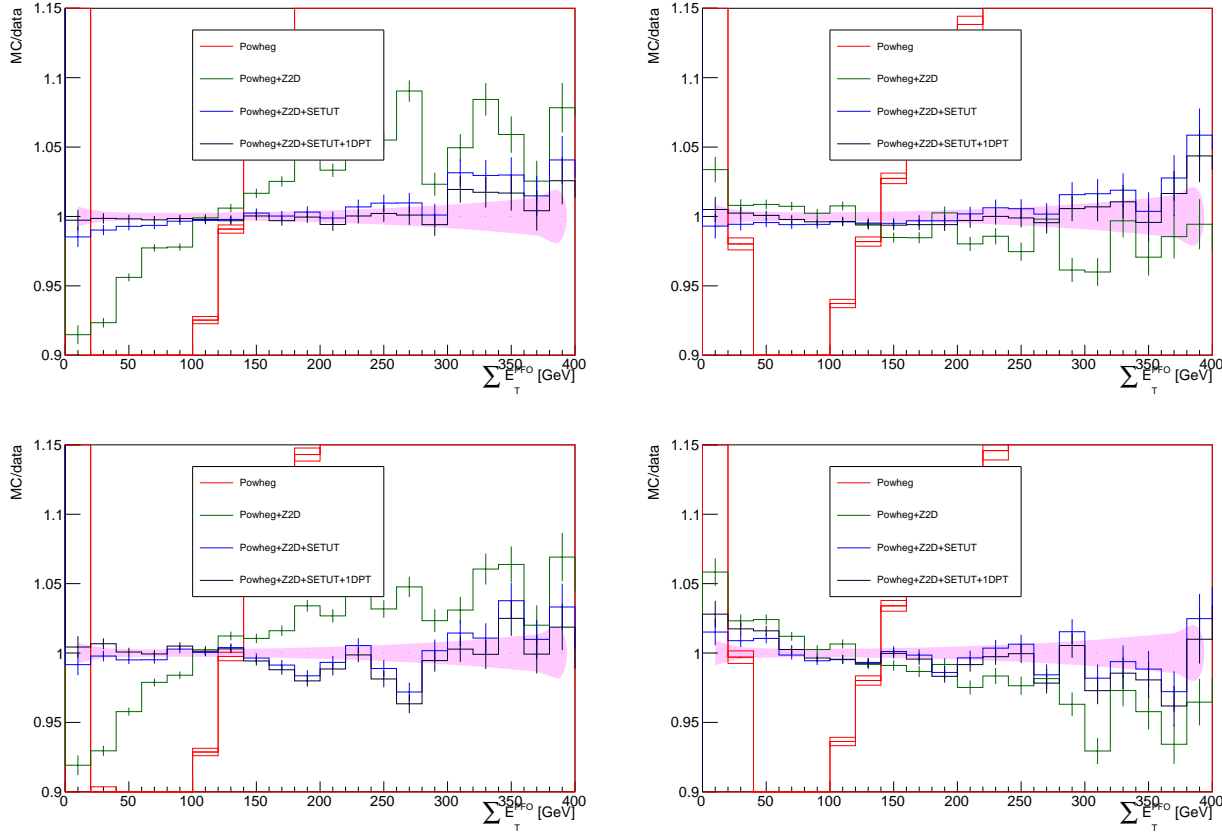


**Figure 728:** Ratio of data to predictions in  $W \rightarrow \mu\nu$  events at 13 TeV for the  $\Sigma\bar{E}_T$  distribution, before and after each  $\Sigma\bar{E}_T$  modeling reweighting step. The color band is the data statistical uncertainty. The prediction uncertainty only includes the statistical uncertainty. 'Powheg' uses the baseline MC for the signal. 'Powheg+Z2D' has the 2D ( $\Sigma\bar{E}_T$ ,  $p_T^{true,V}$ ), Z-based reweighting applied. 'Powheg+Z2D+SETUT' adds the  $\Sigma\bar{E}_T$  reweighting in bins of  $u_T$ . 'Powheg+Z2D+SETUT+1DPT' adds the 1D reweighting to recover the initial  $p_T^{true,V}$  spectrum [13].

where  $h_j$  stands for the normalized  $\Sigma\bar{E}_T$  distribution in the  $u_T$  bin number  $j$  after the standard selection. This reweighting improves the  $\Sigma\bar{E}_T$  modelling, but distorts the  $p_T^V$  spectrum. This motivates the third correction reweighting with the following weight:

$$w_{1D}^{W^\pm}(p_T^{true,V}) = \frac{h^{MC,W^\pm,\text{mod}}(p_T^{true,V})}{h^{MC,W^\pm,\text{orig}}(p_T^{true,V})}. \quad (7.12)$$

The  $h^{MC,W^\pm,\text{orig}}(p_T^{true,V})$  stands for the original  $p_T^{true,V}$  spectrum before any reweightings were applied. The total weight applied to an event is the product of the three weights described above:  $w_{2D}^Z(\Sigma\bar{E}_T, p_T^{true,V}) \times w_{j,\text{sliced}}^{W^\pm}(\Sigma\bar{E}_T) \times w_{1D}^{W^\pm}(p_T^{true,V})$ . The results on the reweighting are shown in Fig. 728 and 729 for 13 and 5 TeV respectively.

2368

2369 The closure of the procedure is checked with SHERPA MC simulation used as pseudo-data, as we

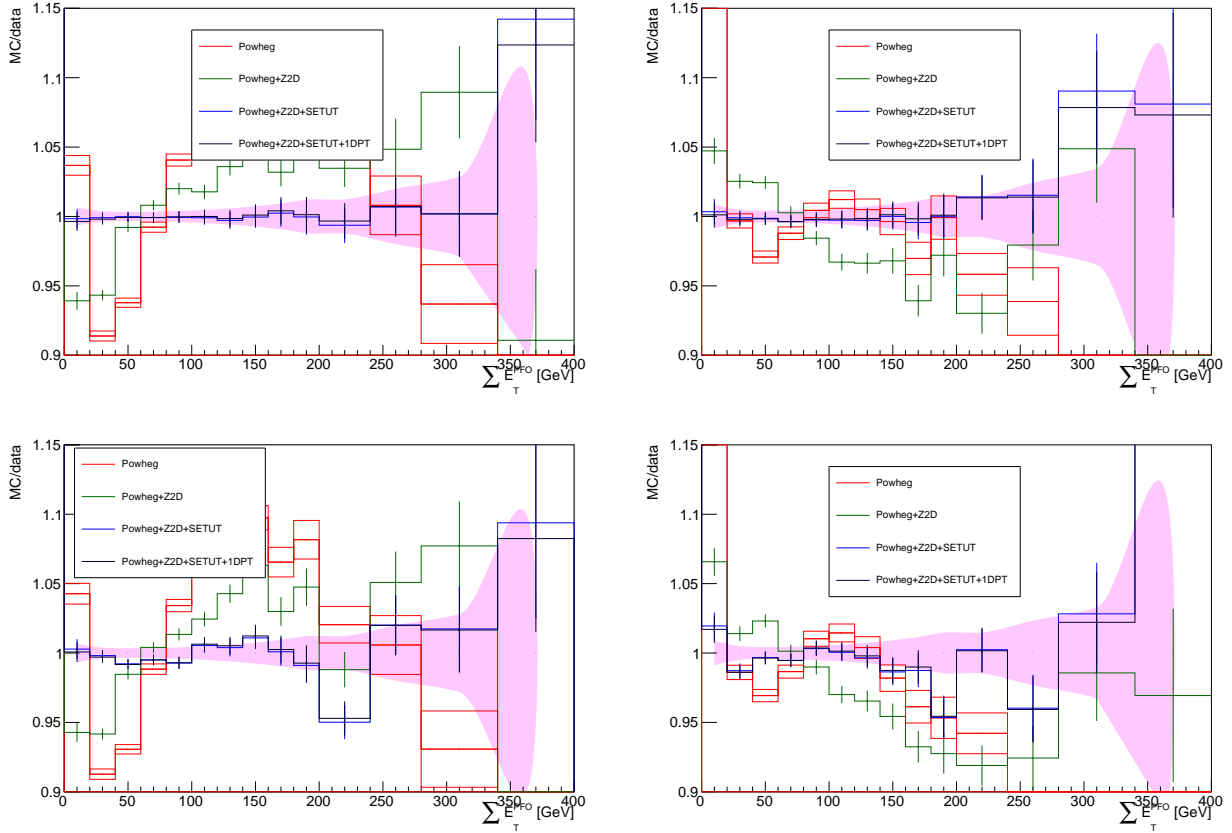


**Figure 729:** Ratio of data to predictions in  $W \rightarrow \mu\nu$  events at 5 TeV for the  $\Sigma\bar{E}_T$  distribution, before and after each  $\Sigma\bar{E}_T$  modeling reweighting step. The color band is the data statistical uncertainty. The prediction uncertainty only includes the statistical uncertainty. 'Powheg' uses the baseline MC for the signal. 'Powheg+Z2D' has the 2D ( $\Sigma\bar{E}_T, p_T^{true,V}$ ), Z-based reweighting applied. 'Powheg+Z2D+SETUT' adds the  $\Sigma\bar{E}_T$  reweighting in bins of  $u_T$ . 'Powheg+Z2D+SETUT+1DPT' adds the 1D reweighting to recover the initial  $p_T^{true,V}$  spectrum [13].

2370 don't have the  $p_T^V$  distribution from the data. The residual non-closure of less than 1% is treated as a  
 2371 systematic uncertainty.

### 2372 7.3.2 $u_X$ and $u_Y$ correction

2373 The azimuthal angle distribution of the recoil is another source of discrepancy between the MC  
 2374 simulation and the data. While the simulated events have a flat  $u_\phi$  distribution, the data events  
 2375 show a non-uniform distribution which is probably caused by detector imperfections or ageing. The  
 2376 correction is performed by introducing additive corrections to the  $u_X$  and  $u_Y$  components of the HR.  
 2377 The corrections are derived as a mean difference between the data and MC as a function of  $\Sigma\bar{E}_T$  in Z

2378 events:

$$\begin{aligned} u_X^{\text{MC,corr}} &= u_X^{\text{MC}} + [(\langle u_X^{\text{data}} \rangle - \langle u_X^{\text{MC}} \rangle)(\Sigma \bar{E}_T)] \\ u_Y^{\text{MC,corr}} &= u_Y^{\text{MC}} + [(\langle u_Y^{\text{data}} \rangle - \langle u_Y^{\text{MC}} \rangle)(\Sigma \bar{E}_T)] \end{aligned} \quad (7.13)$$

2379 The dependence of the mean differences  $\langle u_X^{\text{data}} \rangle - \langle u_X^{\text{MC}} \rangle$  and  $\langle u_Y^{\text{data}} \rangle - \langle u_Y^{\text{MC}} \rangle$  on  $\Sigma \bar{E}_T$  is fitted with a  
 2380 linear function. The corrected  $\phi$  distributions are shown in Fig. 730. It was shown that the correlation  
 2381 between the correction and the magnitude of the recoil is weak and the effect of the correction on  
 2382 the measured W spectrum is of per mille level. For this reason no uncertainty was assigned to this  
 2383 correction.

2384 **7.3.3 Resolution and response corrections**

2385 The correction function for  $\sigma(u_{\perp})(\Sigma \bar{E}_T, p_T^{\ell\ell})$  is constructed in bins of  $p_T^{\ell\ell}$  in the following way:

$$r(\Sigma \bar{E}_T, p_T^{\ell\ell}) = \frac{\sigma(u_{\perp})^{\text{data}}}{\sigma(u_{\perp})^{\text{MC}}}, \quad (7.14)$$

2386 where both  $\sigma(u_{\perp})$  functions are obtained as a linear fit to  $\sqrt{\Sigma \bar{E}_T}$ :

$$\sigma(u_{\perp})(\Sigma \bar{E}_T) = c + d \cdot \sqrt{\Sigma \bar{E}_T}. \quad (7.15)$$

2387 with the following  $p_T^{\ell\ell}$  binning:

2388 • 5 TeV:  $p_T^{\ell\ell} = [0, 3, 4, 6, 7, 9, 11, 13, 16, 20, 26, 40, \infty] \text{ GeV}$

2389 • 13 TeV is  $p_T^{\ell\ell} = [0, 3, 4, 6, 7, 9, 10, 12, 14, 17, 21, 26, 33, 49, \infty] \text{ GeV}$

2390 Then the correction for the W boson events is performed using the ratio function as a factor:

$$u_{\perp}^{\text{MC,corr}} = u_{\perp}^{\text{MC}} \times r(\Sigma \bar{E}_T, p_T^{\text{true}, V}). \quad (7.16)$$

2391 The correction of the parallel component  $u_{\parallel}$  is done as follows:

$$u_{\parallel}^{\text{MC,corr}} = \langle u_{\parallel}^{\text{data}} \rangle + (\langle b^{\text{data}} \rangle - \langle b^{\text{MC}} \rangle) \cdot r_{\parallel} + (u_{\parallel}^{\text{MC}} - \langle u_{\parallel}^{\text{data}} \rangle) \cdot r_{\parallel}. \quad (7.17)$$

2392 Here the resolution correction factor  $r_{\parallel}$  is in equation 7.14, but reads as  $\sigma(u_{\parallel})^{\text{data}} / \sigma(u_{\perp})^{\text{MC}}$ .

2393 The average  $\langle u_{\parallel}^{\text{data}} \rangle$  assumes averaging over all data events in bins of  $p_T^{\ell\ell}$  and  $\Sigma \bar{E}_T$ . The  $\Sigma \bar{E}_T$  bins are  
 2394 10 GeV wide for 5 TeV and 20 GeV wide for 13 TeV. Then in each  $\Sigma \bar{E}_T$  bin the  $p_T^{\ell\ell}$  dependence is fitted  
 2395 with a linear function:

$$\langle u_{\parallel}^{\text{data}} \rangle(p_T^{\ell\ell}) = e + f \cdot p_T^{\ell\ell}. \quad (7.18)$$

2396 Similarly the difference of the biases  $(\langle b^{\text{data}} \rangle - \langle b^{\text{MC}} \rangle)$  is computed in the same bins of  $p_T^{\ell\ell}$  and  $\Sigma \bar{E}_T$  and  
 2397 fitted in each  $\Sigma \bar{E}_T$  bin with a linear function of  $p_T^{\ell\ell}$ .

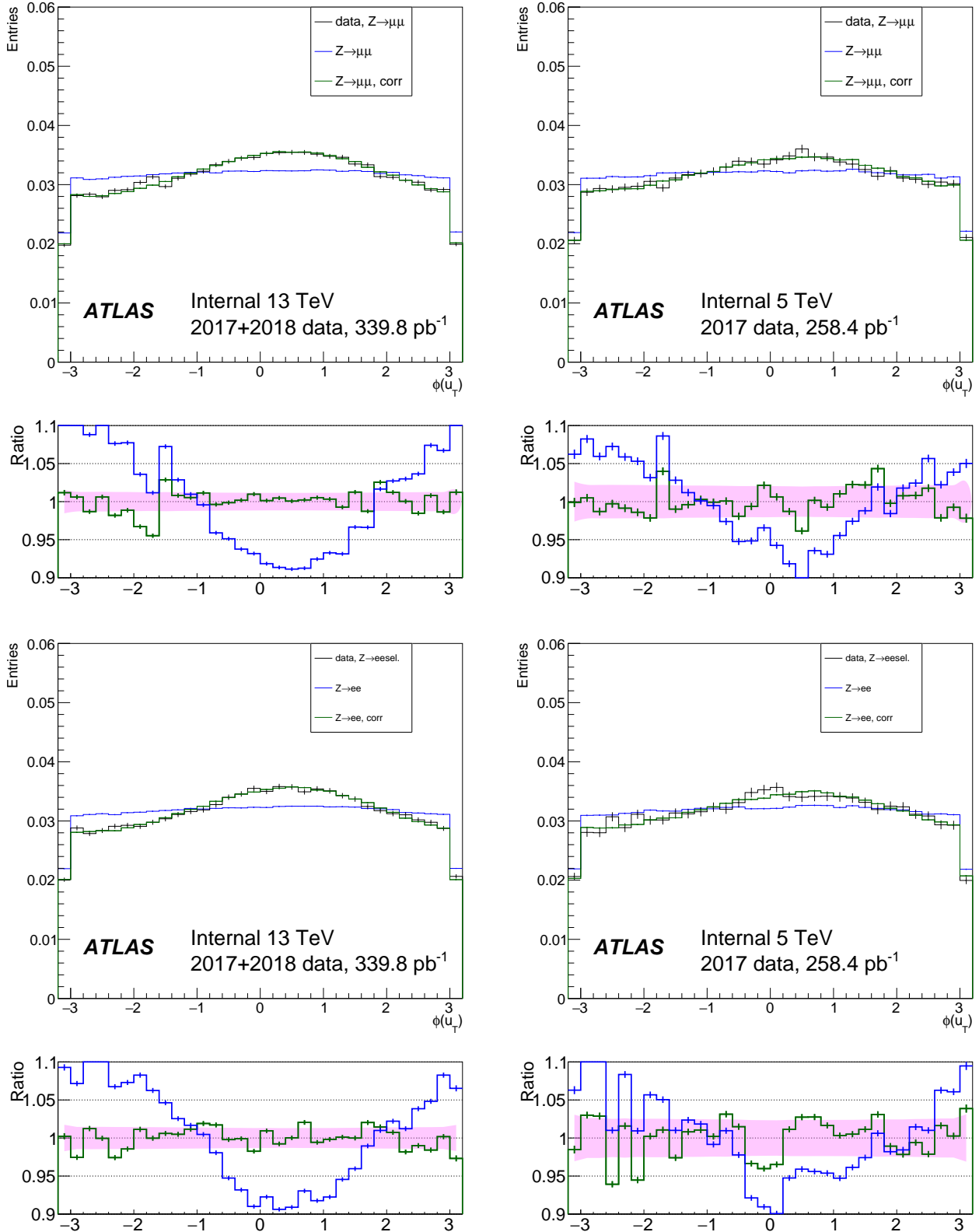


**Figure 730:**  $\phi(u_T)$  at 5 and 13 TeV, for the data and the simulation before and after  $u_X$  and  $u_Y$  correction, in  $Z$  events. The band in the ratio panel is the data statistical uncertainty [13].

2398 **7.3.4 Hadronic recoil calibration uncertainties**

2399 The uncertainties associated with hadronic recoil calibration are mainly of statistical nature for resolu-  
2400 tion and response corrections. The uncertainty of the SET- $u_T$  correction comes from the non-closure of  
2401 Z to W extrapolation mentioned in the dedicated section.

## 2402 7.4 Angular coefficients correction

2403 The fully differential cross-section of the fully leptonic Drell-Yan process can be factorized in the  
 2404 following way [14]:

$$\frac{d\sigma}{dp_1 dp_2} = \left[ \frac{d\sigma(m)}{dm} \right] \left[ \frac{d\sigma(y)}{dy} \right] \left[ \frac{d\sigma(p_T, y)}{dp_T dy} \left( \frac{d\sigma}{dy} \right)^{-1} \right] \left[ (1 + \cos^2 \theta + \sum_{i=0}^7 A_i(p_T, y) P_i(\cos \theta, \phi)) \right], \quad (7.19)$$

2405 where  $p_1$  and  $p_2$  are the 4-momenta of the two leptonic decay products;  $m$ ,  $p_T$  and  $y$  are the dilepton  
 2406 system invariant mass, transverse momentum and rapidity respectively;  $\theta$  is the polar and  $\phi$  is azimuthal  
 2407 coordinates of the lepton ( $e^-$  in  $W^- \rightarrow e^- \nu$  or  $\nu$  in  $W^+ \rightarrow e^+ \nu$ ). The angular dependence is decomposed  
 2408 in seven spherical harmonics  $P_i$  with numerical coefficients  $A_i$ . The numerical coefficients  $A_i$  are in  
 2409 general case are a function of  $p_T$ ,  $y$  and  $m$ , but the mass dependence may be neglected [15]. The  $A_i$   
 2410 coefficients were derived to the NNLO precision using the DYNNLO program for fixed-order cross-  
 2411 section calculations [16].

2412 The default MC samples generated by PowHEG+PYTHIA8 were reweighted at the event level in order to  
 2413 introduce the corrections:

$$w(\cos \theta, \phi, p_T, y) = \frac{1 + \cos^2 \theta + \sum_i A'_i(p_T, y) P_i(\cos \theta, \phi)}{1 + \cos^2 \theta + \sum_i A_i(p_T, y) P_i(\cos \theta, \phi)}, \quad (7.20)$$

2414 where  $A_i(p_T, y)$  are the angular coefficients, predicted by the PowHEG+PYTHIA8 simulation and  $A'_i(p_T, y)$   
 2415 are the NNLO coefficients evaluated at  $O(\alpha^2)$  precision.

2416 **Bibliography**

- 2417 [1] Jan Kretzschmar. *Samples and Physics modelling for low pile-up runs taken in 2017 and 2018.*  
2418 Tech. rep. ATL-COM-PHYS-2019-075. Geneva: CERN, Feb. 2019. URL: <https://cds.cern.ch/record/2657141>.
- 2420 [2] Morad Aaboud et al. “Electron and photon energy calibration with the ATLAS detector using  
2421 2015–2016 LHC proton-proton collision data”. In: *JINST* 14.03 (2019), P03017. doi: 10.1088/  
2422 1748-0221/14/03/P03017. arXiv: 1812.03848 [hep-ex].
- 2423 [3] “Electron and photon performance measurements with the ATLAS detector using the 2015-2017  
2424 LHC proton-proton collision data”. In: *JINST* 14. arXiv:1908.00005. 12 (Aug. 2019). 31 figures,  
2425 3 tables. All figures including auxiliary figures are available at <https://atlas.web.cern.ch/Atlas/GROUPS/PHYSICS/PAPERS/EGAM-2018-01>, P12006. 70 p. doi: 10.1088/1748-0221/14/  
2426 12/P12006. URL: <https://cds.cern.ch/record/2684552>.
- 2428 [4] ATLAS Collaboration. “Electron and photon energy calibration with the ATLAS detector using  
2429 LHC Run 1 data”. In: *Eur. Phys. J. C* 74 (2014), p. 3071. doi: 10.1140/epjc/s10052-014-3071-4.  
2430 arXiv: 1407.5063 [hep-ex].
- 2431 [5] Tairan Xu, Hicham Atmani, and Ludovica Aperio Bella. *Electron corrections for low pile-up runs  
2432 taken in 2017 and 2018.* Tech. rep. ATL-COM-PHYS-2019-077. Geneva: CERN, Feb. 2019. URL:  
2433 <https://cds.cern.ch/record/2657152>.
- 2434 [6] Nansi Andari et al. *Electron and photon energy calibration with the ATLAS detector using 2015-2017  
2435 LHC proton-proton collision data.* Tech. rep. ATL-COM-PHYS-2018-1720. Geneva: CERN, 2018.  
2436 URL: <https://cds.cern.ch/record/2651890>.
- 2437 [7] Morad Aaboud et al. “Electron reconstruction and identification in the ATLAS experiment using  
2438 the 2015 and 2016 LHC proton-proton collision data at  $\sqrt{s} = 13$  TeV”. In: *Eur. Phys. J. C* 79.8  
2439 (2019), p. 639. doi: 10.1140/epjc/s10052-019-7140-6. arXiv: 1902.04655 [physics.ins-  
2440 det].
- 2441 [8] Georges Aad et al. “Electron and photon performance measurements with the ATLAS detector  
2442 using the 2015–2017 LHC proton-proton collision data”. In: *JINST* 14.12 (2019), P12006. doi:  
2443 10.1088/1748-0221/14/12/P12006. arXiv: 1908.00005 [hep-ex].
- 2444 [9] Georges Aad et al. “Muon reconstruction performance of the ATLAS detector in proton–proton  
2445 collision data at  $\sqrt{s} = 13$  TeV”. In: *Eur. Phys. J. C* 76.5 (2016), p. 292. doi: 10.1140/epjc/s10052-  
2446 016-4120-y. arXiv: 1603.05598 [hep-ex].
- 2447 [10] Alexander Sydorenko, Jakub Andrzej Kremer, and Tairan Xu. *Muon corrections for low pile-up  
2448 runs taken in 2017 and 2018.* Tech. rep. ATL-COM-PHYS-2019-072. Geneva: CERN, Feb. 2019.  
2449 URL: <https://cds.cern.ch/record/2657116>.
- 2450 [11] *Study of alignment-related systematic effects on the ATLAS Inner Detector tracking.* Tech. rep. ATLAS-  
2451 CONF-2012-141. Geneva: CERN, Oct. 2012. URL: <https://cds.cern.ch/record/1483518>.

- 2452 [12] Nicolas Maximilian Koehler et al. *Muon Efficiency Measurements on the Full Run 2 dataset*. Tech.  
2453 rep. ATL-COM-PHYS-2019-176. Geneva: CERN, Mar. 2019. URL: <https://cds.cern.ch/record/2665704>.
- 2455 [13] Mengran Li et al. *Hadronic recoil reconstruction and calibration for low pile-up runs taken in*  
2456 *2017 and 2018*. Tech. rep. ATL-COM-PHYS-2019-078. Geneva: CERN, Feb. 2019. URL: <https://cds.cern.ch/record/2657182>.
- 2458 [14] Sidney D. Drell and Tung-Mow Yan. “Massive Lepton-Pair Production in Hadron-Hadron Col-  
2459 lisions at High Energies”. In: *Phys. Rev. Lett.* 25 (5 Aug. 1970), pp. 316–320. doi: 10.1103/  
2460 PhysRevLett.25.316. URL: <https://link.aps.org/doi/10.1103/PhysRevLett.25.316>.
- 2461 [15] E. Mirkes. “Angular decay distribution of leptons from W-bosons at NLO in hadronic collisions”.  
2462 In: *Nuclear Physics B* 387.1 (1992), pp. 3–85. ISSN: 0550-3213. doi: [https://doi.org/10.1016/0550-3213\(92\)90046-E](https://doi.org/10.1016/0550-3213(92)90046-E). URL: <http://www.sciencedirect.com/science/article/pii/055032139290046E>.
- 2465 [16] Stefano Catani et al. “Vector Boson Production at Hadron Colliders: A Fully Exclusive QCD  
2466 Calculation at Next-to-Next-to-Leading Order”. In: *Phys. Rev. Lett.* 103 (8 Aug. 2009), p. 082001.  
2467 doi: 10.1103/PhysRevLett.103.082001. URL: <https://link.aps.org/doi/10.1103/PhysRevLett.103.082001>.



# 8

## MC samples and selection

2469

2470

### 2471 8.1 Data and MC samples

#### 2472 8.1.1 Data samples

2473 The data and MC samples for this study were collected under special beam conditions that ensure low  
2474 pile-up. The data samples were collected in three runs:

- 2475 •  $\sqrt{s} = 5.02\text{TeV}$  data taken in November 2017, ATLAS data period M, preliminary calibrated  
2476 luminosity  $256.827\text{pb}^{-1}$  with an uncertainty of  $\pm 1.6\%$
- 2477 •  $\sqrt{s} = 13\text{TeV}$  data taken in November 2017, ATLAS data period N, preliminary online luminosity  
2478  $146.6\text{pb}^{-1}$
- 2479 •  $\sqrt{s} = 13\text{TeV}$  data taken in June 2018, ATLAS data period G4+J, preliminary online luminosity  
2480  $193.2\text{pb}^{-1}$

2481 The luminosity calibration for the 13 TeV runs is not available yet, the corresponding uncertainty is  
2482 not known, but is expected to be around 3%. The runs of November 2017 and the run of June 2018 had  
2483 the same bunch spacing of 25 ns, but a different filling scheme. The two main differences from the  
2484 high- $\mu$  data collection are the following:

- 2485 • In order to optimize topo-cluster response for the HR lower topo-cluster thresholds were used.
- 2486 • Single  $e$  and  $\mu$  triggers with significantly lower thresholds and looser identification criteria are  
2487 run without prescale, most notably `HLT_e15_1hloose_nod0_L1EM12` and `HLT_mu14`.

2488 At the beginning of 5 TeV fills the pile-up reached  $\mu \sim 5$ , slowly descending to  $\mu \sim 1$  by the end of  
2489 the run. In the case of 13 TeV the luminosity was levelled at  $\mu = 2$  in the course of the run. The  
2490 corresponding distributions for  $\mu$  and  $N_{PV}$  for the 5 TeV and 13 TeV runs are shown in Fig. 81 and Fig.  
2491 82.

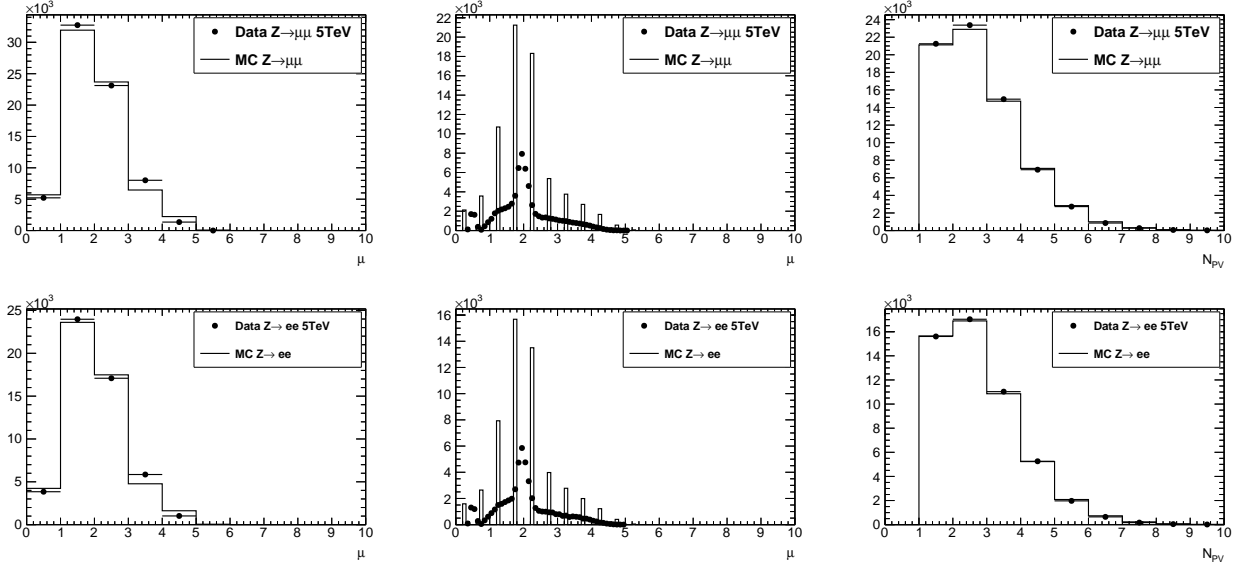


**Figure 81:** Distributions for the 5 TeV low- $\mu$  dataset in a  $Z/\gamma^* \rightarrow \mu\mu$  (top row) and a  $Z/\gamma^* \rightarrow ee$  (bottom row) selection. The data (points) is compared to  $Z/\gamma^* \rightarrow \mu\mu$  or  $Z/\gamma^* \rightarrow ee$  signal MC, respectively. The left and middle plots show the actual  $\mu$  in a coarsely-binned and a finely-binned version. The right plot shows the number of reconstructed primary vertices  $N_{PV}$  [1].

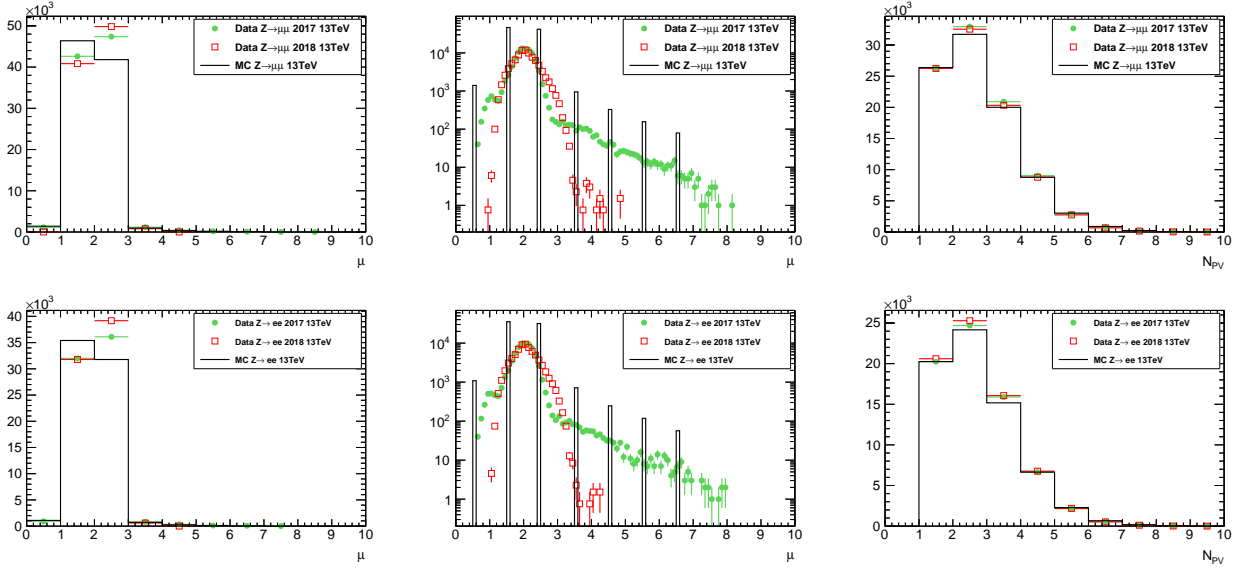


**Figure 82:** Distributions for the 13 TeV low- $\mu$  datasets taken in 2017 and 2018 in a  $Z/\gamma^* \rightarrow \mu\mu$  (top row) and a  $Z/\gamma^* \rightarrow ee$  (bottom row) selection. The data (points) is compared to  $Z/\gamma^* \rightarrow \mu\mu$  or  $Z/\gamma^* \rightarrow ee$  signal MC, respectively. All distributions are (roughly) normalised to the same number of selected events in the 2017 dataset. The left and middle plots show the actual  $\mu$  in a coarsely-binned and a finely-binned version. The right plot shows the number of reconstructed primary vertices  $N_{PV}$  [1].

**2492 8.1.2 MC samples and cross-sections**

2493 Signal and background processes (except for the multijet background) are modelled using fully  
2494 simulated and reconstructed MC samples, specifically tuned for the special run conditions, namely the  
2495 low pileup, lower topo-cluster noise thresholds and adapted trigger menu. No pileup reweighting is  
2496 performed.

2497 The information on the simulated samples and their properties is given in Tables 81, 82, 83, 84 [2]. The  
2498 predicted event counts are normalized to the data luminosity using the cross-sections quoted in the  
2499 table.

2500 The primary signal event samples for W and Z production are obtained using PowHEG [3, 4, 5, 6] event  
2501 generator with CT10 PDF, linked with Pythia8 [7] with AZNLO tune [8]. PowHEG+Pythia8samples are  
2502 interfaced to Photos++ [9] for final state QED effects simulation.

2503 A set of alternative samples at  $\sqrt{s} = 13\text{TeV}$  was prepared with SHERPA2.2.2 [10] using the NNPDF3.0  
2504 PDFs and merging V + 0, 1, 2 at NLO accuracy with V + 3, 4 at LO accuracy with the MEPS@NLO scheme.  
2505 A similar set for  $\sqrt{s} = 5\text{TeV}$  was prepared with SHERPA2.2.5 with a setup similar to 13 TeV samples.

2506 Pileup is modelled by overlaying simulated soft events over the original hard-scattering event. These  
2507 soft events were modelled using Pythia8 with NNPDF2.3LO set of PDFs [11] and the A3 tune [12].

2508 The W and Z processes samples are normalized to NNLO calculations for the cross-sections performed  
2509 using DYTURBO, an optimised version of DYNNLO [13, 14] using the MMHT2014nnlo PDF set [15].  
2510 Corresponding numerical values were taken from the corresponding ATLAS publications of the 2015  
2511 data at 13 TeV [16] and 5.02 TeV [17] and are presented in Table 81 for 13 TeV and Table 84 for 5  
2512 TeV. The uncertainties on those cross-sections arise from the choice of PDF set, from factorization and  
2513 renormalisation scale dependence, and the strong coupling constant  $\alpha_s$  uncertainty resulting in the  
2514 total uncertainty estimate of about 5%.

2515 Backgrounds from top-quark pair-production  $t\bar{t}$  and single-top production ( $Wt$ , t-channel, s-  
2516 channel) were generated with PowHEG+Pythia8. The 5 TeV  $t\bar{t}$  cross section is taken as the Top++ [18]  
2517 prediction reported in CMS publication [19]. Di-boson combinations  $VV$ ,  $V = W, Z$  are generated with  
2518 SHERPA in all decay channels with a requirement of having at least one real lepton in the final state.

Process	Data set	Generator	$\sigma \cdot \text{BR} \cdot \epsilon_{\text{filter}}$ [nb] (th. unc.)	$N_{\text{evt}}^{\text{skim}} [10^6]$	$N_{\text{evt}}^{\text{unskim}} [10^6]$
$W^+ \rightarrow e^+ \nu$	361100	POWHEG+PYTHIA8	11.61 (5%)	40	40
$W^+ \rightarrow \mu^+ \nu$	361101	POWHEG+PYTHIA8	11.61 (5%)	40	40
$W^+ \rightarrow \tau^+ \nu$	361102	POWHEG+PYTHIA8	11.61 (5%)	0.28	5.0
$W^- \rightarrow e^- \bar{\nu}$	361103	POWHEG+PYTHIA8	8.630 (5%)	30	30
$W^- \rightarrow \mu^- \bar{\nu}$	361104	POWHEG+PYTHIA8	8.630 (5%)	29	29
$W^- \rightarrow \tau^- \bar{\nu}$	361105	POWHEG+PYTHIA8	8.630 (5%)	0.24	4.0
$Z \rightarrow ee$	361106	POWHEG+PYTHIA8	$1.910 \times 1.03$ (5%)	10	10
$Z \rightarrow \mu\mu$	361107	POWHEG+PYTHIA8	$1.910 \times 1.025$ (5%)	10	10
$Z \rightarrow \tau\tau$	361108	POWHEG+PYTHIA8	$1.910 \times 1.025$ (5%)	0.12	1.0
$ZZ(q\bar{q}\ell\ell)$	363356	SHERPA 2.2.1	$0.01556 \times 0.141$ (10%)	0.0064	0.010
$WZ(q\bar{q}\ell\ell)$	363358	SHERPA 2.2.1	0.003433 (10%)	0.0063	0.010
$WW(q\bar{q}\ell\nu)$	363359	SHERPA 2.2.1	0.02472 (10%)	0.0093	0.020
$WW(\ell\nu q\bar{q})$	363360	SHERPA 2.2.1	0.02472 (10%)	0.0093	0.020
$WZ(\ell\nu q\bar{q})$	363489	SHERPA 2.2.1	0.01142 (10%)	0.0047	0.010
$ZZ(4\ell)$	364250	SHERPA 2.2.2	0.001252 (10%)	0.0057	0.010
$WZ(3\ell\nu)$	364253	SHERPA 2.2.2	0.004583 (10%)	0.0062	0.010
$WW(2\ell 2\nu)$	364254	SHERPA 2.2.2	0.01250 (10%)	0.0073	0.010
$WZ(\ell 3\nu)$	364255	SHERPA 2.2.2	0.003235 (10%)	0.0050	0.010
$Wt$	410013	POWHEG+PYTHIA8	0.03582 (10%)	0.0037	0.010
$W\bar{t}$	410014	POWHEG+PYTHIA8	0.03399 (10%)	0.0037	0.010
$t\bar{t}$ (nominal)	410470	POWHEG+PYTHIA8	$0.8318 \times 0.544$ (7%)	1.2	2.0
$t(t-\text{chan.}t)$	410642	POWHEG+PYTHIA8	0.03699 (10%)	0.016	0.030
$t(t-\text{chan.}\bar{t})$	410643	POWHEG+PYTHIA8	0.02217 (10%)	0.011	0.020
$t(s-\text{chan.}t)$	410644	POWHEG+PYTHIA8	0.002027 (10%)	0.0050	0.010
$t(s-\text{chan.}\bar{t})$	410645	POWHEG+PYTHIA8	0.001268 (10%)	0.0052	0.010
$t\bar{t}$ (syst.)	410480	POWHEG+PYTHIA8	$0.8318 \times 0.438$ (7%)	0.85	1.5
$t\bar{t}$ (syst.)	410482	POWHEG+PYTHIA8	$0.8318 \times 0.105$ (7%)	0.40	0.50
$t\bar{t}$ (syst.)	410557	POWHEG+PYTHIA8	$0.8318 \times 0.438$ (7%)	0.85	1.5
$t\bar{t}$ (syst.)	410558	POWHEG+PYTHIA8	$0.8318 \times 0.105$ (7%)	0.40	0.50

**Table 81:** Monte Carlo samples at  $\sqrt{s} = 13\text{TeV}$ . Given is a short description of the process, the ATLAS MC data set number (DSID), the names and version numbers of the MC generator(s), the used value of the higher order cross section times any branching and filter efficiencies ( $\sigma \cdot \text{BR} \cdot \epsilon_{\text{filter}}$ ) with the theoretical uncertainty in percent (“th. unc.”), and finally the number of events analysed after skimming at derivation production ( $N_{\text{evt}}^{\text{skim}}$ ) as well as the number of events originally processed and simulated ( $N_{\text{evt}}^{\text{unskim}}$ ). In the case of  $Z \rightarrow \ell\ell$  samples, the given  $\epsilon_{\text{filter}} > 1$  is related to the fact, that the cross sections were calculated for  $66 < m_{\ell\ell} < 116\text{GeV}$ , but the generated mass range is larger. The last section of  $t\bar{t}$  samples refers to variation samples for systematics studies. The MC equivalent luminosity  $N_{\text{evt}}^{\text{unskim}} / (\sigma \cdot \text{BR} \cdot \epsilon_{\text{filter}})$  is generally above  $3\text{fb}^{-1}$  for signal and significant backgrounds, the exception are Powheg  $W \rightarrow \tau\nu$  and  $Z \rightarrow \tau\tau$  samples, that have about  $0.45\text{fb}^{-1}$  only [1].

Process	Data set	Generator	$\sigma \cdot BR \cdot \epsilon_{\text{filter}} [\text{nb}] (\text{th. unc.})$	$N_{\text{evt}}^{\text{skim}} [10^6]$	$N_{\text{evt}}^{\text{unskim}} [10^6]$
$Z \rightarrow \mu\mu$	364100	SHERPA 2.2.1	$1.932 \times 0.822 (5\%)$	8.0	8.0
$Z \rightarrow \mu\mu$	364101	SHERPA 2.2.1	$1.933 \times 0.114 (5\%)$	1.5	1.5
$Z \rightarrow \mu\mu$	364102	SHERPA 2.2.1	$1.932 \times 0.0660 (5\%)$	1.1	1.1
$Z \rightarrow \mu\mu$	364103	SHERPA 2.2.1	$0.1063 \times 0.690 (5\%)$	1.5	1.5
$Z \rightarrow \mu\mu$	364104	SHERPA 2.2.1	$0.1062 \times 0.200 (5\%)$	0.40	0.40
$Z \rightarrow \mu\mu$	364105	SHERPA 2.2.1	$0.1063 \times 0.114 (5\%)$	0.25	0.25
$Z \rightarrow \mu\mu$	364106	SHERPA 2.2.1	$0.03889 \times 0.593 (5\%)$	0.20	0.20
$Z \rightarrow \mu\mu$	364107	SHERPA 2.2.1	$0.03885 \times 0.235 (5\%)$	0.060	0.060
$Z \rightarrow \mu\mu$	364108	SHERPA 2.2.1	$0.03889 \times 0.156 (5\%)$	0.035	0.035
$Z \rightarrow \mu\mu$	364109	SHERPA 2.2.1	$0.008310 \times 0.561 (5\%)$	0.020	0.020
$Z \rightarrow \mu\mu$	364110	SHERPA 2.2.1	$0.008310 \times 0.266 (5\%)$	0.010	0.010
$Z \rightarrow \mu\mu$	364111	SHERPA 2.2.1	$0.008320 \times 0.177 (5\%)$	0.0050	0.0050
$Z \rightarrow \mu\mu$	364112	SHERPA 2.2.1	$0.001740 (5\%)$	0.0050	0.0050
$Z \rightarrow \mu\mu$	364113	SHERPA 2.2.1	$0.0001400 (5\%)$	0.0050	0.0050
$Z \rightarrow ee$	364114	SHERPA 2.2.1	$1.933 \times 0.821 (5\%)$	8.0	8.0
$Z \rightarrow ee$	364115	SHERPA 2.2.1	$1.932 \times 0.114 (5\%)$	1.5	1.5
$Z \rightarrow ee$	364116	SHERPA 2.2.1	$1.932 \times 0.0658 (5\%)$	1.1	1.1
$Z \rightarrow ee$	364117	SHERPA 2.2.1	$0.1080 \times 0.694 (5\%)$	1.5	1.5
$Z \rightarrow ee$	364118	SHERPA 2.2.1	$0.1077 \times 0.191 (5\%)$	0.40	0.40
$Z \rightarrow ee$	364119	SHERPA 2.2.1	$0.1078 \times 0.119 (5\%)$	0.25	0.25
$Z \rightarrow ee$	364120	SHERPA 2.2.1	$0.03964 \times 0.616 (5\%)$	0.20	0.20
$Z \rightarrow ee$	364121	SHERPA 2.2.1	$0.03967 \times 0.233 (5\%)$	0.060	0.060
$Z \rightarrow ee$	364122	SHERPA 2.2.1	$0.04068 \times 0.150 (5\%)$	0.035	0.035
$Z \rightarrow ee$	364123	SHERPA 2.2.1	$0.008460 \times 0.569 (5\%)$	0.020	0.020
$Z \rightarrow ee$	364124	SHERPA 2.2.1	$0.008450 \times 0.266 (5\%)$	0.010	0.010
$Z \rightarrow ee$	364125	SHERPA 2.2.1	$0.008470 \times 0.177 (5\%)$	0.0050	0.0050
$Z \rightarrow ee$	364126	SHERPA 2.2.1	$0.001760 (5\%)$	0.0050	0.0050
$Z \rightarrow ee$	364127	SHERPA 2.2.1	$0.0001451 (5\%)$	0.0050	0.0050

**Table 82:** Alternative signal  $Z \rightarrow \ell\ell$  Monte Carlo samples at  $\sqrt{s} = 13\text{TeV}$  produced with SHERPA. General description of the table see Table 81. The samples are split into a long list of orthogonal slices based on “max(pTV,HT)” and filtered further into “b/c/light-jet” subcomponents. For the purpose of this analysis, the number of events in each slice is such that the samples are about  $2\text{fb}^{-1}$  each (after application of a penalty factor for negative weight events) and an “inclusive sample” is restored after merging the slices [1].

Process	Data set	Generator	$\sigma \cdot BR \cdot \epsilon_{\text{filter}}$ [nb] (th. unc.)	$N_{\text{evt}}^{\text{skim}} [10^6]$	$N_{\text{evt}}^{\text{unskim}} [10^6]$
$W \rightarrow \mu\nu$	364156	SHERPA 2.2.1	$18.58 \times 0.825$ (5%)	31	31
$W \rightarrow \mu\nu$	364157	SHERPA 2.2.1	$18.57 \times 0.131$ (5%)	8.1	8.1
$W \rightarrow \mu\nu$	364158	SHERPA 2.2.1	$18.57 \times 0.0433$ (5%)	2.6	2.6
$W \rightarrow \mu\nu$	364159	SHERPA 2.2.1	$0.9173 \times 0.674$ (5%)	6.3	6.3
$W \rightarrow \mu\nu$	364160	SHERPA 2.2.1	$0.9172 \times 0.244$ (5%)	2.1	2.1
$W \rightarrow \mu\nu$	364161	SHERPA 2.2.1	$0.9163 \times 0.0847$ (5%)	0.23	0.23
$W \rightarrow \mu\nu$	364162	SHERPA 2.2.1	$0.3296 \times 0.600$ (5%)	0.80	0.80
$W \rightarrow \mu\nu$	364163	SHERPA 2.2.1	$0.3297 \times 0.293$ (5%)	0.27	0.27
$W \rightarrow \mu\nu$	364164	SHERPA 2.2.1	$0.3295 \times 0.111$ (5%)	0.099	0.099
$W \rightarrow \mu\nu$	364165	SHERPA 2.2.1	$0.06993 \times 0.548$ (5%)	0.068	0.068
$W \rightarrow \mu\nu$	364166	SHERPA 2.2.1	$0.06995 \times 0.320$ (5%)	0.034	0.034
$W \rightarrow \mu\nu$	364167	SHERPA 2.2.1	$0.06991 \times 0.125$ (5%)	0.014	0.014
$W \rightarrow \mu\nu$	364168	SHERPA 2.2.1	0.01456 (5%)	0.020	0.020
$W \rightarrow \mu\nu$	364169	SHERPA 2.2.1	0.001200 (5%)	0.004	0.004
$W \rightarrow e\nu$	364170	SHERPA 2.2.1	$18.58 \times 0.825$ (5%)	31	31
$W \rightarrow e\nu$	364171	SHERPA 2.2.1	$18.57 \times 0.131$ (5%)	8.3	8.3
$W \rightarrow e\nu$	364172	SHERPA 2.2.1	$18.57 \times 0.0448$ (5%)	2.5	2.5
$W \rightarrow e\nu$	364173	SHERPA 2.2.1	$0.9168 \times 0.675$ (5%)	6.4	6.4
$W \rightarrow e\nu$	364174	SHERPA 2.2.1	$0.9176 \times 0.244$ (5%)	2.1	2.1
$W \rightarrow e\nu$	364175	SHERPA 2.2.1	$0.9173 \times 0.0851$ (5%)	0.79	0.79
$W \rightarrow e\nu$	364176	SHERPA 2.2.1	$0.3295 \times 0.599$ (5%)	0.76	0.76
$W \rightarrow e\nu$	364177	SHERPA 2.2.1	$0.3297 \times 0.288$ (5%)	0.28	0.28
$W \rightarrow e\nu$	364178	SHERPA 2.2.1	$0.3295 \times 0.111$ (5%)	0.10	0.10
$W \rightarrow e\nu$	364179	SHERPA 2.2.1	$0.06993 \times 0.548$ (5%)	0.070	0.070
$W \rightarrow e\nu$	364180	SHERPA 2.2.1	$0.06996 \times 0.320$ (5%)	0.034	0.034
$W \rightarrow e\nu$	364181	SHERPA 2.2.1	$0.06994 \times 0.137$ (5%)	0.014	0.014
$W \rightarrow e\nu$	364182	SHERPA 2.2.1	0.01460 (5%)	0.020	0.020
$W \rightarrow e\nu$	364183	SHERPA 2.2.1	0.001200 (5%)	0.0050	0.0050

**Table 83:** Alternative signal  $W \rightarrow \ell\nu$  Monte Carlo samples at  $\sqrt{s} = 13\text{TeV}$  produced with SHERPA. See Table 82 for a description of the table. The samples are split into a long list of orthogonal slices based on “max(pTV,HT)” and filtered further into “b/c/light-jet” subcomponents. For the purpose of this analysis, the number of events in each slice is such that the samples are about  $1\text{fb}^{-1}$  each (after application of a penalty factor for negative weight events) and an “inclusive sample” is restored after merging the slices [1].

Process	Data set	Generator	$\sigma \cdot \text{BR} \cdot \epsilon_{\text{filter}}$ [nb] (th. unc.)	$N_{\text{evt}}^{\text{skim}} [10^6]$	$N_{\text{evt}}^{\text{unskim}} [10^6]$
$W^+ \rightarrow e^+ \nu$	361100	POWHEG+PYTHIA8	4.357 (5%)	11	11
$W^+ \rightarrow \mu^+ \nu$	361101	POWHEG+PYTHIA8	4.357 (5%)	11	11
$W^+ \rightarrow \tau^+ \nu$	361102	POWHEG+PYTHIA8	4.357 (5%)	0.065	0.94
$W^- \rightarrow e^- \bar{\nu}$	361103	POWHEG+PYTHIA8	2.902 (5%)	7.0	7.0
$W^- \rightarrow \mu^- \bar{\nu}$	361104	POWHEG+PYTHIA8	2.902 (5%)	7.0	7.0
$W^- \rightarrow \tau^- \bar{\nu}$	361105	POWHEG+PYTHIA8	2.902 (5%)	0.039	0.59
$Z \rightarrow ee$	361106	POWHEG+PYTHIA8	$0.6600 \times 1.025$ (5%)	6.3	6.3
$Z \rightarrow \mu\mu$	361107	POWHEG+PYTHIA8	$0.6600 \times 1.025$ (5%)	3.4	3.4
$Z \rightarrow \tau\tau$	361108	POWHEG+PYTHIA8	$0.6600 \times 1.025$ (5%)	0.039	0.29
$Z \rightarrow ee$	364381	SHERPA 2.2.5	$0.6600 \times 1.12$ (5%)	5.0	5.0
$Z \rightarrow \mu\mu$	364382	SHERPA 2.2.5	$0.6600 \times 1.12$ (5%)	5.0	5.0
$Z \rightarrow \tau\tau$	364383	SHERPA 2.2.5	$0.6600 \times 1.12$ (5%)	1.5	1.5
$W \rightarrow e\nu$	364384	SHERPA 2.2.5	7.259 (5%)	25	25
$W \rightarrow \mu\nu$	364385	SHERPA 2.2.5	7.259 (5%)	25	25
$W \rightarrow \tau\nu$	364386	SHERPA 2.2.5	7.259 (5%)	6.0	6.0
$ZZ(4\ell)$	361063	SHERPA 2.1	0.004624 (10%)	0.017	0.049
$WZ(\ell\ell\ell^-\nu\text{SF})$	361064	SHERPA 2.1	0.0005324 (10%)	0.0073	0.015
$WZ(\ell\ell\ell^-\nu\text{OF})$	361065	SHERPA 2.1	0.001041 (10%)	0.012	0.030
$WZ(\ell\ell\ell^+\nu\text{SF})$	361066	SHERPA 2.1	0.0008433 (10%)	0.010	0.020
$WZ(\ell\ell\ell^+\nu\text{OF})$	361067	SHERPA 2.1	0.001633 (10%)	0.016	0.039
$WW(2\ell 2\nu)$	361068	SHERPA 2.1	0.003356 (10%)	0.068	0.090
$WW(q\bar{q}\ell\nu)$	361091	SHERPA 2.1	0.006059 (10%)	0.078	0.15
$WW(\ell\nu q\bar{q})$	361092	SHERPA 2.1	0.006082 (10%)	0.14	0.26
$WZ(\ell\nu q\bar{q})$	361093	SHERPA 2.1	0.002503 (10%)	0.039	0.075
$WZ(q\bar{q}\ell\ell)$	361094	SHERPA 2.1	0.0007518 (10%)	0.017	0.025
$ZZ(q\bar{q}\ell\ell)$	361096	SHERPA 2.1	$0.003789 \times 0.148$ (10%)	0.0070	0.010
$t\bar{t}$	410470	POWHEG+PYTHIA8	$0.06890 \times 0.544$ (7%)	1.8	2.8
$t(s - \text{chan.} t)$	410644	POWHEG+PYTHIA8	0.0005400 (10%)	0.028	0.050
$t(s - \text{chan.} \bar{t})$	410645	POWHEG+PYTHIA8	0.0002751 (10%)	0.028	0.050
$Wt$	410646	POWHEG+PYTHIA8	0.002990 (10%)	0.018	0.050
$W\bar{t}$	410647	POWHEG+PYTHIA8	0.002983 (10%)	0.019	0.050
$t(t - \text{chan.} t)$	410658	POWHEG+PYTHIA8	0.005414 (10%)	0.028	0.050
$t(t - \text{chan.} \bar{t})$	410659	POWHEG+PYTHIA8	0.002682 (10%)	0.028	0.050

**Table 84:** Monte Carlo samples at  $\sqrt{s} = 5\text{TeV}$ . The table follows the same format as Table 81. The MC equivalent luminosity  $N_{\text{evt}}^{\text{unskim}} / (\sigma \cdot \text{BR} \cdot \epsilon_{\text{filter}})$  is generally above  $2.5\text{fb}^{-1}$  for signal and significant backgrounds, the exception are Powheg  $W \rightarrow \tau\nu$  and  $Z \rightarrow \tau\tau$  samples, that have about  $0.20\text{fb}^{-1}$  and  $0.45\text{fb}^{-1}$  only [1].

---

## 2519 8.2 Multijet background

2520 The estimate of the multijet background, which contain contributions from fake leptons produced in  
 2521 semi-leptonic decays of heavy quarks, in-flight kaon decays, photon conversions, mis-identified pions,  
 2522 is done using a data-driven technique. The W boson signal region is defined by the following cuts:

2523 •  $p_T^\ell > 25 \text{ GeV}$ ,  $|\eta_\ell| < 2.4$ ;

2524 •  $E_T^{\text{miss}} > 25 \text{ GeV}$ ,

2525 •  $m_T > 50 \text{ GeV}$ .

2526 • lepton isolation.

2527 The production of multijet events is mainly concentrated at lower values of  $p_T^l$ ,  $E_T^{\text{miss}}$  and  $m_T$ , such  
 2528 that the largest part of the multijet background events is removed by the cuts described above. The  
 2529 background estimate is obtained by fitting the signal and multijet yields in  $p_T^l$ ,  $E_T^{\text{miss}}$  and  $m_T$  kinematic  
 2530 distributions, but with  $E_T^{\text{miss}}$  and  $m_T$  cuts relaxed. These kinematic distributions for the signal are  
 2531 modelled using the MC simulation and include the calibrations and corrections presented in the  
 2532 previous chapter. The templates of the multijet distributions are obtained using the data with the  
 2533 same kinematic selection, but with inverted isolation cuts. The multijet yield is obtained in the region  
 2534 with relaxed kinematic cuts and then extrapolated to the signal region, correcting for the efficiency of  
 2535 kinematic cuts.

2536 The first step consists in defining four different regions in phase-isolation space:

2537 • signal region (SR): isolated leptons, signal requirement on  $p_T^{\text{lep}}$ ,  $E_T^{\text{miss}}$  and  $m_T$ ;

2538 • fit region (FR): isolated leptons, relaxed kinematic requirements:  $E_T^{\text{miss}} > 0 \text{ GeV}$ ,  $m_T > 0 \text{ GeV}$ ;

2539 • control region 1 (CR1): anti-isolated leptons with FR kinematic requirements;

2540 • control region 2 (CR2): anti-isolated leptons with SR kinematic requirements.

2541 The multijet template is extracted from CR1 and normalized using the fraction fit, obtained from fit  
 2542 region (FR). Then the multijet(MJ) yield is estimated in the SR through the ratio of MJ events in the two  
 2543 control regions:  $\epsilon = N_{\text{MJ}}^{\text{CR2}} / N_{\text{MJ}}^{\text{CR1}}$ . The number of MJ background events is estimated in the following  
 2544 way:

2545 • The number of multijet background events in CR1 ( $N_{\text{MJ}}^{\text{CR1}}$ ) and their distributions ( $H_{\text{MJ}}^{\text{CR1}}$ ) are  
 2546 derived as follows:

$$N_{\text{MJ}}^{\text{CR1}} = N_{\text{data}}^{\text{CR1}} - N_{\text{EW}}^{\text{CR1}}, \quad (8.1)$$

$$H_{\text{MJ}}^{\text{CR1}} = H_{\text{data}}^{\text{CR1}} - H_{\text{EW}}^{\text{CR1}} \quad (8.2)$$

2547 where  $H^{CR1}$  stands for one of the kinematic distributions used in the fit, namely  $p_T^\ell$ ,  $E_T^{\text{miss}}$  or  $m_T$ .

- 2548 • The fraction fit is performed in FR, which has looser kinematics cuts and the same isolation cuts  
2549 as the signal. The fit has the following form:

$$H_{\text{data}}^{\text{FR}} = \alpha \cdot H_{\text{EW}}^{\text{FR}} + T \cdot H_{\text{MJ}}^{\text{CR1}}. \quad (8.3)$$

2550 The fitting parameter  $T$  gives the factor for the MJ contribution in FR:  $N_{\text{MJ}}^{\text{FR}} \approx T \cdot N_{\text{MJ}}^{\text{CR1}}$ . A  
2551 normalization factor for the EW+top contribution,  $\alpha$ , is also fitted and should be unity within the  
2552 uncertainties in the luminosity and the cross-sections of the MC-simulated processes.

- 2553 • Then the fitted multijet yield is extrapolated to the signal region. The extrapolation factor  $\varepsilon$  that  
2554 was mentioned before can be obtained as follows:

$$\varepsilon \equiv \frac{N_{\text{data}}^{\text{CR2}} - N_{\text{EW}}^{\text{CR2}}}{N_{\text{data}}^{\text{CR1}} - N_{\text{EW}}^{\text{CR1}}}, \quad (8.4)$$

2555 and assuming that this factor does not depend on the isolation cuts, one obtains

$$N_{\text{MJ}}^{\text{SR}} = \varepsilon N_{\text{MJ}}^{\text{FR}}. \quad (8.5)$$

2556 This method relies on the anti-isolation procedure which may introduce a bias into the results. The  
2557 dependence of the MJ yield on the isolation criteria must be taken into account. In order to do this the  
2558 control regions CR1 and CR2 are estimated in the slices of anti-isolation with  $\text{ptvarcone20}/\text{pT}$  ranging  
2559 in the following intervals: [0.10, 0.15, 0.20, 0.25, 0.30, 0.35, 0.40].

2560 The change of isolation criterion also biases the hadronic recoil reconstruction procedure, where the  
2561 cone replacement appears to be isolation-dependent. This bias is overcome by introducing a correction  
2562 to the hadronic recoil vector:

$$\vec{u}^{\text{corr}} = \vec{u}^{\text{baseline}} + \vec{u}^{\text{iso}}, \text{ where} \quad (8.6)$$

$$\vec{u}^{\text{iso}} \equiv \text{ptcone20} \cdot \vec{n}_\ell. \quad (8.7)$$

2563 The unit vector  $\vec{n}_\ell$  is aligned with the lepton direction. This correction vanishes at low isolation in the  
2564 signal region but introduces a sizable correction in the anti-isolated region (see Fig. 83). Some residual  
2565 dependence of the extrapolated distributions on the isolation criteria is still present and requires  
2566 shape extrapolation procedure. The shape of the distribution of interest is estimated in three slices of  
2567  $\text{ptvarcone20}/\text{pT}$  isolation within [0.10, 0.20, 0.30 0.40] in CR2. For every observable  $X$  the difference  
2568  $\Delta[X]$  of the distribution  $X$  between consecutive isolation slices is defined as:

$$H_{\text{MJ}}^{[0.1,0.2]}[X] = H_{\text{data}}^{[0.1,0.2]}[X] - H_{\text{MC}}^{[0.1,0.2]}[X]; \quad (8.8)$$

$$\Delta[X] = 1/2 \left[ (H_{\text{MJ}}^{[0.1,0.2]}[X] - H_{\text{MJ}}^{[0.2,0.3]}[X]) + (H_{\text{MJ}}^{[0.2,0.3]}[X] - H_{\text{MJ}}^{[0.3,0.4]}[X]) \right], \quad (8.9)$$

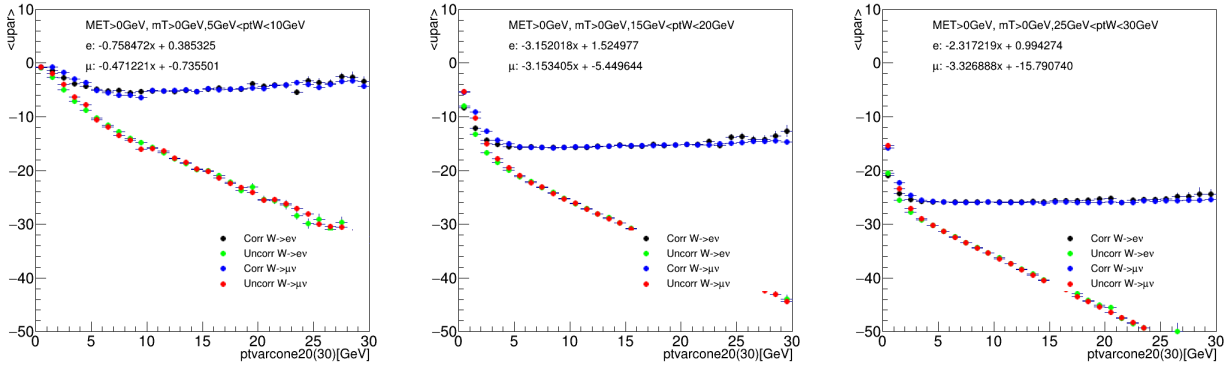


**Figure 83:**  $\langle u_{\parallel}^{\ell} \rangle$  as a function of  $\text{ptvarcone20}$ , before and after correction using data samples at  $\sqrt{s} = 13 \text{ TeV}$ .

where  $H_X^{[x,y]}$  is the normalized distribution of  $X$  in CR2 (anti-isolated signal region) satisfying  $x < \text{ptvarcone20}/\text{pT} < y$ , estimated from the MC-subtracted data in CR2.  
 $\Delta[X]$  is supposed to be the difference between MJ spectrum in the signal region ( $\text{ptvarcone20}/\text{pT} < 0.1$ ) and the isolation slice next to it ( $0.10 < \text{ptvarcone20}/\text{pT} < 0.20$ ). So the extrapolated distribution to the signal region is the following:

$$H_X^{\text{sig}} = H_X^{[0.1, 0.2]} - \Delta[X] \quad (8.10)$$

The applied shift  $\Delta[X]$  is assigned a 100% relative uncertainty because of the large statistical uncertainty. Figures 84 and 85 contain the results of the isolation scan in electron and muon channels respectively.

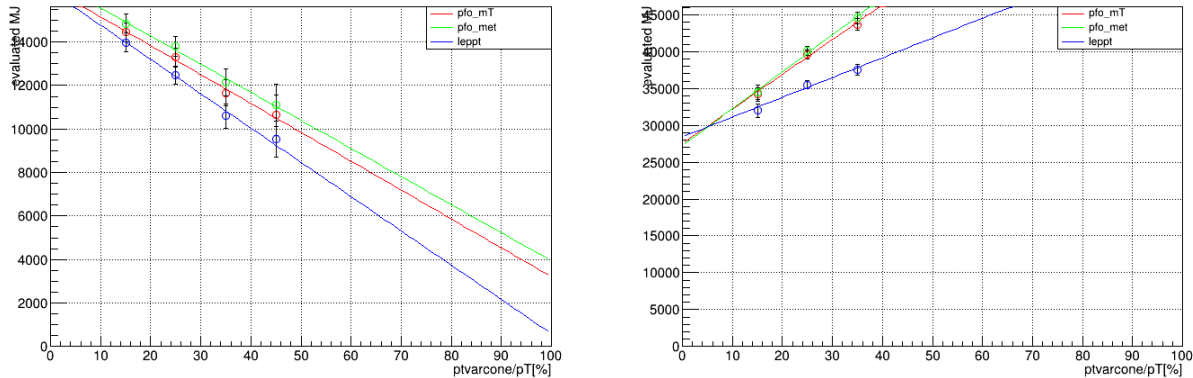


**Figure 84:** Isolation scan in the  $W^+ \rightarrow e^+ \nu$  channel without (left) and with (right) recoil correction [20].

The MJ contributions to the kinematic distributions in slices of isolation along with the extrapolation to the signal region for the 13 TeV for electrons and muons are shown in Figures 86 and 87. The kinematic distributions with the contributions from the multijets for 5 and 13 TeV are presented in sections 8.4.3 and 8.4.2 respectively.

The multijet yields for all channels and energies are presented in Table 85 along with the associated

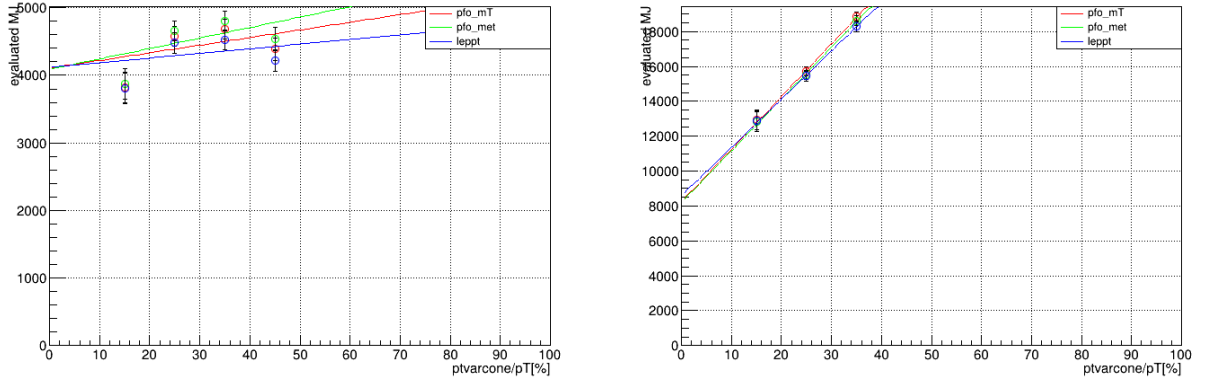


**Figure 85:** Isolation scan in the  $W^+ \rightarrow \mu^+ \nu$  channel without (left) and with (right) recoil correction [20].

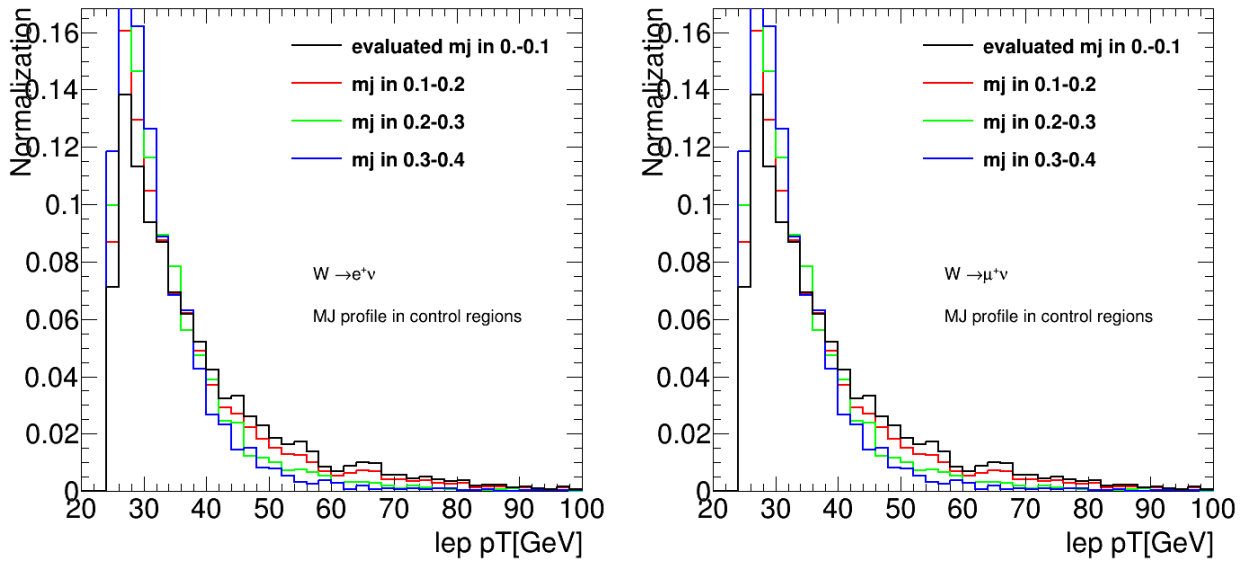


**Figure 86:** Extrapolation of the multijet distributions for the lepton transverse momentum in the  $W^+ \rightarrow e^+\nu$  (left) and  $W^+ \rightarrow \mu^+\nu$  (right) channels at  $\sqrt{s} = 13$  TeV [20].

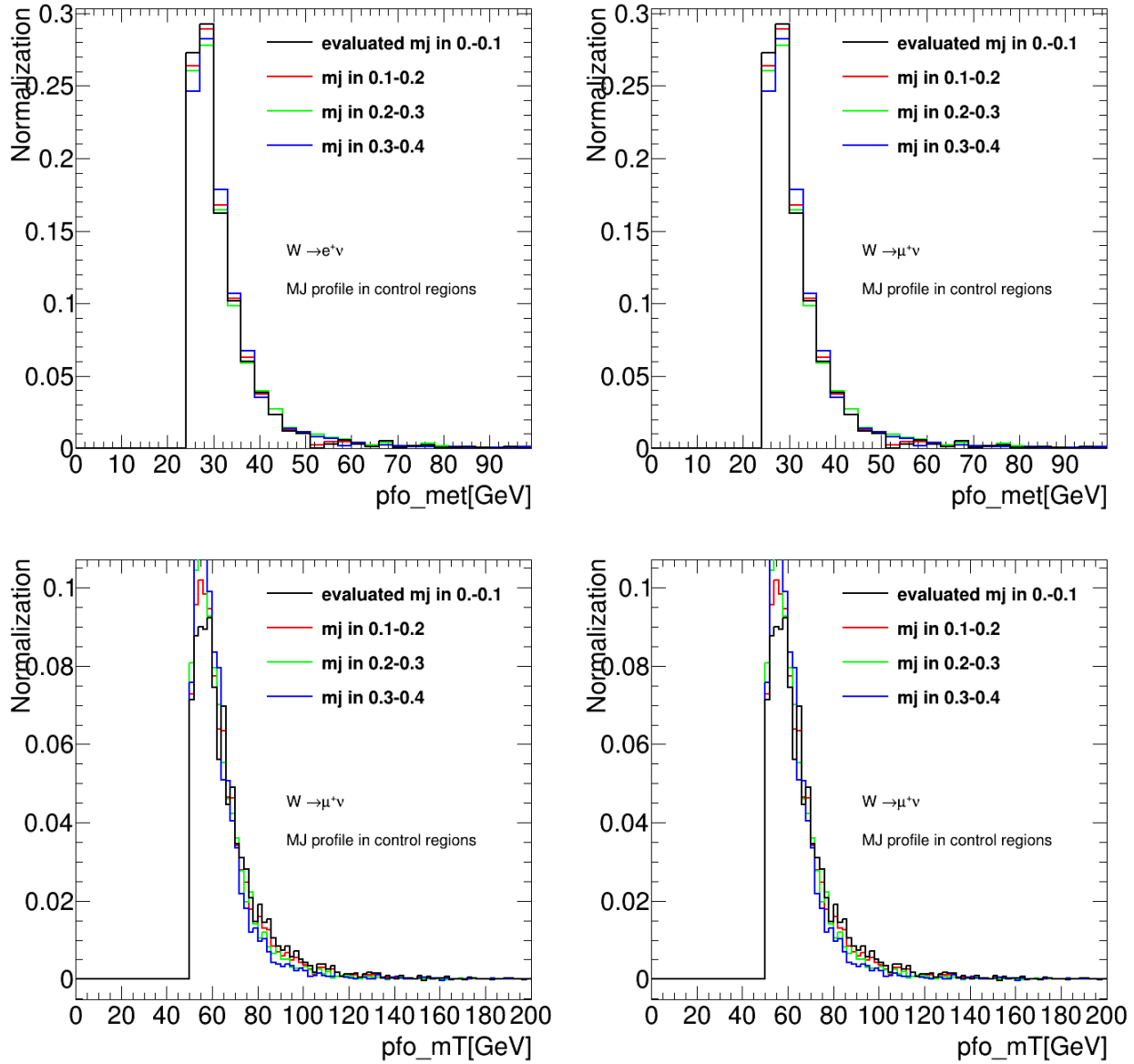


**Figure 87:** Extrapolation of the multijet distributions for the missing transverse energy (top) and transverse mass (bottom), in the  $W^+ \rightarrow e^+\nu$  (left) and  $W^+ \rightarrow \mu^+\nu$  (right) channels at  $\sqrt{s} = 13$  TeV [20].

2582 uncertainties. The table shows that the MJ background is significantly higher in the electron channel than in the muon channel.

Channel	13 TeV	5 TeV
$W^+ \rightarrow e^+ \nu$	$27973 \pm 1756$	$3027 \pm 554$
$W^+ \rightarrow e^- \nu$	$27388 \pm 1962$	$2401 \pm 495$
$W^+ \rightarrow \mu^+ \nu$	$9044 \pm 796$	$724 \pm 192$
$W^+ \rightarrow \mu^- \nu$	$9053 \pm 617$	$755 \pm 160$

**Table 85:** Evaluation of multijet background yields at 13 TeV and 5 TeV [20].

2583

2584 

### 8.3 Z vertex reweighting

2585 The 5 TeV MC samples have been generated to be perfectly matched to the data. Although this is not  
 2586 the case for 13 TeV samples, which can be seen at Fig. 88. It is also seen from these plots that the  
 2587 2017 and 2018 data were collected at two different runs under different beam conditions. To avoid  
 2588 possible impact on the acceptance the MC samples were reweighted to the data using  $Z \rightarrow ee$  and  
 2589  $Z \rightarrow \mu\mu$  selections.

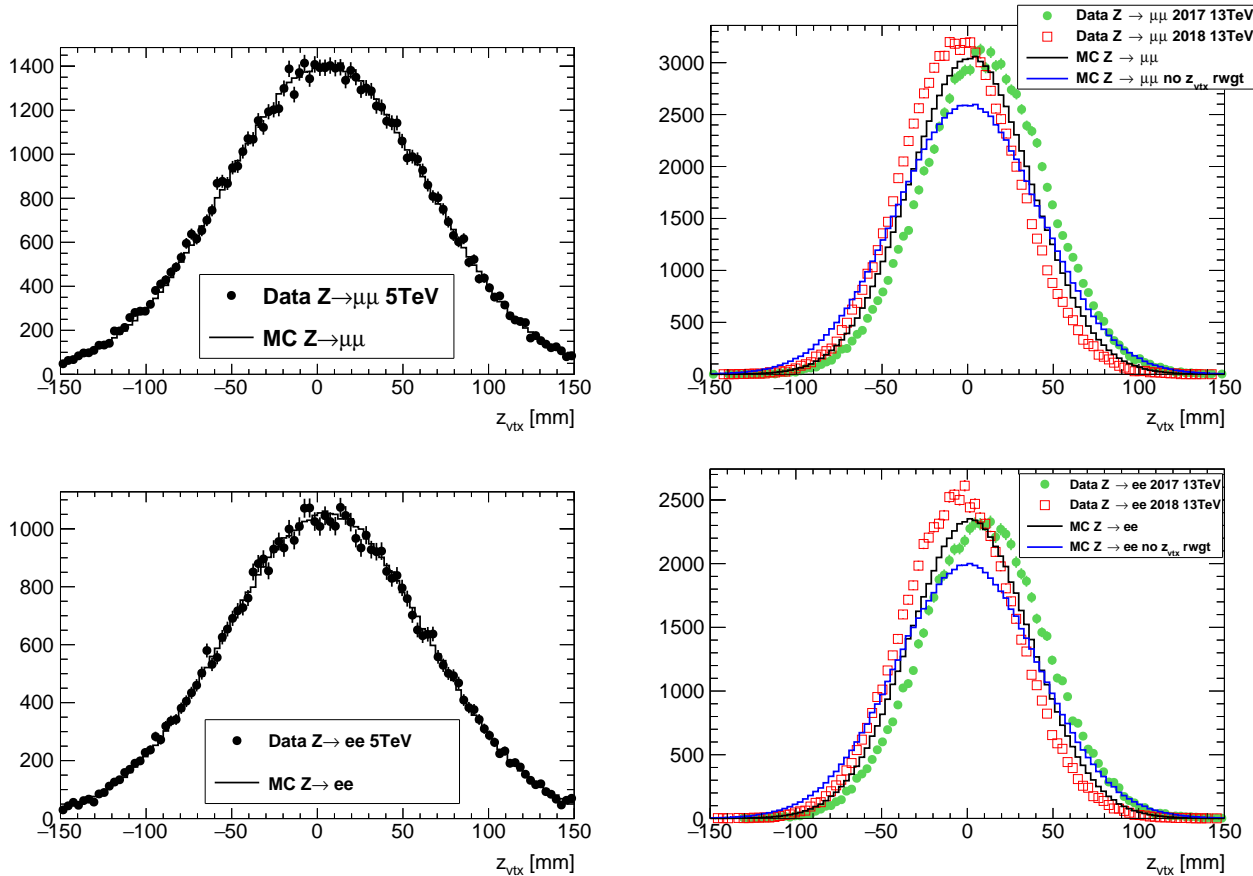


**Figure 88:** Distributions for the 5 TeV (left) and 13 TeV (right) low- $\mu$  dataset(s) in a  $Z/\gamma^* \rightarrow \mu\mu$  (top row) and a  $Z/\gamma^* \rightarrow ee$  (bottom row) selection. The data (points) is compared to  $Z/\gamma^* \rightarrow \mu\mu$  or  $Z/\gamma^* \rightarrow ee$  signal MC, respectively. The distributions of the  $z$ -position of the primary vertex selected as the hard interaction are compared for the dataset(s) and the MC simulation before (“no  $z_{vtx}$  rwgt”, blue, only 13 TeV) and after reweighting (black). For the 13 TeV data the 2017 and 2018 data are shown separately and all distributions are (roughly) normalised to the same number of selected events in the 2017 dataset [1].

 2590 

### 8.4 W analysis event selection and control plots

---

### 2591 8.4.1 Event selection

2592 In both cases of 5 and 13 TeV events with  $W \rightarrow \ell\nu$  candidate were selected based on a single-lepton  
 2593 trigger requirement. The trigger for  $W \rightarrow e\nu$  event candidate `HLT_e15_1hloose_nod0_L1EM12`, requires  
 2594 at least one reconstructed electron with  $E_T$  larger than 15 GeV passing *loose* identification requirements.  
 2595 Candidates for  $W \rightarrow \mu\nu$  were triggered by `HLT_mu14` trigger, requiring one medium muon with  $E_T$   
 2596 larger than 14 GeV.

2597 Events are required to contain exactly one lepton (muon or electron) candidate having  $p_T > 25\text{GeV}$ .  
 2598 Electrons are required to have  $|\eta| < 2.47$  excluding transition region  $1.37 < |\eta| < 1.52$ . Muons Events  
 2599 with additional leptons of the same flavour with transverse momentum greater than 20 GeV satisfying  
 2600 some ID criteria are discarded, to better reject the  $Z$  background. The ID point is *medium* for the muon  
 2601 channel, and *loose* for the electron channel. There is no requirement on the number of leptons with  
 2602 different flavour than the channel under study.

2603 To suppress background, in particular from multijet processes, events are required to have  $E_T^{\text{miss}}$   
 2604 greater than 25 GeV. The  $W$  boson transverse mass  $m_T$  is demanded to be larger than 50 GeV. This  
 2605 transverse mass is defined as follows:

$$m_T = \sqrt{2p_T^\nu p_T^l(1 - \cos \Delta\phi^\nu)} \quad (8.11)$$

2606 Tables 86,88,810,812 contain signal selection event yields for the  $W^\pm \rightarrow \ell^\pm\nu$  at  $\sqrt{s} = 5$  TeV low- $\mu$   
 2607 dataset. Similarly the tables 87,89,811,813 contain the corresponding numbers for the 13 TeV low- $\mu$   
 2608 dataset. The listed uncertainties are statistical. Table 814 provides a comparison between observed and  
 2609 expected yields. Events denoted as  $W \rightarrow \ell\nu$  in the tables and the plots contain the sum of background  
 2610 events coming from  $W \rightarrow \tau\nu$  and  $W$  leptonic decays other than the signal.

Cut	Data	Signal	$W^\pm \rightarrow \ell^\pm\nu$ BG	$Z \rightarrow \ell\ell$	Top	Diboson	Multijet
One electron	1993720	643610 $\pm$ 260	32940 $\pm$ 190	44338 $\pm$ 71	1754.4 $\pm$ 3.9	772.2 $\pm$ 3.7	-
Electron trig matched	1907724	612940 $\pm$ 250	30790 $\pm$ 190	42100 $\pm$ 69	1698.5 $\pm$ 3.8	741.1 $\pm$ 3.6	-
Isolation	1438941	610320 $\pm$ 250	30590 $\pm$ 190	41923 $\pm$ 69	1663.6 $\pm$ 3.8	722.5 $\pm$ 3.6	-
$p_T^e > 25\text{GeV}$	720284	482240 $\pm$ 220	14790 $\pm$ 130	31955 $\pm$ 53	1464.5 $\pm$ 3.5	592.1 $\pm$ 3.2	-
$E_T^{\text{miss}} > 25\text{GeV}$	440605	421510 $\pm$ 210	9650 $\pm$ 100	1336 $\pm$ 20	1223 $\pm$ 3.2	420.8 $\pm$ 2.4	-
$m_T > 50\text{GeV}$	430620	417430 $\pm$ 210	8800 $\pm$ 96	1047 $\pm$ 16	944.3 $\pm$ 2.9	373.5 $\pm$ 2.2	3030 $\pm$ 550

**Table 86:** Analysis cut flow for  $W^+ \rightarrow e^+\nu$  5 TeV signal selection. Lepton  $p_T$  is required to be over 18 GeV before the final cut.

---

### 2611 8.4.2 $\sqrt{s} = 13$ TeV dataset control plots

2612 Control plots for the 13 TeV low- $\mu$  dataset are provided here after applying all corrections described  
 2613 in Section 7, and after applying the selection described above in this section. In each figure, the  
 2614 right(left)-hand column shows distributions for the  $W^+$  ( $W^-$ ) process. The top (bottom) row shows the

Cut	Data	Signal		$W^\pm \rightarrow \ell^\pm \nu$ BG		$Z \rightarrow \ell\ell$		Top		Diboson	Multijet
One electron	7915023	1797340	$\pm$ 390	92520	$\pm$ 270	147490	$\pm$ 140	63207	$\pm$ 89	3069	$\pm$ 63
Electron trig matched	7840239	1709140	$\pm$ 380	86370	$\pm$ 260	139760	$\pm$ 140	61110	$\pm$ 88	2967	$\pm$ 62
Isolation	5413483	1698430	$\pm$ 380	85560	$\pm$ 260	138890	$\pm$ 140	59834	$\pm$ 87	2939	$\pm$ 61
$p_T^e > 25\text{GeV}$	2452868	1342200	$\pm$ 330	44450	$\pm$ 190	106270	$\pm$ 110	53811	$\pm$ 82	2565	$\pm$ 58
$E_T^{\text{miss}} > 25\text{GeV}$	1275513	1136520	$\pm$ 310	28580	$\pm$ 150	8313	$\pm$ 46	45707	$\pm$ 75	1990	$\pm$ 53
$m_T > 50\text{GeV}$	1207776	1117560	$\pm$ 310	24760	$\pm$ 130	6443	$\pm$ 36	34580	$\pm$ 65	1718	$\pm$ 50
										28000	$\pm$ 1800

**Table 87:** Analysis cut flow for  $W^+ \rightarrow e^+ \nu$  13 TeV signal selection. Lepton  $p_T$  is required to be over 18 GeV before the final cut.

Cut	Data	Signal		$W^\pm \rightarrow \ell^\pm \nu$ BG		$Z \rightarrow \ell\ell$		Top		Diboson	Multijet
One muon	2434459	760980	$\pm$ 280	35090	$\pm$ 200	37015	$\pm$ 82	2025.3	$\pm$ 4.1	864.7	$\pm$ 3.7
Muon trig matched	2353403	664100	$\pm$ 260	30610	$\pm$ 190	32554	$\pm$ 76	1725.6	$\pm$ 3.8	746.6	$\pm$ 3.4
Isolation	1186616	659200	$\pm$ 260	30400	$\pm$ 190	32303	$\pm$ 76	1574.6	$\pm$ 3.7	710.1	$\pm$ 3.3
$p_T^\mu > 25\text{GeV}$	632016	508270	$\pm$ 230	13900	$\pm$ 130	22556	$\pm$ 57	1335.3	$\pm$ 3.4	568.2	$\pm$ 2.9
$E_T^{\text{miss}} > 25\text{GeV}$	470856	442600	$\pm$ 210	8700	$\pm$ 100	9959	$\pm$ 31	1111.8	$\pm$ 3	424.5	$\pm$ 2.5
$m_T > 50\text{GeV}$	457053	438280	$\pm$ 210	7879	$\pm$ 97	9649	$\pm$ 27	879.7	$\pm$ 2.8	381.7	$\pm$ 2.3
										720	$\pm$ 190

**Table 88:** Analysis cut flow for  $W^+ \rightarrow \mu^+ \nu$  5 TeV signal selection. Lepton  $p_T$  is required to be over 18 GeV before the final cut.

Cut	Data	Signal		$W^\pm \rightarrow \ell^\pm \nu$ BG		$Z \rightarrow \ell\ell$		Top		Diboson	Multijet
One muon	9570104	2100770	$\pm$ 410	83110	$\pm$ 270	2019400	$\pm$ 2200	71602	$\pm$ 94	3442	$\pm$ 63
Muon trig matched	9382783	1840550	$\pm$ 390	72820	$\pm$ 250	1750400	$\pm$ 2000	61519	$\pm$ 87	2956	$\pm$ 59
Isolation	3905612	1821750	$\pm$ 380	71780	$\pm$ 250	595700	$\pm$ 1100	56849	$\pm$ 84	2916	$\pm$ 59
$p_T^\mu > 25\text{GeV}$	1930655	1393330	$\pm$ 340	34470	$\pm$ 170	170840	$\pm$ 490	49338	$\pm$ 78	2471	$\pm$ 54
$E_T^{\text{miss}} > 25\text{GeV}$	1321407	1173860	$\pm$ 310	21450	$\pm$ 140	51090	$\pm$ 180	41956	$\pm$ 72	1930	$\pm$ 49
$m_T > 50\text{GeV}$	1244892	1153800	$\pm$ 310	18270	$\pm$ 130	38304	$\pm$ 81	32375	$\pm$ 63	1705	$\pm$ 44
										9040	$\pm$ 800

**Table 89:** Analysis cut flow for  $W^+ \rightarrow \mu^+ \nu$  13 TeV signal selection. Lepton  $p_T$  is required to be over 18 GeV before the final cut.

2615 muon (electron) decay channel. In the ratio panels, the grey band is the total systematic uncertainty,  
 2616 whilst the brown band adds the MC statistical uncertainty in quadrature on top of it. In regions  
 2617 of the distributions insensitive to the modelling of  $p_T^W$  there is generally good agreement between  
 2618 data and predictions. The bulk of the  $m_T$  distribution is a typical example of distribution that is  
 2619 mostly insensitive to the modeling of  $p_T^W$ . The  $u_T$  distribution is an exception, and it can therefore be  
 2620 concluded that the baseline simulation is not modeling  $p_T^W$  satisfactorily.

Cut	Data	Signal	$W^\pm \rightarrow \ell^\pm v$ BG		$Z \rightarrow \ell\ell$		Top		Diboson	Multijet
One electron	1724472	374900 $\pm$ 200	24150	$\pm$ 160	41995	$\pm$ 70	1590.5	$\pm$ 2.9	684.8 $\pm$ 4	-
Electron trig matched	1645694	359010 $\pm$ 200	22070	$\pm$ 160	39854	$\pm$ 68	1539.9	$\pm$ 2.9	655.7 $\pm$ 3.9	-
Isolation	1176976	357660 $\pm$ 200	21920	$\pm$ 160	39686	$\pm$ 68	1504.6	$\pm$ 2.8	640.7 $\pm$ 3.8	-
$p_T^e > 25\text{GeV}$	529183	302070 $\pm$ 180	11920	$\pm$ 110	30214	$\pm$ 52	1330.8	$\pm$ 2.6	532.9 $\pm$ 3.5	-
$E_T^{\text{miss}} > 25\text{GeV}$	281957	266750 $\pm$ 170	8084	$\pm$ 90	1293	$\pm$ 20	1112.5	$\pm$ 2.4	380 $\pm$ 3	-
$m_T > 50\text{GeV}$	274329	264540 $\pm$ 170	7317	$\pm$ 84	994	$\pm$ 16	855.2	$\pm$ 2.1	338.1 $\pm$ 2.9	2400 $\pm$ 500

**Table 810:** Analysis cut flow for  $W^- \rightarrow e^- \nu$  5 TeV signal selection. Lepton  $p_T$  is required to be over 18 GeV before the final cut.

Cut	Data	Signal	$W^\pm \rightarrow \ell^\pm \nu$ BG	$Z \rightarrow \ell\ell$	Top	Diboson	Multijet
One electron	7471742	1323710 $\pm$ 330	78230 $\pm$ 230	140980 $\pm$ 140	61951 $\pm$ 86	3059 $\pm$ 58	-
Electron trig matched	7402574	1267710 $\pm$ 330	72240 $\pm$ 230	133580 $\pm$ 140	59950 $\pm$ 85	2968 $\pm$ 57	-
Isolation	4949352	1260540 $\pm$ 330	71550 $\pm$ 230	132740 $\pm$ 140	58689 $\pm$ 84	2937 $\pm$ 57	-
$p_T^e > 25\text{GeV}$	2113364	1053510 $\pm$ 300	39660 $\pm$ 160	101350 $\pm$ 110	52923 $\pm$ 79	2544 $\pm$ 53	-
$E_T^{\text{miss}} > 25\text{GeV}$	1008915	900640 $\pm$ 280	25900 $\pm$ 130	7954 $\pm$ 45	45065 $\pm$ 73	1962 $\pm$ 48	-
$m_T > 50\text{GeV}$	949362	887810 $\pm$ 270	22400 $\pm$ 120	6052 $\pm$ 35	34177 $\pm$ 64	1695 $\pm$ 44	27400 $\pm$ 2000

**Table 811:** Analysis cut flow for  $W^- \rightarrow e^- \nu$  13 TeV signal selection. Lepton  $p_T$  is required to be over 18 GeV before the final cut.

Cut	Data	Signal		$W^\pm \rightarrow \ell^\pm \nu$ BG		$Z \rightarrow \ell\ell$		Top		Diboson	Multijet
One muon	2075709	440560	$\pm$ 220	22510	$\pm$ 170	34440	$\pm$ 80	1835.6	$\pm$ 3.1	751.5	$\pm$ 3.3
Muon trig matched	2002955	383720	$\pm$ 200	19640	$\pm$ 160	30277	$\pm$ 75	1561.6	$\pm$ 2.9	648	$\pm$ 3.1
Isolation	883078	381010	$\pm$ 200	19450	$\pm$ 160	30046	$\pm$ 74	1411	$\pm$ 2.7	616.9	$\pm$ 2.9
$p_T^\mu > 25\text{GeV}$	426119	314370	$\pm$ 180	9370	$\pm$ 110	20749	$\pm$ 56	1202.1	$\pm$ 2.5	505	$\pm$ 2.5
$E_T^{\text{miss}} > 25\text{GeV}$	298992	276060	$\pm$ 170	5893	$\pm$ 89	8716	$\pm$ 29	1004.2	$\pm$ 2.3	372.6	$\pm$ 2
$m_T > 50\text{GeV}$	287870	273710	$\pm$ 170	5158	$\pm$ 82	8408	$\pm$ 26	788.2	$\pm$ 2	335.6	$\pm$ 1.9

**Table 812:** Analysis cut flow for  $W^- \rightarrow \mu^-\nu$  5 TeV signal selection. Lepton  $p_T$  is required to be over 18 GeV before the final cut.

Cut	Data	Signal		$W^\pm \rightarrow \ell^\pm \nu$ BG		$Z \rightarrow \ell\ell$		Top		Diboson	Multijet								
One muon	8773414	1518070	$\pm$	360	64930	$\pm$	230	2019900	$\pm$	2200	70580	$\pm$	90	3230	$\pm$	60	-		
Muon trig matched	8597493	1322980	$\pm$	330	56520	$\pm$	210	1750300	$\pm$	2000	60579	$\pm$	84	2806	$\pm$	56	-		
Isolation	3298569	1310310	$\pm$	330	55680	$\pm$	210	593700	$\pm$	1100	55949	$\pm$	80	2751	$\pm$	55	-		
$p_T^\mu > 25\text{GeV}$	1561721	1069770	$\pm$	300	28230	$\pm$	150	166810	$\pm$	490	48544	$\pm$	75	2362	$\pm$	52	-		
$E_T^{\text{miss}} > 25\text{GeV}$	1030406	910150	$\pm$	280	17380	$\pm$	120	47370	$\pm$	180	41259	$\pm$	69	1842	$\pm$	46	-		
$m_T > 50\text{GeV}$	963568	896850	$\pm$	270	14710	$\pm$	110	34572	$\pm$	80	31772	$\pm$	61	1598	$\pm$	43	9050	$\pm$	620

**Table 813:** Analysis cut flow for  $W^- \rightarrow \mu^- \nu$  13 TeV signal selection. Lepton  $p_T$  is required to be over 18 GeV before the final cut.

Selection	Observed	Expected		
5TeV $W^+ \rightarrow e^+ \nu$	430620	431620	$\pm$	600
5TeV $W^+ \rightarrow \mu^+ \nu$	457053	457790	$\pm$	300
5TeV $W^- \rightarrow e^- \nu$	274329	276450	$\pm$	530
5TeV $W^- \rightarrow \mu^- \nu$	287870	289160	$\pm$	250
13TeV $W^+ \rightarrow e^+ \nu$	1207776	1213000	$\pm$	1800
13TeV $W^+ \rightarrow \mu^+ \nu$	1244892	1253490	$\pm$	870
13TeV $W^- \rightarrow e^- \nu$	949362	979500	$\pm$	2000
13TeV $W^- \rightarrow \mu^- \nu$	963568	988560	$\pm$	690

**Table 814:** Observed and Expected yield comparison for all signal selections.

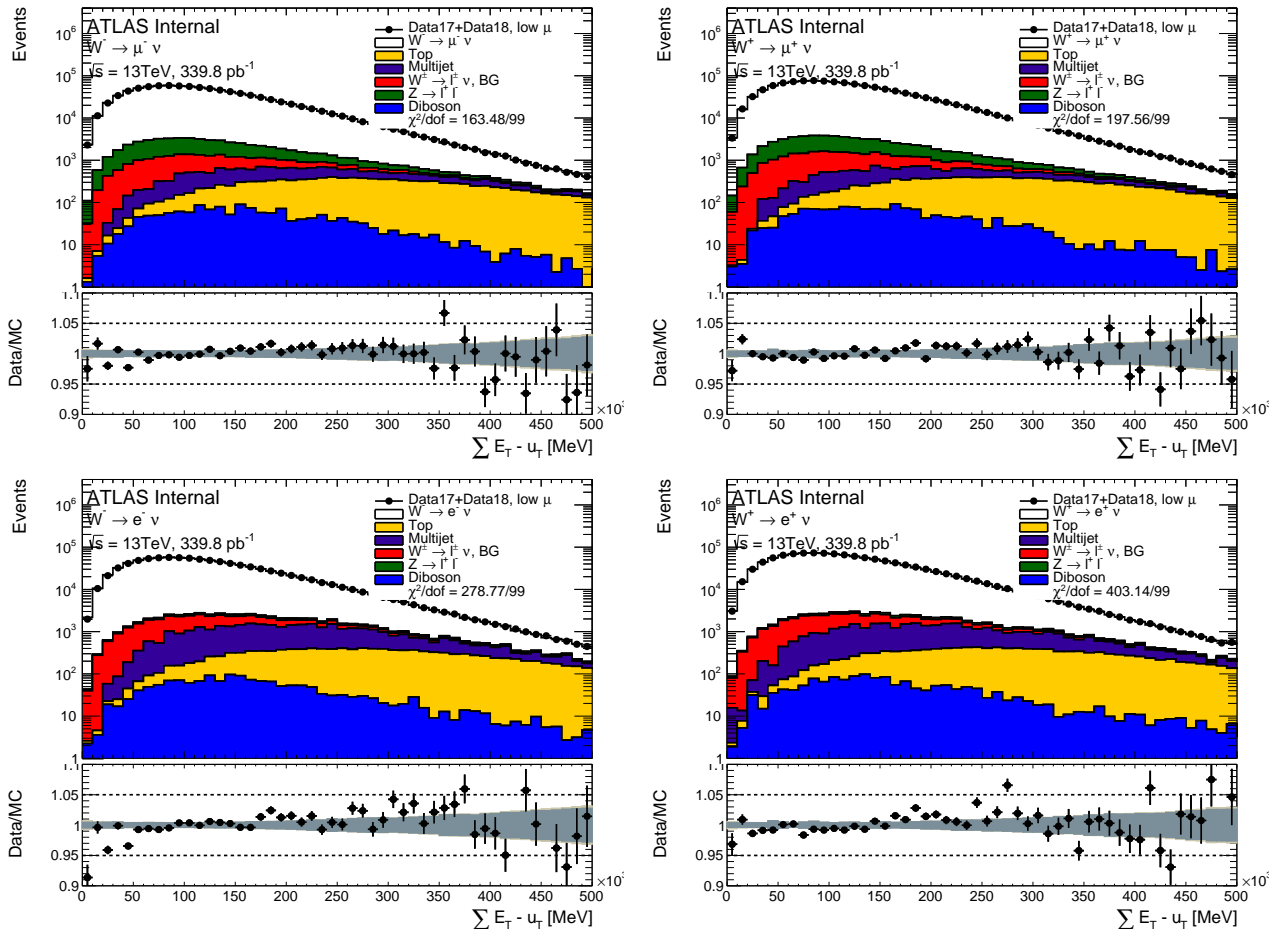


**Figure 89:**  $\Sigma E_T$  distribution in the muon and electron channel for the  $\sqrt{s} = 13$  TeV dataset.

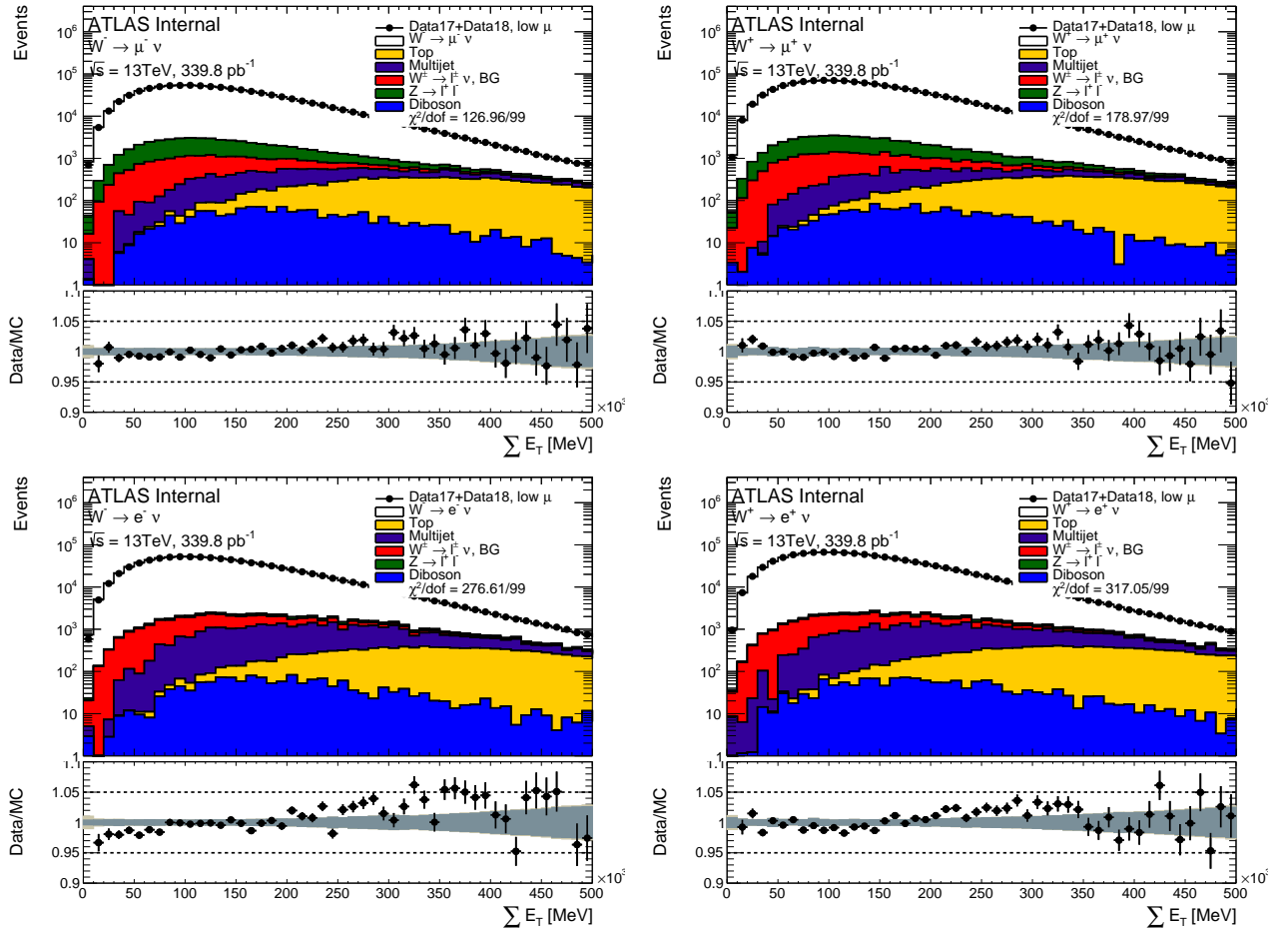


**Figure 810:**  $\Sigma E_T$  distribution in the muon and electron channel for the  $\sqrt{s} = 13$  TeV dataset.

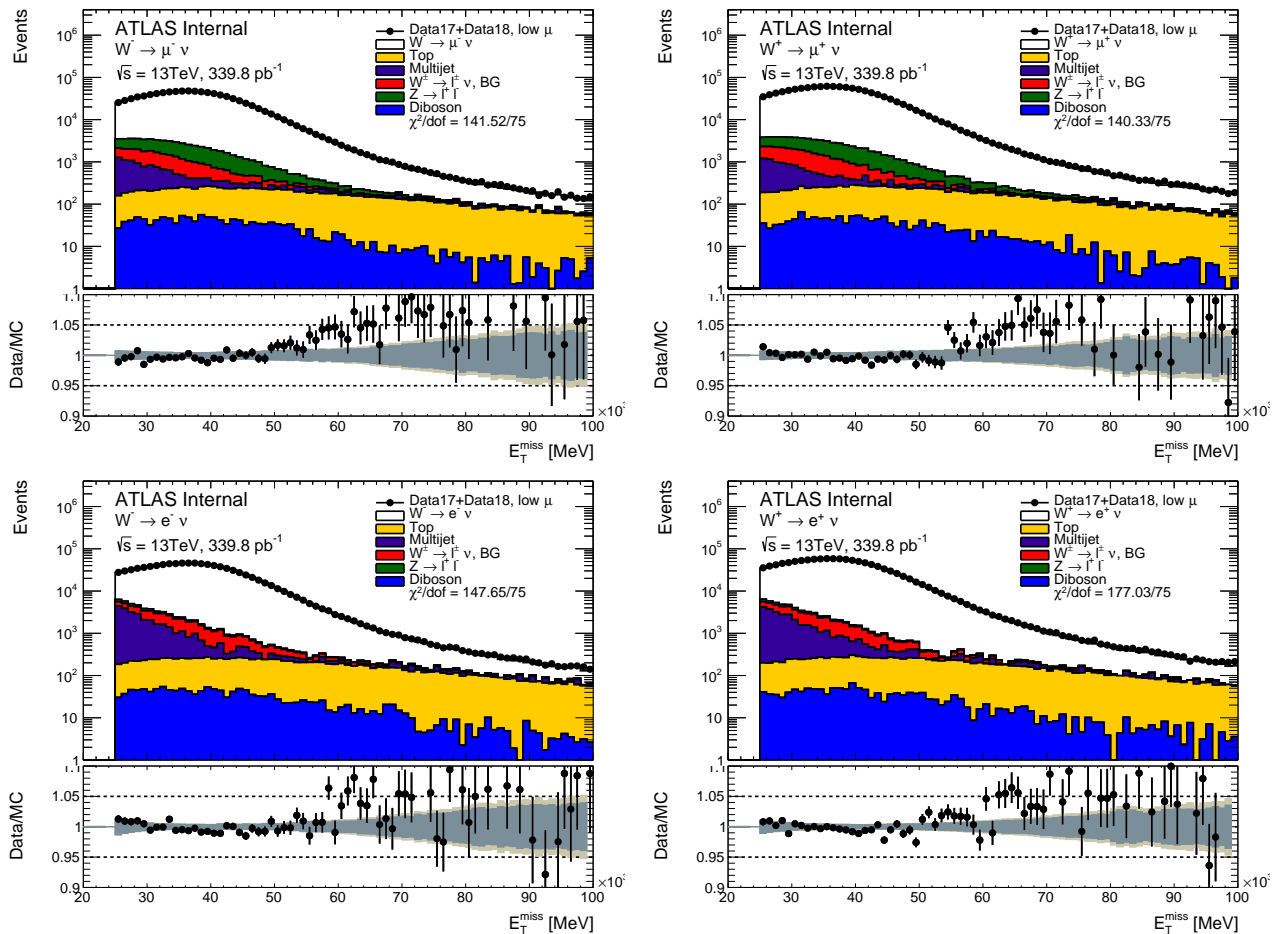
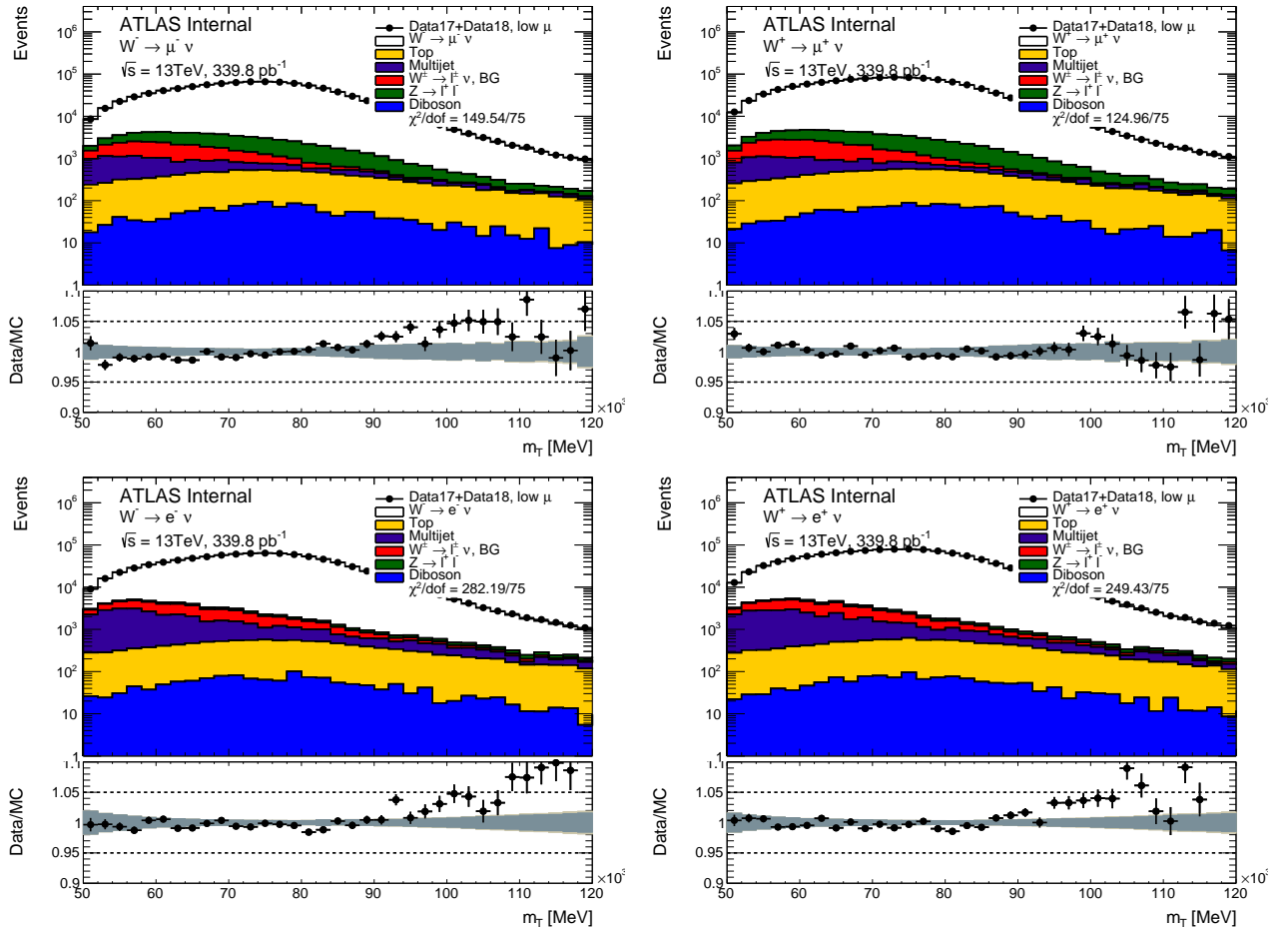
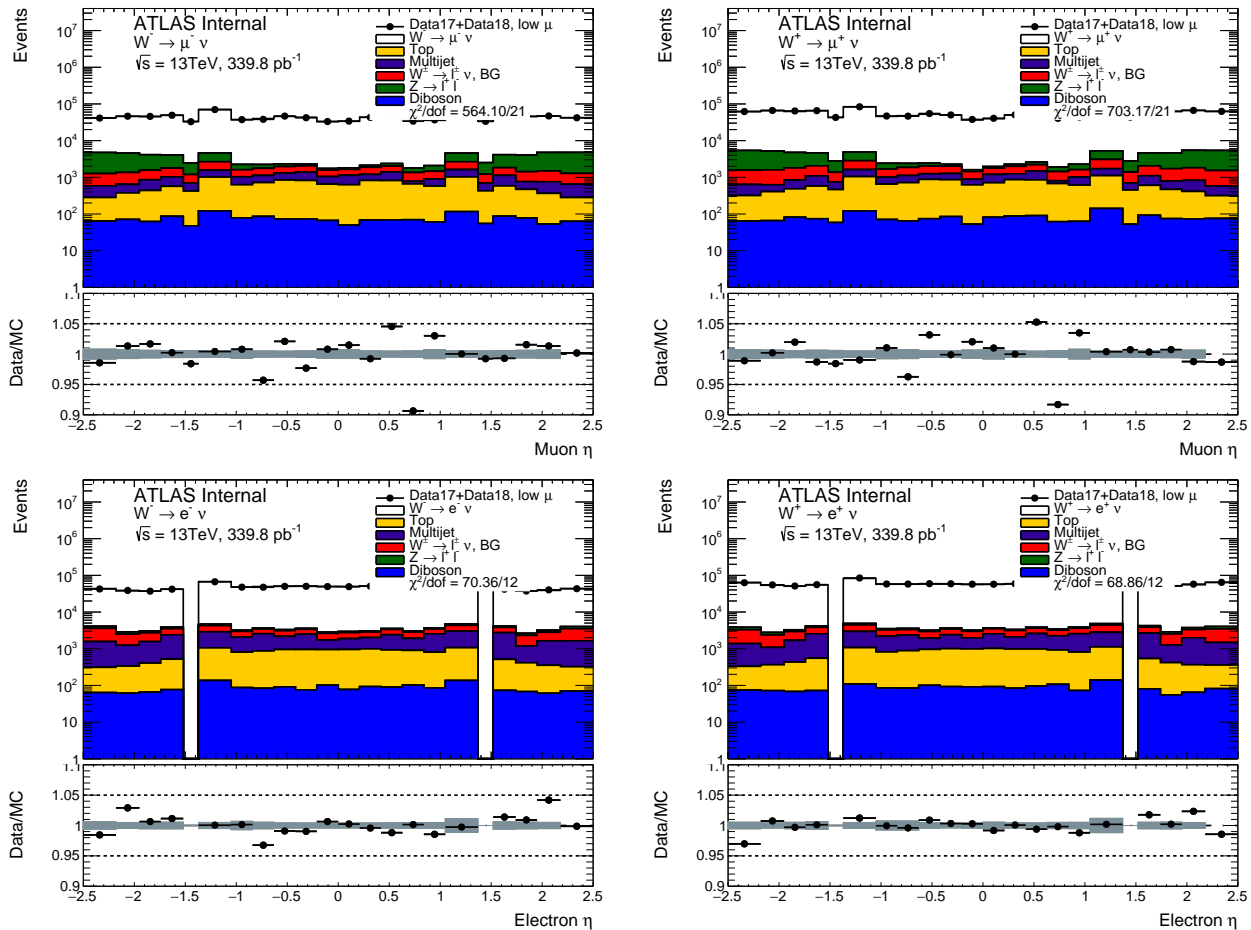


Figure 811:  $\vec{E}_T^{\text{miss}}$  distribution in the muon and electron channel for the  $\sqrt{s} = 13\text{ TeV}$  dataset.



**Figure 812:** Transverse mass distribution of the W boson in the muon and electron channel for the  $\sqrt{s} = 13\text{ TeV}$  dataset.



**Figure 813:** Lepton pseudorapidity distribution in the muon and electron channel for the  $\sqrt{s} = 13 \text{ TeV}$  dataset.

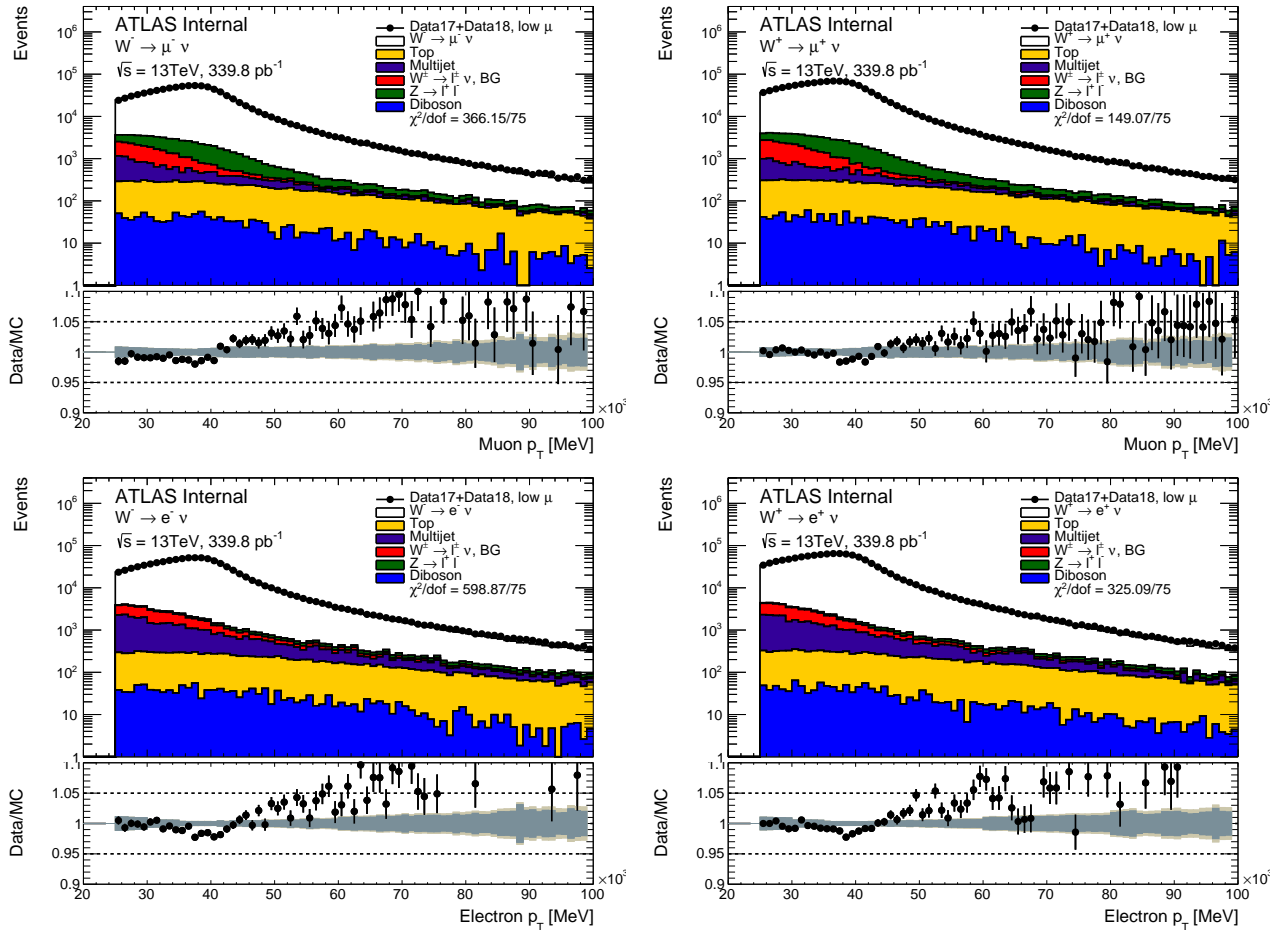


**Figure 814:** Lepton transverse momentum distribution in the muon and electron channel for the  $\sqrt{s} = 13\text{TeV}$  dataset.

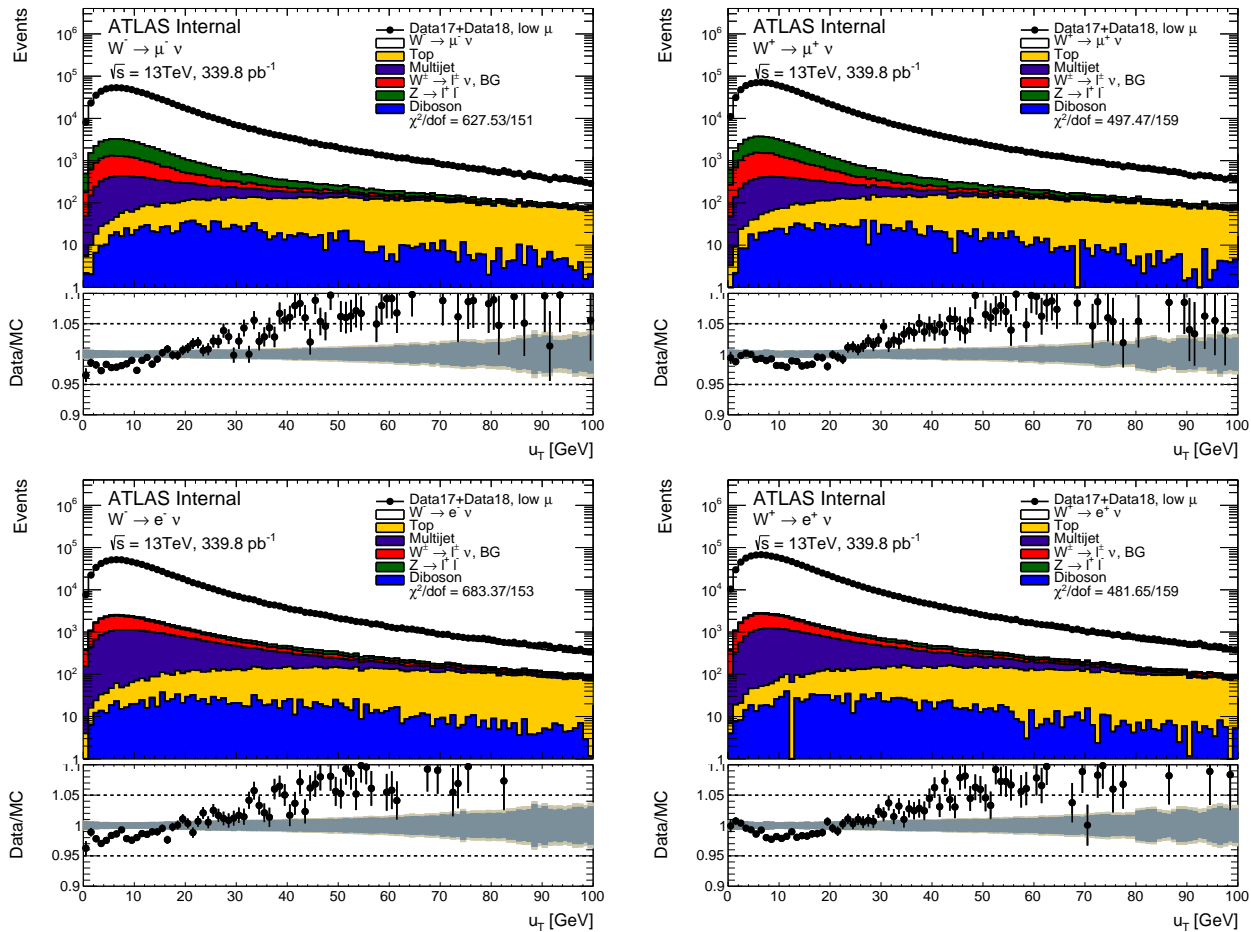


**Figure 815:** W transverse momentum distribution in the muon and electron channel for the  $\sqrt{s} = 13$  TeV dataset.

### 8.4.3 $\sqrt{s} = 5$ TeV dataset control plots

Control plots for the 5 TeV low- $\mu$  dataset are provided here after applying all corrections described in Section 7, and after applying the selection described above in this section. In each figure, the right(left)-hand column shows distributions for the  $W^+$  ( $W^-$ ) process. The top (bottom) row shows the muon (electron) decay channel. In the ratio panels, the grey band is the total systematic uncertainty, whilst the brown band adds the MC statistical uncertainty in quadrature on top of it. In regions of the distributions insensitive to the modelling of  $p_T^W$  there is generally good agreement between data and predictions. The bulk of the  $m_T$  distribution is a typical example of distribution that is mostly insensitive to the modeling of  $p_T^W$ . Compared to the 13 TeV situation, the  $u_T$  distribution seems to indicate that the baseline simulation models  $p_T^W$  more satisfactorily.

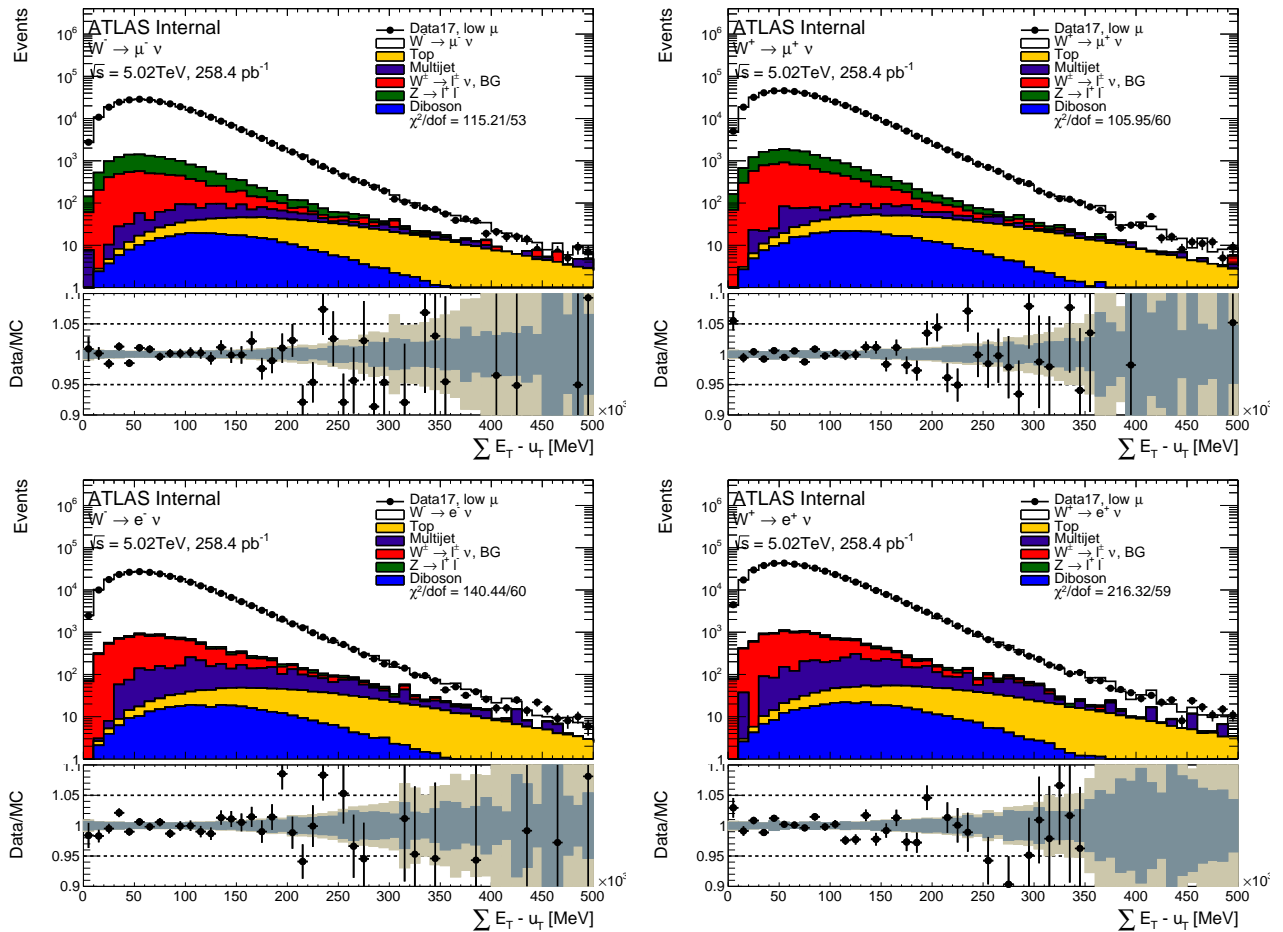


**Figure 816:**  $\Sigma E_T$  distribution in the muon and electron channel for the  $\sqrt{s} = 5$  TeV dataset.

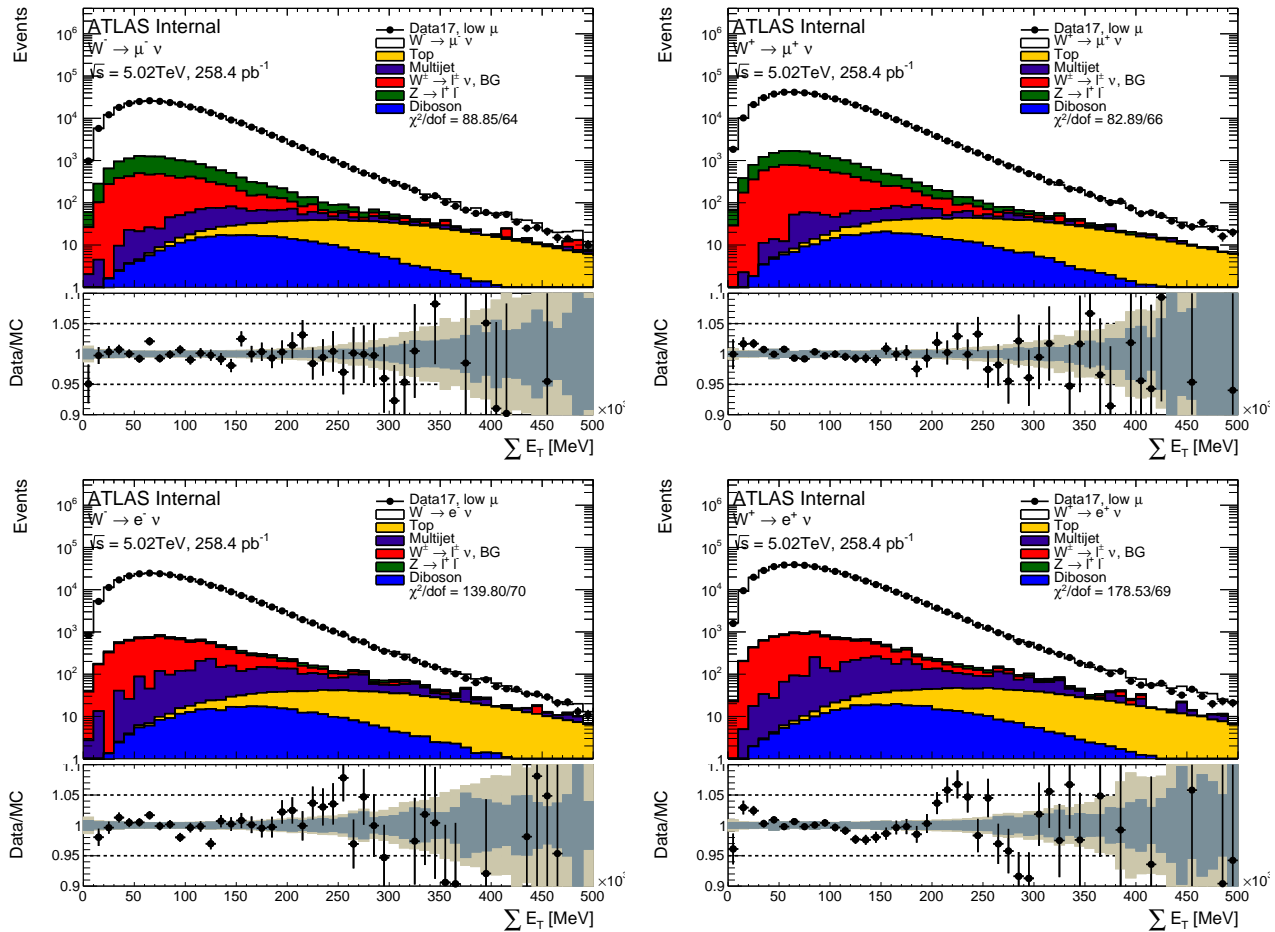
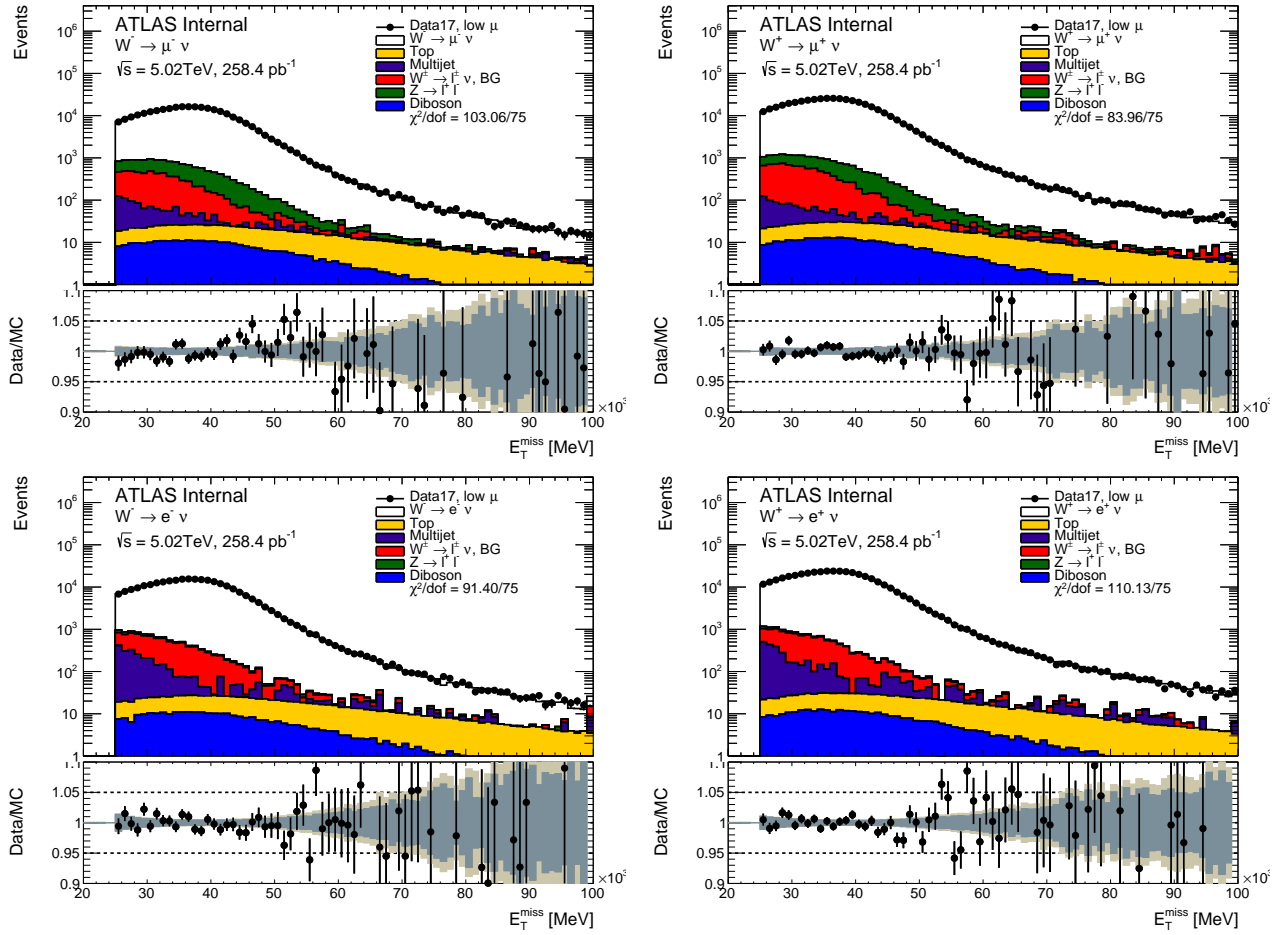
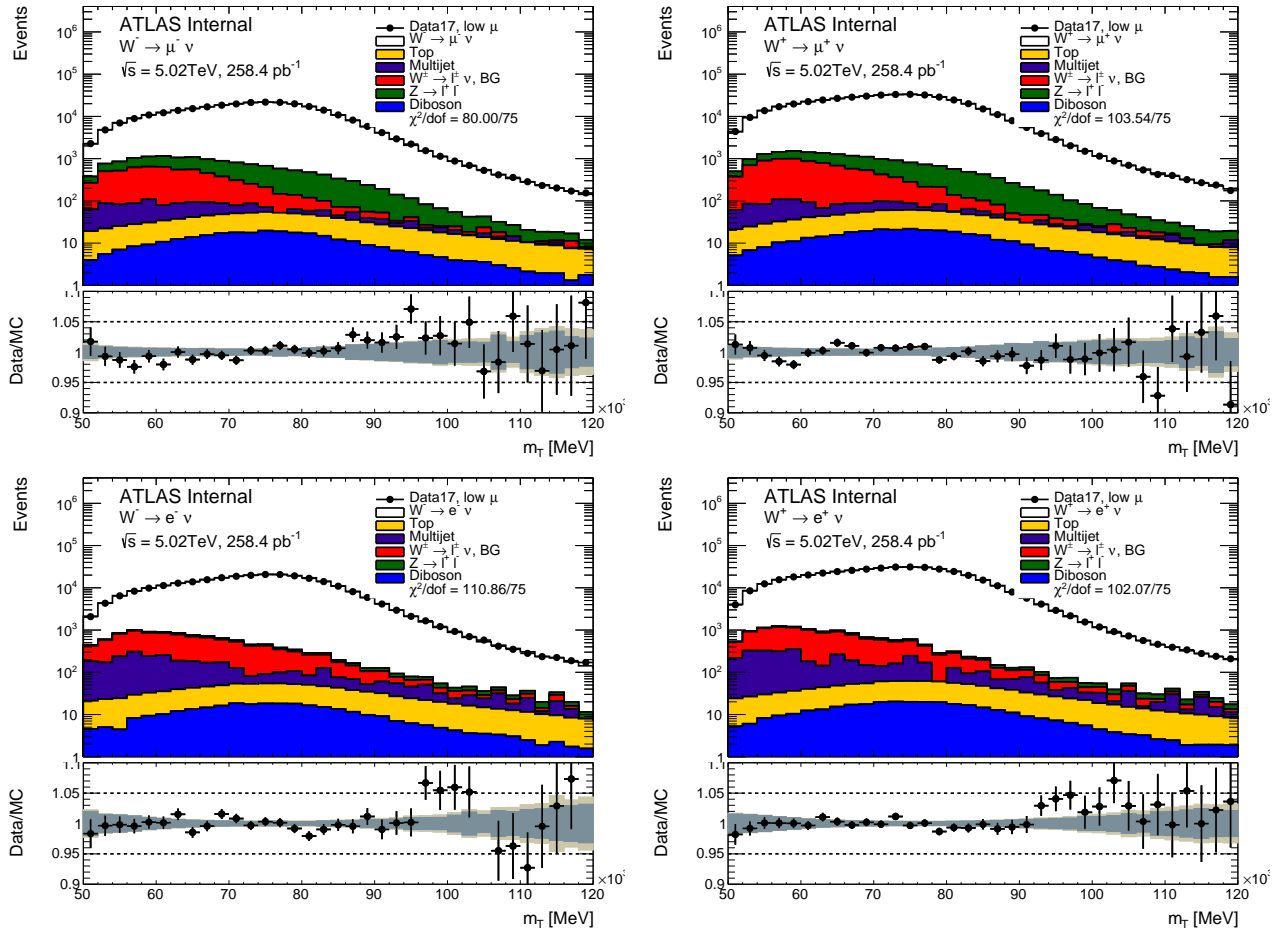


Figure 817:  $\Sigma E_T$  distribution in the muon and electron channel for the  $\sqrt{s} = 5$  TeV dataset.



**Figure 818:**  $\vec{E}_T^{miss}$  distribution in the muon and electron channel for the  $\sqrt{s} = 5$  TeV dataset.



**Figure 819:** Transverse mass distribution of the  $W$  boson in the muon and electron channel for the  $\sqrt{s} = 5$  TeV dataset.

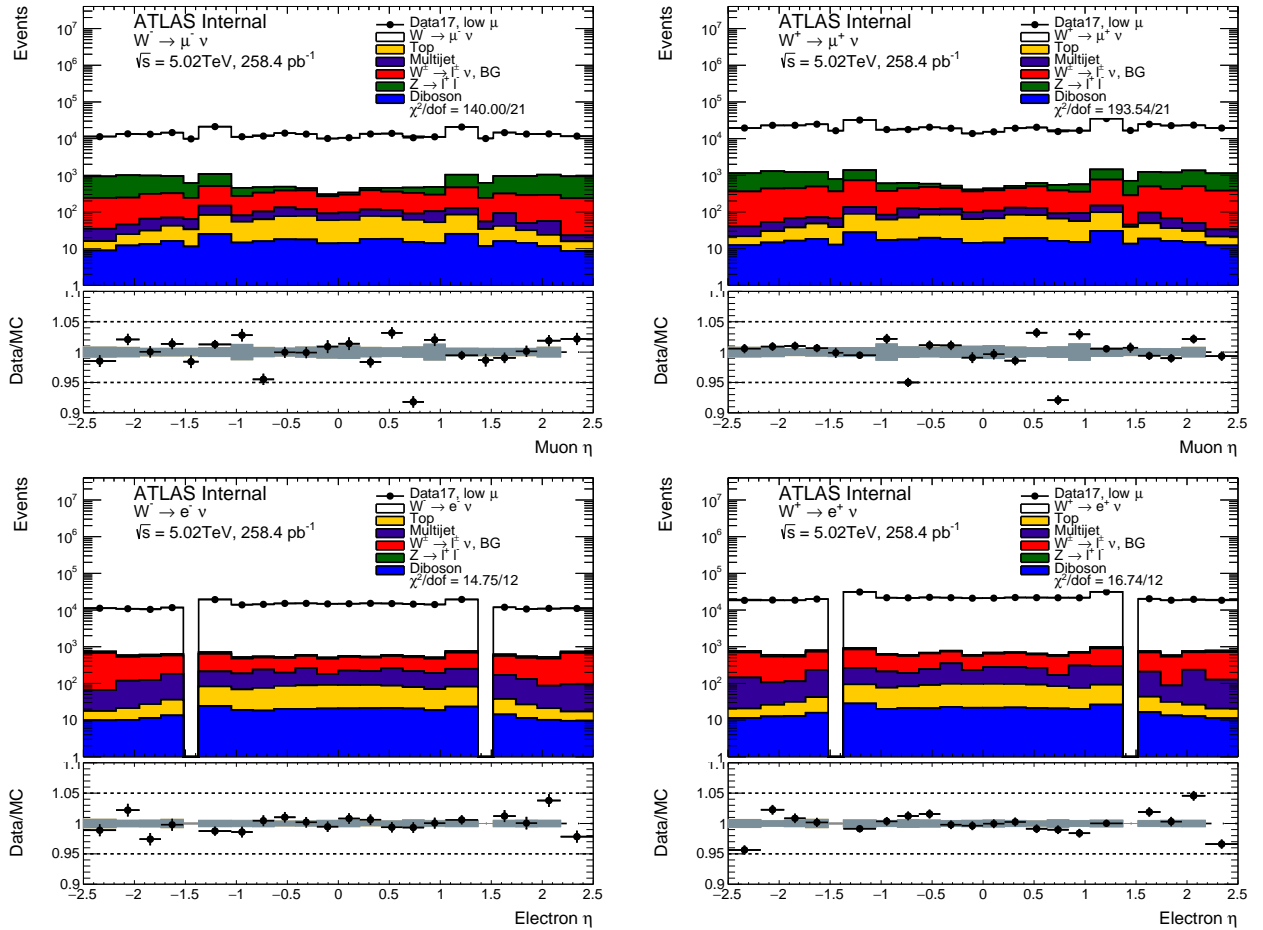


**Figure 820:** Lepton pseudorapidity distribution in the muon and electron channel for the  $\sqrt{s} = 5\text{ TeV}$  dataset.

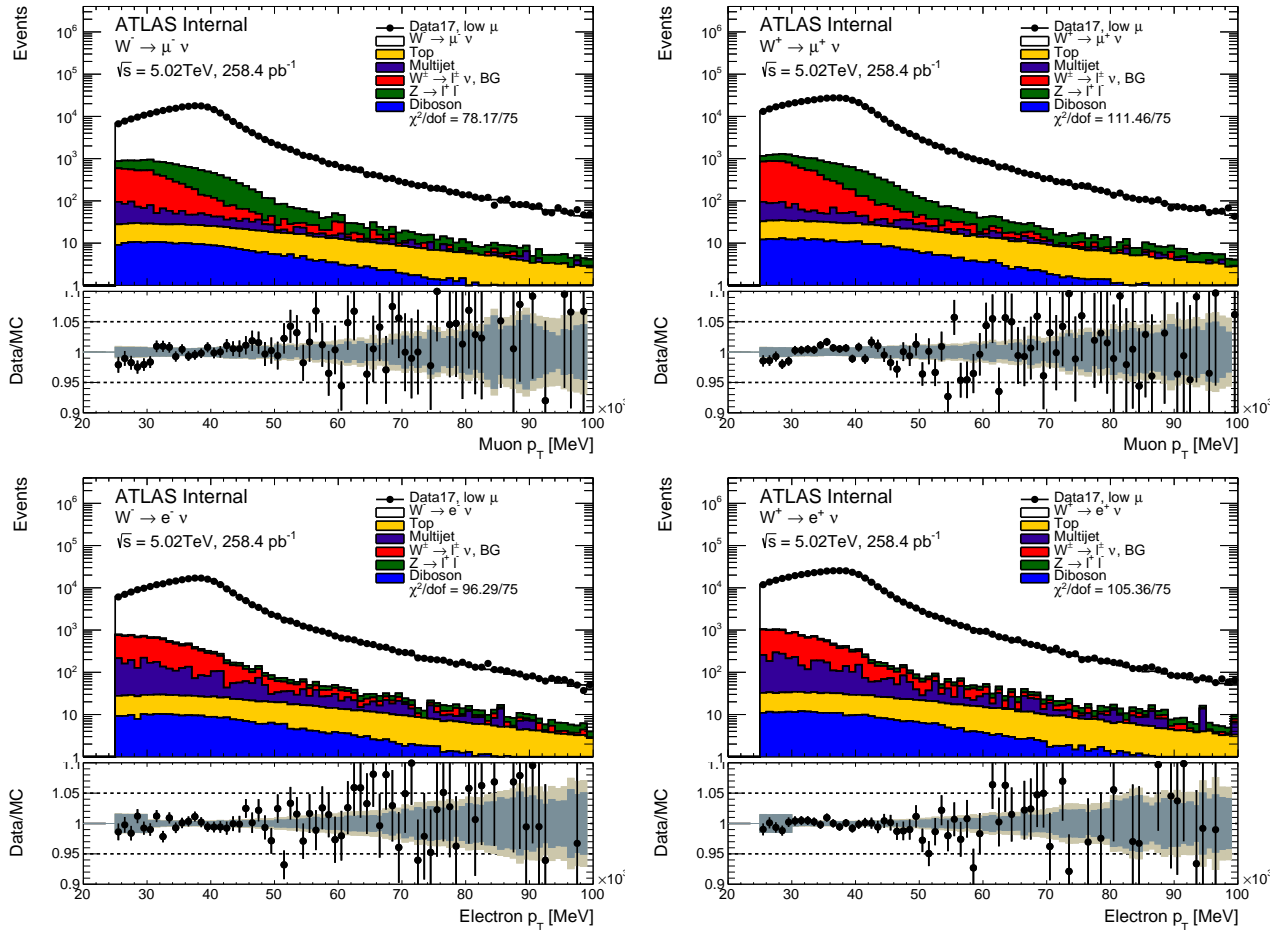


**Figure 821:** Lepton transverse momentum distribution in the muon and electron channel for the  $\sqrt{s} = 5\text{ TeV}$  dataset.

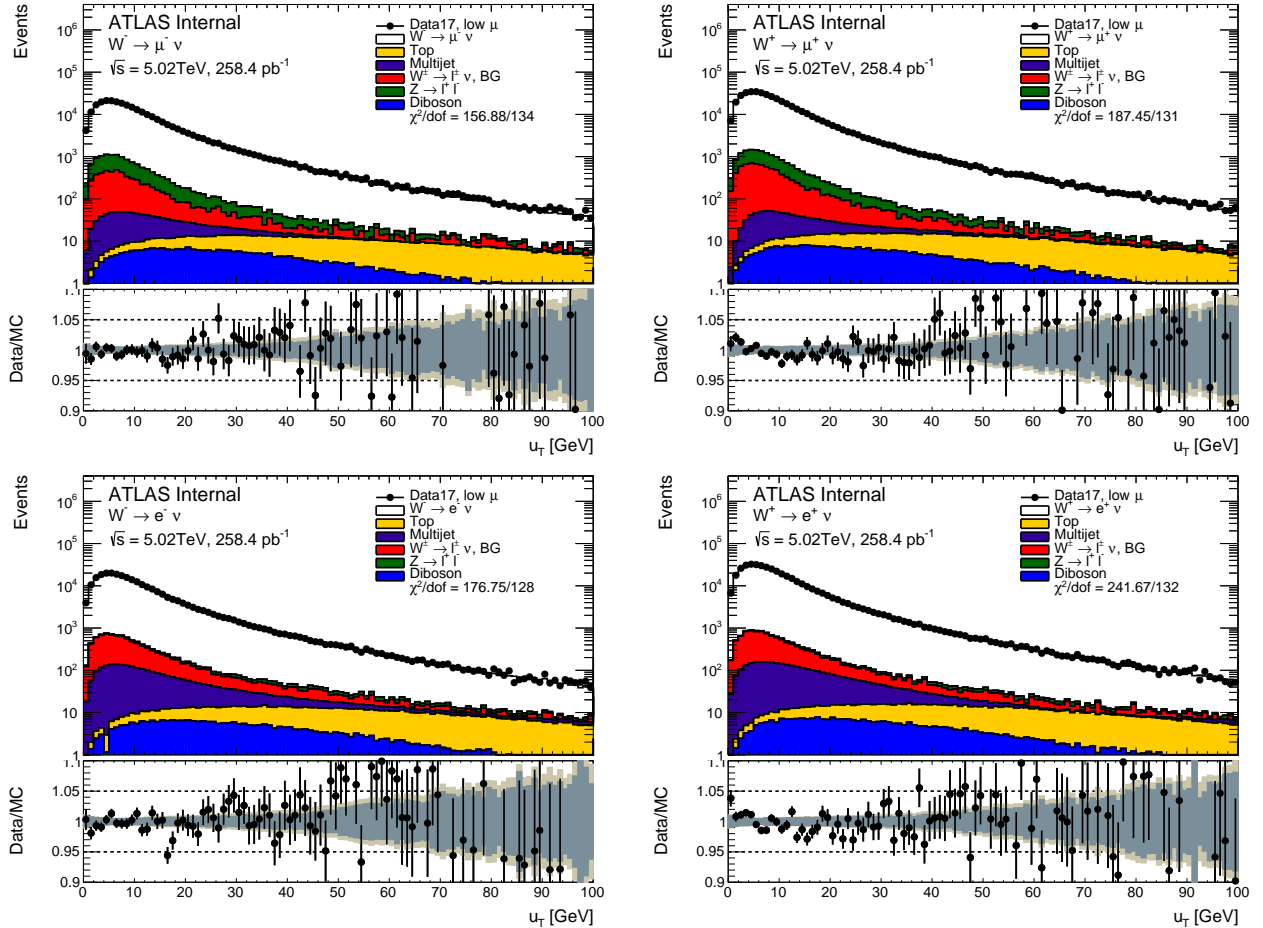


**Figure 822:**  $W$  transverse momentum distribution in the muon and electron channel for the  $\sqrt{s} = 5 \text{ TeV}$  dataset.

---

2631 **Bibliography**

- 2632 [1] Jan Kretzschmar. *Samples and Physics modelling for low pile-up runs taken in 2017 and 2018.*  
2633 Tech. rep. ATL-COM-PHYS-2019-075. Geneva: CERN, Feb. 2019. URL: [https://cds.cern.ch/](https://cds.cern.ch/record/2657141)  
2634 record/2657141.
- 2635 [2] Jan Kretzschmar. *Samples and Physics modelling for low pile-up runs taken in 2017 and 2018.*  
2636 Tech. rep. ATL-COM-PHYS-2019-075. Geneva: CERN, Feb. 2019. URL: [https://cds.cern.ch/record/2206965](https://cds.cern.ch/</a><br/>2637 record/2657141.</p><p>2638 [3] Paolo Nason. “A New method for combining NLO QCD with shower Monte Carlo algorithms”.<br/>2639 In: <i>JHEP</i> 11 (2004), p. 040. doi: 10.1088/1126-6708/2004/11/040. arXiv: hep-ph/0409146.</p><p>2640 [4] Stefano Frixione, Paolo Nason, and Carlo Oleari. “Matching NLO QCD computations with Parton<br/>2641 Shower simulations: the POWHEG method”. In: <i>JHEP</i> 11 (2007), p. 070. doi: 10.1088/1126-<br/>2642 6708/2007/11/070. arXiv: 0709.2092 [hep-ph].</p><p>2643 [5] Simone Alioli et al. “NLO vector-boson production matched with shower in POWHEG”. In: <i>JHEP</i><br/>2644 0807 (2008), p. 060. doi: 10.1088/1126-6708/2008/07/060. arXiv: 0805.4802 [hep-ph].</p><p>2645 [6] Simone Alioli et al. “A general framework for implementing NLO calculations in shower Monte<br/>2646 Carlo programs: the POWHEG BOX”. In: <i>JHEP</i> 06 (2010), p. 043. doi: 10.1007/JHEP06(2010)043.<br/>2647 arXiv: 1002.2581 [hep-ph].</p><p>2648 [7] T. Sjöstrand, S. Mrenna, and P. Skands. “Brief Introduction to PYTHIA 8.1”. In: <i>Comput. Phys.<br/>2649 Comm.</i> 178 (2008), p. 85. doi: 10.1016/j.cpc.2008.01.036. arXiv: 0710.3820v1 [hep-ph].</p><p>2650 [8] ATLAS Collaboration. “Measurement of the <math>Z/\gamma^*</math> boson transverse momentum distribution in<br/>2651 <math>pp</math> collisions at <math>\sqrt{s} = 7\text{ TeV}</math> with the ATLAS detector”. In: <i>JHEP</i> 09 (2014), p. 145. doi: 10.1007/<br/>2652 JHEP09(2014)145. arXiv: 1406.3660 [hep-ex].</p><p>2653 [9] Piotr Gonolka and Zbigniew Was. “PHOTOS Monte Carlo: A Precision tool for QED corrections<br/>2654 in <math>Z</math> and <math>W</math> decays”. In: <i>Eur. Phys. J.</i> C45 (2006), pp. 97–107. doi: 10.1140/epjc/s2005-02396-4.<br/>2655 arXiv: hep-ph/0506026.</p><p>2656 [10] Stefan Höche et al. “NLO matrix elements and truncated showers”. In: <i>JHEP</i> 1108 (2011), p. 123.<br/>2657 doi: 10.1007/JHEP08(2011)123. arXiv: 1009.1127 [hep-ph].</p><p>2658 [11] Richard D. Ball et al. “Parton distributions with LHC data”. In: <i>Nucl. Phys. B</i> 867 (2013), p. 244.<br/>2659 doi: 10.1016/j.nuclphysb.2012.10.003. arXiv: 1207.1303 [hep-ph].</p><p>2660 [12] ATLAS Collaboration. <i>The Pythia 8 A3 tune description of ATLAS minimum bias and inelastic</i><br/>2661 <i>measurements incorporating the Donnachie–Landshoff diffractive model.</i> ATL-PHYS-PUB-2016-017.<br/>2662 2016. URL: <a href=).
- 2663 [13] S. Catani and M. Grazzini. “An NNLO subtraction formalism in hadron collisions and its  
2664 application to Higgs boson production at the LHC”. In: *Phys. Rev. Lett.* 98 (2007), p. 222002. doi:  
2665 10.1103/PhysRevLett.98.222002. arXiv: hep-ph/0703012 [hep-ph].

- 2666 [14] S. Catani et al. “Vector boson production at hadron colliders: A Fully exclusive QCD calculation  
2667 at NNLO”. In: *Phys. Rev. Lett.* 103 (2009), p. 082001. doi: 10.1103/PhysRevLett.103.082001.  
2668 arXiv: 0903.2120 [hep-ph].
- 2669 [15] L.A. Harland-Lang, A. D. Martin, P. Motylinski, R. S. Thorne. “Parton distributions in the LHC  
2670 era: MMHT 2014 PDFs”. In: *Eur. Phys. J. C* 75.5 (2015), p. 204. doi: 10.1140/epjc/s10052-015-  
2671 3397-6. arXiv: 1412.3989 [hep-ph].
- 2672 [16] ATLAS Collaboration. “Measurement of  $W^\pm$  and Z-boson production cross sections in  $pp$  col-  
2673 lisions at  $\sqrt{s} = 13\text{TeV}$  with the ATLAS detector”. In: *Phys. Lett. B* 759 (2016), p. 601. doi:  
2674 10.1016/j.physletb.2016.06.023. arXiv: 1603.09222 [hep-ex].
- 2675 [17] ATLAS Collaboration. “Measurements of W and Z boson production in  $pp$  collisions at  $\sqrt{s} =$   
2676 5.02 TeV with the ATLAS detector”. In: *Eur. Phys. J. C* 79 (2019), p. 128. doi: 10.1140/epjc/  
2677 s10052-019-6622-x. arXiv: 1810.08424 [hep-ex].
- 2678 [18] Michal Czakon and Alexander Mitov. “Top++: A Program for the Calculation of the Top-Pair  
2679 Cross-Section at Hadron Colliders”. In: *Comput. Phys. Commun.* 185 (2014), p. 2930. doi: 10.  
2680 1016/j.cpc.2014.06.021. arXiv: 1112.5675 [hep-ph].
- 2681 [19] CMS Colaboration. “Measurement of the inclusive  $t\bar{t}$  cross section in  $pp$  collisions at  $\sqrt{s} = 5.02$   
2682 TeV using final states with at least one charged lepton”. In: *JHEP* 03 (2018), p. 115. doi: 10.1007/  
2683 JHEP03(2018)115. arXiv: 1711.03143 [hep-ex].
- 2684 [20] Tairan Xu and Maarten Boonekamp. *Multi-jet background in low-pile-up runs taken in 2017 and*  
2685 *2018*. Tech. rep. ATL-COM-PHYS-2019-076. Geneva: CERN, July 2019. URL: <https://cds.cern.ch/record/2657146>.



# 9

## W boson pT spectrum

2687

2688

### 2689 9.1 Unfolding

2690 The measured W  $p_T$  spectrum is subject to various detector effects (finite resolution and acceptance,  
 2691 reconstruction efficiency, etc.) that distort the true underlying spectrum. Mathematically, the unfolding  
 2692 problem is an integral equation of the following form:

$$\int K(x, y) \cdot f(x) dx = g(y), \quad (9.1)$$

2693 where we seek the function  $f(x)$  assuming that  $g(y)$  and the kernel  $K(x, y)$  are known [1]. The function  
 2694  $g(y)$  is convoluted (or folded) with the kernel hence the name of the problem. In experimental physics  
 2695 it is more common to use binned distributions instead of continuous functions:

$$\sum_i \mathbf{R}_{ij} \cdot \mathbf{T}_i + \mathbf{B}_j = \mathbf{D}_j, \quad (9.2)$$

2696 with  $\mathbf{D}$ ,  $\mathbf{T}$  and  $\mathbf{B}$  being vectors that represent detector-level (measured), truth and background dis-  
 2697 tributions respectively; each vector has  $n$  components that represent the bins in the corresponding  
 2698 distribution. The response matrix  $\mathbf{R}$  represents bin-to-bin migrations caused by the detector effects.  
 2699 The response matrix is usually obtained through MC simulation, along with the corrections for the  
 2700 fiducial volume acceptance and selection efficiency. Each event is simulated on the truth and recon-  
 2701 structed levels, this means that element  $R_{il}$  of the migration matrix contains events that pass both  
 2702 reconstruction and truth cuts (R&T) and would go to bin  $i$  of the truth distribution and to bin  $j$  of  
 2703 the reconstructed distribution. Detector acceptance for bin  $i$  is defined as the ratio  $A_i = \sum_j R_{ij}/T_i$ .  
 2704 Similarly the reconstruction efficiency for bin  $j$  is defined as the ratio  $\epsilon_j = \sum_i R_{ij}/D_j$ . The underlying  
 2705 distribution estimate is presented in the following way:

$$\sum_i \mathbf{V}_{ij} \cdot (\mathbf{D}_i - \mathbf{B}_i) = \mathbf{U}_j, \quad (9.3)$$

2706 where  $U$  vector provides the underlying distribution estimate and  $V$  is the unfolding transformation  
 2707 matrix.

2708 There exist a diverse variety of methods to obtain the unfolding transformation. In the current analysis  
 2709 a Bayesian iterative method is used [2], [3]. The method allows to obtain the unfolding transformation

provided that the response matrix, acceptance and efficiency corrections are known and the number of iterations is given. The number of iterations as well as the unfolded distribution binning are adjusted in order to minimize the unfolding bias and keep the uncertainty below the designated level.

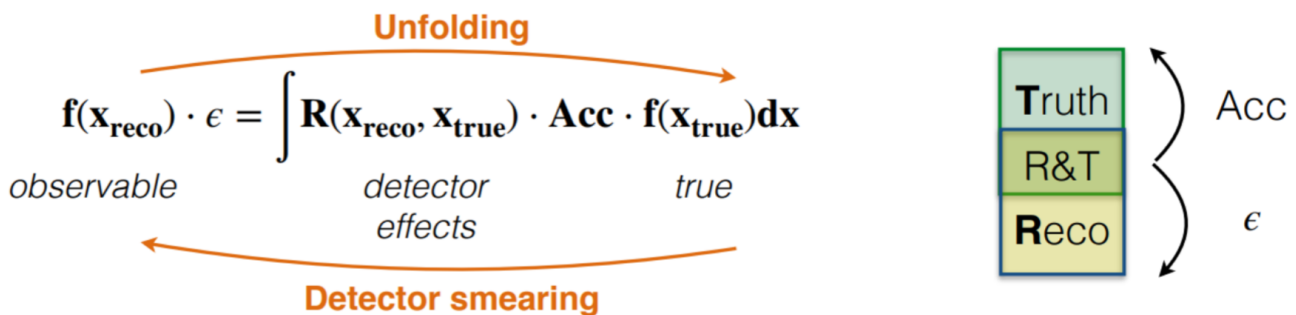


**Figure 91:** Schematic description of the unfolding procedure.

## 9.2 Propagation of uncertainties

The detector-level uncertainties breakdown for the  $p_T$  distribution are presented here. Uncertainties breakdown for the rest of the observables are listed in Appendix A.  
These uncertainties now have to be propagated to the unfolded level.

### 9.2.1 Statistical uncertainty propagation using Bootstrap method

Bootstrap is a computer-based method of dataset parameters estimate and propagation using the analysis distribution resampling. In particular bootstrapping is used for the propagation of statistical uncertainties.  
Both data and MC-simulated datasets have limited number of events, hence the statistical uncertainties due to fluctuations. In order to estimate the statistical uncertainty a number of pseudo-data sets is generated for both data and MC where each event is assigned a random weight  $w$ :

$$w = \mathcal{P}(n, 1), \quad (9.4)$$

where  $n$  is a random number generated with Poisson distribution with mean  $\lambda = 1$ , value  $\mathcal{P}(n, 1)$  is a Poissonian probability of observing  $n$  events while expecting an average of 1 event.  
The bootstrapping defined in this way allows to take into account the correlated effect of statistical fluctuations across all observables and distributions in the analysis. For the determination of statistical uncertainty of the unfolded spectrum 400 bootstrap samples were generated. In both data and MC cases the statistical uncertainty is estimated by composing the covariant matrix  $C_{kl}^{stat}$ :

$$C_{kl}^{stat} = \frac{1}{N_{bs}-1} \sum_{\alpha=1}^{N_{bs}} (U_k^\alpha - \langle U_k \rangle)(U_l^\alpha - \langle U_l \rangle), \quad (9.5)$$

where  $N_{bs}$  is the number of the Bootstrap toys used, vector  $U$  stands for the varied underlying distribution,  $\langle U_k \rangle$  is the average underlying distribution. However, the variation is performed in a different way for Data and MC:

$$U_j^{\alpha,(MC)} = V_{ij}^\alpha \sum_i (D_i - B_i),$$

$$U_j^{\alpha,(Data)} = V_{ij} \sum_i (D_i^\alpha - B_i).$$

- 2730 In the MC case it is the response matrix  $V^\alpha$  to be varied ( $\alpha$  index corresponds to the variation number),  
 2731 whereas in Data the toys are obtained by varying the measured distribution  $D_i^\alpha$ . The statistical  
 2732 uncertainty for both cases is defined as:

$$\delta U_k = \sqrt{C_{kk}^{stat}}. \quad (9.6)$$

### 2733 9.2.2 Systematic uncertainty propagation

Systematic uncertainties are broken down into a number of uncorrelated uncertainty sources, which include signal and background modelling uncertainties, calibration and efficiency uncertainties, physics modelling uncertainties. The systematic variations used for uncertainty estimate on the detector level are propagated to the level of underlying distribution in two different ways. For the background uncertainties:

$$U_j^a = V_{ij} \sum_i (D_i - B_i^a),$$

total background estimate  $B_i^a$  is varied in luminosity and cross-section of every back-ground (index  $a$  numbers the sources of uncertainty). For other sources of systematic uncertainty:

$$U_j^a = V_{ij}^a \sum_i (D_i - B_i),$$

response matrix variation is created. The corresponding covariance matrix is defined as:

$$C_{kj}^a = \delta U_k^a \delta U_l^a,$$

- 2734 where the deltas are  $\delta U_k^a = U_k^a - U_k^{Nom}$ . The total covariance matrix is calculated as a sum:

$$C_{kl}^{tot} = C_{kl}^{stat,Data} + C_{kl}^{stat,MC} + \sum_a C_{kl}^a. \quad (9.7)$$

### 2735 9.2.3 Unfolded uncertainty breakdown

- 2736 Figures 92, 94, contain the systematic uncertainties breakdown for electron and muon channels for  
 2737 the reconstructed level distributions for 5 and 13 TeV. Similarly figures 93, 95 contain unfolded-level  
 2738 uncertainties.

2739 At the detector level the designated level of uncertainty of below 1% is preserved up to 25 GeV for 5  
 2740 TeV datasets and up to 50 GeV for 13 TeV samples in every channel. An increased role of background  
 2741 uncertainty is observed at 13 TeV due to the significantly higher cross-sections of diboson and top-  
 2742 antitop backgrounds. The scale and hierarchy of uncertainties are preserved at the unfolded level.  
 2743 The uncertainties in 5 TeV are dominated by the statistical uncertainty and by the contribution from the  
 2744 hadronic recoil calibration, which is also of statistical nature. On the other hand, at 13 TeV background  
 2745 uncertainty also starts to play a significant role due to increased cross-sections of leading backgrounds.

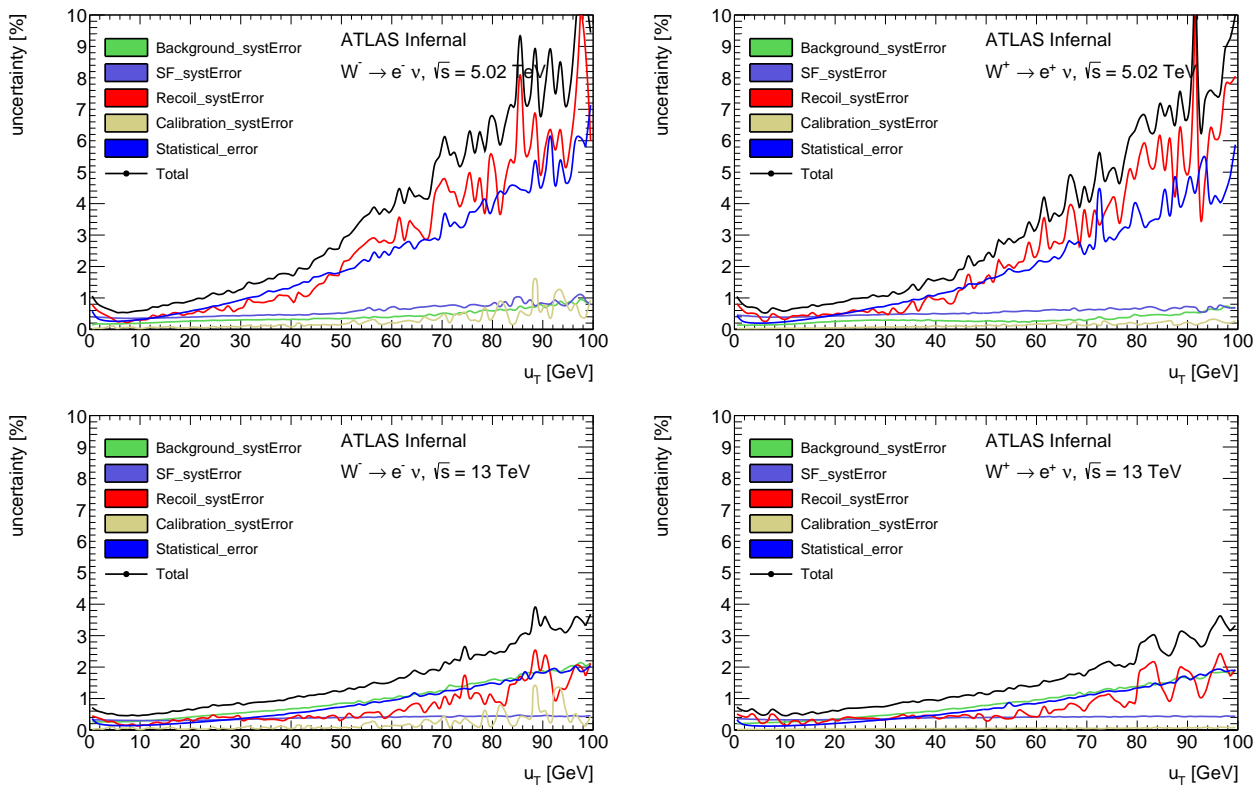


**Figure 92:** Breakdown of systematic uncertainties for 5 (a,b) and 13 (c,d) TeV in the electron channel at the reconstructed level.

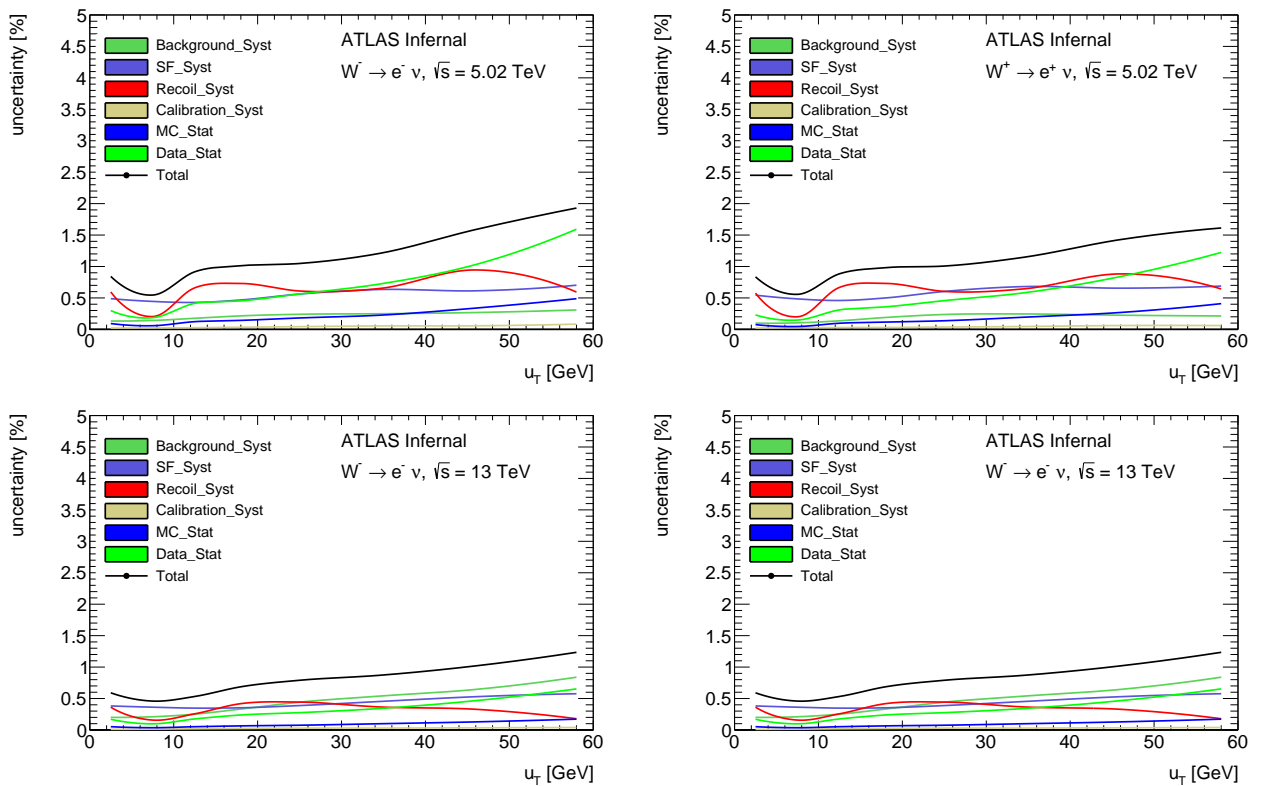


**Figure 93:** Breakdown of systematic uncertainties for 5 (a,b) and 13 TeV (c,d) in the electron channel at the unfolded level.

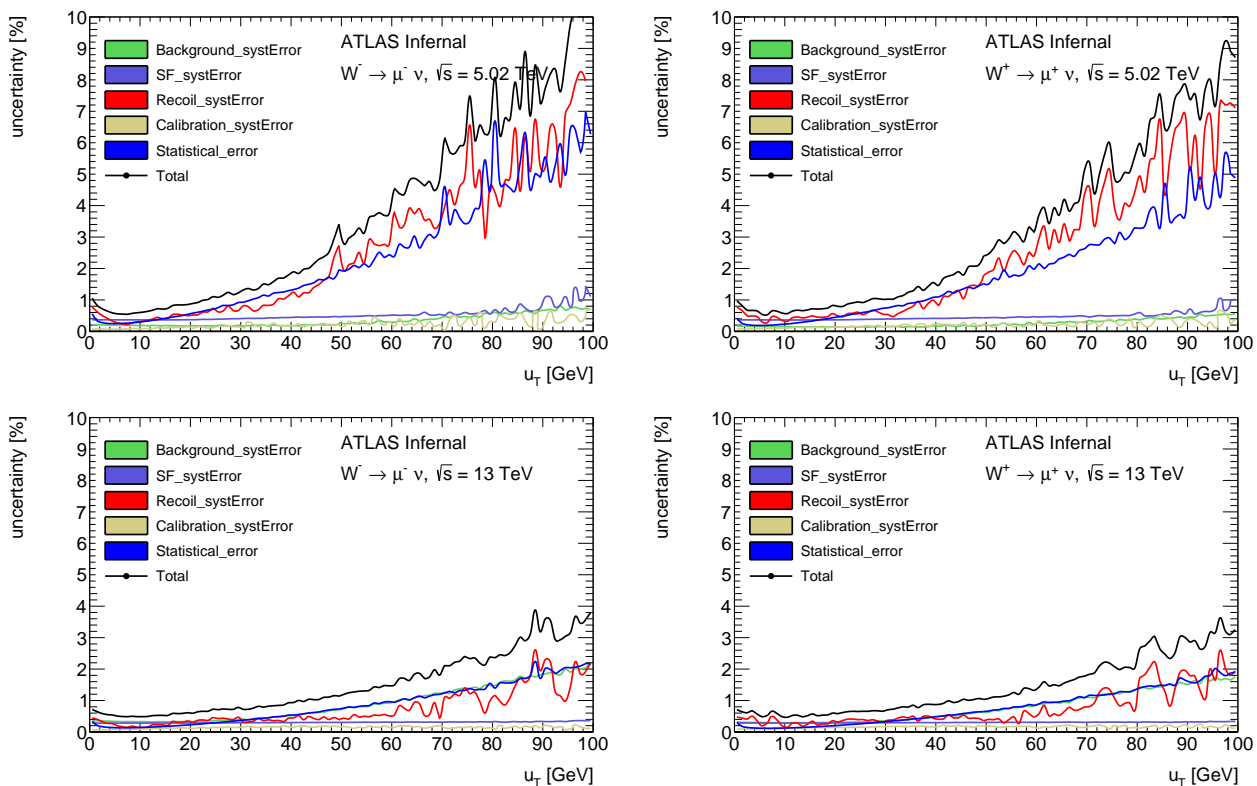


**Figure 94:** Breakdown of systematic uncertainties for 5 (a,b) and 13 (c,d) TeV in the muon channel at the reconstructed level.

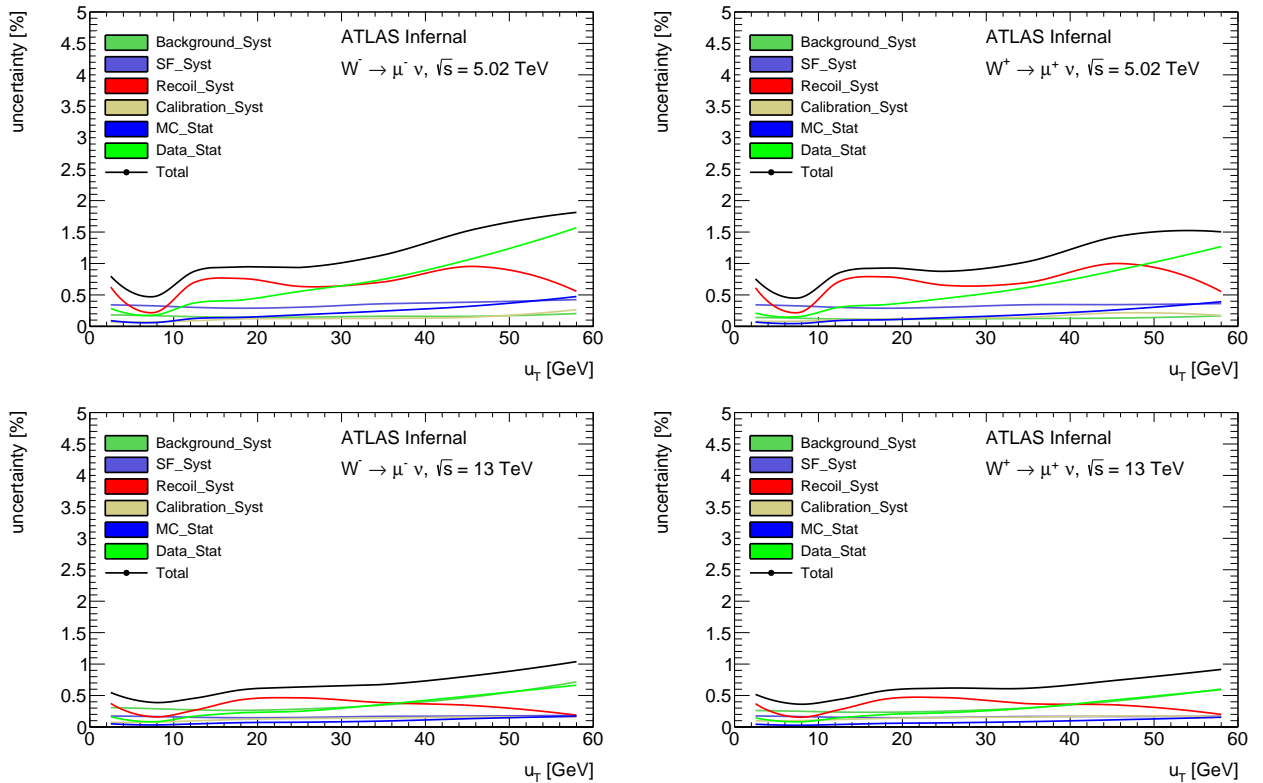


**Figure 95:** Breakdown of systematic uncertainties for 5 (a,b) and 13 TeV (c,d) in the muon channel at the unfolded level.

2746 **9.3 Unfolding bias**

2747 One of the uncertainties associated with unfolding usage is called unfolding bias and may arise because  
2748 the procedure relies on the MC simulation of the distribution, which is used as a prior hypothesis for  
2749 the Bayesian algorithm. Possible discrepancies between the modelled and true distribution lead to  
2750 erroneous bin-to-bin migrations and can lead to distortions of the spectrum.

2751 In order to estimate the bias induced by the unfolding procedure it is necessary to quantify how much  
2752 the unfolded result is impacted by the assumed MC distribution. A set of samples with a different  
2753 distribution at the truth level though compatible at the detector level is generated.

2754

2755 The truth distribution is reweighted until a good agreement between the data and MC is reached at  
2756 the reconstruction level. The agreement is estimated in the kinematic region of  $u_T < 100\text{GeV}$  using the  
2757  $\chi^2$  criterion. The truth reweighting procedure is applied to MC samples with a different distribution:  
2758 PYTHIA8, Sherpa and DYRES were used. Fig. demonstrates the initial difference in the distributions.

2759

2760 The results are presented on fig 96 for 5 GeV bins and 3 unfolding iterations. The obtained bias is  
2761 close to the precision goal of the measurement ( $\sim 1\%$ ) for the 5 TeV dataset. The 13 TeV dataset shows  
2762 a larger bias, which can be explained by a larger discrepancy between data and Monte-Carlo. Worse  
2763 resolution in 13 TeV suggests a necessity to try a broader binning comparing to 5 GeV.

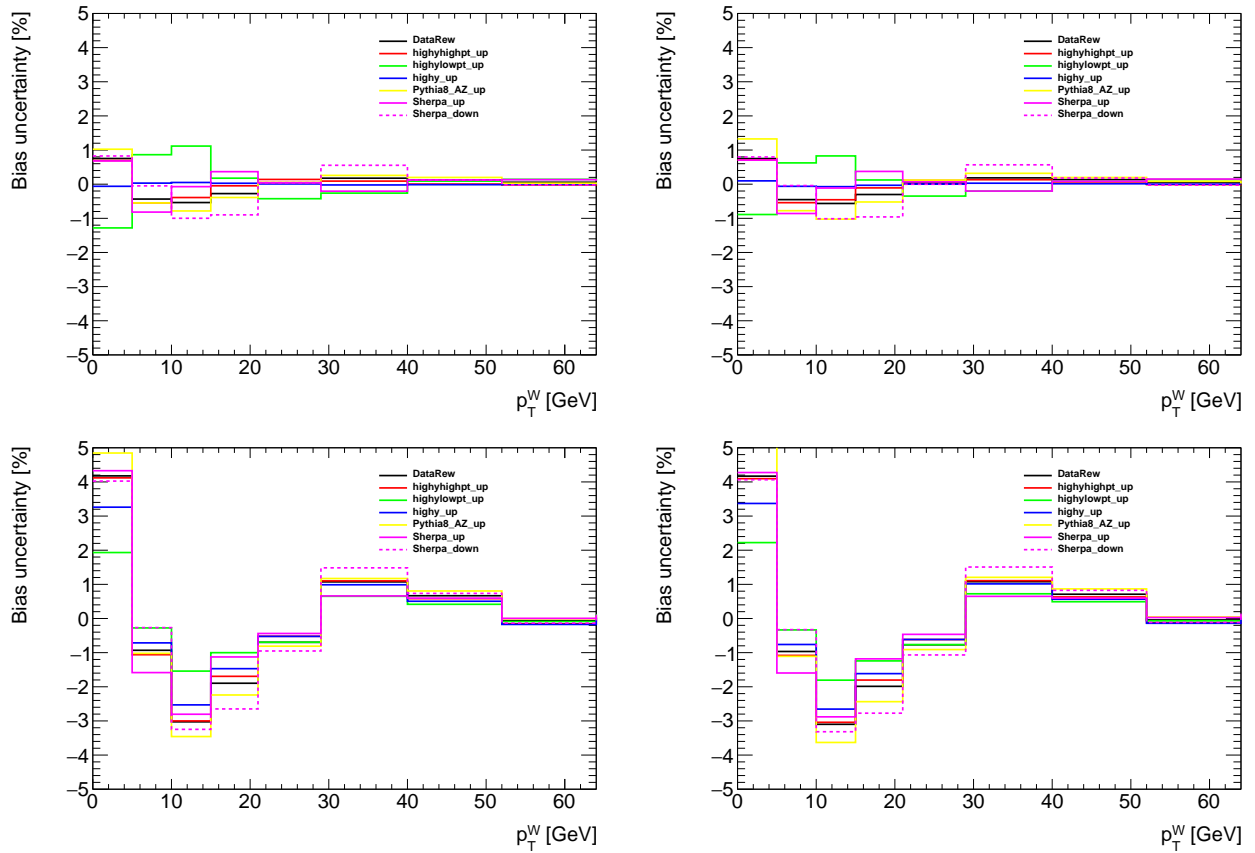


**Figure 96:** Unfolding bias on  $p_T^W$  in the electron channel after 3 iterations, for  $W^-$  (left) and  $W^+$  (right), at 5 TeV (top) and 13 TeV (bottom) [4].

2764 **9.4 Results**

2765 The comparison of unfolded spectrum to different theoretical predictions is presented at Figure 97 for  
 2766 electron channel and at 98 for the muon channel. The estimated experimental uncertainties raise from  
 2767 1% at low  $p_T^W$  to about 5% (2%) at  $p_T^W = 100$  GeV, at 5 TeV (13 TeV).

2768 The predictions are generated using Powheg AZNLO, Pythia AZ, Sherpa and DYRES. Powheg and  
 2769 Pythia agree with the data to a similar extent. A softer spectrum is predicted by Sherpa, while DYRES  
 2770 is on the opposite side compared to the data. The observed behaviour holds for both energies, both  
 2771 charges and both decay channels.

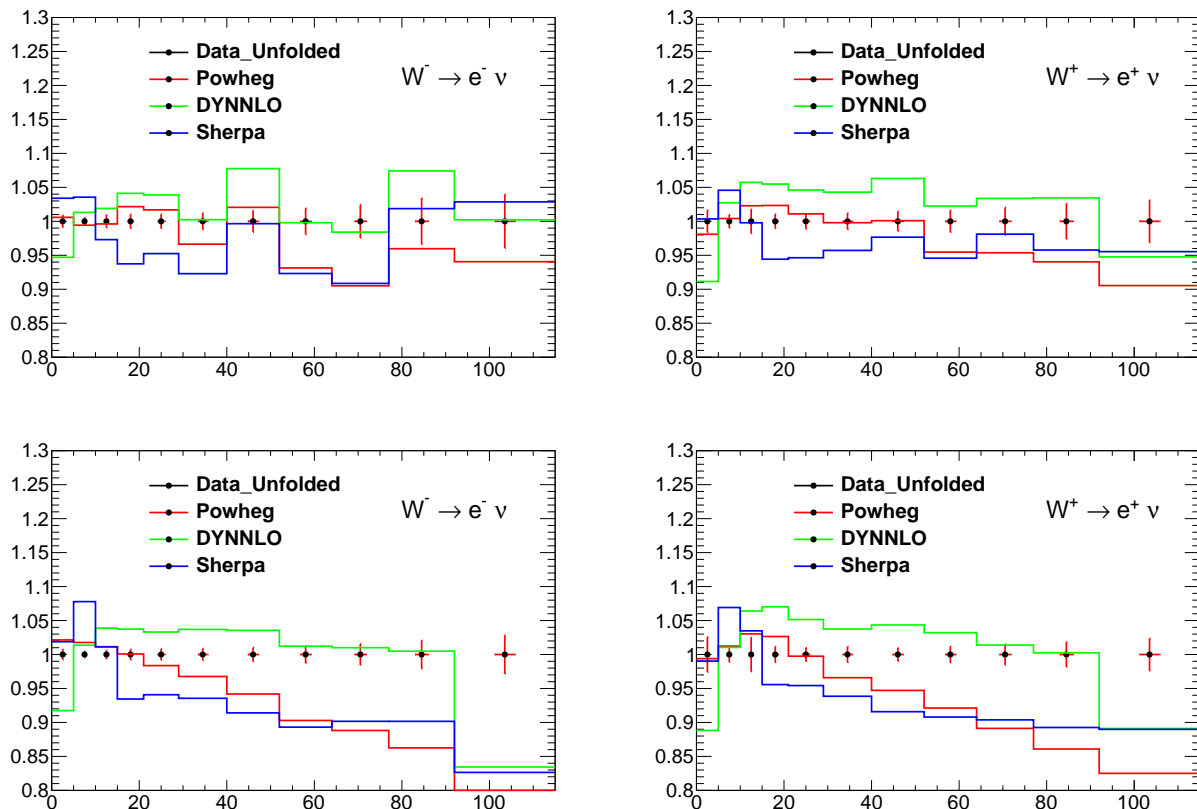


**Figure 97:** Unfolded measurement results in the  $W^-$  (left) and  $W^+$  (right) electron channels, at 5 TeV (top) and 13 TeV (bottom).

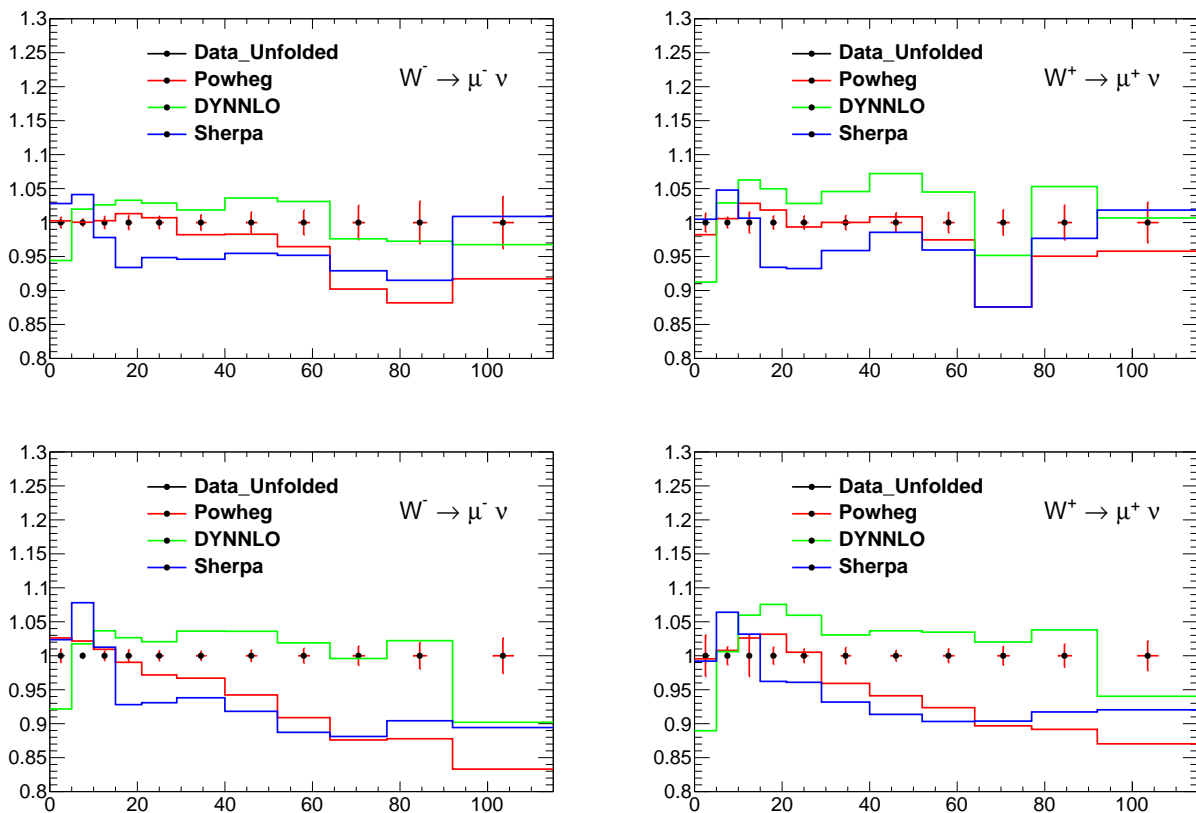


**Figure 98:** Unfolded measurement results in the  $W^-$  (left) and  $W^+$  (right) muon channels, at 5 TeV (top) and 13 TeV (bottom).

## 2772 Bibliography

- 2773 [1] Stefan Schmitt. “Data Unfolding Methods in High Energy Physics”. In: *EPJ Web Conf.* 137 (2017).  
2774 Ed. by Y. Foka, N. Brambilla, and V. Kovalenko, p. 11008. doi: 10.1051/epjconf/201713711008.  
2775 arXiv: 1611.01927 [physics.data-an].
- 2776 [2] G. D’Agostini. “A multidimensional unfolding method based on Bayes’ theorem”. In: *Nuclear  
2777 Instruments and Methods in Physics Research Section A: Accelerators, Spectrometers, Detectors and  
2778 Associated Equipment* 362.2 (1995), pp. 487–498. ISSN: 0168-9002. doi: [https://doi.org/10.1016/0168-9002\(95\)00274-X](https://doi.org/10.1016/0168-9002(95)00274-X). URL: <http://www.sciencedirect.com/science/article/pii/016890029500274X>.
- 2781 [3] G. D’Agostini. “Improved iterative Bayesian unfolding”. In: *Alliance Workshop on Unfolding and  
2782 Data Correction*. Oct. 2010. arXiv: 1010.0632 [physics.data-an].
- 2783 [4] Hicham Atmani et al. *Measurment of the  $p_T$  spectrum of  $W$ - and  $Z$ -bosons produced in  $pp$  collisions  
2784 at  $\sqrt{s} = 5$  TeV and 13 TeV in low-pileup runs*. Tech. rep. ATL-COM-PHYS-2018-1084. Geneva:  
2785 CERN, July 2018. URL: <https://cds.cern.ch/record/2632159>.



2786

2787

# Hadronic recoil regression with deep neural networks

2788 In the recent years a significant progress was achieved in the field of big datasets analysis. There is a  
 2789 number of principles available for solving a wide variety of tasks. In this thesis a deep neural network  
 2790 (DNN) was used for the regression of the 2-component hadronic recoil vector.

## 2791 10.1 Deep neural networks

2792 Normally a machine learning problem has a number of ingredients: a dataset  $\mathbf{X}$ , a set of parameters  
 2793  $\theta$ , a model  $g(\theta)$  and a loss function  $C(\mathbf{X})$  that tells us how well the model  $g(\theta)$  describes the dataset.  
 2794 Finding the values of  $\theta$  that would minimize the loss function we fit the model.

### 2795 10.1.1 Gradient descent optimization

2796 One of the most powerful and used class of methods in minimizing the loss function is called the  
 2797 *gradient descent*, [1] especially its sub-class, the stochastic gradient descent (SGD) [2], [3]. One of its  
 2798 modifications called ADAM [4] was used as an optimization algorithm in the work presented in this  
 2799 thesis.

2800 Let's assume that a loss function  $E(\theta)$  may be estimated as a sum over n data points:

$$E(\theta) = \sum_{i=1}^n e_i(x_i, \theta), \quad (10.1)$$

2801 where  $x_i$  is a data point and  $e_i$  is an estimate of performance. In the simplest case of the gradient  
 2802 descent (GD) algorithm we start looking for the values of parameters  $\theta$  such that the sum of functions  
 2803  $\sum_{i=1}^n e_i$  is minimal. We start with a certain value  $\theta_0$  and then iteratively perform the following:

$$\begin{aligned} v_t &= \eta_t \nabla_{\theta} E(\theta_t), \\ \theta_{t+1} &= \theta_t - v_t, \end{aligned} \quad (10.2)$$

2804 where  $\nabla_{\theta} E(\theta_t)$  is the gradient of  $E(\theta)$  with respect to  $\theta$ ; factor  $\eta_t$  is called the *learning rate* and defines  
 2805 the length of the step in the direction of  $\theta$  performed with every iteration. Balancing learning rate  
 2806 is very important for learning process and convergence. A value too low can make the convergence

2807 "stuck" in a local minimum, it also increases the number of iterations. Picking a very high learning  
 2808 rate we risk to miss the minimum so the algorithm would never converge to a minimum. Also, if the  
 2809 number of data points  $n$  is high, calculating the gradient is a costly task in terms of CPU time.  
 2810 Some of the problems accompanying the use of GD are dealt with by using its modification - the SGD.  
 2811 The idea is the following: instead of using all the available data points  $n$  at each iteration of the GD, we  
 2812 split the data into  $k$  *minibatches*, each having  $M$  data points, such that  $k = n/M$ . Normally the size of  
 2813 the batch is few hundreds of data points, to provide a certain degree of variance and incorporating  
 2814 stochasticity. The transition to SGD algorithm is done in the following way:

$$\nabla_{\theta} E(\theta) = \sum_{i=1}^n \nabla_{\theta} e_i(x_i, \theta) \rightarrow \sum_{i \in B_l} \nabla_{\theta} e_i(x_i, \theta), \quad (10.3)$$

2815 where  $B_l$  is a set of data points belonging to a minibatch  $l \in 1, \dots, n/M$ . Now every next iteration of  $\theta$   
 2816 parameters update is performed over a different batch, consecutively running over all the batches:

$$\begin{aligned} \nabla_{\theta} E^{EM}(\theta) &= \sum_{i \in B_l} \nabla_{\theta} e_i(x_i, \theta), \\ v_t &= \eta_t \nabla_{\theta} E^{EM}(\theta_t), \\ \theta_{t+1} &= \theta_t - v_t. \end{aligned} \quad (10.4)$$

2817 A full iteration over all the  $n/M$  batches is called an *epoch*. Now stochasticity prevents the gradient  
 2818 algorithm from getting stuck in a local minimum. Also computing the gradient over fewer data point  
 2819 notably decreases the CPU time spent.  
 2820 The algorithm may be further improved, adding a "memory", that is to say making every next step  $t$   
 2821 dependent on the direction of the previous step  $t - 1$ :

$$\begin{aligned} v_t &= \gamma v_{t-1} \eta_t \nabla_{\theta} E^{EM}(\theta_t), \\ \theta_{t+1} &= \theta_t - v_t. \end{aligned} \quad (10.5)$$

2822 Because of an analogy from physics the parameter  $\gamma$  is called a *momentum*, having  $0 \leq \gamma \leq 1$  [5], [6].  
 2823 This parameter provides a certain "inertia" in the change of the direction of the gradient descent.  
 2824 Introduction of the momentum helps for quicker convergence in the case of a slow but steady change  
 2825 of a certain parameter during the gradient descent.  
 2826 The convergence of the GD may be significantly improved if the learning rate could be different in  
 2827 different directions, depending on the landscape of the parameter space  $\theta$ : the steeper the gradient  
 2828 in a certain direction - the smaller the corresponding step. The optimal step could be estimated by  
 2829 obtaining the *Hessian matrix* in the vicinity of a point  $\theta_0$ , providing a description of the local curvature  
 2830 in a multidimensional space. Although calculating Hessian matrix is complicated and slow-converging  
 2831 process [7]. However, a number of methods use the second moment of the gradient to efficiently  
 2832 estimate the optimal learning rate. One of such methods is called ADAM (ADAptive Momentum) [4],

2833 its iterative relations are the following:

$$\begin{aligned}
 g_t &= \nabla_{\theta} E(\theta_t) \\
 m_t &= \beta_1 m_{t-1} + (1 - \beta_1) g_t \\
 s_t &= \beta_2 s_{t-1} + (1 - \beta_2) g_t^2 \\
 \hat{m}_t &= \frac{m_t}{1 - (\beta_1)^t} \\
 \hat{s}_t &= \frac{s_t}{1 - (\beta_2)^t} \\
 \theta_{t+1} &= \theta_t - \eta_t \frac{\hat{m}_t}{\sqrt{\hat{s}_t} + \epsilon}.
 \end{aligned} \tag{10.6}$$

2834 Here the parameters  $\beta_1$  and  $\beta_2$  set the memory lifetime for the first and second moment;  $\eta$  is the learning  
 2835 rate and  $\epsilon$  is a small regularization constant keeping the denominators from vanishing. Like in other  
 2836 cases of the SGD here the iterations are performed batch-wise. Parameter  $s_t$  is linked to the variance of  
 2837 the gradient size. This basically means that the learning rate is proportional to the first momentum of  
 2838 the gradient and inverse proportional to its standard deviation.

### 2839 10.1.2 DNN structure and training

2840 A neural network is composed of single neurons, also called nodes, arranged in layers. The first layer is  
 2841 called the input layer, the last one is called the output layer; all the layers in between are named hidden  
 2842 layers (see Fig. 101).

2843 A single node  $i$  takes a vector of  $k$  input features  $\mathbf{x} = (x_1, x_2, \dots, x_k)$  and produces a scalar input  $a_i(\mathbf{x})$ .  
 2844 Function  $a_i$  may have a different form, although it normally can be decomposed into two steps. The  
 2845 first step is a linear transformation of the inputs into a scalar value assigning each input a weight:

$$z^i = w_k^i \cdot x_k + b^i, \tag{10.7}$$

2846 where  $\mathbf{w}^i = (w_1^i, w_2^i, \dots, w_k^i)$  is a set of  $k$  weights assigned to corresponding inputs. The weights  $\mathbf{w}^i$  are  
 2847 specific to a neuron  $i$ , as well as the scalar bias  $b^i$ . The next step is where the non-linear function  $\sigma_i$   
 2848 comes into play: we can express the output function  $a_i(\mathbf{x})$  as follows:

$$a_i(\mathbf{x}) = \sigma_i(z^i). \tag{10.8}$$

2849 There exists a number of options for the non-linear function  $\sigma$ ; in current thesis a tanh is used. When  
 2850 the neurons are arranged in layers in a feed-forward neural network - the outputs from neurons of  
 2851 the previous layer serve as inputs for the succeeding layers neurons. The universal approximation  
 2852 theorem states, that a neural network with a single hidden layer can approximate any continuous  
 2853 multiparametric function with arbitrary accuracy [8], [9]. However, in practice it is easier to reach the  
 2854 possible precision having more hidden layers.

2855 So in terms of a DNN fitting the model means tuning the weights and biases  $(\mathbf{w}^i, b^i)$  in such a way  
 2856 that a loss function applied to the new dataset would be minimal. It is reached through iterative  
 2857 process called *training*, that involves the GD with an algorithm called *backpropagation* [10]. The  
 2858 backpropagation algorithm allows to calculate the gradients and adjust the corresponding parameters

2859 in a very computation-efficient way.

Let us assume that there are  $L$  layers in the network  $l = 1, \dots, L$ , that  $w_{jk}^l$  and  $b_j^l$  are the weight of an

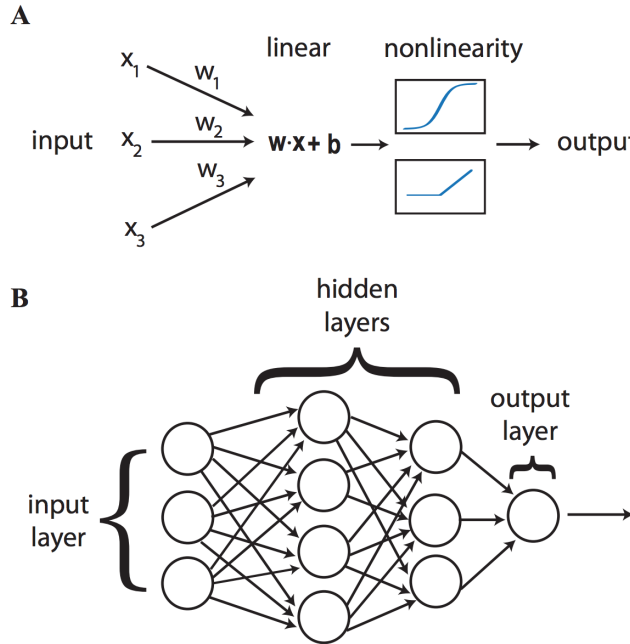


**Figure 101:** A: The nodes perform a linear transformation of the inputs, then apply a non-linear activation function. B: The architecture of a deep neural network: neurons are arranged into layers [11].

2860  
2861 input parameter  $k$  and the bias for node  $k$  in layer  $l$  respectively. The layered structure of the neural  
2862 network ensures that the inputs for the nodes in layer  $l$  depend only on the outputs of the nodes from  
2863 layer  $l - 1$ , hence:

$$a_j^l = \sigma \left( \sum_k w_{jk}^l a_k^{l-1} + b_j^l \right) = \sigma(z_j^l), \quad (10.9)$$

2864 where the linear weighted sum is denoted as:

$$\sigma(z_j^l) = \sum_k w_{jk}^l a_k^{l-1} + b_j^l. \quad (10.10)$$

2865 The cost function  $E$  is computed from the output of the neural network, so it directly depends only on  
2866 the values of  $a_j^L$ . Let us define the error  $\Delta_j^L$  of the  $j$ -th node in the output ( $L$ -th) layer as a change in the  
2867 cost function with respect to the weighted output of the last layer:

$$\Delta_j^L = \frac{\partial E}{\partial z_j^L}. \quad (10.11)$$

2868 At the same time the loss depends indirectly on all the preceding layers, so keeping in mind eq. 10.9  
2869 we can define the error of an arbitrary node  $j$  in arbitrary layer  $l$  as the change in the cost function  $E$   
2870 with respect to the weighted input  $z_j^l$ :

$$\Delta_j^l = \frac{\partial E}{\partial z_j^l} = \frac{\partial E}{\partial a_j^l} \sigma'(z_j^l), \quad (10.12)$$

2871 where  $\sigma'(z_j^l)$  is the derivative of the non-linear activation function  $\sigma$  with respect to its input at  $z_j^l$ . But  
 2872 on the other hand we can also interpret the error function  $\Delta_j^L$  in terms of bias partial derivatives:

$$\Delta_j^l = \frac{\partial E}{\partial z_j^l} = \frac{\partial E}{\partial b_j^l} \frac{\partial b_j^l}{\partial z_j^l} = \frac{\partial E}{\partial b_j^l} \cdot \mathbf{1}. \quad (10.13)$$

2873 So starting from the output layer we can compute the error in any layer  $l$ , provided we know it for the  
 2874 subsequent layer  $l+1$ :

$$\begin{aligned} \Delta_j^l &= \frac{\partial E}{\partial z_j^l} = \sum_k \frac{\partial E}{\partial z_j^{l+1}} \frac{\partial z_j^{l+1}}{\partial z_j^l} = \\ &= \sum_k \Delta_j^l \frac{\partial z_j^{l+1}}{\partial z_j^l} \left( \sum_k \Delta_j^l w_{kj}^{l+1} \right) \sigma'(z_j^l). \end{aligned} \quad (10.14)$$

2875 And finally we can get the gradient of the cost function  $E$  with respect to a weight of an arbitrary  
 2876 neuron:

$$\frac{\partial E}{\partial w_{jk}^l} = \frac{\partial E}{\partial z_j^l} \frac{\partial z_j^l}{\partial w_{jk}^l} = \Delta_j^l a_k^{l-1}. \quad (10.15)$$

2877 Using these four equations (10.11, 10.13, 10.14, 10.15) it is possible to "backpropagate" the error back  
 2878 from the output layer and once we can compute the gradient - we know how we should tune the  
 2879 weights and biases in order to minimize the loss function.

### 2880 10.1.3 Batch normalization

2881 Batch normalization is a regularization scheme that helps to improve the speed and stability of the  
 2882 DNN training. The main idea behind the method is to prevent an *internal covariant shift* - a change in  
 2883 the distribution of network activations due to the change in network parameters during training by  
 2884 means of normalization of the parameters transferred from layer  $l$  to layer  $l+1$  [12]. So let us consider  
 2885 a layer  $l$  that has  $d$  inputs  $\mathbf{x} = (x^1, x^2, \dots, x^d)$ , then for every  $x^k$  we perform the following transformation:

$$\hat{x}^k = \frac{x^k - E[x^k]}{\sqrt{Var[x^k]}}, \quad (10.16)$$

2886 where  $E[x^k]$  and  $Var[x^k]$  are the expectation and variance of the parameter  $x$ , calculated over the  
 2887 training dataset, respectively. Although we have to be sure that we preserve the non-linearity of the  
 2888 activation function output. In order to do this the two additional parameters are introduced:

$$y^k = \gamma \hat{x}^k + \beta^k, \quad (10.17)$$

2889 where the parameters  $\gamma$  and  $\beta$  are trained just like the rest of the network parameters. Practically  
 2890 if the training is performed within the mini-batch scheme with batch size  $B = x_1, \dots, x_m$  the batch  
 2891 normalization layer is inserted between the DNN layers the transformations for the input  $x$  are the

2892 following:

$$\begin{aligned} \frac{1}{m} \sum_{i=1}^m x_i &\rightarrow \mu_B \\ \frac{1}{m} \sum_{i=1}^m (x_i - \mu_B)^2 &\rightarrow \sigma_B^2 \\ \frac{x_i - \mu_B}{\sqrt{\sigma_B^2 + \epsilon}} &\rightarrow \hat{x}_i \\ \gamma \hat{x}_i + \beta &\rightarrow y_i \equiv BN_{\gamma, \beta}(x_i), \end{aligned} \tag{10.18}$$

2893 where  $\epsilon$  is a small regularization constant.

## 2894 10.2 HR regression

2895 Considering that hadronic recoil is an observable that uses many inputs from ID, EMC and HC it is  
2896 reasonable to expect improvement of the result using modern MultiVariate Analysis (MVA) techniques.

### 2897 10.2.1 Input features and model

2898 Training, testing and validation was performed using a simulated MC sample  $W^+ \rightarrow \mu\nu$  at 13 TeV,  
2899 following the selection presented in Section 8. From the 3625136 events that have passed the selection  
2900 12 734 109 were used for training and 3 034 130 for testing the performance. Below is the list of 38  
2901 input features:

- 2902 • **Vector sums** of charged PFO, neutral PFO (see Section 6.5) and the vector sum of both. All three  
2903 vector sums are included into the input features having two Cartesian components each, making  
2904 6 input features.
- 2905 • **Transverse energy sum**  $\sum E_T$  is also defined in three similar ways, adding three input features.
- 2906 • Cartesian components of the two leading jets momenta in the transverse plane. The jets were  
2907 demanded to have  $p_T > 20$  GeV. If one or both jets don't make the cut or there is less than two jets  
2908 in the event - the corresponding features were assigned zero value.
- 2909 • Cartesian components of the five leading Neutral Particle Flow Objects (nPFOs) and five leading  
2910 Charged Particle Flow Objects (cPFOs) momenta in the transverse plane.
- 2911 • Number of primary vertices in the event.
- 2912 • Pile-up value  $\mu$ .
- 2913 • Total number of jets in the event.
- 2914 • Total number of nPFOs and cPFOs in the event.

2915 All input features were pre-processed using the StandardScaler module from Scikit Learn package [13].  
 2916 The model contains 3 dense layers with 256 neurons each, alternated with batch normalization layers  
 2917 (see Fig. 102). Using batch normalization layers has allowed to reduce the training time by a factor  
 10. The model has used Adam optimizer with learning step 0.001 and batch size of 4000 data points.

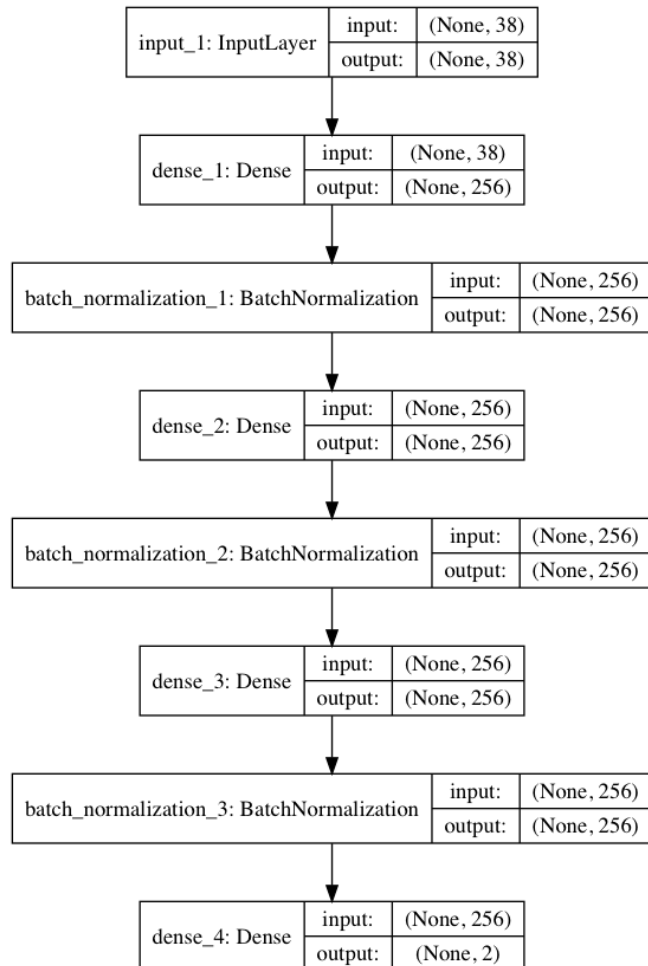


**Figure 102:** A model of the DNN used in the analysis.

2918  
 2919 Twenty percent of events were used for validation. The two target values were Cartesian components  
 2920 of the truth  $p_T^W$  vector.  
 2921 The loss function used is the mean square error, which means that for every batch of size  $B$  the loss is  
 2922 defined as:

$$\mathcal{L} = \sum_{i=1}^B (x_i^{pred} - x_i^{target})^2, \quad (10.19)$$

2923 where  $x_i^{target}$  and  $x_i^{pred}$  are the target (truth) and predicted values for the  $i^{th}$  event respectively. For our  
 2924 case of two target values, namely  $u_X$  and  $u_Y$  the loss takes the following form:

$$\mathcal{L} = \sum_{i=1}^B \left( (x_i^{pred} - x_i^{target})^2 + (y_i^{pred} - y_i^{target})^2 \right). \quad (10.20)$$

2925 Figure 103 shows dependence of loss on training epochs. Eventually the model with weights obtained after 38 epochs of training was used in the analysis.

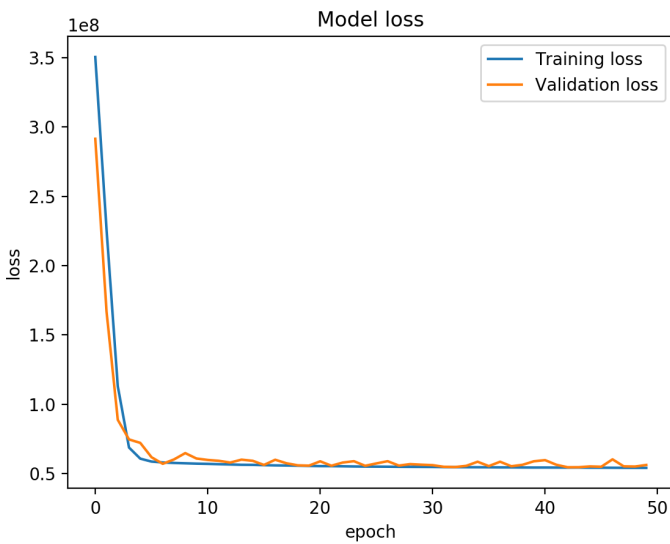


**Figure 103:** Learning curve of the model.

2926

### 2927 10.2.2 Kinematic distributions

2928 The results presented here show the regression plots obtained with the trained DNN. The regression  
2929 was tested for the four W channels in MC and for the two Z channels in both data and MC. Below the  
2930 plots for  $W^- \rightarrow \mu\nu$  channel are presented, the rest of the results are presented in Appendix B.

2931 In Figure 104 the difference between the reconstructed hadronic recoil and truth distributions (targets)  
2932 are shown. For the two target components  $u_X$  and  $u_Y$  a sharper peak centred at zero is observed in the  
2933 MVA-reconstructed recoil comparing to the standard algorithm. Similar comparison is shown in Fig.  
2934 ?? for HR vector components in polar coordinates. The polar angle  $u_\phi$  of the HR vector shows a very  
2935 small, nearly negligible improvement from the MVA. The  $u_T$  vector magnitude demonstrates a shift  
2936 from zero for the  $u_T^{MVA}$ , indicating a bias. Figure 106 shows that the MVA-reconstructed recoil has a  
2937 softer spectrum comparing to both  $p_T^{truth}$  and standard recoil spectra.

2938 The bias is shown in Fig. ?? together with the  $u_{perp}$  component. Indeed the  $u_T^{MVA}$  demonstrates a  
2939 larger bias as compared to the standard algorithm. At the same time the standard deviation of the  $u_\perp$   
2940 component indicates an improvement in the resolution.

2941 The dependence of the bias and  $u_\perp$  on the momentum is studied in Fig. 108. The  $u_T^{MVA}$  recoil  
2942 demonstrates improvement in the resolution and a larger bias in the region of  $p_T < 80\text{GeV}$ . However,  
2943 for a quantitative resolution comparison we need to make sure that  $u_\perp$  and  $u_\perp^{MVA}$  are on the same scale.  
2944 A possible way to achieve this is to normalize them to average recoil  $\langle u_T \rangle$ . The resulting normalized  
2945 curves on Fig. 109 show that the MVA provides 5-10% resolution improvement at  $p_T < 10\text{GeV}$  and a

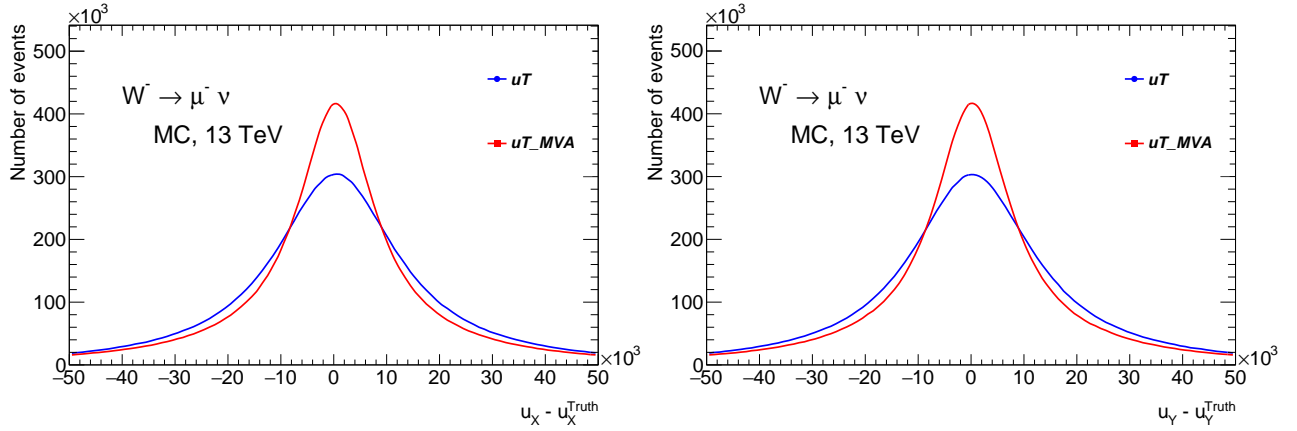


**Figure 104:** The difference between the Cartesian components of the HR vector for the standard  $u_T$  and  $u_T^{MVA}$ .

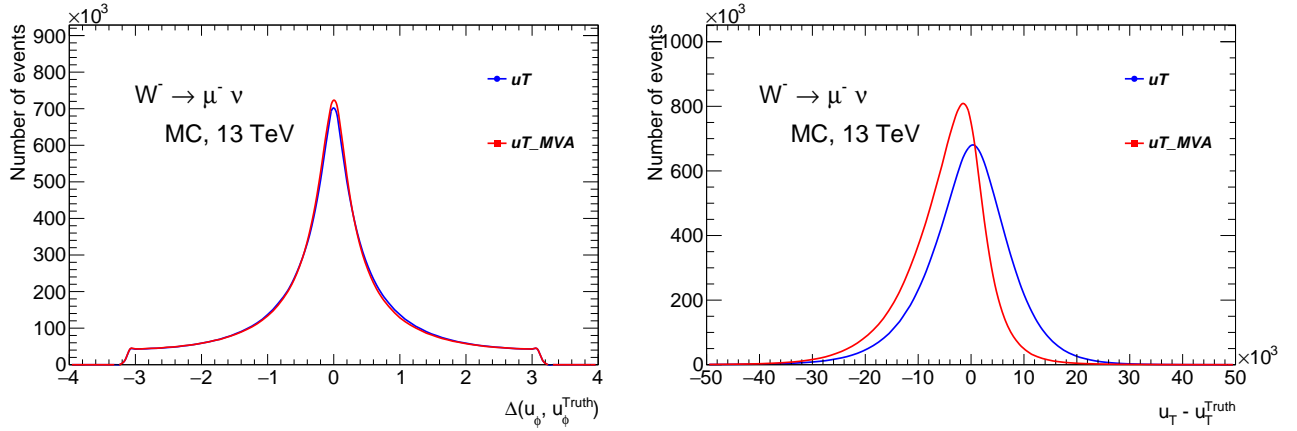


**Figure 105:** The difference between the polar components of the HR vector for the standard  $u_T$  and  $u_T^{MVA}$ .

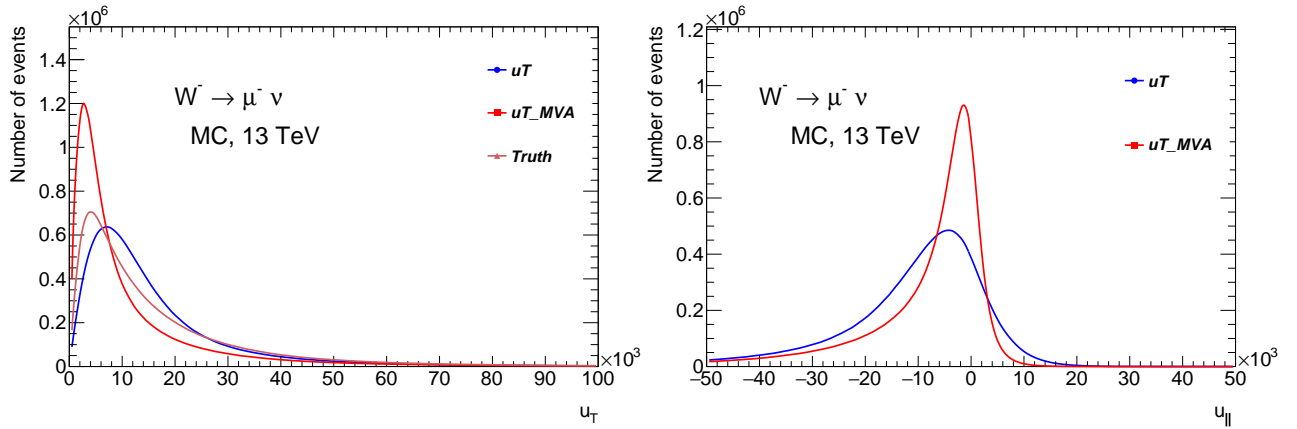


**Figure 106:** Comparison of  $u_T$  and  $u_T^{MVA}$  spectra and response.

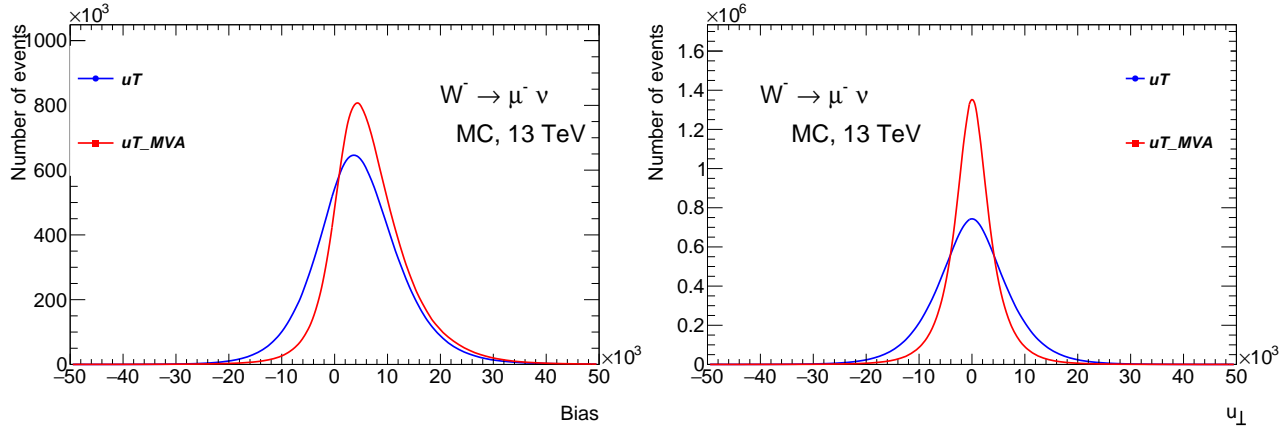


**Figure 107:** Bias and  $u_{\perp}$  for the standard  $u_T$  and  $u_T^{MVA}$ .

2946 bit more than 10% in  $10 < p_T < 30$  GeV transverse momentum region.

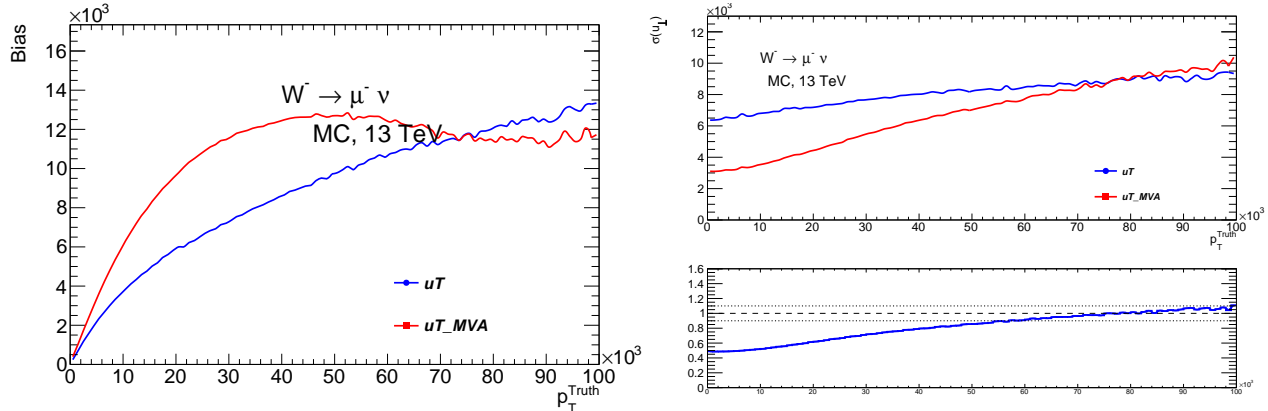


**Figure 108:** Bias and  $u_{\perp}$  as a function of  $p_T^{\text{truth}}$ .

2947

2948 The same neural network was applied for the HR regression for both Z channels, for data and MC  
 2949 events. In case of data the  $p_T^{\text{truth}}$  vector was replaced with  $p_T^{\ell\ell}$ . A qualitatively similar picture holds for  
 2950 both Z channels, confirming recoil universality for W and Z events (see Fig. 1010). The complete set of  
 2951  $u_T$  vs  $u_T^{MVA}$  comparison plots for all W and Z channels can be found in Appendix B.

### 2952 10.3 Conclusions

2953 The application of contemporary analysis methods like the regression using DNNs shows a promising  
 2954 potential for improving the measurements precision.

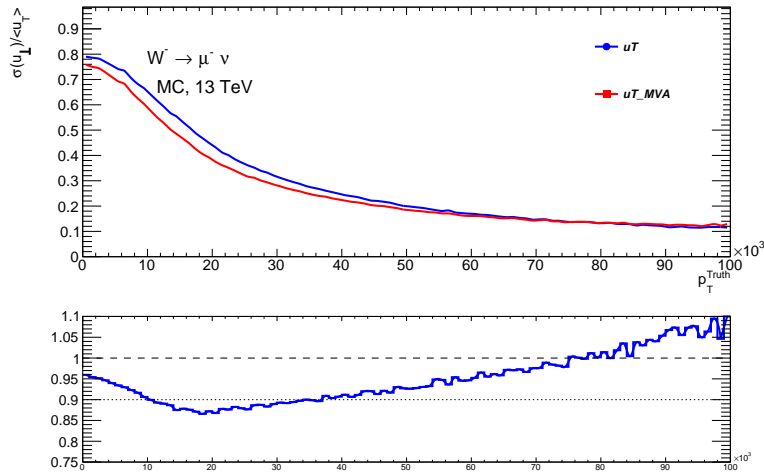


**Figure 109:** Normalized  $\frac{\sigma(u_T)}{\langle u_T \rangle}$  as a function of  $p_T^{truth}$ .

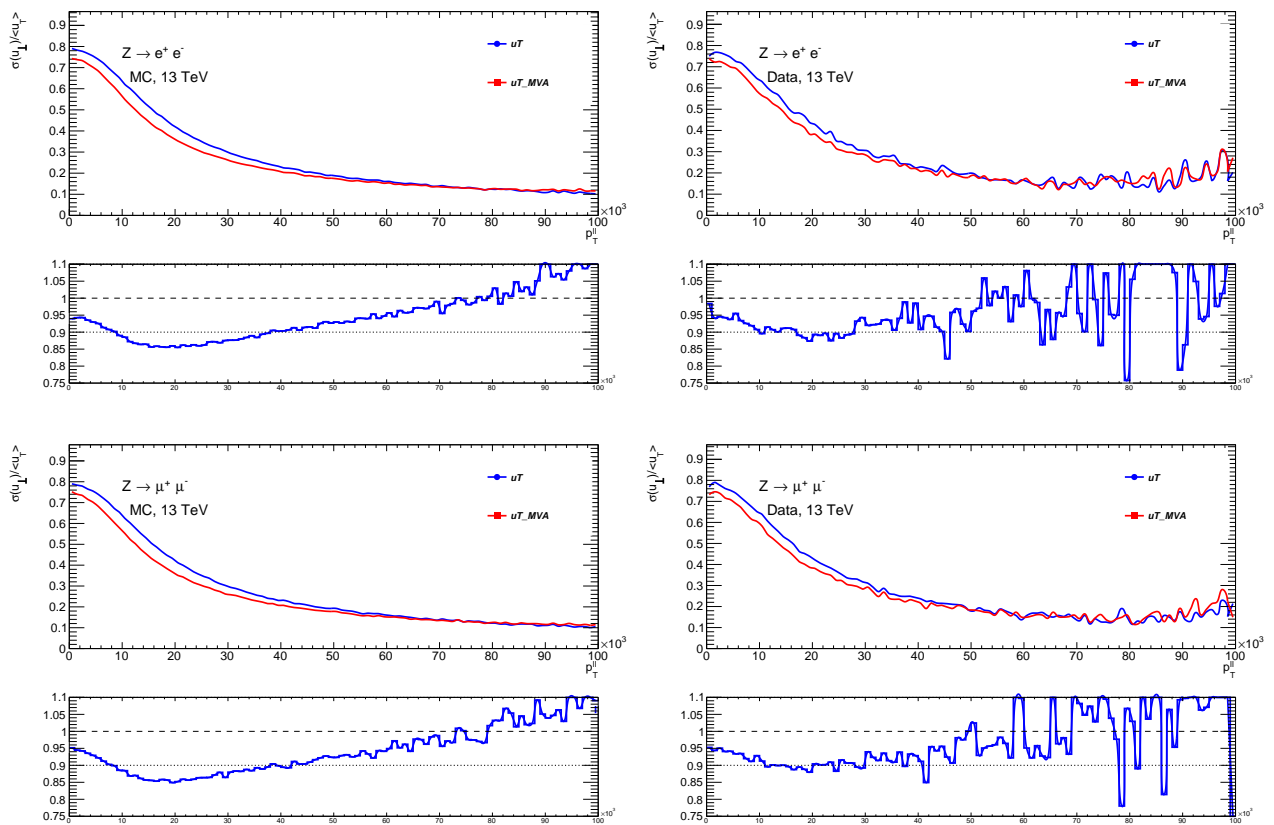


**Figure 1010**

2955 **Bibliography**

- 2956 [1] Yann LeCun et al. "Gradient-based learning applied to document recognition". In: *Proceedings of*  
2957 *the IEEE*. 1998, pp. 2278–2324.
- 2958 [2] Léon Bottou. "Stochastic Gradient Descent Tricks". In: vol. 7700. Jan. 2012, pp. 421–436. doi:  
2959 [10.1007/978-3-642-35289-8\\_25](https://doi.org/10.1007/978-3-642-35289-8_25).
- 2960 [3] David E. Rumelhart, Geoffrey E. Hinton, and Ronald J. Williams. "Learning representations by  
2961 back-propagating errors". In: *Nature* 323 (1986), pp. 533–536.
- 2962 [4] Diederik P. Kingma and Jimmy Ba. *Adam: A Method for Stochastic Optimization*. cite arxiv:1412.6980Com-  
2963 ment: Published as a conference paper at the 3rd International Conference for Learning Repre-  
2964 sentations, San Diego, 2015. 2014. url: <http://arxiv.org/abs/1412.6980>.
- 2965 [5] Yu Nesterov. "A method of solving a convex programming problem with convergence rate  
2966  $O(1/k^2)$ ". In: vol. 27. Jan. 1983, pp. 372–376.
- 2967 [6] Boris Polyak. "Some methods of speeding up the convergence of iteration methods". In: *Ussr  
2968 Computational Mathematics and Mathematical Physics* 4 (Dec. 1964), pp. 1–17. doi: [10.1016/0041-  
2969 5553\(64\)90137-5](https://doi.org/10.1016/0041-5553(64)90137-5).
- 2970 [7] Yann LeCun et al. "Efficient BackProp". In: *Neural Networks: Tricks of the Trade*. Ed. by Genevieve  
2971 B. Orr and Klaus-Robert Müller. Berlin, Heidelberg: Springer Berlin Heidelberg, 1998, pp. 9–50.  
2972 ISBN: 978-3-540-49430-0. doi: [10.1007/3-540-49430-8\\_2](https://doi.org/10.1007/3-540-49430-8_2). url: [https://doi.org/10.1007/3-540-49430-8\\_2](https://doi.org/10.1007/3-540-49430-8_2).
- 2974 [8] Kurt and Hornik. "Approximation capabilities of multilayer feedforward networks". In: *Neural  
2975 Networks* 4.2 (1991), pp. 251–257. doi: [10.1016/0893-6080\(91\)90009-T](https://doi.org/10.1016/0893-6080(91)90009-T). url: <http://www.sciencedirect.com/science/article/pii/089360809190009T>.
- 2977 [9] G. Cybenko. "Approximation by superpositions of a sigmoidal function". In: *Mathematics of  
2978 Control, Signals and Systems* 2.4 (Dec. 1989), pp. 303–314. issn: 1435-568X. doi: [10.1007/BF02551274](https://doi.org/10.1007/BF02551274). url: <https://doi.org/10.1007/BF02551274>.
- 2980 [10] D. E. Rumelhart and D. Zipser. "Feature Discovery by Competitive Learning". In: *Parallel Dis-  
2981 tributed Processing*. MIT Press, 1986, pp. 151–193.
- 2982 [11] Pankaj Mehta et al. "A high-bias, low-variance introduction to Machine Learning for physicists".  
2983 In: *Phys. Rept.* 810 (2019), pp. 1–124. doi: [10.1016/j.physrep.2019.03.001](https://doi.org/10.1016/j.physrep.2019.03.001). arXiv: [1803.08823](https://arxiv.org/abs/1803.08823)  
2984 [[physics.comp-ph](#)].
- 2985 [12] Sergey Ioffe and Christian Szegedy. "Batch Normalization: Accelerating Deep Network Training  
2986 by Reducing Internal Covariate Shift". In: *Proceedings of the 32nd International Conference on  
2987 International Conference on Machine Learning - Volume 37*. ICML15. Lille, France: JMLR.org, 2015,  
2988 pp. 448–456.

- 2989 [13] F. Pedregosa et al. “Scikit-learn: Machine Learning in Python”. In: *Journal of Machine Learning*  
2990 *Research* 12 (2011), pp. 2825–2830.



2991

2992

# 11 Appendix A

## 2993 11.1 Experimental uncertainties of main observables

## Mesure de la masse du boson W avec le détecteur ATLAS au LHC

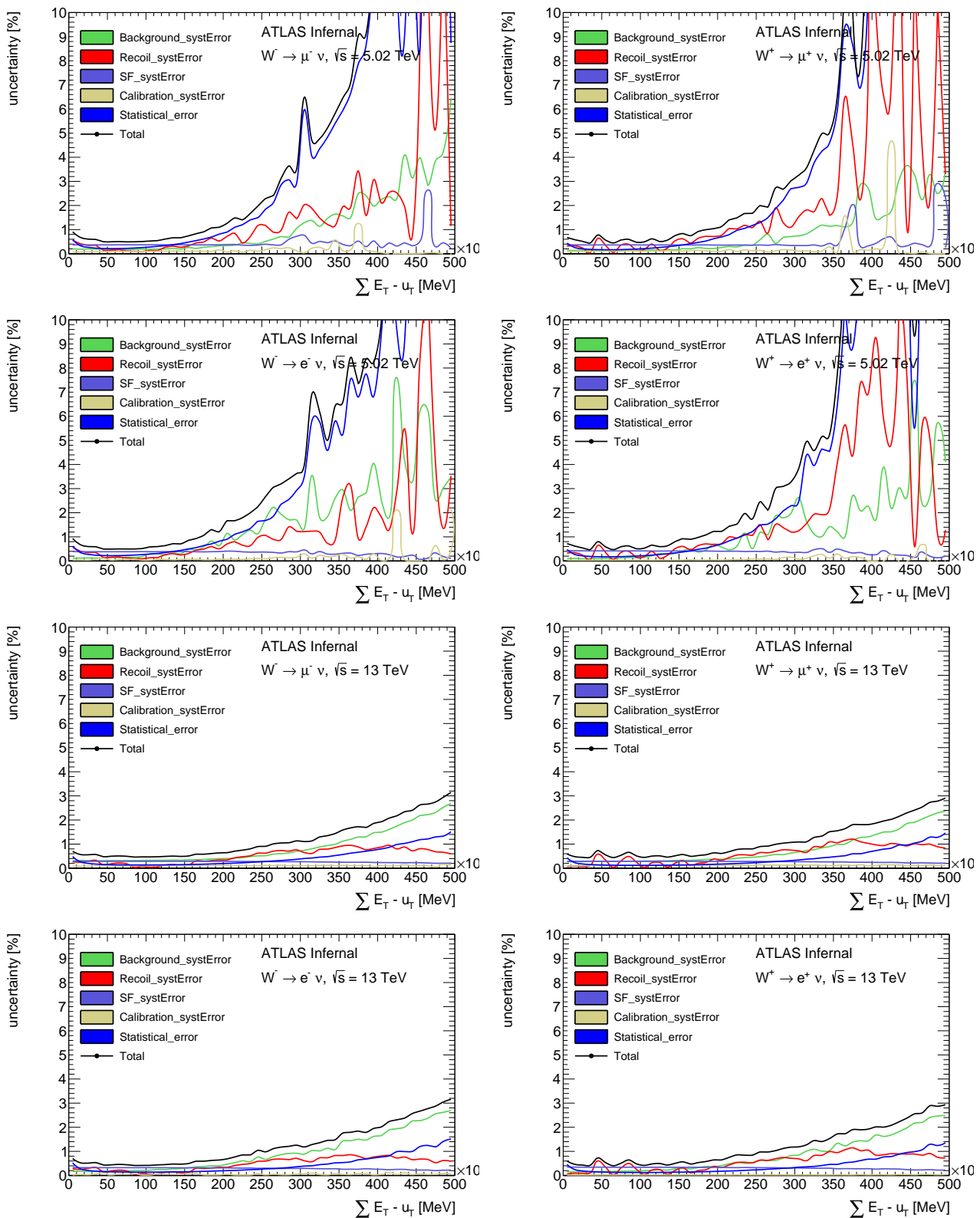


**Figure 111:**  $\Sigma E_T$  systematic error breakdown in the muon and electron channel for the  $\sqrt{s} = 5 \text{ TeV}$  and  $\sqrt{s} = 13 \text{ TeV}$  datasets.

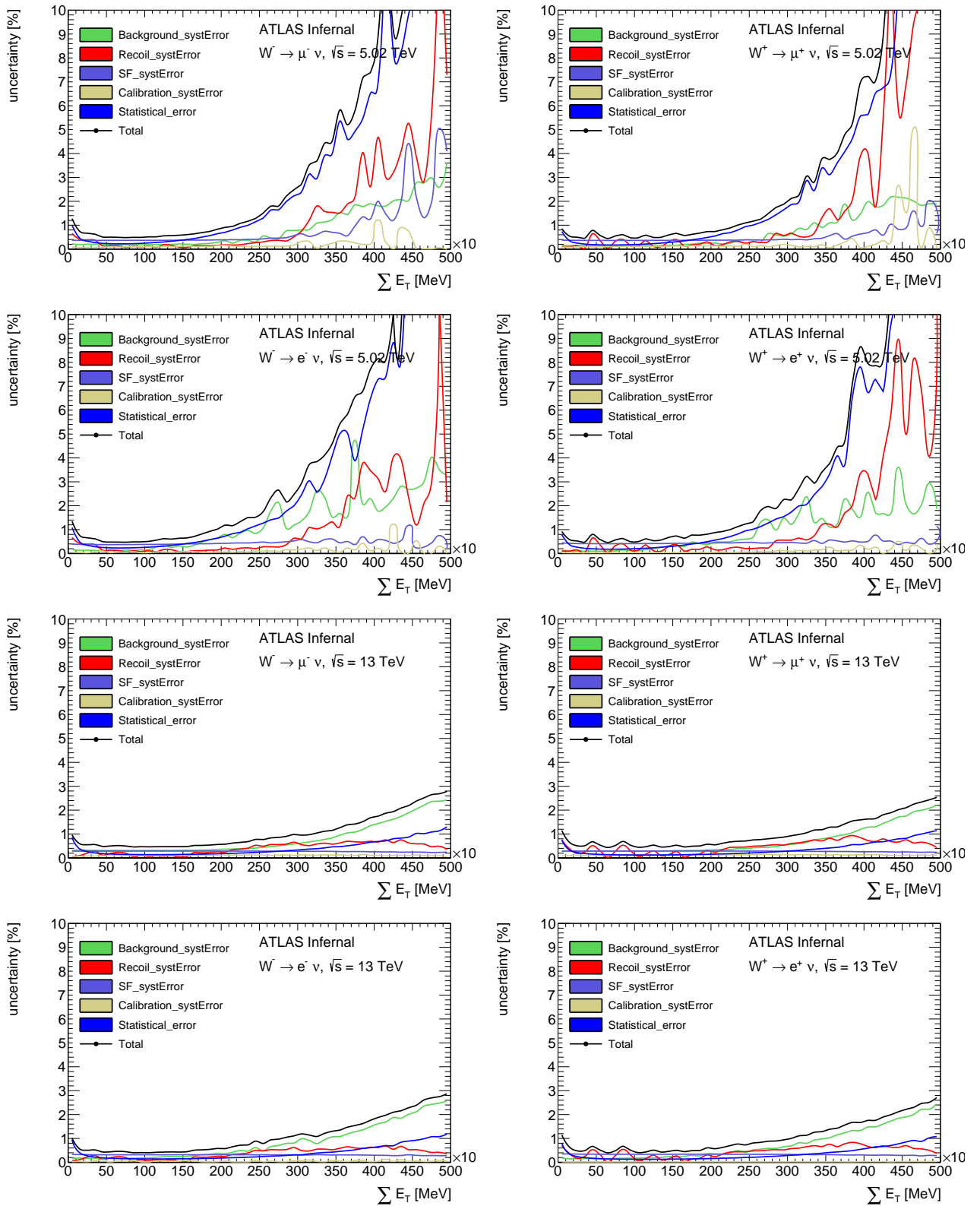


**Figure 112:**  $\Sigma E_T$  systematic error breakdown in the muon and electron channel for the  $\sqrt{s} = 5 \text{ TeV}$  and  $\sqrt{s} = 13 \text{ TeV}$  datasets.

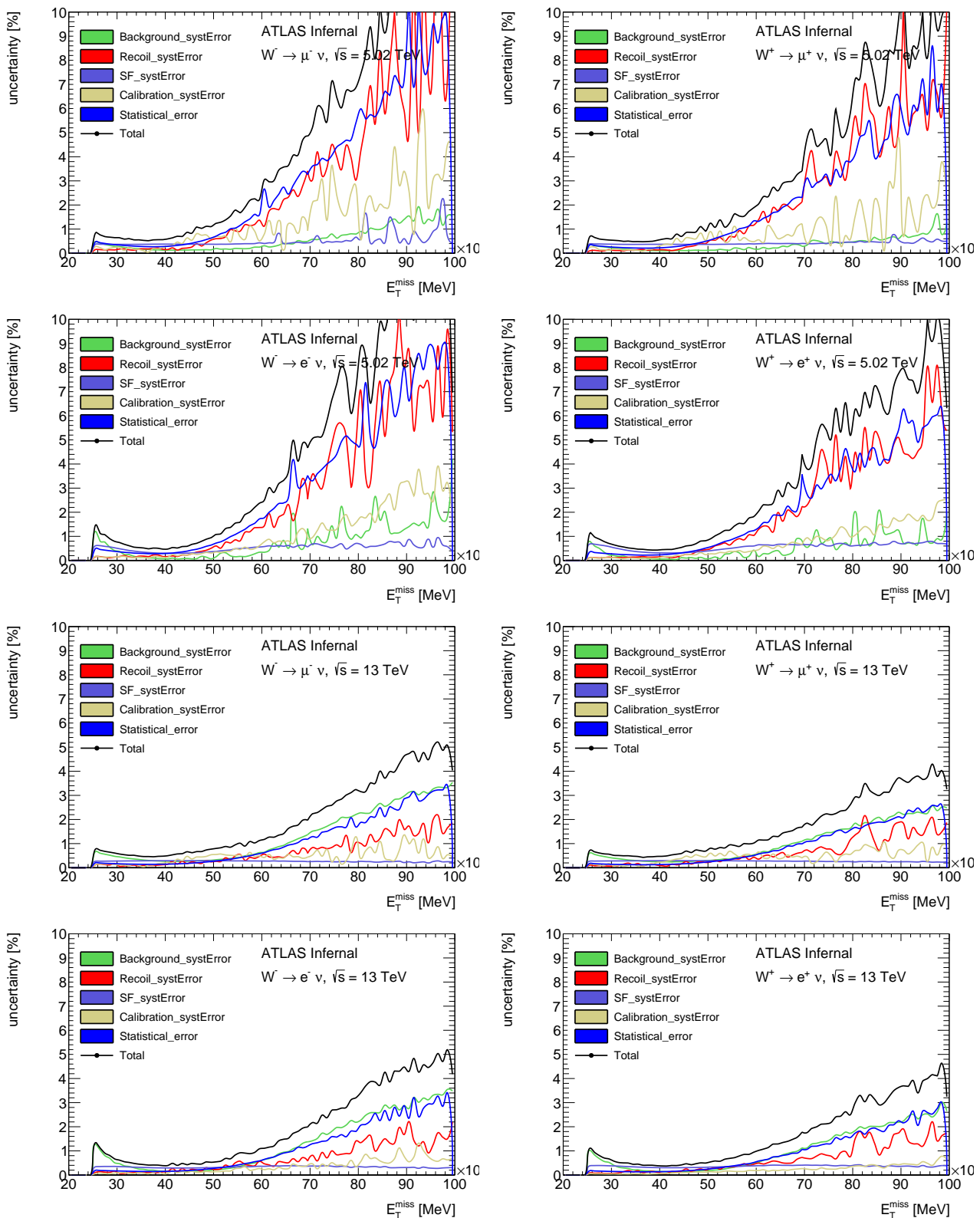


**Figure 113:**  $\vec{E}_T^{\text{miss}}$  systematic error breakdown in the muon and electron channel for the  $\sqrt{s} = 5 \text{ TeV}$  and  $\sqrt{s} = 13 \text{ TeV}$  datasets.

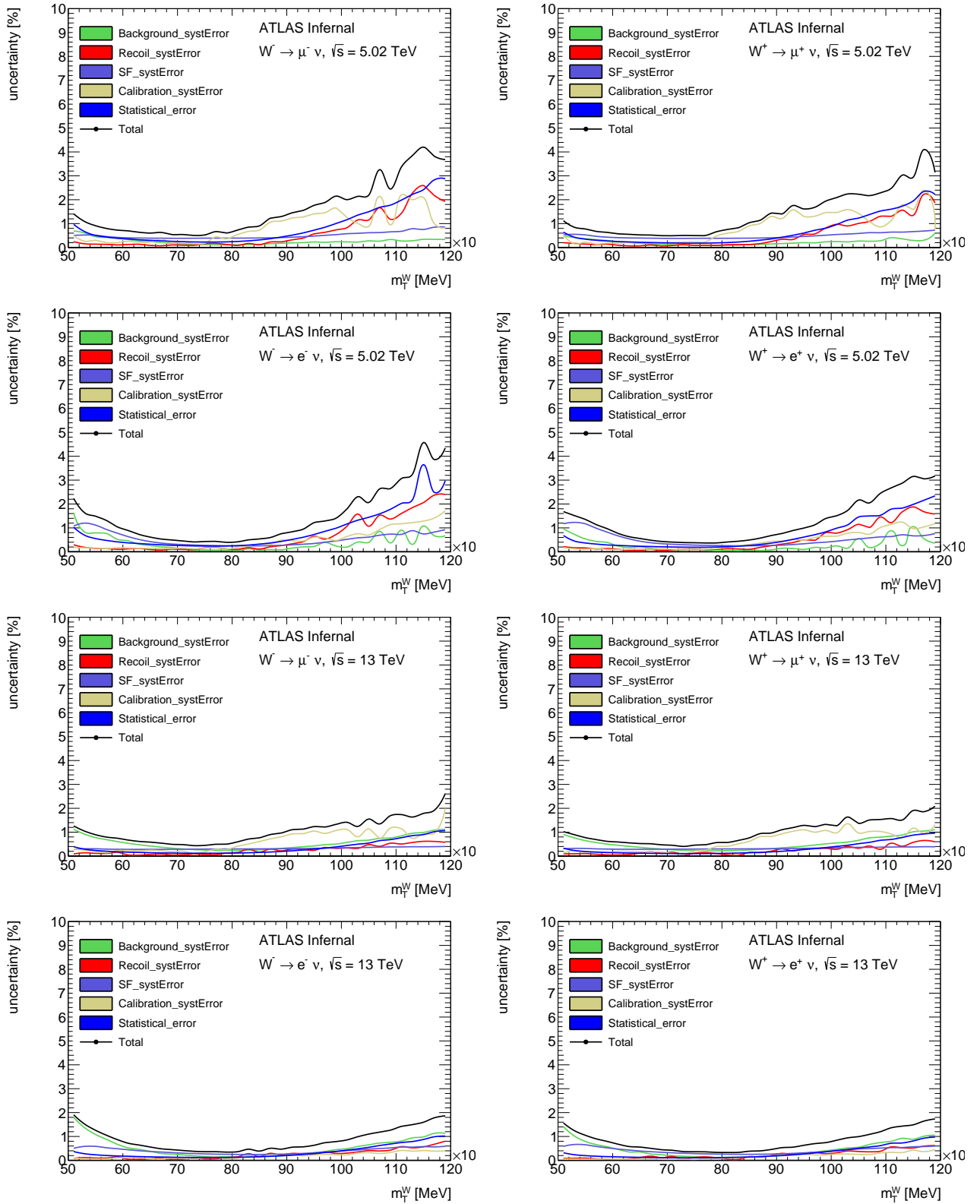


**Figure 114:** Transverse mass systematic error breakdown of the W boson in the muon and electron channel for the  $\sqrt{s} = 5 \text{ TeV}$  and  $\sqrt{s} = 13 \text{ TeV}$  datasets.

## Mesure de la masse du boson W avec le détecteur ATLAS au LHC

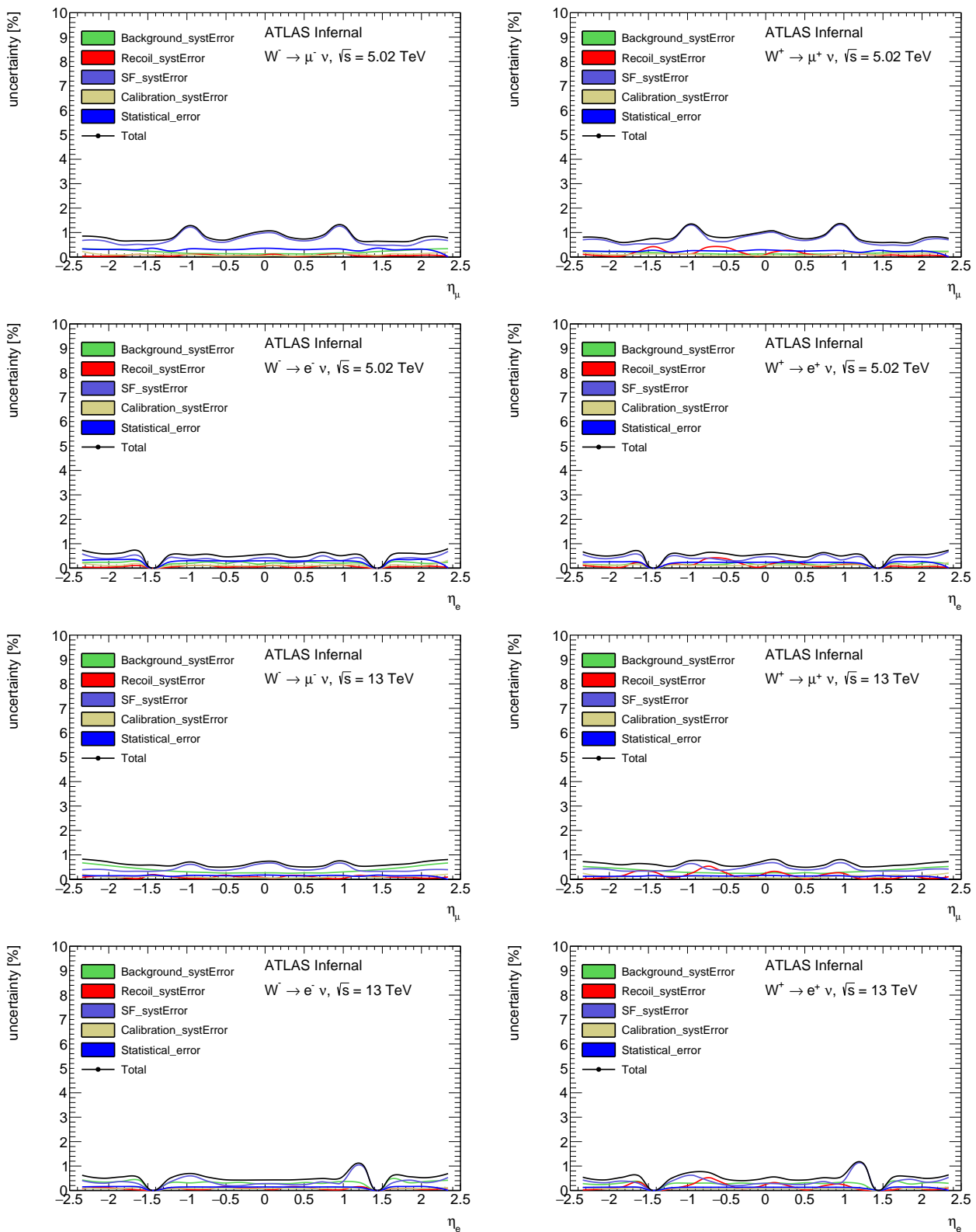


**Figure 115:** Lepton pseudorapidity systematic error breakdown in the muon and electron channel for the  $\sqrt{s} = 5 \text{ TeV}$  and  $\sqrt{s} = 13 \text{ TeV}$  datasets.

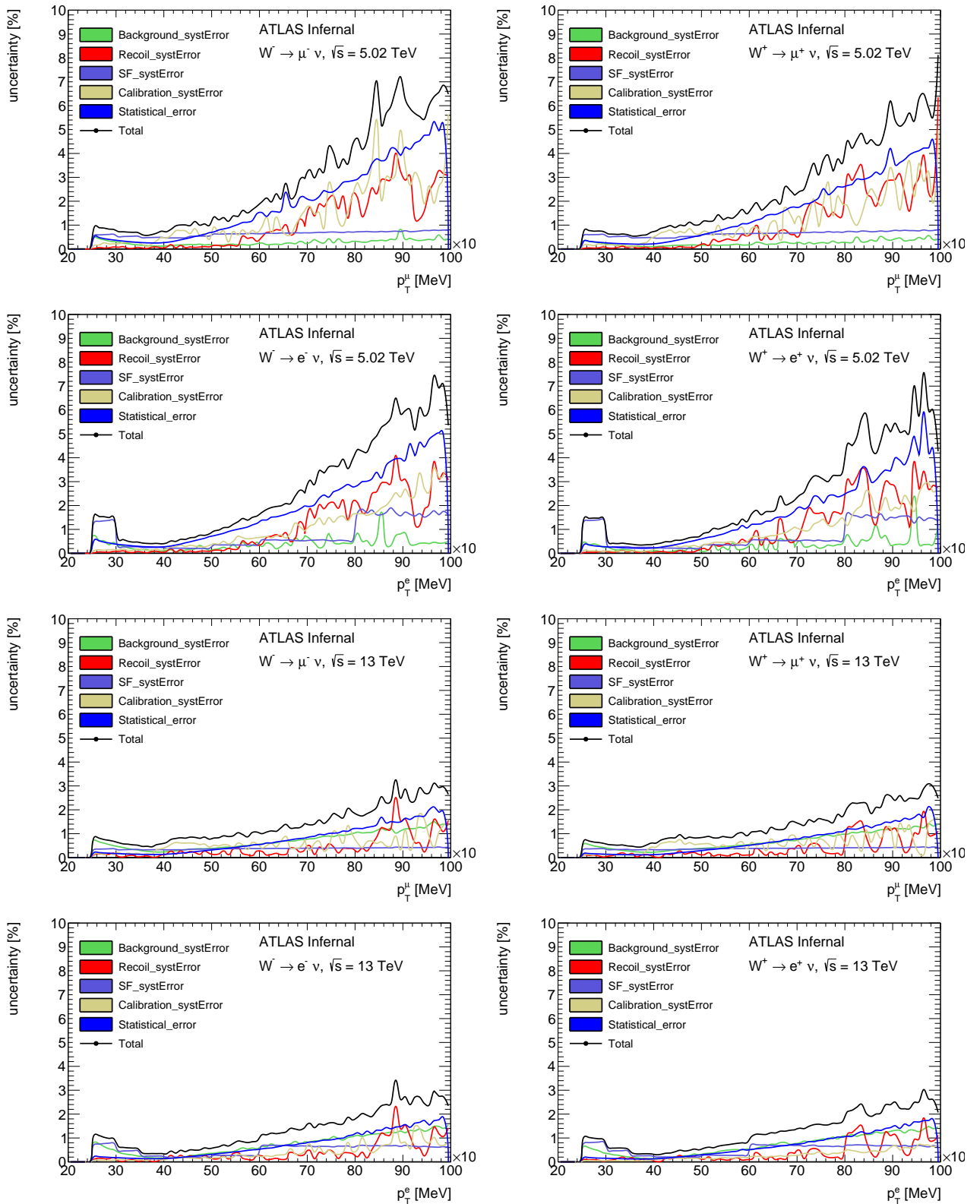


**Figure 116:** Lepton transverse systematic error breakdown distribution in the muon and electron channel for the  $\sqrt{s} = 5 \text{ TeV}$  and  $\sqrt{s} = 13 \text{ TeV}$  datasets.

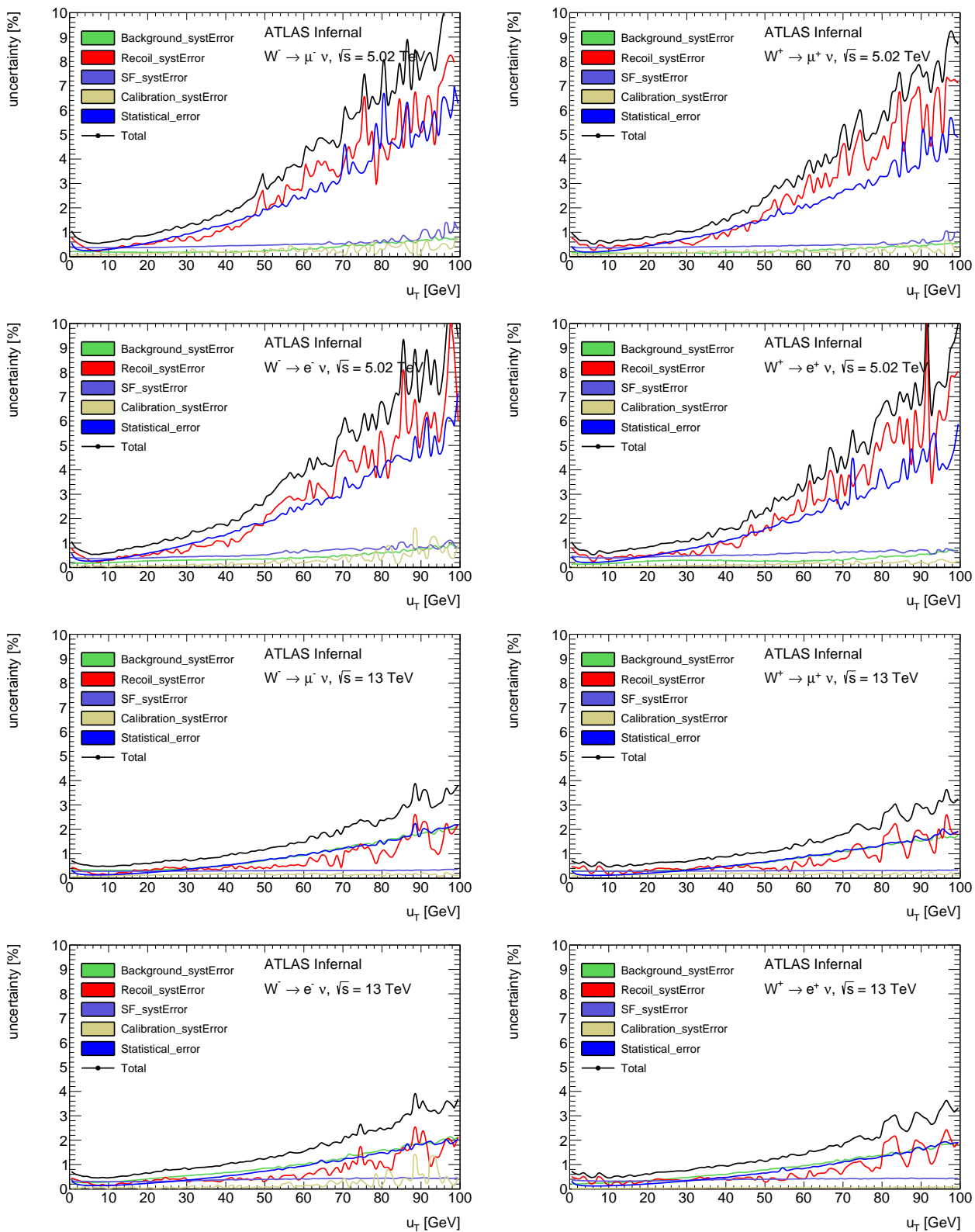


**Figure 117:** W transverse momentum systematic error breakdown in the muon and electron channel for the  $\sqrt{s} = 5$  TeV and  $\sqrt{s} = 13$  TeV datasets.

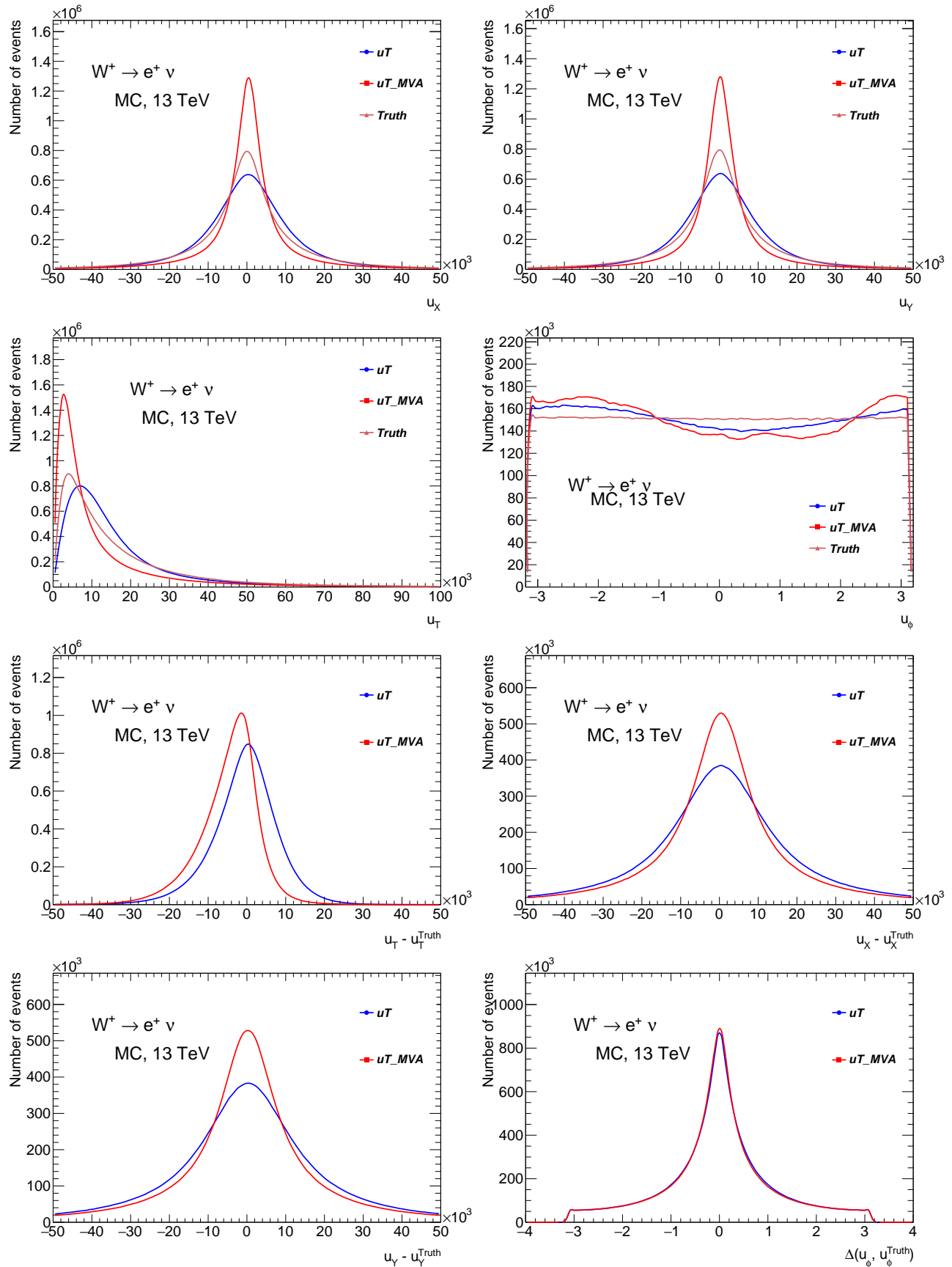
2994

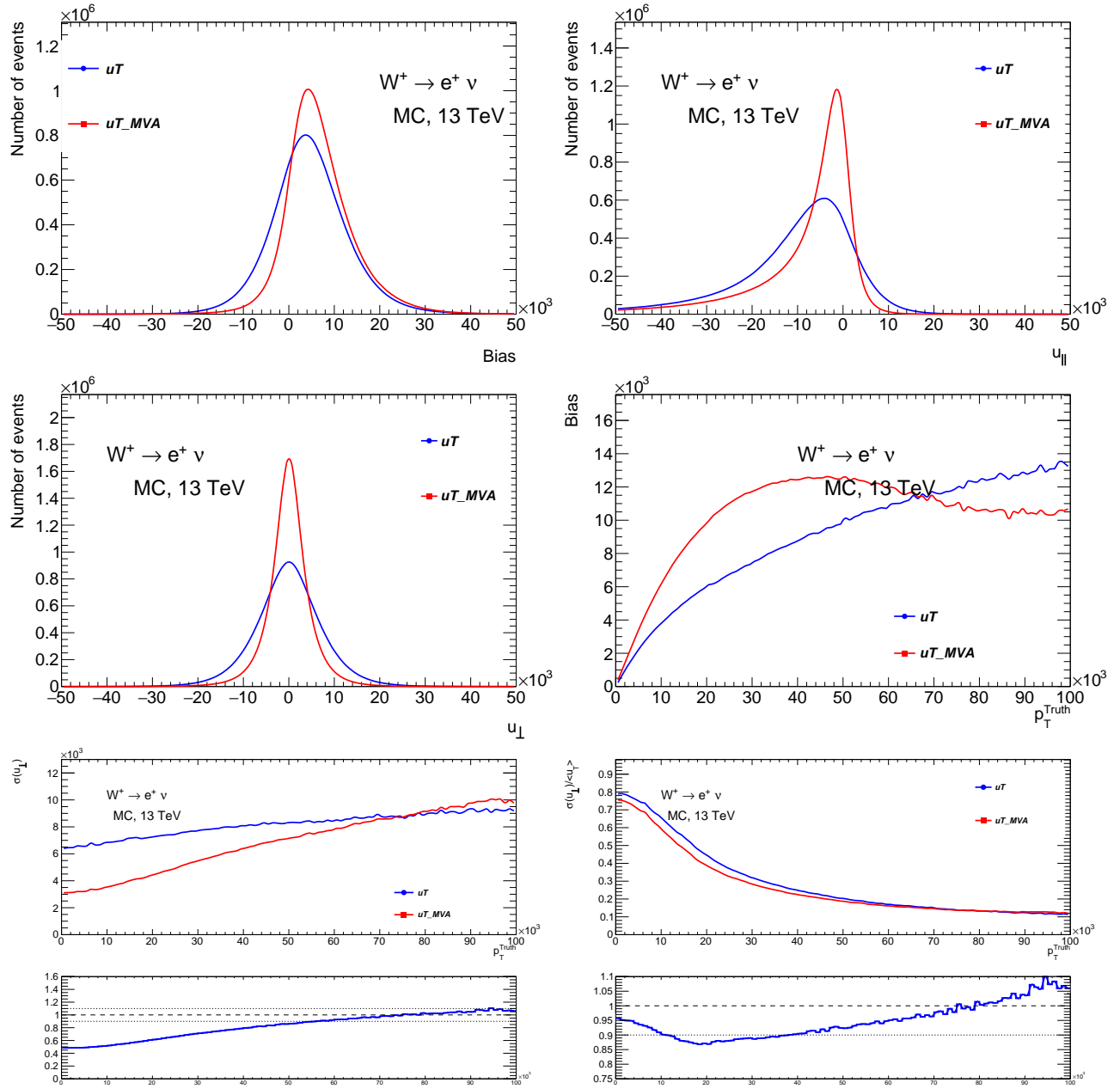
2995

# 12

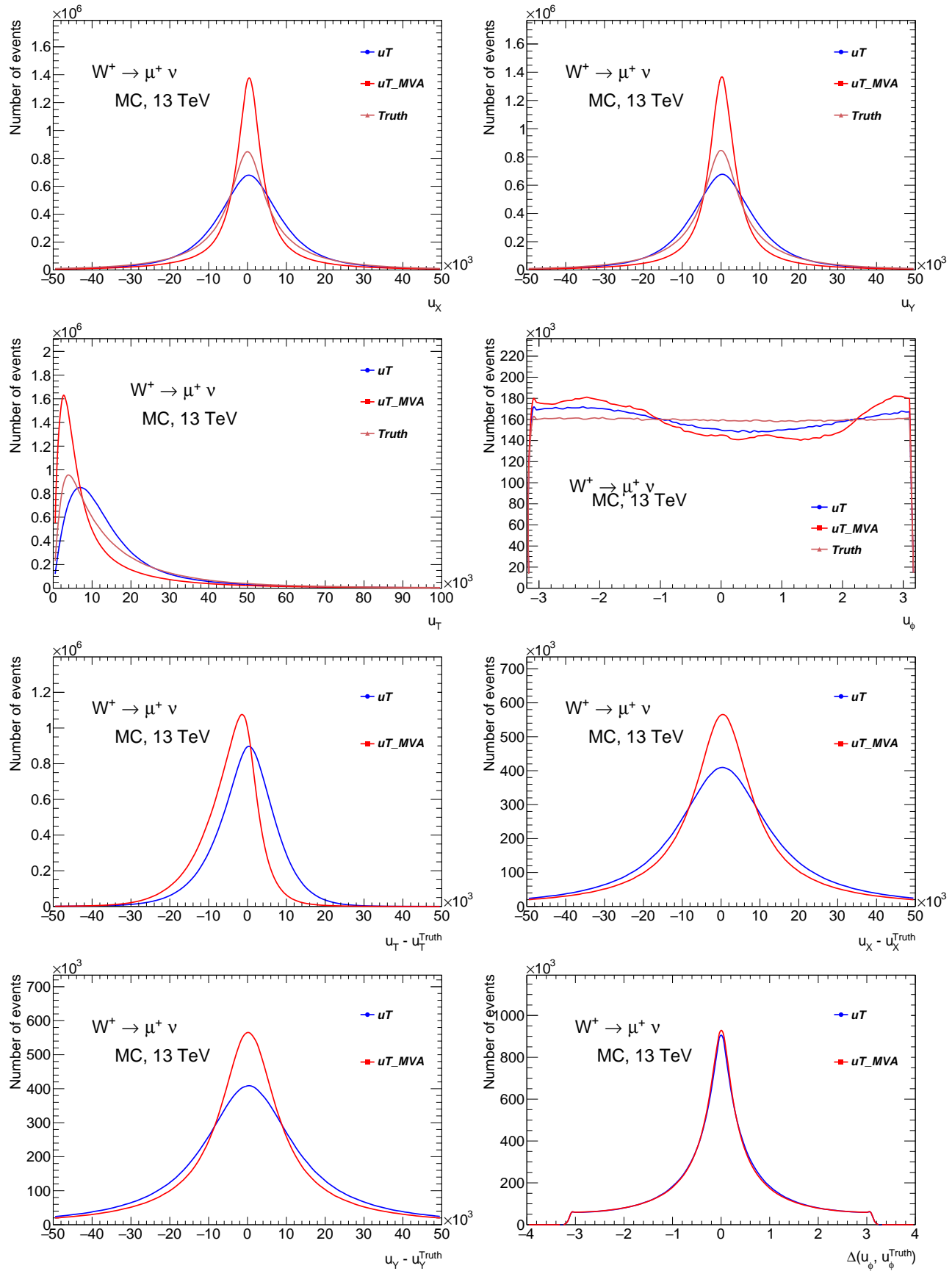
## Appendix B

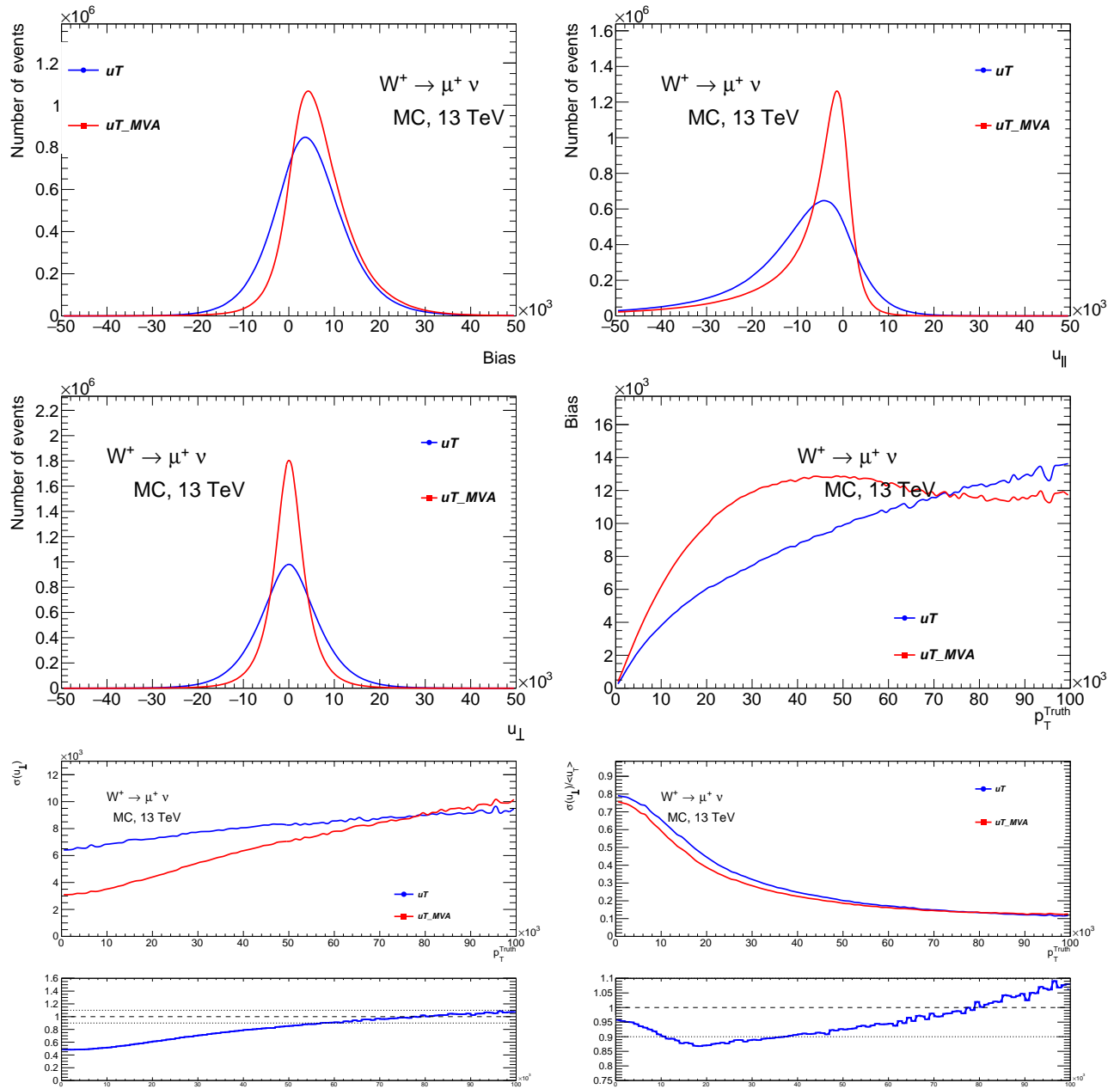
2996 Current appendix contains the comparison of all the kinematic distributions for all W and Z channels.



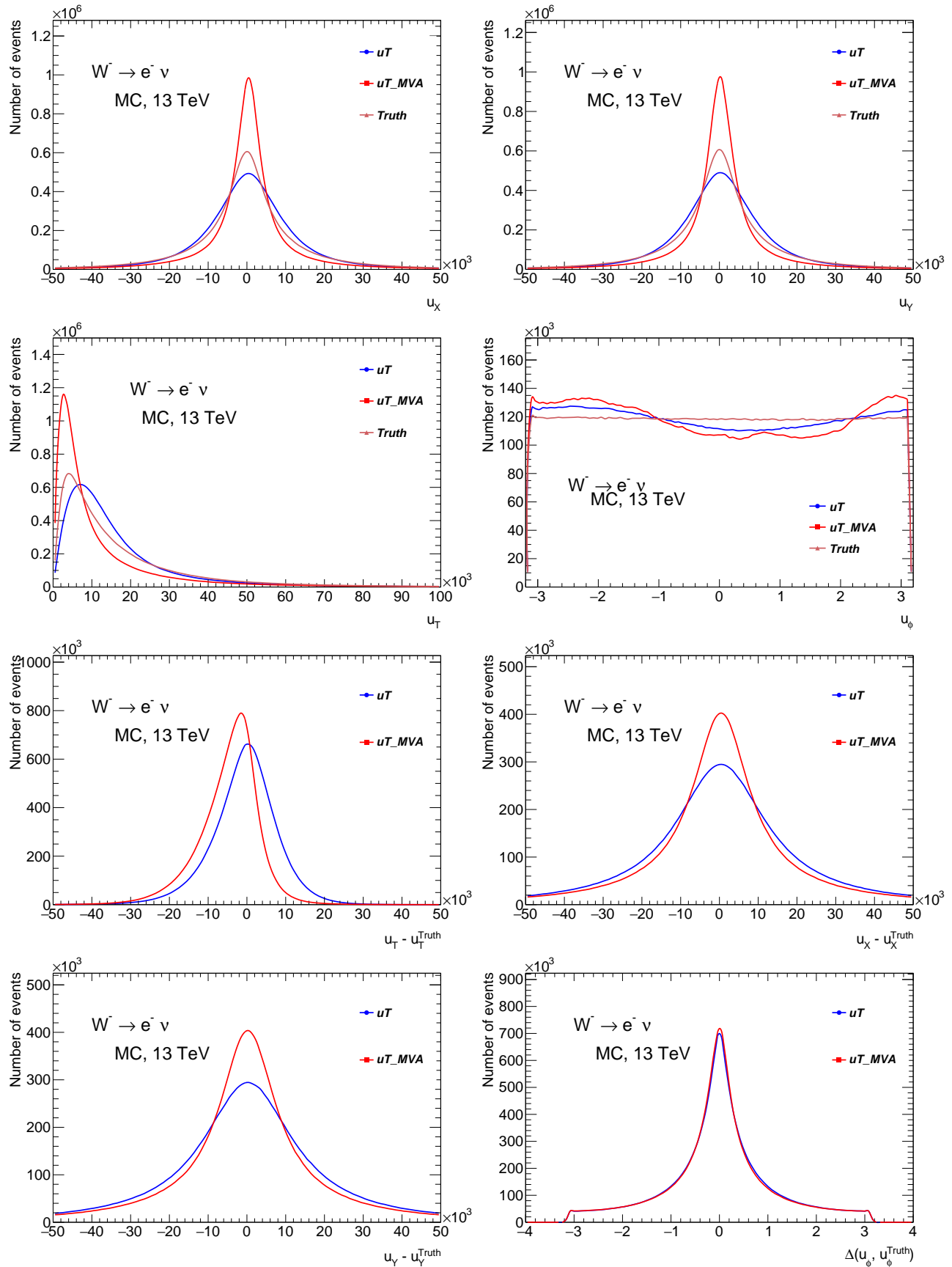


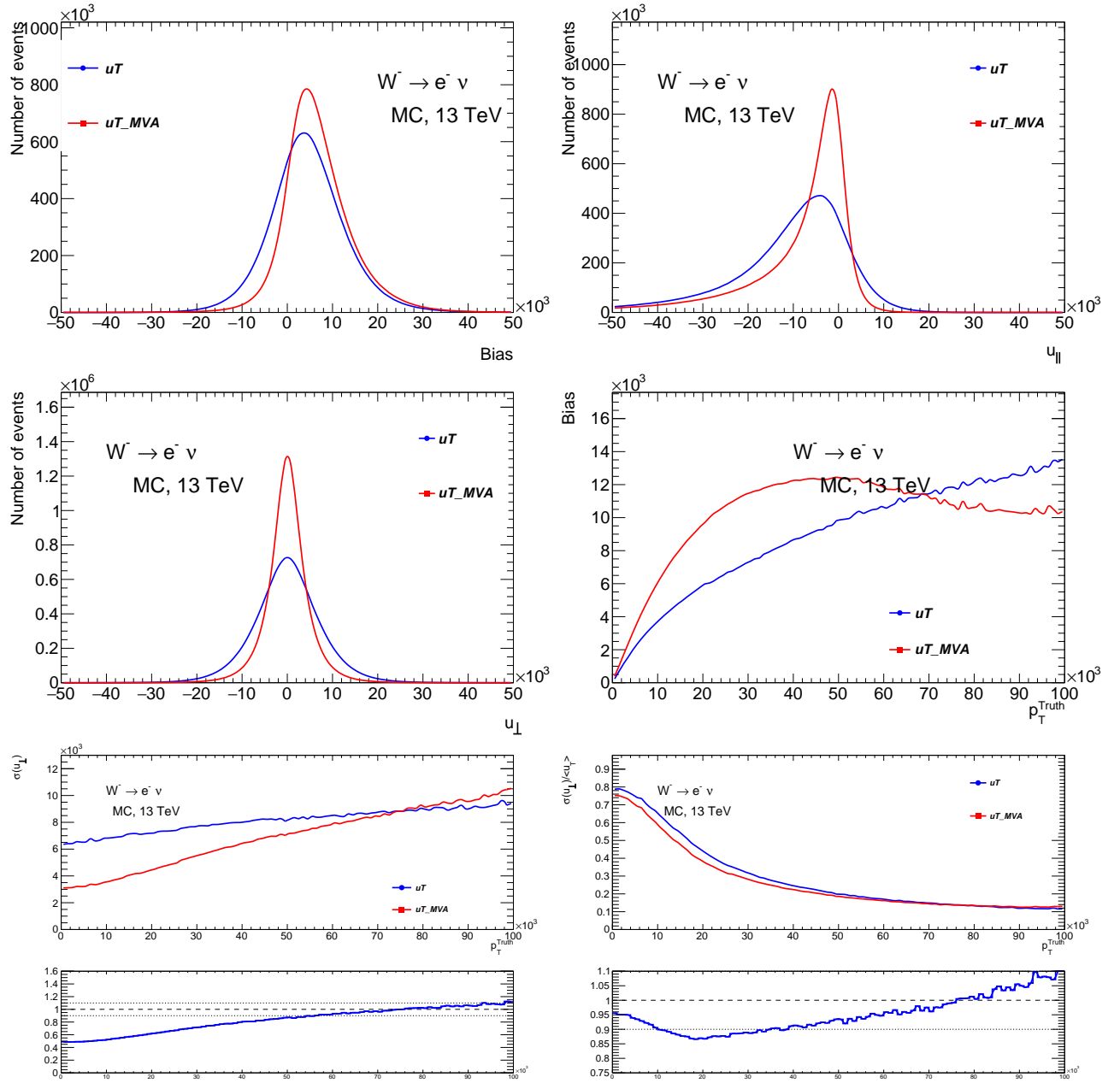
**Figure 121:** Comparison of kinematic distributions of  $u_T$  vs  $u_T^{MVA}$  for  $W^+ \rightarrow e^+ \nu$  data sample.



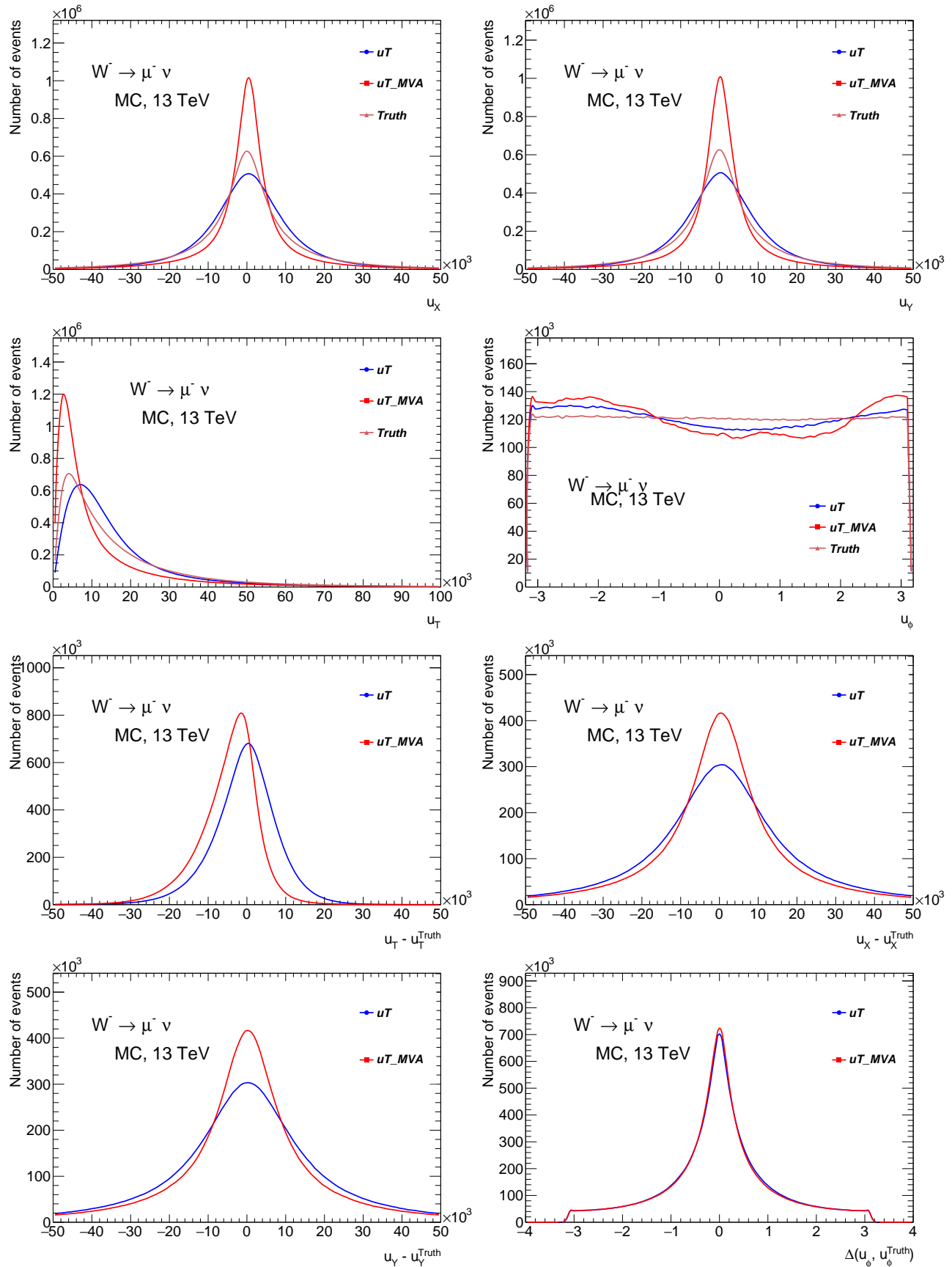


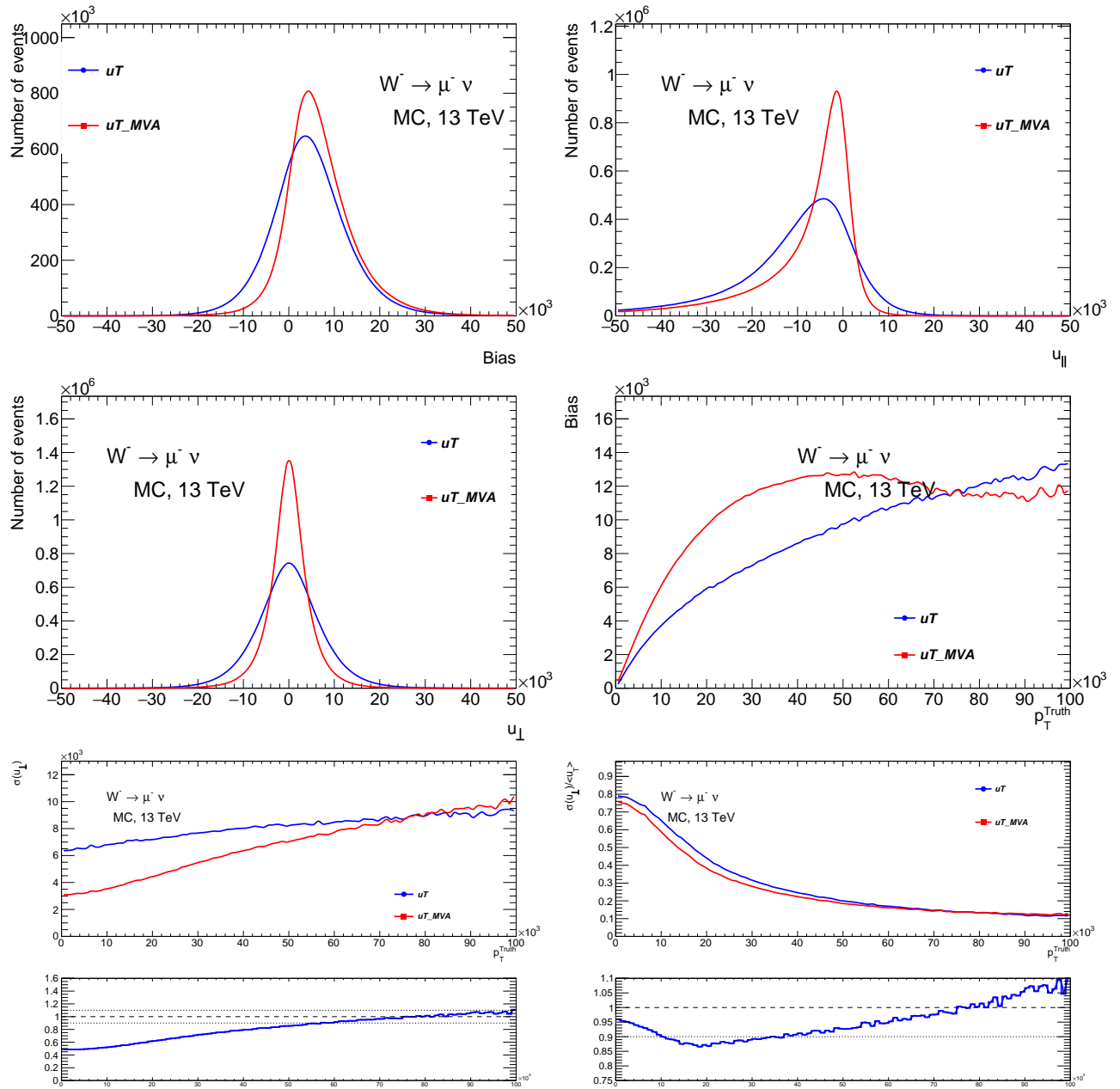
**Figure 122:** Comparison of kinematic distributions of  $u_T$  vs  $u_T^{\text{MVA}}$  for  $W^- \rightarrow e^- \nu$  data sample.



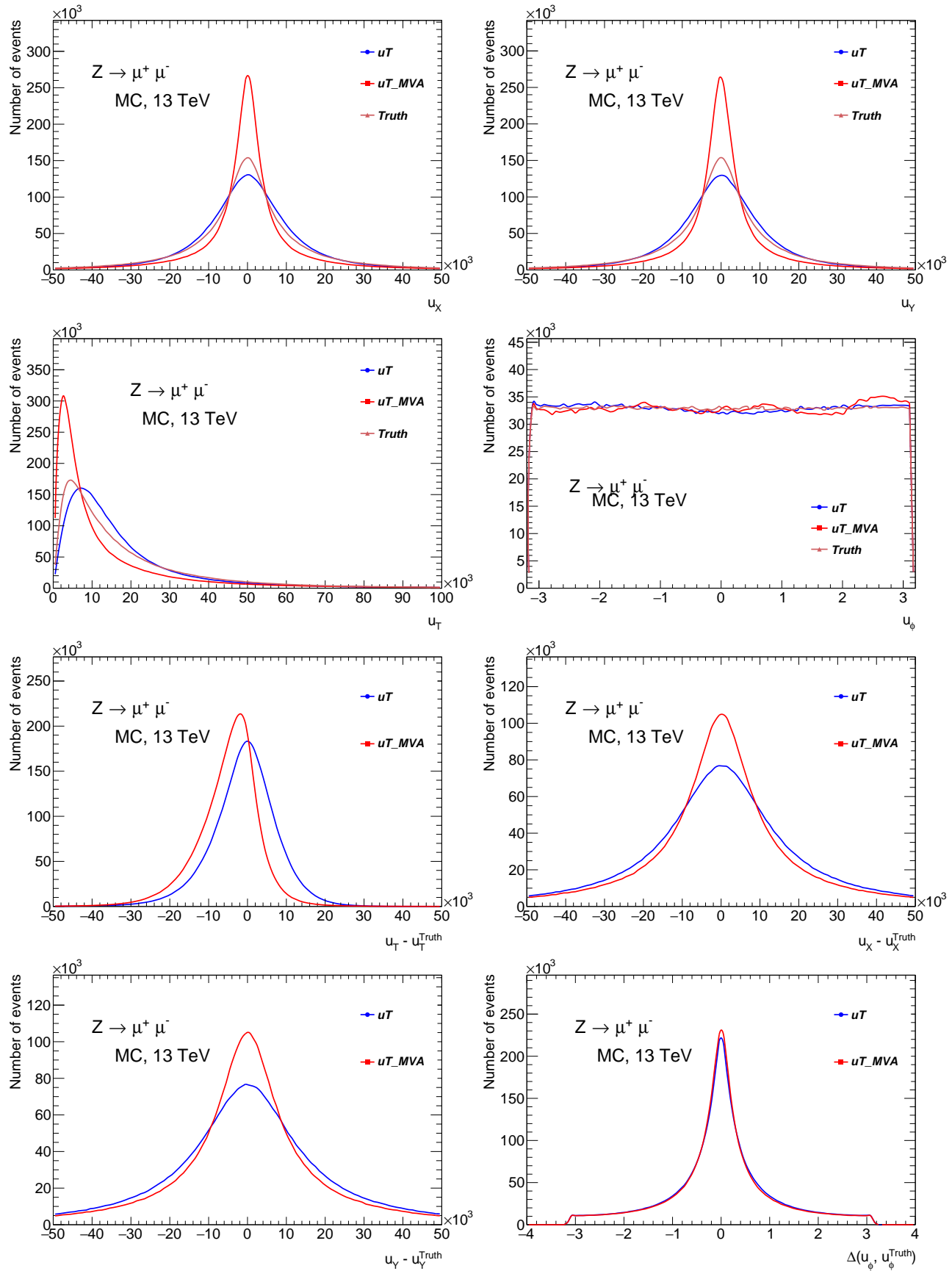


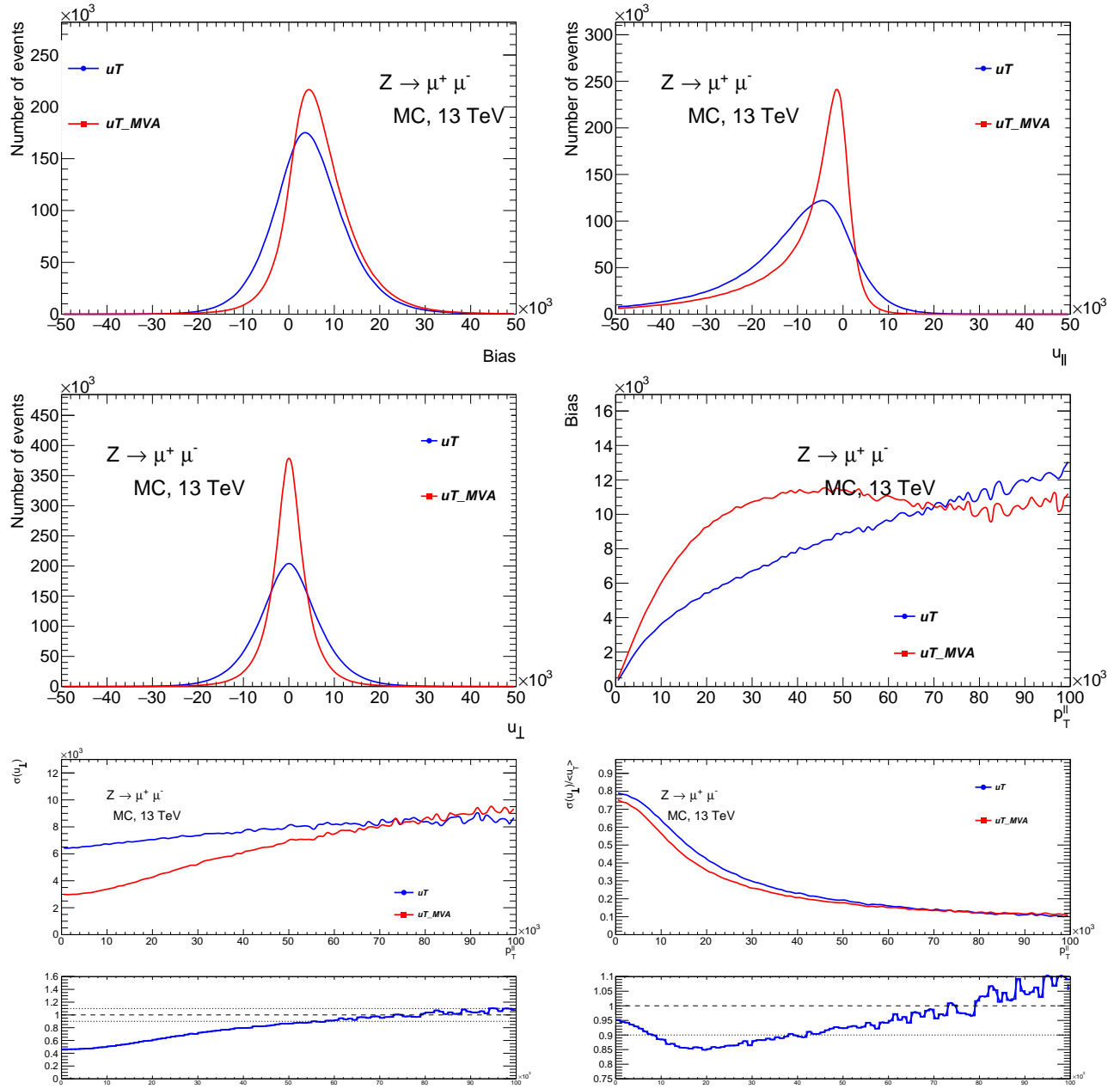
**Figure 123:** Comparison of kinematic distributions of  $u_T$  vs  $u_T^{MVA}$  for  $W^+ \rightarrow \mu^+ \nu$  data sample.



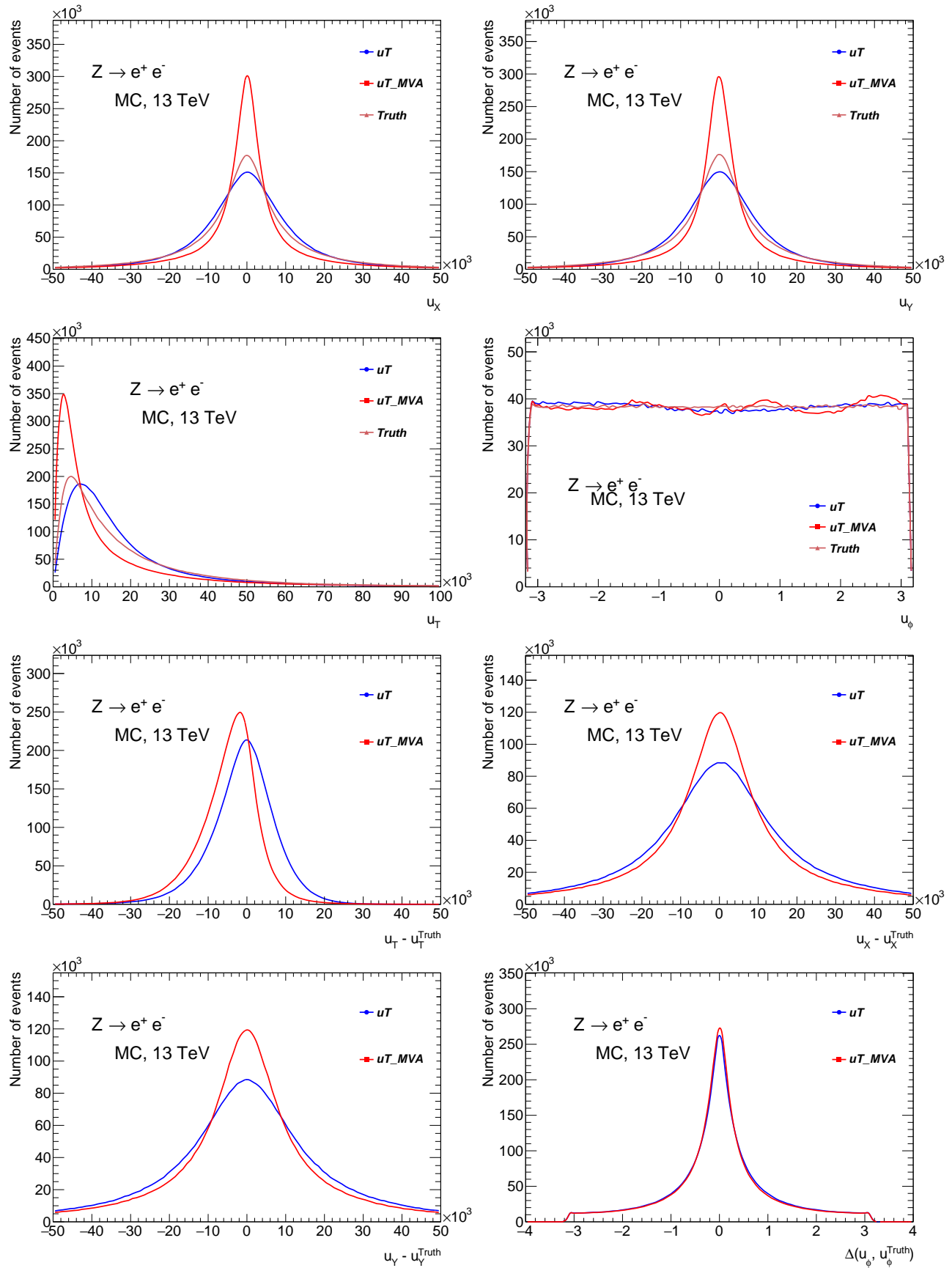


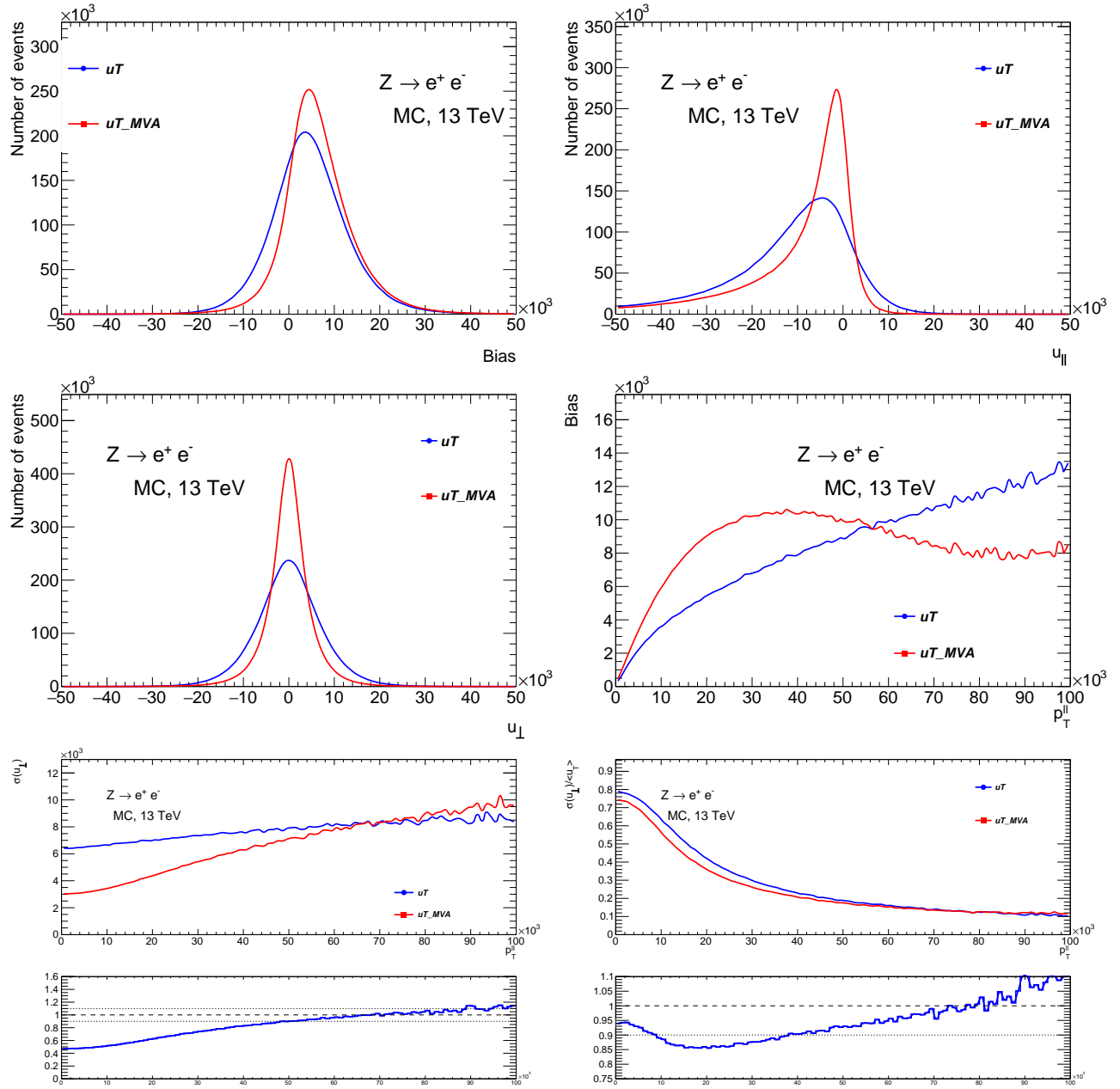
**Figure 124:** Comparison of kinematic distributions of  $u_T$  vs  $u_T^{MVA}$  for  $W^- \rightarrow \mu^- \nu$  data sample.



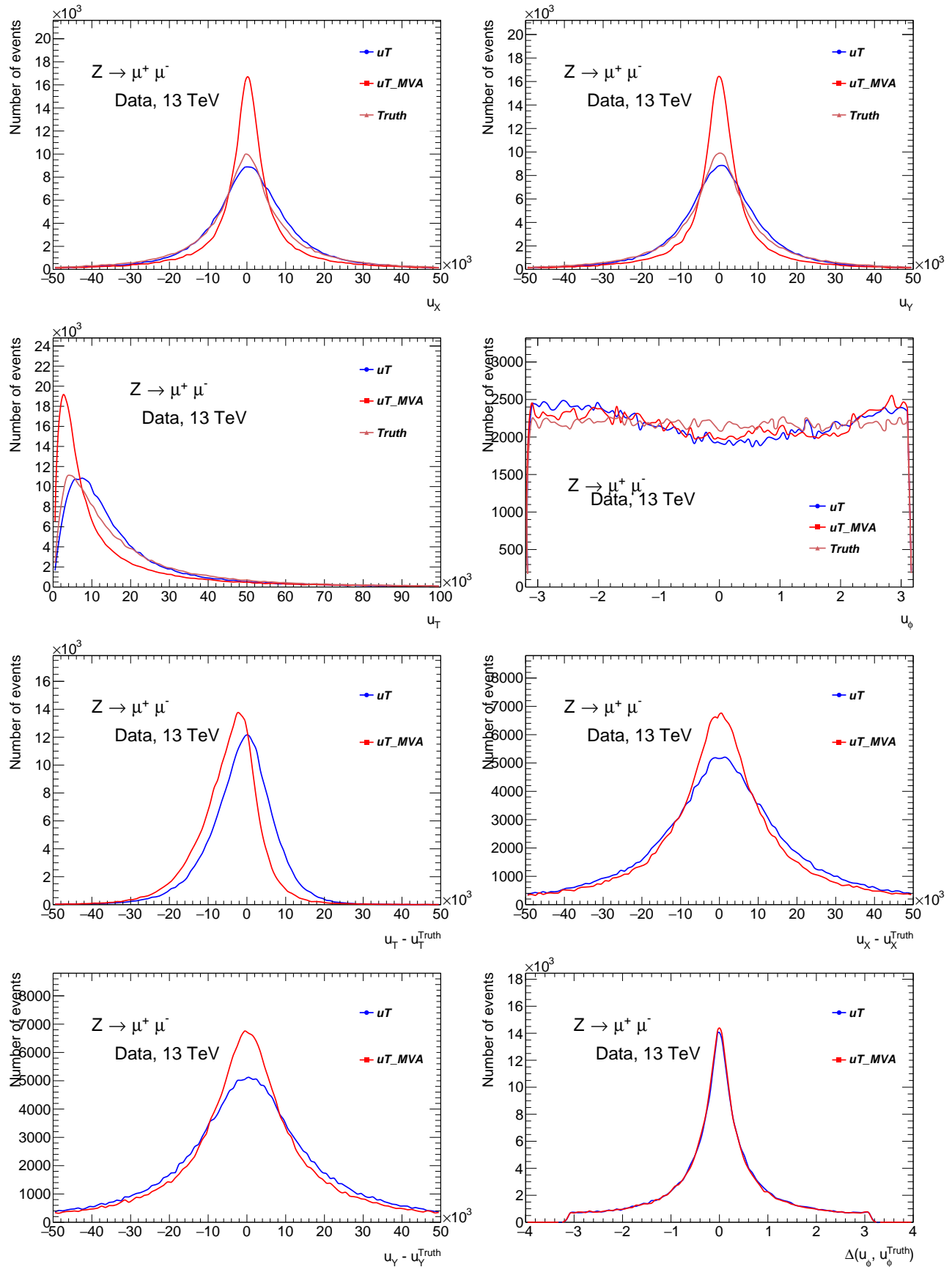


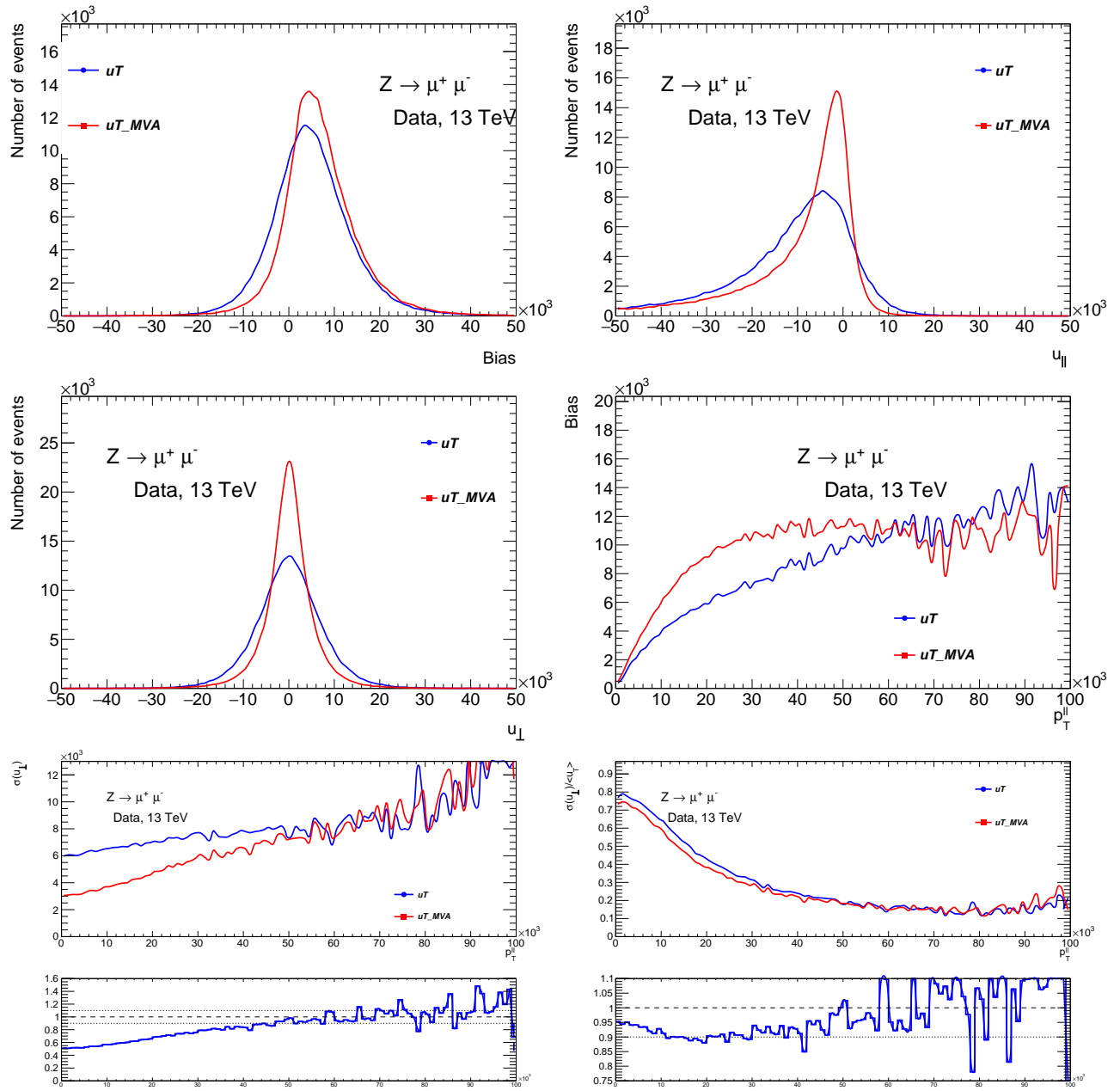
**Figure 125:** Comparison of kinematic distributions of  $u_T$  vs  $u_T^{MVA}$  for  $Z \rightarrow \mu\mu$  MC sample.



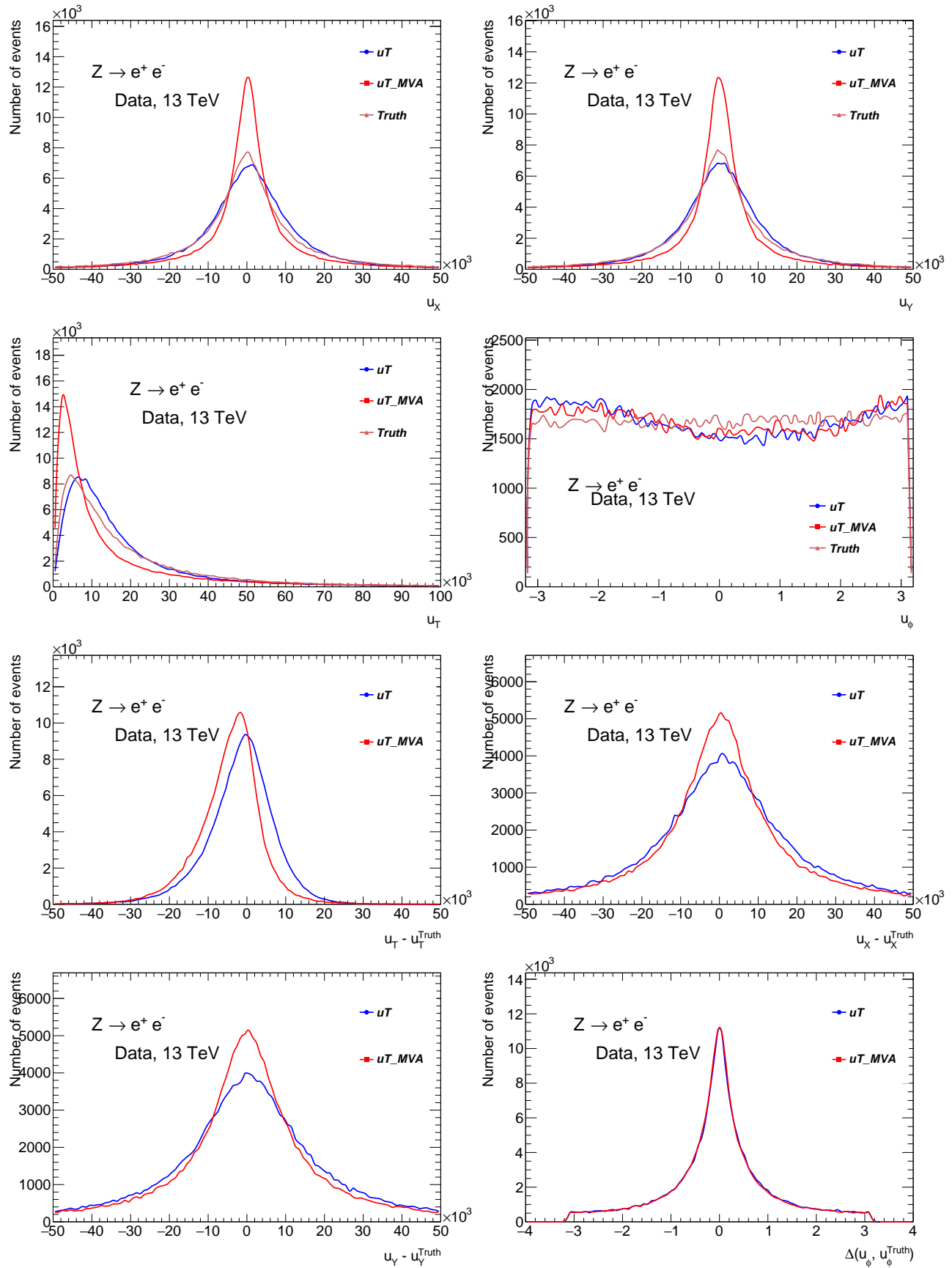


**Figure 126:** Comparison of kinematic distributions of  $u_T$  vs  $u_T^{MVA}$  for  $Z \rightarrow ee$  MC sample.





**Figure 127:** Comparison of kinematic distributions of  $u_T$  vs  $u_{T,MVA}^{MVA}$  for  $Z \rightarrow \mu\mu$  data sample.



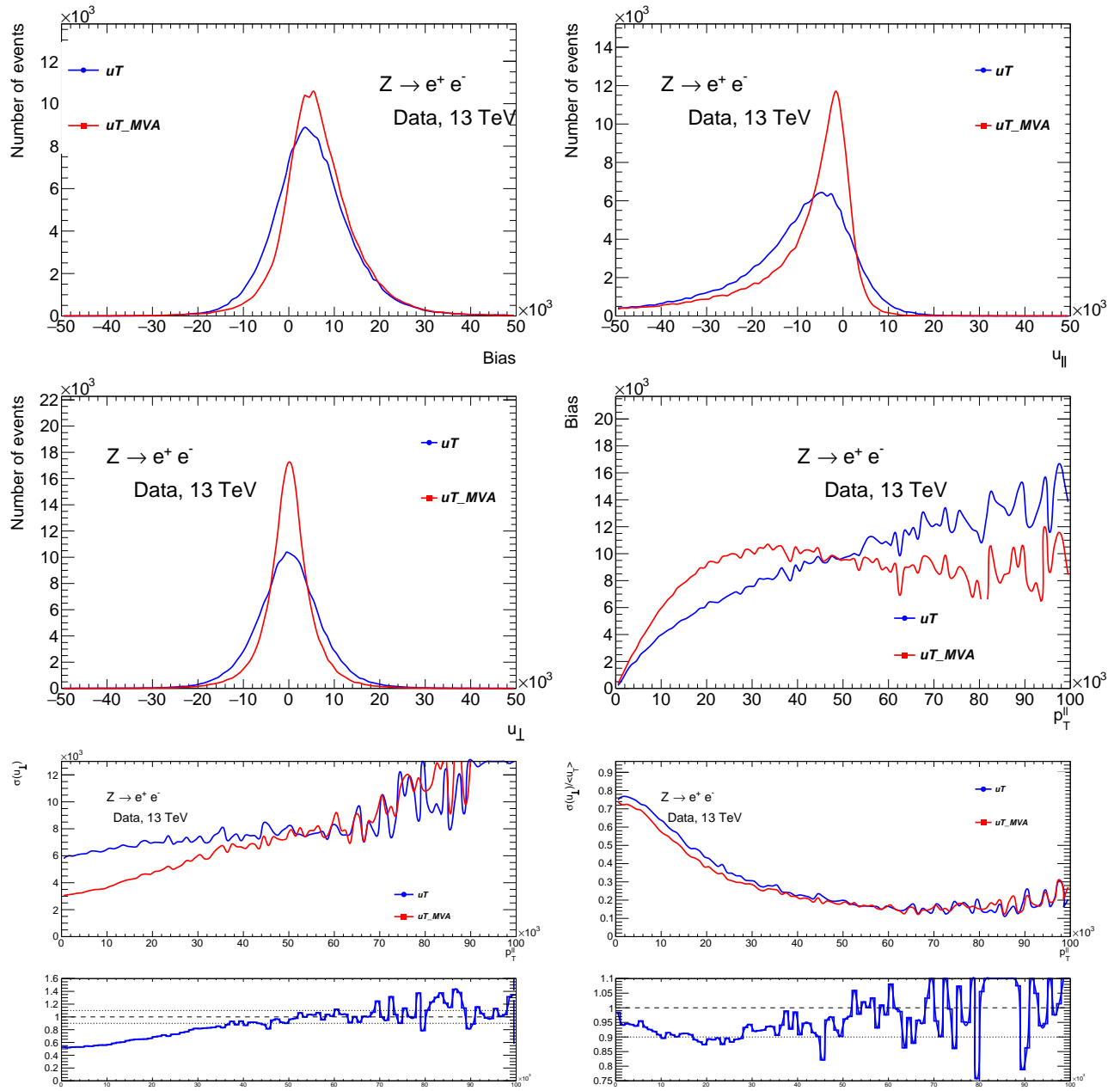


**Figure 128:** Comparison of kinematic distributions of  $u_T$  vs  $u_T^{MVA}$  for  $Z \rightarrow ee$  data sample.